

# **Characterization of low-threshold cryogenic detectors and study of backgrounds for rare event searches**

*By*

**MOULI CHAUDHURI**

PHYS11201804008

**National Institute of Science Education and Research Bhubaneswar**

*A thesis submitted  
to the Board of Studies in  
Physical Sciences*

*In partial fulfillment of requirements  
For the Degree of*

**DOCTOR OF PHILOSOPHY**

*of*

**HOMI BHABHA NATIONAL INSTITUTE**



**April, 2024**



## DECLARATION

I hereby declare that the investigation presented in the thesis has been carried out by me. The work is original and has not been submitted earlier as a whole or in part for a degree/diploma at this or any other Institution/University.

**Date** : 03.07.2024

**Place** : Bhubaneswar

*Mouli Chaudhuri*  
(MOULI CHAUDHURI)

# Homi Bhabha National Institute

## Recommendations of the Viva Voce Committee

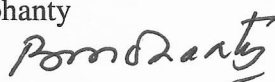
As members of the Viva Voce Committee, we certify that we have read the dissertation prepared by **Mouli Chaudhuri** entitled “**Characterization of low-threshold cryogenic detectors and study of backgrounds for rare event searches**” and recommend that it may be accepted as fulfilling the thesis requirement for the award of Degree of Doctor of Philosophy.

Chairman - Prof. Sanjay Kumar Swain



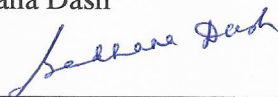
Date: 03/07/2024

Guide / Convener - Prof. Bedangadas Mohanty




Date: 03/07/2024

External examiner - Prof. Sadhana Dash



Date: 03/07/2024


Member 1 - Dr. Kartikeswar Senapati



Date: 03/07/2024

Member 2 - Dr. Tuhin Ghosh

Tuhin Ghosh



Date: 03/07/2024

Member 3 - Dr. Seema Bahinipati



Date:

Final approval and acceptance of this thesis is contingent upon the candidate's submission of the final copies of the thesis to HBNI.

I hereby certify that I have read this thesis prepared under my direction and recommend that it may be accepted as fulfilling the thesis requirement.

Date : 03.07.2024

Place : Bhubaneswar



(Guide)





## STATEMENT BY THE AUTHOR

This dissertation has been submitted in partial fulfillment of requirements for an advanced degree at Homi Bhabha National Institute (HBNI) and is deposited in the library to be made available to borrowers under rules of the HBNI.

Brief quotations from this dissertation are allowable without special permission, provided that accurate acknowledgement of source is made. Requests for permission for extended quotation from or reproduction of this manuscript in whole or in part may be granted by the Competent Authority of HBNI when in his or her judgment the proposed use of the material is in the interests of scholarship. In all other instances, however, permission must be obtained from the author.

**Date** : 03.07.2024

**Place** : Bhubaneswar

*Mouli Chaudhuri*

(MOULI CHAUDHURI)



## DECLARATION

I hereby declare that the investigation presented in the thesis has been carried out by me. The work is original and has not been submitted earlier as a whole or in part for a degree/diploma at this or any other Institution/University.

**Date** : 03.07.2024

**Place** : Bhubaneswar

*Mouli Chaudhuri*

(MOULI CHAUDHURI)



## CERTIFICATION OF ACADEMIC INTEGRITY

### Undertaking by the student

1. I **Mouli Chaudhuri**, HBNI Enrolment No. **PHYS11201804008** hereby undertake that the thesis, titled “**Characterization of low-threshold cryogenic detectors and study of backgrounds for rare event searches**” is prepared by me and is the original work undertaken by me.
2. I also hereby undertake that this document has been duly checked through a plagiarism detection tool and the document is found to be plagiarism free as per the guidelines of the Institute/UGC.
3. I am aware and undertake that if plagiarism is detected in my thesis at any stage in the future, suitable penalty will be imposed as applicable as per the guidelines of the Institute/UGC.

*Mouli Chaudhuri* 03/07/2024  
Signature of the student with date

### Endorsed by the thesis supervisor

I certify that the thesis written by the student is plagiarism free as mentioned above.

*Bedangadas Mohanty* 3/7/2024  
Signature of the thesis supervisor with date

**Name** : Prof. Bedangadas Mohanty  
**Designation** : Professor  
**Department / Centre** : School of Physical Sciences  
**Name of the CI / OCC** : National Institute of Science Education and Research  
Bhubaneswar



---

# List of Publications arising from the thesis

## Journal

### Published

1. M. Chaudhuri et al. “A novel active veto prototype detector with an inner target for improved rare event searches”. *Nuclear Instruments and Methods in Physics Research Section A: Accelerators, Spectrometers, Detectors and Associated Equipment* 1039 (2022), p. 167150.
2. M. Chaudhuri et al. “Development of a large-mass, low-threshold detector system with simultaneous measurements of athermal phonons and scintillation light”. *Nuclear Instruments and Methods in Physics Research Section A: Accelerators, Spectrometers, Detectors and Associated Equipment* 1053 (2023), p. 168374.
3. S. Verma et al. “Low-threshold sapphire detector for rare event searches”. *Nuclear Instruments and Methods in Physics Research Section A: Accelerators, Spectrometers, Detectors and Associated Equipment* 1046 (2023), p. 167634.

### Paperwork under progress

1. M. F. Albakry et al. “Si32 and P32 activity in Si detectors for CDMS II” (2023).



## Conferences

1. Mouli Chaudhuri. “The Mitchell Institute Neutrino Experiment at Reactor (MINER)”. In: *Proceedings of the XXIV DAE-BRNS High Energy Physics Symposium, Jatni, India*. Ed. by Bedangadas Mohanty et al. Singapore: Springer Nature Singapore, 2022, p. 589–593.
2. Mouli Chaudhuri. “Characterization of Sapphire Detector for CE $\nu$ NS Search at MINER”. In: *Advanced Radiation Detector and Instrumentation in Nuclear and Particle Physics*. Ed. by Rajendra Nath Patra. Cham: Springer International Publishing, 2023, p. 97–102.
3. Mouli Chaudhuri et al. “Simultaneous detection of phonon and light in Sapphire scintillation detector for rare event search experiments”. In: *Proceedings of the 66th DAE Symposium on Nuclear Physics*. 2023, p. 1078–1079.
4. Mouli Chaudhuri et al. “Reduction in radioactivity-induced backgrounds using a novel active veto detector for rare event search experiments”. In: *Proceedings of the 14th International Conference on Identification of Dark Matter*. SciPost, 2023, p. 017.
5. Mouli Chaudhuri. “Estimation of  $^{32}\text{Si}$  and  $^{32}\text{P}$  background rate in CDMS II experiment”. In: *Proceedings of the XXV DAE-BRNS High Energy Physics (HEP) Symposium 2022, Mohali, India*. To be published in Springer Nature Singapore, 2024.

## Other publications

1. I. Alkhatib et al. “Light Dark Matter Search with a High-Resolution Athermal Phonon Detector Operated Above Ground”. *Phys. Rev. Lett.* 127 (2021), p. 061801. arXiv: [2007.14289 \[hep-ex\]](#).
2. I. Alkhatib et al. “Constraints on Lightly Ionizing Particles from CDMSlite”. *Phys. Rev. Lett.* 127.8 (2021), p. 081802. arXiv: [2011.09183 \[hep-ex\]](#).

3. Prakruth Adari et al. “EXCESS workshop: Descriptions of rising low-energy spectra”. *SciPost Phys. Proc.* 9 (2022). Ed. by A. Fuss et al., p. 001. arXiv: [2202.05097 \[astro-ph.IM\]](#).
4. M. F. Albakry et al. “Ionization yield measurement in a germanium CDMSlite detector using photo-neutron sources”. *Phys. Rev. D* 105.12 (2022), p. 122002. arXiv: [2202.07043 \[physics.ins-det\]](#).
5. Musaab Al-Bakry et al. “A Search for Low-mass Dark Matter via Bremsstrahlung Radiation and the Migdal Effect in SuperCDMS” (Mar. 2022). arXiv: [2203.02594 \[hep-ex\]](#).
6. M. F. Albakry et al. “A Strategy for Low-Mass Dark Matter Searches with Cryogenic Detectors in the SuperCDMS SNOLAB Facility”. In: *Snowmass 2021*. Mar. 2022. arXiv: [2203.08463 \[physics.ins-det\]](#).
7. M. F. Albakry et al. “Investigating the sources of low-energy events in a SuperCDMS-HVeV detector”. *Phys. Rev. D* 105.11 (2022), p. 112006. arXiv: [2204.08038 \[hep-ex\]](#).
8. M. F. Albakry et al. “Effective Field Theory Analysis of CDMSlite Run 2 Data” (May 2022). arXiv: [2205.11683 \[astro-ph.CO\]](#).
9. M. F. Albakry et al. “First measurement of the nuclear-recoil ionization yield in silicon at 100 eV” (Mar. 2023). arXiv: [2303.02196 \[physics.ins-det\]](#).

**Date** : 03.07.2024

**Place** : Bhubaneswar

*Mouli Chaudhuri*  
(MOULI CHAUDHURI)



## **DEDICATED TO**

*to my parents and all the remarkable minds whose wisdom, guidance, and unwavering belief in me have shaped not only my academic journey but also the person I have become*



## ACKNOWLEDGEMENTS

In the journey of knowledge, gratitude is the compass that guides us, humility is the vessel that carries us, and collaboration is the wind that propels us forward. During my Ph.D. journey, I am grateful to many who have motivated and supported me endlessly. First and foremost, I would like to express my heartfelt appreciation to my parents and my elder sister for their constant source of support. They have made this challenging journey much easier for me. I am thankful to all my family members for their blessings and trust in me that motivate me a lot. My Thakuma and my Dida have always been my strongest pillars of support. I am truly blessed to have such a loving and supportive family by my side.

I extend my deepest gratitude to my supervisor Prof. Bedangadas Mohanty for giving me the opportunity to work with such a wonderful group at NISER. His consistent support and encouragement have been invaluable in helping me maintain my focus and determination throughout this journey. His dedication to his work and responsibilities has been a tremendous source of inspiration for me. I am particularly thankful for his patience and willingness to spend countless hours guiding me through moments of frustration, keeping me motivated and driven. I want to express my gratitude to Dr. Ranbir Singh and Dr. Varchaswi KS Kashyap for always being there for me whenever I needed help. Their consistent support and availability have been invaluable throughout my journey. A special mention goes to Dr. Varchaswi KS Kashyap, who has been a second guide to me. I am sincerely grateful for his efforts in helping me understand the work and all the physics discussion we had. I have learned so many things from him. I extend my deepest thanks for his willingness to dedicate countless hours to me whenever I needed his guidance.

I am very much grateful to Prof. Rupak Mahapatra, Prof. Nader Mirbolfathi, and Dr. Andrew Jastram for our collaborative efforts that led to three publications related to my

PhD thesis. A special thanks to Prof. Rupak Mahapatra for his continuous support and belief in me. Our numerous discussions have been invaluable, and I have gained significant knowledge into detector fabrication and development from him. I also want to express my warm regards to all my colleagues at MINER Dr. Glenn Agnolet, Dr. Andy Kubik, Mr. Mathew Lee, Mr. Mark Platt, and Mr. Sandro Maludze. It has been a pleasure working with such a wonderful group.

I would like to express my heartfelt gratitude to all my SuperCDMS collaborators for their ongoing discussions and feedback on my work within the SuperCDMS project. I extend my thanks to Dr. Robert Calkins, Prof. Alan Robinson, Prof. Wolfgang Rao, Dr. Sagar Poudel, and Prof. Richard Schnee for their invaluable feedback on my work. A special acknowledgment is due to the background group coordinators, Dr. Robert Calkins, Prof. Alan Robinson, and Dr. Sagar Poudel, for consistently encouraging me to progress with my analysis. I also wish to thank Dr. Ziqing Hong, Dr. Emanuele Michielin, and Dr. Valentina Novati, who served as the analysis meeting coordinators for SuperCDMS, for their continuous support in helping me receive positive feedback from the collaboration. A special mention goes to Dr. Michael Kelsey, Dr. Stefan Zatschler, Dr. Elias Lopez Asamar, and Dr. Birgit Zatschler for their ongoing guidance with the simulation work.

I want to express my heartfelt gratitude to my doctoral committee members: Prof. Bedangadas Mohanty, Prof. Sanjay Kumar Swain, Dr. Kartik Senapati, Dr. Tuhin Ghosh, and Dr. Seema Bahinipati. I am also thankful to my thesis reviewers: Prof. Huan Huang, Prof. Nu Xu, and Prof. Sadhana Dash for their positive and insightful comments. Addressing their comments and suggestions has substantially improved my thesis. They have dedicated their time to review my work and provide valuable feedback. I am grateful to the DAE, DST, and HBNI for their financial support both in funding my academic visits and enabling NISER to acquire a dilution refrigerator which has greatly influenced

my thesis topic. I must acknowledge the Garuda high performance computing cluster at NISER which was extensively used by me during my PhD. I am also thankful to Cedar computing cluster at Canada for performing simulation related work for SuperCDMS.

I am truly blessed to be surrounded by such a wonderful group at NISER, which has become like a second home to me. I want to express my deep appreciation to Dr. Vijay Iyer, whose motivation led me to choose this field of research. I owe him many thanks for the insightful discussions we have had and for his constructive criticism, which has taught me valuable lessons throughout my journey. A special acknowledgment goes to my wonderful seniors, including Dr. Vijay Iyer, Dr. Samir Banik, Dr. Dukhishyam Mallick, Dr. Debashis Mallick, Dr. Ashutosh Dash, Dr. Sourav Kundu, Dr. Rihan Haque, Dr. Kishora Nayak, Dr. Yousuf Jamal, and Dr. Ajit Maurya, Dr. Sandeep Dudi. Their kindness and availability to help whenever I faced challenges have been truly appreciated. I also want to extend my special regards to Dr. Ashish Pandav, Mr. Rik Bhattacharaya, Mr. Prottay Das, Ms. Swati Saha, Mr. Sudipta Das, Mr. Bappaditya Mondal, Mr. Sawan, Ms. Sarjeeta Gami, and Ms. Dipanwita Mondal for making my journey extra special. They have always been there for me when I needed them the most. Warm regards to the master students of our lab, including Mr. Ganesh Parida, Mr. Viraj Thakkar, Mr. Soumik Chandra, Mr. Tanmay Pani, Mr. Aranya Giri, Mr. Sharada Prasad Sahoo, Mr. Aman Upadhyay, Mr. Danush S., Mr. Aman Dimri, Mr. Abhishek Anil Deshmukh, and Mr. Rajesh Acharya, Ms. Anna Binoy. A special thanks to Aman for his collaboration on the machine learning technique, resulting in a joint publication. Each one of them holds a special place in my PhD journey.

With the utmost sincerity, I extend my warmest regards to Dr. Shuddha Shankar Dasgupta, Dr. Raveendrababu Karnam, Dr. Ganesh Tambave, Dr. Lusaka Bhattacharya, and Mr. Kirti Prakash Sharma for their guidance and for infusing every moment with joy and enlightenment as I continue to learn and grow.



I express my heartfelt gratitude to my dearest friends: Payal Midya, Ujjaini Banik, Roshni Mandal, Shubham Ghar, Tisthanjeet Dutta, Anibrata Banerjee, Sandeep Mondal, Souvik Bhattacharya, and others, for always standing by my side. I am eternally thankful to my dearest friend, the late Sarkar Intekhab Alam. Your absence is deeply felt, and I wish you were here with me, just as you always were. My deepest regards go out to my friends at NISER, with whom I've shared countless memorable days: Utkalika Sahoo, Shubhasree Sahoo, Shakti Ranjan Mohanty, Abhishek Mishra, Shuvayu Roy, Sourav Bhakta, Akshaya Sahoo, and others. Additionally, I am grateful for the cherished memories with Ishu Aggarwal, Arushi Dhamija, and Navneet Kumar from Chandigarh. I am also thankful to my immediate seniors at NISER, who made my initial days unforgettable: Rashmi Rekha Sahoo, Anupa Kumari, Dipika Dash, Tanim Firdoshi, Charanpreet Singh, Bimalesh Giri, Abhishek Mondal, Shailja Sharma, Surbhi Chauhan, Dola Chakraborty, Tusharadri Mohapatra, Prafulla Saha, Jobin Sebastian, Sujit Garain, Soumya Ranjan Mishra, Sk Jamaluddin. Your guidance and support have meant the world to me.

Lastly, I am thankful to God for giving me such a wonderful journey to experience, providing strength during challenging times, and blessing me with opportunities for growth and learning to achieve my goals.

---

# Summary

Rare event search experiments like Dark Matter searches, Coherent Elastic Neutrino-Nucleus Scattering ( $\text{CE}\nu\text{NS}$ ), and Neutrino-less Double Beta Decay (NDBD) are exciting and challenging as they address unanswered physics questions and push the boundaries of current technology. Dark Matter, constituting 26.8% of the Universe's mass-energy, remains an enigma. In direct detection experiments, Dark Matter particles scatter off target nuclei, producing signals such as light, phonons, charge, or a combination of them, depending on the detector material. The absence of GeV-scale Dark Matter signals compels the exploration of low-mass Dark Matter, requiring detectors with low-energy thresholds.  $\text{CE}\nu\text{NS}$ , which scatters neutrinos coherently with nuclei, faces similar challenges. Another challenge is the mitigation of high background rates from radiogenic and cosmogenic sources, necessitating underground laboratory with passive shielding, and active shielding for in-situ background reduction.

In this thesis, we discuss the development and performance of an annular, cryogenic phonon-mediated active veto detector designed to significantly reduce radiogenic backgrounds in rare event search experiments. The detector consists of a germanium veto

detector weighing approximately 500 g, with an outer diameter of 76 mm and an inner diameter of 28 mm. The veto detector can host a 25 mm diameter germanium inner target detector weighing around 10 g. Using inputs from a GEANT4 based simulation, the detector was optimized to be positioned between two germanium detectors, resulting in a  $> 90\%$  reduction in background rates dominated by gamma interactions. Operating at mK temperatures in the experimental setup, the prototype veto detector achieved a baseline resolution of  $1.24 \pm 0.02$  keV, while maintaining a functional inner target detector with a baseline resolution of  $147 \pm 2$  eV. Experimental results closely matched simulation predictions, affirming the efficiency of the design for aggressive background reduction necessary for neutrino and dark matter search experiments.

This thesis also presents experimental results from a  $\sim 100$  g single-crystal sapphire detector, with a diameter of 76 mm and a thickness of 4 mm, equipped with transition edge sensors (TES). Sapphire, composed of aluminum oxide ( $\text{Al}_2\text{O}_3$ ), emerges as a promising candidate for light mass dark matter search experiments due to its lower atomic mass compared to materials like germanium and silicon. This novel phonon-assisted sapphire detector exhibits a baseline recoil energy resolution of  $28.4 \pm 0.4$  eV. We combine two low-threshold detector technologies, sapphire and  $\sim 100$  g Si High Voltage (HV), to develop a large-mass, low-threshold detector system. It simultaneously measures athermal phonons in a sapphire detector while an adjacent Si HV detector detects scintillation light from the sapphire detector utilizing NTL amplification. This setup allows for event-by-event discrimination between electron and nuclear events due to differences in their scintillation light yield. While previous systems with simultaneous phonon and light detection have employed smaller detectors, this system is designed to provide a large detector mass with high amplification for the limited scintillation light.

This thesis also discusses an ongoing study to precisely measure the decay rates of  $^{32}\text{Si}$

and  $^{32}\text{P}$  using data from Cryogenic Dark Matter Search (CDMS) experiment, collected between 2003 and 2012 at the Soudan Underground Laboratory. The experiment employed 19 Ge and 11 Si cryogenic detectors in a five-tower configuration to detect recoil energy from particle interactions, measuring both phonon and charge energy.  $^{32}\text{Si}$ , a naturally occurring isotope in Si detector material, decays to  $^{32}\text{P}$ , which further decays to stable  $^{32}\text{S}$ , emitting  $\beta$  particles contributing to background for dark matter signals. The analysis comprises three parts: (i) obtaining the main observable, the charge energy after applying all data quality cuts, (ii) modeling the beta decay spectrum of  $^{32}\text{Si}$  and  $^{32}\text{P}$  using Betashape software and comparing it to the Fermi theory of beta decay, and (iii) conducting GEANT4 simulations to model other relevant backgrounds present in the experimental setup. A profile likelihood analysis will be performed, utilizing the three aforementioned inputs, to determine the precise level of  $^{32}\text{Si}$  contamination within Si detectors. The analysis is currently in progress, and this thesis will discuss the current status and future prospects of this investigation. This measurement is crucial not only for SuperCDMS SNOLAB, a future upgrade of the CDMS and SuperCDMS experiment, but also for all rare event search experiments utilizing Si detectors.



---

# Contents

<b>Summary</b>	<b>xxi</b>
<b>List of Figures</b>	<b>xxix</b>
<b>List of Tables</b>	<b>xliv</b>
<b>List of Abbreviations</b>	<b>xlix</b>
<b>1 Introduction</b>	<b>1</b>
1.1 Dark Matter . . . . .	2
1.1.1 Galactic rotation curve . . . . .	3
1.1.2 Gravitational lensing and Bullet cluster . . . . .	5
1.1.3 Large scale structure . . . . .	6
1.2 A picture of dark matter . . . . .	8
1.2.1 Properties of dark matter . . . . .	8
1.2.2 Dark matter candidates . . . . .	10
1.2.3 Methods of detection . . . . .	11
1.3 Direct dark matter detection . . . . .	13
1.3.1 WIMP event rate . . . . .	13
1.3.2 Direct detection experiments . . . . .	19
1.4 Neutrino . . . . .	20
1.4.1 Coherent Elastic Neutrino Nucleus Scattering (CE $\nu$ NS) . . . . .	21

1.5	State-of-the-art detectors in rare event searches and their current status . . .	25
1.5.1	Direct Dark matter searches . . . . .	25
1.5.2	CE $\nu$ NS searches at reactor . . . . .	28
1.6	Backgrounds in rare event searches . . . . .	29
1.7	Preface to work in this thesis . . . . .	30
1.7.1	Cryogenic detectors with veto system . . . . .	31
1.7.2	Simultaneous measurement of phonon and light from Al <sub>2</sub> O <sub>3</sub> . . .	31
1.7.3	Background measurement for dark matter searches . . . . .	32
<b>2</b>	<b>Active veto detector</b>	<b>39</b>
2.1	Types of backgrounds . . . . .	40
2.1.1	Mitigation strategies . . . . .	42
2.1.2	Impact of radiogenic backgrounds on SuperCDMS SNOLAB . . .	45
2.2	Detector technology . . . . .	47
2.2.1	Phonons . . . . .	48
2.2.2	Phonon detection . . . . .	49
2.2.3	Detector geometry and channel layout . . . . .	51
2.2.4	Fabrication challenges and signal readout . . . . .	51
2.2.5	Veto technique . . . . .	54
2.3	Results . . . . .	54
2.3.1	Experimental setup and analysis framework . . . . .	55
2.3.2	Thermal performance . . . . .	57
2.3.3	Calibration . . . . .	59
2.3.4	Baseline resolution . . . . .	60
2.3.5	Test facility: simulation vs. experiment . . . . .	61
2.4	Improvement in background reduction with 4 $\pi$ veto coverage . . . . .	62
2.4.1	MINER: simulation vs. experiment . . . . .	63
2.5	Summary and outlook . . . . .	66
<b>3</b>	<b>Low-threshold detectors for CE<math>\nu</math>NS search at MINER</b>	<b>71</b>
3.1	MINER . . . . .	71
3.1.1	Proposed experimental setup . . . . .	74
3.1.2	MINER detectors . . . . .	75

	Silicon High Voltage (HV) detector . . . . .	78
	Hybrid detector . . . . .	79
	Sapphire ( $\text{Al}_2\text{O}_3$ ) detector . . . . .	81
3.2	Simultaneous detection of phonon and light in sapphire . . . . .	84
3.2.1	Phonon-light measurement . . . . .	85
3.2.2	Experimental setup and data set . . . . .	85
3.3	Analysis and Result . . . . .	87
3.3.1	Processing raw data with Optimal filter (OF) method . . . . .	90
3.3.2	Calibration of Si HV . . . . .	90
3.3.3	Amplification of light in Si detector . . . . .	92
3.3.4	Section summary . . . . .	94
3.4	Detector performance at NSC . . . . .	95
3.4.1	Experimental setup at NSC . . . . .	95
3.4.2	Si HV detector . . . . .	96
	Analysis and results . . . . .	97
3.4.3	Sapphire detector . . . . .	100
	Calibration with $^{57}\text{Co}$ source . . . . .	100
	Al fluorescence . . . . .	102
	Analysis and result . . . . .	103
3.5	Current status of MINER . . . . .	104
3.6	Summary . . . . .	104
<b>4</b>	<b><math>^{32}\text{Si}</math> background estimation in CDMS II experiment</b>	<b>111</b>
4.1	Motivation . . . . .	112
4.1.1	Presence of $^{32}\text{Si}$ isotope in Silicon detectors . . . . .	112
4.1.2	Effect of $^{32}\text{Si}$ background on SuperCDMS SNOLAB sensitivity . . . . .	114
4.2	$^{32}\text{Si}$ background measurement for CDMS II . . . . .	116
4.2.1	CDMS II experiment . . . . .	116
	Cryogenics . . . . .	117
	Shielding . . . . .	118
	Data type . . . . .	119
	Detectors and towers . . . . .	120
	Ionization signal detection . . . . .	121



4.2.2	Analysis flowchart . . . . .	124
4.2.3	Data selection criteria . . . . .	124
	Cut lists . . . . .	125
	Basic cuts . . . . .	125
	Quality cuts . . . . .	129
4.2.4	Data spectrum . . . . .	137
4.2.5	Detector resolution . . . . .	138
	Baseline resolution . . . . .	140
	Resolution of 356 keV events in Si . . . . .	140
	Energy dependent resolution . . . . .	143
4.2.6	Modeling other backgrounds with simulation . . . . .	145
	Gamma simulation for CDMS-II . . . . .	146
	Resolution applied . . . . .	147
	Fitting Results . . . . .	149
4.2.7	Signal modeling . . . . .	150
	Fermi theory of beta decay . . . . .	151
	Relativistic Fermi function: Bethe-Bacher function . . . . .	152
	Betashape . . . . .	153
4.3	Summary and outlook . . . . .	153
<b>5</b>	<b>Conclusion</b>	<b>159</b>
<b>A</b>	<b>Noise and Optimal Filter algorithm</b>	<b>169</b>
A.1	Preliminaries: Fourier transforms and convolution theorem . . . . .	169
	A.1.1 Convolution theorem . . . . .	169
A.2	Noise Power spectral density . . . . .	170
A.3	Optimal filter algorithm . . . . .	172

---

## List of Figures

1.1	The mass-energy distribution of our universe is divided into components: dark energy, dark matter, and ordinary matter. The specific percentages for each component are derived from Ref. [2]. . . . .	3
1.2	Galaxy rotation curve: rotational velocity distribution as a function of the distance from the centre of the galaxy for several spiral galaxies. The flat behaviour at higher radii indicates the presence of additional matter or “Dark Matter”. The figure is taken from Ref. [4] . . . . .	4
1.3	This illustration shows the gravitational lensing effect. The light from a distant quasar bends as it curves around the distorted space near a massive galaxy. Consequently, Earth observes multiple images of the quasar. Image credit: R. Hurt (IPAC/Caltech)/The GrAL Collaboration/ESA [6]. . . . .	5
1.4	The combined optical images from the Magellan and Hubble Space Telescopes depict galaxies in orange and white. The Chandra X-ray image reveals hot intracluster gas (pink), representing the bulk of normal matter. Gravitational lensing exposes the dominance of dark matter (blue), marking the first distinct separation between normal and dark matter in a cluster. Image credit: X-ray: NASA/CXC/CfA; Optical: NASA/STScI; Magellan/U.Arizona; Lensing Map: NASA/STScI; ESO WFI; Magellan/U. Arizona [9]. . . . .	7

1.5	The figure represents a comparison between N-body simulation results and galaxy survey measurements. The red wedges (bottom and right) are extracted from the Millennium simulation. In contrast, the blue wedges (top and left) represent diverse galaxy surveys: Sloan Digital Sky Survey (large top wedge), Center for Astrophysics Survey (small top wedge), and 2dF Galaxy Redshift Survey (left). The observations and simulations closely resemble each other on comparable length scales. The figure is taken from the Ref. [12]. . . . .	9
1.6	The figure illustrates potential solutions to the dark matter problem. The term "little Higgs" denotes candidates within the context of little Higgs models, while "extra dimensions" indicates candidates associated with theories involving additional spatial dimensions. Specific theories include TeVeS (tensor–vector–scalar theory), MOND (modified Newtonian dynamics), and MaCHOs (massive compact halo objects). The figure is taken from Ref. [13] . . .	10
1.7	A cartoon Feynman diagram shows interactions between two SM particles ( $\psi$ ) and two DM particles ( $\chi$ ), featuring collider production (left to right), indirect detection (right to left), and direct detection (bottom to top) methods. . . . .	12
1.8	Helm factor as a function of nuclear recoil energy for germanium target. . . .	16
1.9	The differential rate, measured in counts/kg.days.keV, is calculated for spin-independent WIMP-nucleon elastic scattering with a cross-section value of $\sigma_0^{SI} = 10^{-44} \text{ cm}^2$ . Various WIMP masses are considered, and the target is germanium. . . . .	18
1.10	Summary of direct detection experiments based on the measurement of three types of signals: phonons (heat), scintillation (light) and ionization (charge) caused by the recoil energy transfer by the interacting particles. . . . .	19
1.11	The total cross-section for CE $\nu$ NS (blue) is compared to other neutrino couplings. Cross-sections from charged-current (CC) interaction with iodine (green), inverse beta decay (IBD) (red), and neutrino-electron scattering (dotted red) are shown. CE $\nu$ NS exhibits the largest cross-section, surpassing any charged-current interaction for incoming neutrino energies below 55 MeV. The figure is adapted from Ref. [39]. . . . .	22

1.12	The outcomes of various dark matter search experiments are illustrated in the parameter space of DM-nucleon versus DM mass. The area above each solid curve, associated with a specific experiment, has been ruled out. The region below these solid curves remains unexplored. The neutrino floor, described in the text, is represented by the brown dashed line. This delineates the parameter space region where a DM signal cannot be distinguished from $\text{CE}\nu\text{NS}$ . The figure is created using Ref. [41] . . . . .	24
1.13	(a) Schematic of XENON TPC detector showing the detection principle. The top section of the detector contains a gaseous phase (GXe), while the bottom has a liquid phase (LXe). PMTs positioned at the top and bottom collect light signals. An electric field is applied to gather electrons from the liquid phase. (b) Standard CRESST module detector design. Energy deposition generates phonons, detected by the TES on the target crystal ( $\text{CaWO}_4$ ), and photons, collected by the light detector. Both detectors have a weak coupling to a heat bath at $T_0 \sim 10$ mK. (c) SuperCDMS SNOLAB iZIP detector showing interleaved ionization and phonon sensors on the surface. . . . .	26
2.1	A summary of common backgrounds in rare event search experiments and corresponding mitigation strategies. . . . .	40
2.2	Cosmic muon and neutron fluxes at different underground laboratories with varying overburden depths. The muon flux data points are obtained through measurements, whereas neutron flux data points are computed using simulations and the measured muon fluxes. The depth is expressed in km-water-equivalent. Each data set is fitted with models, and both data and fits are sourced from [1, 3]. . . . .	42

2.3	A Monte Carlo simulation is performed to estimate the expected background rate for SuperCDMS SNOLAB experiment. In the figures it is shown in units of events/kg·yr·keV as a function of recoil energy. (a) and (b) represent background rate in germanium and silicon detector respectively. $^3\text{H}$ (pink) in germanium and $^{32}\text{Si}$ (purple) in silicon are the main contributors to the backgrounds. The remaining relevant backgrounds are Compton scatters from gamma rays (curve in red), surface betas (curve in green), decay daughters of $^{222}\text{Rn}$ (curve in orange), neutrons (curve in blue), and coherent elastic neutrino-nucleus scattering (curve in cyan). The black lines indicate the activation lines in germanium from the electron capture process [16]. . . . .	45
2.4	The sensitivity projection of the SuperCDMS SNOLAB direct detection dark matter experiment demonstrates variations in limits due to different levels of $^{222}\text{Rn}$ contamination. The blue and red lines represent contamination in the silicon and germanium detectors. The lines vary for no contamination (dashed line), standard contamination (dash-dotted line), and contamination 10 times higher than usual (dotted line), with the standard contamination level set at 50 nBq/cm <sup>2</sup> [16]. The figure is taken from [17]. . . . .	46
2.5	A detector schematic showing the phonon generation from a particle interaction. Primary recoil phonons are shown in blue. Green represents NTL phonons generated as electrons and holes drift towards the surface due to the applied bias voltage ( $\Delta V$ ). . . . .	48
2.6	A schematic of TES collecting phonons at the surface of the detector. After entering the Al absorber, phonons break Cooper pairs and produce quasiparticles. They diffuse through Al and are trapped in the W [23]. . . . .	50
2.7	(a) The veto detector is in a copper cage, ready for wire bonding and cryogenic testing. (b) A picture showing the sensor's arrangement, with the inner part missing in the core drill region. Aluminium lines (vias) help wire the inner detector using standard interface boards. The "outer" channel is in green, while the other sensors of the "inner" channels (blue, pink, and orange) are connected to make one big inner channel. (c) The copper nest holds the inner detector, hanging it inside the veto while keeping them well connected for thermal conductivity. (d) The inner detector nest is inside the veto detector, making the whole setup 76 mm wide and 25 mm thick [17]. . . . .	52

- 2.8 (a) Image of the testing facility, showing the dilution refrigerator on the right and the DAQ system on the left. The detector tower mounted on the refrigerator can be seen in (b). (c) Experimental site at MINER with primary Lead and Cooper shielding. . . . . 56
- 2.9 (a) Illustration showing the thermal conduction path from the inner detector to the refrigerator (bath). Dashed lines with dots denote planes of symmetry. Copper is represented in orange, and germanium is in gray. (b) A typical muon pulse in the inner target detector is shown as voltage vs time, indicating quick thermal recovery. The gain was minimized to prevent saturation of the digitizer by the muon pulses [17]. . . . . 57
- 2.10 (a) A typical 60 keV pulse from the inner detector. (b) The noise PSD of inner and outer channels of the active veto detector and the inner detector channel. The noise in inner detector channel behaves differently from veto detector channels due to the application of higher bias voltage on the Quasiparticle-trap-assisted Electrothermal-feedback Transition-edge-sensors (QET) electronics. (c) In the inner target detector, the  $^{241}\text{Am}^9\text{Be}$  source produces a 10.4 keV germanium activation peak, 13.9 keV and 59.5 keV peaks from the  $^{241}\text{Am}$  source, and a 122 keV peak from the external  $^{57}\text{Co}$  source. The spread in the 122 keV peak is due to the external placement of the  $^{57}\text{Co}$  source, while the  $^{241}\text{Am}$  source is internal. Gaussian and linear functions are used for fitting the visible gamma energy peaks. (d) The mean of the gamma energy peaks in arbitrary units is plotted against the energy in keV, confirming the linearity of the energy scale up to 122 keV [17]. . . . . 58
- 2.11 (a) The measured baseline resolution for the inner detector is 147 eV [17]. (b) The veto detector exhibits a baseline resolution of 1.24 keV when coupled with the inner detector. The error bars on the data points represent statistical uncertainties. . . . . 60

- 2.12 (a) An image of an active veto detector with an inner target detector used in the simulation. (b) Simulated energy deposition spectrum (upper panel) for a  $^{137}\text{Cs}$  source and tagging efficiency ( $\eta_{tag}$ ) (lower panel) as a function of energy deposition in the inner detector. The red dashed line in the figure shows the energy deposition spectrum in the inner detector before tagging, while the solid black line represents after tagging with the veto. It indicates that  $\eta_{tag}$  of the veto detector is expected to be between 50%–80% [17]. . . . . 61
- 2.13 (a) and (b) show the distribution of shared energy between the veto detector (on the X-axis) and the inner detector (on the Y-axis) from simulation of  $^{137}\text{Cs}$  source and experimental data, respectively. Compton scatter events are tagged via coincidence [17]. Color code represents the number of events. . . . . 63
- 2.14 (a) A cross-sectional view of the detector stack in CAD used in simulations, consisting of an inner target detector made of germanium and silicon. The inner germanium and silicon detectors have a 25 mm diameter and are placed within an annular germanium veto detector with a 76 mm outer diameter and 28 mm inner diameter. These modules are sandwiched between two 76 mm diameter and 25 mm thick germanium detectors. (b) Simulated energy deposition spectrum (upper panel) and  $\eta_{tag}$  (lower panel) are depicted for germanium inner detectors. The black histogram shows the energy deposition distribution in the inner detector without any veto consideration. The red dotted, blue solid, and green dotted distributions represent energy deposition in the inner detector when tagged with the active veto only, with the active veto and top germanium detector, and with the veto, top, and bottom germanium detectors, respectively. At low energies ( $< 100$  keV), exceeds 70% with only the active veto and increases to  $> 90\%$  when including top and bottom germanium detectors, as explained in (a) [17]. . . . . 64

- 2.15 (a) Simulated background spectra (upper panel) in the inner detector using expected background sources for SuperCDMS SNOLAB, and (b) Background spectra measured by the inner detector (upper panel) at the MINER experimental site with and without a single scatter cut. In both (a) and (b), the black histogram indicates the total energy deposition measured in the inner detector. In contrast, the green histogram represents the energy deposition by single scatter events in the inner detector (upper panel). The lower panel shows the ratio of these two histograms, which measure background reduction. . . . . 65
- 3.1 Reactor neutrino spectrum, where on the horizontal axis, we have neutrino energy measured in MeV, and on the vertical axis, it shows the anti-neutrino flux per fission per MeV. The dashed blue line indicates the Inverse Beta Decay (IBD) threshold. . . . . 73
- 3.2 The GEANT4 geometry model of the experimental cavity with an initial shield design. Various materials are shown in different colours: Blue for water, Dark Blue for graphite, Green for 5% Borated polyethene, Light Gray for high-density (HD) concrete, Dark Gray for Lead, Gold for Copper, and Yellow for Plastic Scintillator. Inside the copper, small disks represent germanium and silicon detectors [1]. . . . . 74
- 3.3 The left axis shows the maximum recoil energy in keV versus neutrino energy in MeV, where Al and O indicate higher recoil energy. On the right axis, the cross-section versus neutrino energy is shown. The blue dash-dotted line represents the cross-section for IBD, while the upper curves represent the cross-section for Al, O, and Si through CE $\nu$ NS, two orders of magnitude higher than IBD. . . . . 76
- 3.4 (a) The mean value of laser energy distributions in arbitrary units across various voltages ranging from 0 V to 320 V. The red line represents a straight line fitted to the data points, and the corresponding fit parameters are also provided. The statistical errors (equivalent to the size of the markers) are shown with each data point. (b) Baseline resolution in units of  $e^-/h^+$  pair units as a function of voltage. The data points are fit to a functional form  $N/S$  where N and S are defined in Eq.3.1 and Eq.3.2. Figures are taken from [13]. . . . . 79



- 3.5 (a) The sharing of phonon energy in the HV and LV phonon channels at a 0 V bias is shown. This is crucial for determining key phonon transport parameters in this hybrid detector. (b) From the  $^{252}\text{Cf}$  calibration source, a distinct separation is seen between the NR (red points) and ER (blue points) events. Figures are sourced from [10]. . . . . 80
- 3.6 The 100 g sapphire detector, with a diameter of 7.6 cm and a thickness of 0.4 cm, used in this work, is kept inside a copper casing. The phonon sensors comprise approximately 1000 TESs, organized into four groups of around 250 sensors each. These groups are independently read out, forming four channels (A, B, C, and D). This arrangement enables the reconstruction of interaction positions in the detector by examining the relative amplitudes among the separate channels. 81
- 3.7 (a) Deposited energy distribution on the sapphire detector, calibrated with the 13.9 keV line (blue). Various dotted lines denote X-ray peaks from  $^{241}\text{Am}$  source and decay products from gold and silver present in  $^{241}\text{Am}$  source. The 59.5 keV gamma from  $^{241}\text{Am}$  source is slightly lower due to the non-linear detector response in this energy range. (b) The distribution of noise amplitude for a single channel (channel D) of sapphire. The standard deviation (STD) of the fitted Gaussian distribution, representing baseline resolution, is  $28.4 \pm 0.4$  eV. (c) For summed over all channels, the baseline resolution is measured at  $39.6 \pm 0.6$  eV. The figures are sourced from [12]. . . . . 82
- 3.8 Diagram of the detector setup in the dilution refrigerator, featuring Si HV and sapphire detectors in cyan and orange, respectively. The detectors are paired to form a module. When a particle interacts with the sapphire, it produces two signals: phonons (read by a TES on the top surface of the sapphire) and photons (collected by the Si detector, also equipped with a TES). Each TES at the surface of both the detectors has four independent readout channels—outer channel A and inner channels B, C, and D. During this run, channel D is not used due to SQUID readout electronics limitations. Calibration involves two known energy sources: an  $^{55}\text{Fe}$  source atop the Si detector and an  $^{241}\text{Am}$  source beneath the sapphire detector [18]. . . . . 86

- 3.9 The t-SNE and DBSCAN input variables are computed using a typical pulse, presented as a voltage variation over time. The parameters extracted include pre-pulse and post-pulse STD (standard deviation) from the first 500  $\mu\text{s}$  and last 256  $\mu\text{s}$  of pulse amplitude. Other features involve the pulse's peak amplitude, the times of its maximum and minimum amplitudes, the maximum of the last 256  $\mu\text{s}$  (max tail), the rise time (time taken for 10% to 90% of the peak from the rising side), and the fall time (time taken for 90% to 10% of the peak from the decay side). Additionally, we calculate the full width at 10%, 50%, and 90% of the pulse amplitude. . . . . 88
- 3.10 (a) Examples of a typical good pulse, pileup pulse, saturated pulse, noise, and ringing pulse are presented for the 100 V dataset. The voltage is plotted against time in microseconds. (b), (c) and (d) depict t-SNE and DBSCAN response plots, where the X and Y axes represent the t-SNE x and t-SNE y axes. The data in 2-dimensional t-SNE space is displayed after clustering with three different voltages: 0 V, 50 V, and 100 V, respectively. In (b) and (c), black, red, and green represent good, saturated, and pileup events, respectively. In (d), we include typical noise and ringing events indicated by blue and pink markers, respectively. Good events (black) are selected for further data analysis across all three voltage datasets. The figure is taken from [18]. . . . . 89

- 3.11 (a) Phonon noise power spectral density (PSD) depicts current amplitude in  $A/\sqrt{\text{Hz}}$  plotted against frequency in Hz. The PSD for two sapphire channels at 0 V is shown in black and red solid curves. For the Si HV detector, PSD for three channels is shown in green, blue, and pink with solid, dotted, and dashed lines corresponding to 0 V, 50 V, and 100 V, respectively. (b) 6 keV peaks from the  $^{55}\text{Fe}$  source in the Si HV detector at 0 V, 50 V, and 100 V are represented by green, blue, and black lines, respectively, along with Gaussian fits shown in red. (c) The mean of the peak in the OF unit is plotted with the applied voltages (0 V, 50 V, and 100 V), revealing a linear amplification of the phonon signal in the experimental data. (d) Baseline resolution in eV is plotted against applied voltages, showing statistical errors with the data points. The lowest baseline resolution value is  $12.33 \pm 0.56$  eV at 100 V, indicating an improvement in the S/N ratio with higher voltages. The data points are fit to a functional form  $N/S$  where N and S are defined in Eq. 3.1 and Eq. 3.2. The figure is sourced from [18]. . . . . 91
- 3.12 (a) The correlation plot showing the relationship between phonon energy measured in sapphire (on the Y-axis) and light output measured in the Si HV detector (on the X-axis) at three different voltages. The light output from 60 keV events originating from an  $^{241}\text{Am}$  source in the sapphire detector is amplified in the Si HV detector. Figure (b) showcases the projected 60 keV events (depicted by black lines) in the Si HV detector, exhibiting the amplified light at different voltages. In (c), the linearity of the amplified light as a function of voltage is demonstrated, with statistical errors associated with the data points. The figure reference is [18]. . . . . 93
- 3.13 (a) A shielding with a 4-inch layer of Lead bricks surrounding the refrigerator, effectively blocking external gamma radiation. (b) A 2 mm thick layer of borated rubber serves as an additional shielding component after Lead shielding. (c) Shows another additional layer of 8-inch thick water bricks. . . . . 96
- 3.14 The TES current amplitude, measured in  $A/\sqrt{\text{Hz}}$ , is plotted against frequency for various voltages ranging from 0 V to 250 V. These plots represent the phonon noise PSDs. The noise performance across all the voltages is consistent. 97

- 3.15 (a) The scatter plot showing the Y partition variable, PyPart versus the X partition variable, PxPart, indicating the positions of  $^{55}\text{Fe}$  events on channel D using Eq. 3.5 and Eq. 3.4. The colour palettes in this representation signify the number of events in each bin. (b) the pulse amplitude distribution from the OF method is presented, showcasing  $^{55}\text{Fe}$  peak fitted with a Gaussian distribution for 100 V data. (c) The mean value of phonon energy distributions in arbitrary units across various voltages ranging from 0 V to 250 V. The red line represents a straight line fitted to the data points, and the corresponding fit parameters are shown. The statistical errors (equivalent to the size of the markers) are shown with each data point [29]. . . . . 98
- 3.16 (a) The distribution of noise energy is shown in the  $e^-/h^+$  pair energy scale for the 100 V dataset. The sigma value from the Gaussian fit represents the baseline resolution of the detector. (b) Baseline resolution in units of  $e^-/h^+$  pair units as a function of voltage. The data points are fit to a functional form  $N/S$  where N and S are defined in Eq. 3.1 and Eq. 3.2 [29]. . . . . 100
- 3.17 The noise performance is compared between NSC and the test facility at Texas A&M University. The noise level at NSC is much higher than at the test facility. 101
- 3.18 (a) A detector tower of low-threshold sapphire with two germanium detectors is placed at NSC. (b) The noise PSDs are shown for four sapphire channels (A, B, C, D) and two channels for each germanium detector. The noise level remains consistent across all detectors. (c) The distribution of phonon amplitudes, obtained through the OF method and summed over all four channels, is shown with  $^{57}\text{Co}$  source. We identify the gamma peak at 122 keV from a  $^{57}\text{Co}$  source, followed by a Compton edge at 39.43 keV. (d) A functional form is used to model the Compton edge at 39.43 keV, and the fitting parameters are provided. 102
- 3.19 (a) The peak identified as Al fluorescence is shown and fitted using a Gaussian. (b) The baseline resolution of sapphire, summed over all channels, is measured at MINER and is  $\sim 61$  eV. This value is higher compared to the resolution at the test facility. The figures are taken from [31]. . . . . 103

- 4.1 Cosmic rays interacting with  $^{40}\text{Ar}$  in the atmosphere create  $^{32}\text{Si}$ , which is transported to Earth through precipitation. This leads to the accumulation of  $^{32}\text{Si}$  in different ways into: A) streams and settling ponds used for silicon mining and refinement water; B) surface sands and near-surface silicon deposits; and C) oceans and lakes, where it can be carried by organisms and end up in sediments [5]. . . . . 113
- 4.2 The projected sensitivity curves of the SuperCDMS SNOLAB experiment are shown in the DM-nucleon cross-section vs. DM mass parameter space for Si HV detector. The black dashed line represents the expected sensitivity using nominal values of  $^{32}\text{Si}$  and  $^3\text{H}$  in Si from literature. The blue dashed lines show sensitivity variations by adjusting the level of  $^{32}\text{Si}$  in Si HV from ten times its nominal value to zero. Similarly, the green dashed lines represent sensitivity variations by adjusting the level of  $^3\text{H}$  in Si from three times its nominal value to zero. The purple dashed line shows the sensitivity curve without the presence of any  $^3\text{H}$  and  $^{32}\text{Si}$  in the detector [8]. . . . . 115
- 4.3 Diagram of the CDMS cooling setup with the dilution refrigerator and internal temperature levels were linked to the icebox via the C stem. The icebox contained six cans, maintained at different temperatures. The detector payload, although not visible, hung in the central can. Detector electronics were supplied from above the payload, connected at the 4 K stage through the E stem [16]. . . 117
- 4.4 Diagrams showing the CDMS shielding viewed from above (a) and the side (b). The outer layer comprises muon veto scintillating panels (light blue) connected to photomultiplier tubes (white and black). Following layers include (from outermost to innermost): 40 cm of polyethylene (green), 18 cm of lead (dark grey), 4.5 cm of ancient lead (light grey), and 10 cm of polyethylene (green). The cryostat (light tan) provides an average of  $\sim 1.9$  cm of copper shielding. Also depicted are the E-stem and C-stem penetrations (brown) and the dilution refrigerator (dark blue) in relation to size and position [16]. . . . . 118

4.5	(a) Shows the type and position of ionization and phonon read-out channels for the oZIP detector (left). On the right, there is an image of a person holding an actual oZIP detector from a tower. (b) Illustrates the arrangement of ZIPs in CDMS-II. The detectors are identified by tower (T1-T5) and position within the tower (Z1-Z6). Different colors represent different types of detectors: aqua for germanium and beige for silicon. This tower arrangement into two rows reflects how the towers were positioned in the icebox [16, 17]. . . . .	121
4.6	Example of ionization pulses from both inner and outer sides for a sample event with a recoil energy of around 511 keV. The pulses from the inner channel is moved up by 5 mV for better visibility [16]. . . . .	123
4.7	Analysis flowchart describing the steps for estimation of $^{32}\text{Si}$ decay rate in Si detectors for CDMS-II experiment. . . . .	125
4.8	Tree diagram showing the different cuts applied in the analysis of $^{32}\text{Si}$ background estimation. The cuts are grouped into two categories: (1) Basic cuts and (2) Quality cuts. . . . .	126
4.9	(a) and (b) show the distributions of QIstd (green curve) and QOstd (blue curve) for the zip27 detector in r125, respectively. The red curve shows the fitted Gaussian function. The mean ( $\mu$ ) and standard deviation ( $\sigma$ ) of the fitted Gaussian are indicated on the plot. The black solid line marks the position of the charge pre-pulse standard deviation cut on the QIstd and QOstd distributions.	129
4.10	(a) A graphic representation of the number of charge and phonon triggers in r128 data. (b) The glitch cut removes events above the black line. . . . .	130
4.11	(a) Correlation between charge $\chi^2$ and charge energy is shown for zip19 in r125. Black solid line shows the cut position. (b) Fit to the $\chi^2$ cut efficiencies as a function of energy for zip19. . . . .	131
4.12	FV cut on qi vs qo parameter space is shown. Red solid line shows the cut position. . . . .	132
4.13	qo distribution for different energy ranges of energies are shown for zip4 for r125.	133
4.14	FV cut efficiencies as a function of phonon recoil energy for zip6 is shown. A polynomial3 function is fitted with the data points. . . . .	134

- 4.15 Alpha cut applied to the parameter space of charge energy (qsum) versus total integrated phonon energy (ptint). The green dots represent events without any cuts, the red dots show events with basic and quality cuts, and the blue open-circle markers denote events with basic, quality, and alpha cuts. The black dotted lines indicate the positions of the cuts where alpha-tagged events are depicted as blue open-circle markers. . . . . 135
- 4.16 (a) Events in yield (yg) vs phonon recoil energy (prg) parameter space is shown. Black, red and green dashed lines represent  $3\sigma$ ,  $4\sigma$  and  $5\sigma$  ER cut. (b) Those above mentioned ER cuts position is shown in  $^{252}\text{Cf}$  data. . . . . 136
- 4.17 Combined charge distribution from all good Si detectors after applying all basic and data quality cuts, comprising a total of 188797 events. . . . . 138
- 4.18 (a) The noise distribution of the combined channel  $q_i+q_o$  is shown for detector zip10 in r125. The baseline resolution, measured by the  $1\sigma$  width, is indicated by the black lines. (b) There is no observed correlation between the  $q_i$  and  $q_o$  channels. . . . . 141
- 4.19 Baseline resolutions of all the Si and their neighboring Ge detector from r125-128 are shown. In the figure open markers represent Si detector baseline resolution and solid marker represent Ge detector baseline resolution. . . . . 141
- 4.20 The graph shows the distribution of shared charge energy (qsum) between the closest Ge detector (zip14) and Si detector (zip15) from  $^{133}\text{Ba}$  events in the combined r125-128. The bands represented by red and green lines are the summed energies of 356 keV and 384 keV, respectively. . . . . 142
- 4.21 (a) Vertical lines show the energy bin 15-30 keV in Si detector, zip15. (b) Shows the histograms of the summed energy (Ge+Si) in the energy bin 15-30 keV. . . . . 143
- 4.22 (a)  $^{133}\text{Ba}$  shared event energy resolution as a function of energy. The distribution is fitted with the resolution model where  $A_1$  and  $A_2$  are fixed for each detector pair with uncertainty on the model keeping  $A_3$  parameter free. (b) Charge energy resolution in Si detectors are shown upto 2000 keV. Solid curves are the resolution for each detectors where dotted line is an average over the resolution of all detectors. . . . . 144

4.23	The CDMS-II setup is depicted in a GEANT4 simulation, showing its geometry. The shielding includes outer layers of poly (green) and lead (grey), followed by inner layers of lead (grey), poly (green), mu metal (yellow), and cryostat cans (blue). At the center of the setup are the detector volumes containing Si and Ge oZIPs arranged in five towers. . . . .	147
4.24	(a) and (b) Simulated energy spectrum with and without resolution applied for Germanium and Silicon detectors respectively. The effect of resolution can be seen by the boardening of gamma peaks for both the detectors. . . . .	148
4.25	Charge energy spectrum (green) compared to the weighted sum of simulation spectra (red) shown for detector zip15 in r125. The fit matches well with the data. . . . .	149
4.26	(a) Beta decay spectrum using Betashape is compared with the distribution from Fermi theory for $^{32}\text{Si}$ . (b) Ratio plot between Betashape and Fermithoery showing a deviation of 2%. . . . .	151
4.27	(a) Beta decay spectrum using Betashape is compared with the distribution from Fermi theory for $^{32}\text{P}$ . (b) Ratio plot between Betashape and Fermithoery showing a deviation of 5%. . . . .	152





---

## List of Tables

3.1	MINER reactor details . . . . .	72
3.2	Detectors developed for MINER experiment . . . . .	77
4.1	CDMS-II detectors . . . . .	120
4.2	Charge energy resolution fit parameters . . . . .	145
4.3	List of other backgrounds . . . . .	146
4.4	Number of simulated decays from each decay-geometry source. . . . .	148
4.5	Contamination levels . . . . .	150



---

## List of Abbreviations

<b>ATLAS</b>	A Toroidal LHC ApparatuS
<b>CDEX</b>	China Dark Matter Experiment
<b>CDMSlite</b>	CDMS Low Ionization Threshold Experiment
<b>CDMS</b>	Cryogenic Dark Matter Search
<b>CDM</b>	Cold Dark Matter
<b>CE<math>\nu</math>NS</b>	Coherent Elastic Neutrino Nucleus Scattering
<b>CERN</b>	Conseil Européen pour la Recherche Nucléaire, The European Organization for Nuclear Research
<b>CMS</b>	Compact Muon Solenoid
<b>CoGeNT</b>	Coherent Germanium Neutrino Technology
<b>COUPP</b>	Chicagoland Observatory for Underground Particle Physics
<b>CPD</b>	Cryogenic PhotoDetector
<b>CP</b>	Charge-Parity
<b>CRESST</b>	Cryogenic Rare Event Search with Superconducting Thermometers
<b>DAMIC</b>	Dark Matter In CCDs
<b>DAQ</b>	Data Acquisition
<b>DEAP</b>	Dark Matter Experiment Using Argon Pulse-Shape Discrimination

<b>DM</b>	Dark Matter
<b>EC</b>	Electron Capture
<b>EDELWEISS</b>	Expérience Pour Détecter les WIMPs En Site Souterrain
<b>ER</b>	Electron Recoil
<b>GEANT</b>	Geometry And Tracking
<b>HV</b>	High Voltage
<b>iZIP</b>	Interleaved Z-sensitive Ionization Phonon
<b>LFN</b>	Low Frequency Noise
<b>LHC</b>	Large Hadron Collider
<b>LMDM</b>	Low Mass Dark Matter
<b>LNGS</b>	Laboratori Nazionali Del Gran Sasso
<b>LSS</b>	Large Scale Structure
<b>LUX</b>	Large Underground Xenon experiment
<b>LZ</b>	LUX-ZEPLIN
<b>News-G</b>	New Experiments With Spheres-Gas
<b>NR</b>	Nuclear Recoil
<b>NTL</b>	Neganov-Trofimov-Luke
<b>OF</b>	Optimal Filter
<b>PandaX</b>	Particle and Astrophysical Xenon Detector
<b>PDF</b>	Probability Distribution Function
<b>PSD</b>	Power Spectral Density
<b>QCD</b>	Quantum Chromodynamics
<b>RMS</b>	Root Mean Squared
<b>S/N</b>	Signal To Noise Ratio
<b>SNO</b>	Sudbury Neutrino Observatory

<b>SQUID</b>	Superconducting Quantum Interference Device
<b>STD</b>	Standard Deviation
<b>SUL</b>	Soudan Underground Lab
<b>SuperCDMS</b>	Super Cryogenic Dark Matter Search
<b>SUSY</b>	Supersymmetry
<b>TES</b>	Transition Edge Sensor
<b>TEXONO</b>	Taiwan Experiment On Neutrino
<b>WIMP</b>	Weakly Interacting Massive Particles
<b>ZEPLIN</b>	Zoned Proportional Scintillation In Liquid Noble Gases



# Introduction

## Contents

1.1	Dark Matter . . . . .	2
1.2	A picture of dark matter . . . . .	8
1.3	Direct dark matter detection . . . . .	13
1.4	Neutrino . . . . .	20
1.5	State-of-the-art detectors in rare event searches and their current status . .	25
1.6	Backgrounds in rare event searches . . . . .	29
1.7	Preface to work in this thesis . . . . .	30

Nowadays, experimental particle physics is concerned with rare events, events with very low interaction probability or uncommon in nature. These processes whether from within the standard model (SM) or beyond the SM, are well studied and understood. The areas where scientists have many unanswered questions and hold the key to unlocking discoveries are precisely where the events are rare. Because of this, experimental particle physics has become popular today, searching for rare and hard-to-detect events amidst the events caused by common particles. The rare events discussed here are related to dark matter particles,



neutrons, and axions interacting with detector material. The most challenging part of the rare event search experiments is deciphering the signal from the huge amount of data collected and identifying the events of interest. This identification process is crucial for any rare event search experiments and is only possible by rigorous analysis and characterization of backgrounds.

In this chapter, we will discuss the exotic particles that cause the rare interactions within the context of this thesis. It will explore the current and past experiments dedicated to their search and the detection methods employed. We will also discuss the backgrounds in rare event searches and a strategy to mitigate those backgrounds.

## 1.1 Dark Matter

The first rare interaction that will be considered is the interaction between ordinary matter and dark matter (DM). This type of interaction has never been observed directly.

According to the  $\Lambda$ CDM model, the universe comprises dark energy ( $\Lambda$ ), cold dark matter (CDM), and ordinary matter. This model describes the expansion of the universe, the formation of galaxies and galaxy clusters, and the observed patterns in the cosmic microwave background radiation (CMBR) [1]. A recent survey on the CMBR by the PLANCK collaboration reveals that around 26.8% of the mass-energy budget of the universe is made up of this unknown DM (see Fig. 1.1), the matter invisible to the eye [2]. Numerous astrophysical observational evidence in the past predicted the existence of DM. Among them, four main pieces of evidence are the galactic rotation curve, the formation of bullet clusters, gravitational lensing measurements, and the large-scale structure of the present universe.

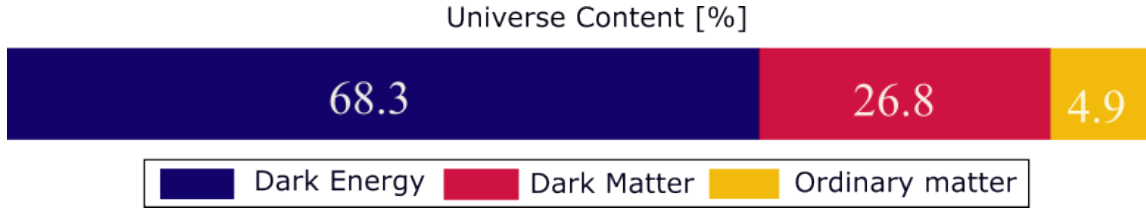


FIGURE 1.1: The mass-energy distribution of our universe is divided into components: dark energy, dark matter, and ordinary matter. The specific percentages for each component are derived from Ref. [2].

### 1.1.1 Galactic rotation curve

In 1933, Fritz Zwicky proposed DM for the first time based on the work measuring the dynamics of galaxies in the Coma cluster [3]. Using the virial theorem, Zwicky calculated the mass of the cluster and found that the measured cluster mass did not agree with the mass estimated from the luminosities of the galaxies in the cluster. To resolve this discrepancy, he proposed that a large portion of the cluster mass comprises non-luminous components, termed “Dark Matter”.

A similar discrepancy has been seen in the galactic rotation curve, the rotational velocity of stars as a function of radius from the centre of the galaxy. By equating the gravitational acceleration

$$a_g = \frac{GM(r)}{r^2} \quad (1.1)$$

with the centripetal acceleration in a uniform circular motion

$$a_c = \frac{v^2}{r} \quad (1.2)$$

where  $G$  is Newton’s gravitational constant,  $r$  is the distance from the centre of the galaxy with mass distribution  $M(r)$ , we find the rotational velocity of the star  $v$  is,

$$v = \sqrt{\frac{GM(r)}{r}} \quad (1.3)$$

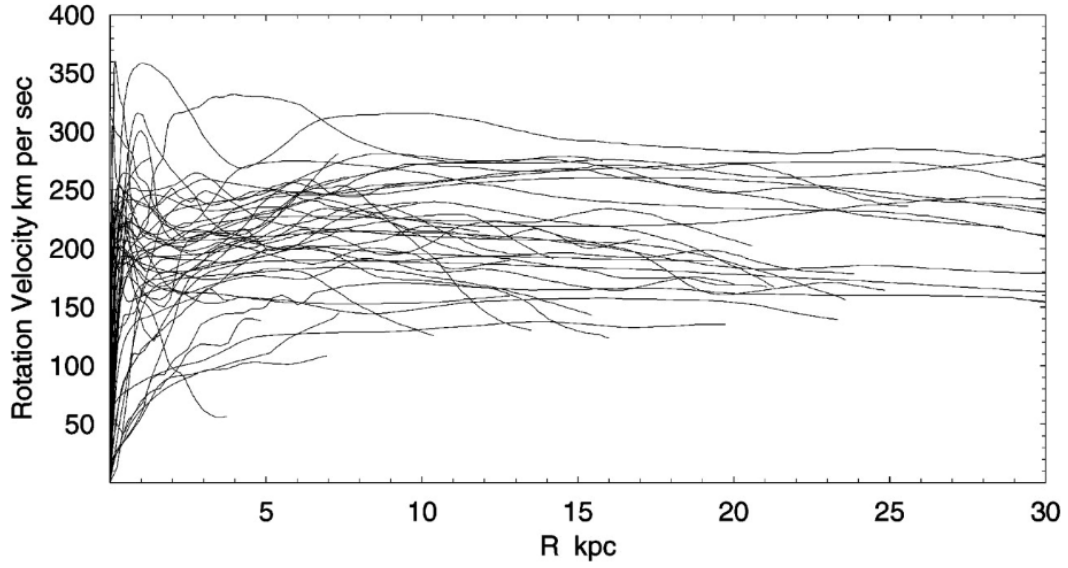


FIGURE 1.2: Galaxy rotation curve: rotational velocity distribution as a function of the distance from the centre of the galaxy for several spiral galaxies. The flat behaviour at higher radii indicates the presence of additional matter or “Dark Matter”. The figure is taken from Ref. [4]

Using Eq. 1.3, we can measure the mass distribution of the galaxy, and a separate estimation can be done by using the mass-luminosity relation. If this luminous mass accounted for the entire galaxy’s mass, the curve would show a rapid increase in velocity near the centre, followed by a decrease as  $r^{-\frac{1}{2}}$ . In 1970, Vera Rubin measured the velocity of spiral galaxies, which showed that  $v$  does not decrease at a high radius but rather becomes constant, indicating  $M(r) \propto r$ . In Fig. 1.2, a collection of galaxy rotation curves of spiral galaxies has been shown [4]. The only way to explain this observation is if non-luminous mass or DM contributes to galaxies’ luminous mass and its distribution extends to large radius.

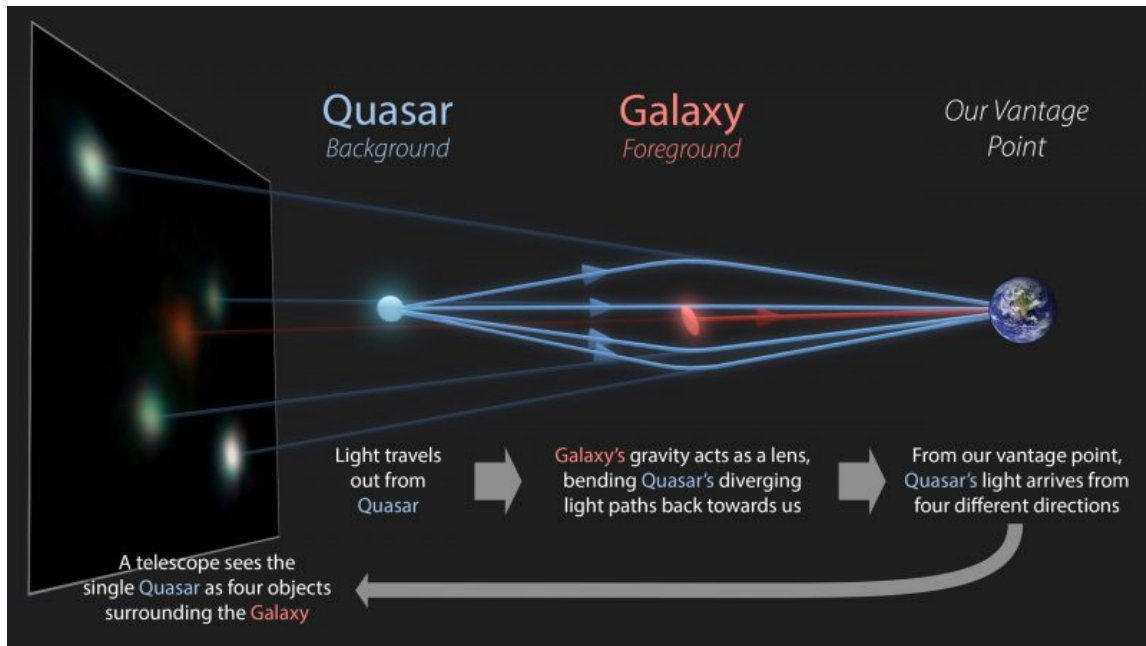


FIGURE 1.3: This illustration shows the gravitational lensing effect. The light from a distant quasar bends as it curves around the distorted space near a massive galaxy. Consequently, Earth observes multiple images of the quasar. Image credit: R. Hurt (IPAC/Caltech)/The GrL Collaboration/ESA [6].

### 1.1.2 Gravitational lensing and Bullet cluster

Gravitational lensing is a phenomenon predicted by Albert Einstein's general theory of relativity [5]. According to this theory, massive objects, such as stars, planets, or black holes, cause space-time to curve around them. When light from a distant object passes near a massive object, the curvature of space-time causes the light to follow a curved trajectory. This bending of light is analogous to how a lens in optics can bend light rays. Figure 1.3 shows the schematic of the bending of light around a galaxy. This bending of light causes the appearance of distant objects to be distorted or magnified when observed from the observer's vantage point. The degree of distortion and how light is bent can be used to estimate the total mass contained within the cluster. In the simplest example for a point-like

lens with mass  $M$ , the angular deflection,  $\theta$  of light is given by [7],

$$\theta = \frac{4GM}{rc^2} \quad (1.4)$$

where  $c$  is the speed of light, and  $r$  is the distance between the light and the lens in the plane perpendicular to the observer. By observing gravitational lensing and using Eq. 1.4, the mass of the lens can be estimated without any knowledge of the lens itself. Several observations consistently indicate that the mass calculated from gravitational lensing is significantly greater than what is accounted for by luminous matter alone, providing evidence for unseen DM within these clusters [8]. The Bullet cluster is a remarkable demonstration of gravitational lensing concerning DM. The Bullet cluster is formed when two sub-clusters collide and merge with each other. It encompasses stars, X-ray emitting interstellar plasma, and, possibly, DM. During their collisions, the stars and galaxies within these clusters pass through without interacting, while the X-ray emitting gas slows due to collisions, causing a spatial separation [10]. After the collision, the stellar and plasma components are spatially decoupled and can be separately observed with optical and X-ray telescopes [9]. This can be seen by the pink region in Fig. 1.4. Simultaneously, the mass distribution within the Bullet cluster can be determined independently through weak gravitational lensing, elegantly represented by the blue region in Fig. 1.4. This dual observation aids in unravelling the mystery of DM's presence within this cosmic collision.

### 1.1.3 Large scale structure

On its largest scales, the universe's structure resembles a grand cosmic tapestry shaped by invisible threads of DM. Imagine DM as the hidden architect orchestrating the formation of this tapestry. When the universe was young, there were small differences in the amount of matter in different places. These variations, like tiny seeds, were scattered throughout the

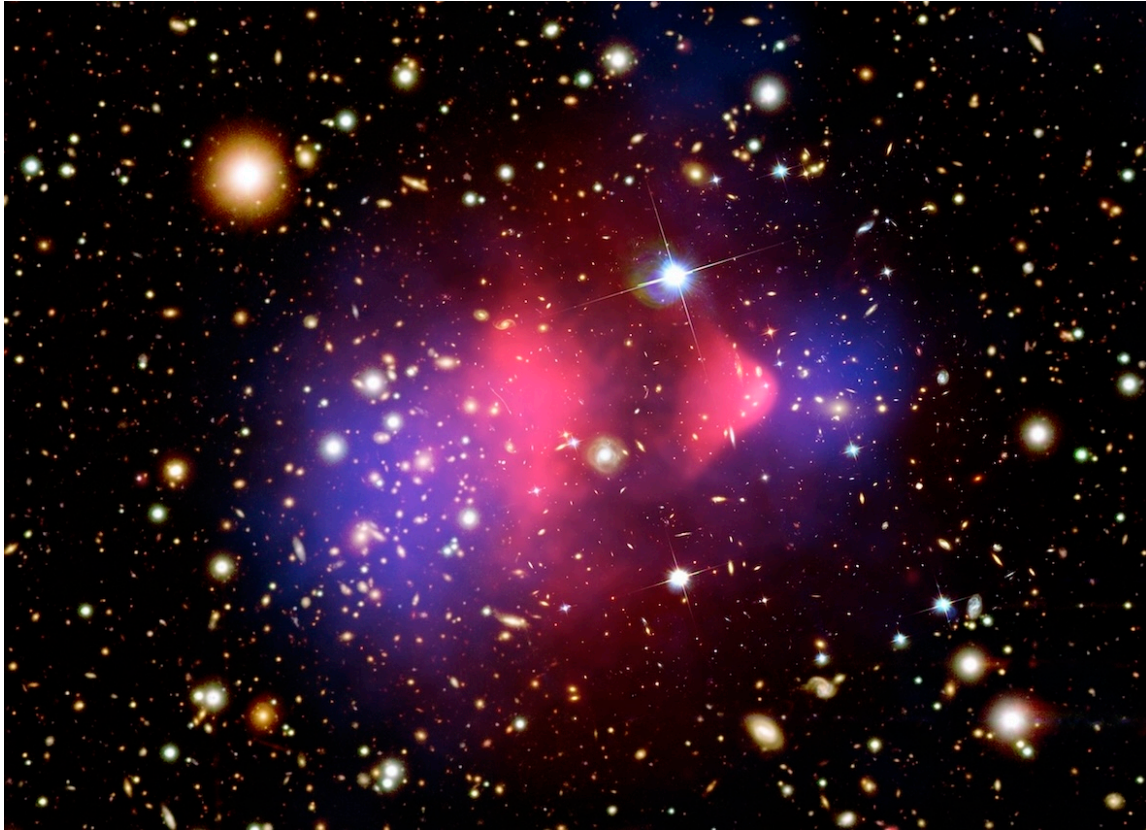


FIGURE 1.4: The combined optical images from the Magellan and Hubble Space Telescopes depict galaxies in orange and white. The Chandra X-ray image reveals hot intracluster gas (pink), representing the bulk of normal matter. Gravitational lensing exposes the dominance of dark matter (blue), marking the first distinct separation between normal and dark matter in a cluster. Image credit: X-ray: NASA/CXC/CfA; Optical: NASA/STScI; Magellan/U.Arizona; Lensing Map: NASA/STScI; ESO WFI; Magellan/U. Arizona [9].

space. Over time, gravity pulled more matter toward these regions, causing them to grow into the colossal structures we see today. Though invisible to telescopes, DM played a crucial role in this growth. It acted as a gravitational glue, pulling things together. Clusters of galaxies formed where matter gathered densely, connected by long threads of DM called filaments. These filaments act like highways connecting cosmic cities, while vast empty spaces called voids separate these cities. Scientists have confirmed this cosmic arrangement by using powerful telescopes to scan the skies. They have spotted clusters, filaments, and

voids—just as theoretical models, based on DM’s influence, predicted. The Millennium simulation [11], a large-scale simulation using 10 billion particles in a cubic region of the universe spanning 2 billion light-years on each side, incorporates the behaviour of dark matter to recreate the cosmic evolution we observe. These simulations show how DM’s gravitational influence drives the formation of large-scale structures mirroring what we see in the real universe [11, 12]. Figure 1.5 compares the simulation outcome and the actual structure of the universe.

## 1.2 A picture of dark matter

A picture of missing components of the universe is presented based on the astrophysical and cosmological evidence. The following briefly describes the main properties attributed to the DM.

### 1.2.1 Properties of dark matter

- Dark matter is neutral: DM do not carry a charge; otherwise, they would interact with light and be visible to us.
- Dark matter is non-baryonic: The CMB observations concluded that ordinary or baryonic matter does not account for the missing DM mass. From the recent CMB survey, the DM abundance corresponds to 26.8% of the total mass-energy budget of the universe [2].
- Dark matter is stable and non-relativistic: The formation of the universe’s large structure and the evidence of DM in the CMB indicate that DM existed in the early universe. Consequently, it is logical to deduce that DM must be non-relativistic or



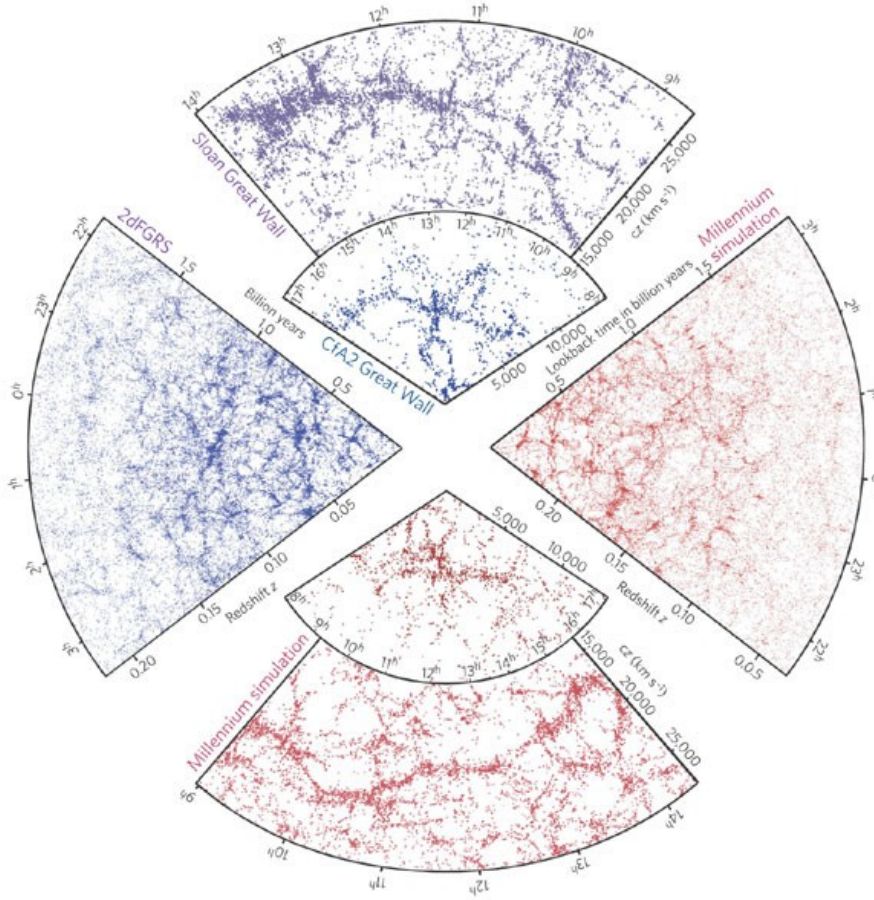


FIGURE 1.5: The figure represents a comparison between N-body simulation results and galaxy survey measurements. The red wedges (bottom and right) are extracted from the Millennium simulation. In contrast, the blue wedges (top and left) represent diverse galaxy surveys: Sloan Digital Sky Survey (large top wedge), Center for Astrophysics Survey (small top wedge), and 2dF Galaxy Redshift Survey (left). The observations and simulations closely resemble each other on comparable length scales. The figure is taken from the Ref. [12].

cold (moving slowly compared to the speed of light) and stable or have an extremely long lifetime.

- Dark matter is almost collisionless: The formation of the Bullet cluster indicates a near-collisionless DM. After the collision, the separation between the mass causing gravity and the visible gas showed that the former remained unaffected and did not





FIGURE 1.6: The figure illustrates potential solutions to the dark matter problem. The term "little Higgs" denotes candidates within the context of little Higgs models, while "extra dimensions" indicates candidates associated with theories involving additional spatial dimensions. Specific theories include TeVeS (tensor–vector–scalar theory), MOND (modified Newtonian dynamics), and MaCHOs (massive compact halo objects). The figure is taken from Ref. [13]

slow down, unlike the visible gas. This supports the idea that dark matter is almost collisionless, i.e. it does not collide or interact like ordinary matter during cosmic events.

### 1.2.2 Dark matter candidates

There are no suitable particles from the SM that explain DM. Different DM candidates are proposed to address discrepancies between visible and gravitational effects, stemming from theories beyond the SM, like supersymmetry [14]. A visualization of several DM

candidates has been shown in Fig 1.6. Primordial black holes [15], Sterile neutrinos [16], and Axions [17] are all considered potential candidates for DM, each offering theoretical explanations for their existence. Among these particles, Weakly Interacting Massive Particles (WIMPs) stand out as the most motivated candidate, and this thesis will specifically focus on them.

**Weakly interacting massive particles(WIMPs)** WIMPs are the most motivated DM candidates due to their theoretical predicted properties in particle physics. These particles, emerging from extensions of the SM like supersymmetry or SUSY, are thought to be electrically neutral and interact weakly with ordinary matter, making them elusive to direct detection [18]. Theoretical models suggest that stable and weakly interacting WIMPs could have existed since the early universe, constituting DM and contributing to the gravitational scaffolding for the formation of cosmic structures observed today. These particles can have a mass ranging from 1 to 1000 GeV and can explain the relic density of DM in the universe. The compelling theoretical framework, their potential to explain the observed large-scale structure of the universe, and the focus of dedicated experimental efforts collectively support WIMPs as one of the leading candidates for DM.

### 1.2.3 Methods of detection

A wide variety of experimental efforts are ongoing to search for DM candidates. Those experiments are broadly classified into three categories: production at particle colliders, indirect detection and direct detection. The schematic of the search methods is shown in Fig. 1.7. The figure represents SM particles as  $\psi$  and DM particles as  $\chi$ .

1. **Collider production** ( $\psi\psi \rightarrow \chi\chi$ ): In particle colliders like the Large Hadron Collider

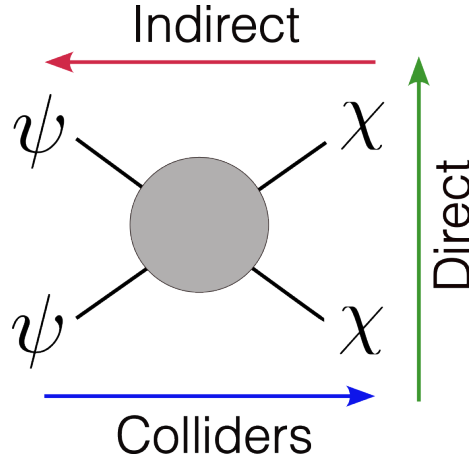


FIGURE 1.7: A cartoon Feynman diagram shows interactions between two SM particles ( $\psi$ ) and two DM particles ( $\chi$ ), featuring collider production (left to right), indirect detection (right to left), and direct detection (bottom to top) methods.

(LHC), two SM particles are collided at high energies. They recreate conditions resembling the early universe where DM might be created from the decay of strongly produced particles. Although DM itself doesn't interact much with regular matter, if it's generated in these collisions, its presence might be inferred from unusual patterns such as missing energy or momentum before and after the collision. ATLAS and CMS are the collider experiments that search for DM [19]. Belle II is another example of the experiment at SuperKEKB electron-positron collider [20].

2. **Indirect detection** ( $\chi\chi \rightarrow \psi\psi$ ): The cosmological annihilation rate of DM particles is almost zero. However, the relic density of DM in the universe is such that it may be locally enhanced due to the gravitational binding at the centre of galaxies. At higher densities, DM particles may, with their own antiparticles, annihilate and create SM particles. PAMELA [21] and AMS-02 [22] are the experiments searching for DM in this method. The SM annihilation products could be neutrinos, charged particles, or gammas. They are then detected in satellites for the DM signature. IceCube [23],

FERMI [24], and HESS [25] are the experiments looking for DM in this method [26].

3. **Direct detection** ( $\chi\psi \rightarrow \chi\psi$ ): In this method, a DM particle scatters off a SM particle, and the detectors directly measure the kinematics of the recoiling SM particle. Using the recoil kinematics, the mass of the scattering DM particle with a particular interaction cross-section can be probed. Depending on the detector material used, the recoiling SM particle can give three types of signals: phonons (heat), ionization (charges) and scintillation (light). The direct detection experiments rely on these signals to search for DM [27]. The upcoming section presents a concise overview of the direct detection of DM.

## 1.3 Direct dark matter detection

Lewin and Smith developed the mathematical framework necessary for the direct detection of DM [28]. Their work expanded upon the conceptual groundwork by Goodman and Witten, which itself was drawn from the formalism used in detecting neutrinos by Drukier and Stodolsky [29, 30]. This section presents a brief mathematical framework based on all the DM direct search experiments.

### 1.3.1 WIMP event rate

In direct detection experiments, we expect individual DM particles to interact with the detector's target through the weak force and scatter off, inducing a nuclear recoil signal in the detector. The most favourable DM candidates searched by these experiments are WIMPs following an assumption that the galaxy is embedded in a WIMP halo. The direct detection experiments look for this nuclear recoil ( $E_R$ ) signal in a very low background

environment. The event rate is extremely low, which requires rigorous measurements to reduce backgrounds.

The differential event rate is defined as  $dR/dE_R$ , expressed as the number of particles detected per unit detector mass per unit recoil energy per unit time. The unit of measurement is counts/kg.day.keV which is known as differential rate unit or DRU. The calculation of the differential event rate presented here follows the discussions in Ref. [18, 28].

To calculate the differential rate, we need first to define the differential number density of WIMP's around the earth:

$$dn = n_0 f(v) dv \quad (1.5)$$

Where,  $n_0 = \frac{\rho_0}{m_\chi}$  is WIMP the number density with local mass density  $\rho_0$  of WIMP mass  $m_\chi$  and  $f(v)$  is the WIMP velocity distribution function, which is normalised as to conserve  $n_0$ .

$$\int_0^{v_{esc}} f(v) dv = 1 \quad (1.6)$$

$v_{esc}$  is the escape velocity of the Milky Way, which is set as an upper limit in the integration. Now, the differential rate unit per unit mass is given by

$$dR = N_n v d\sigma dn \quad (1.7)$$

where,  $N_n$  is the number of target nuclei per unit mass and  $d\sigma$  is the differential WIMP-nucleus interaction cross-section. After combining Eq. 1.5 and Eq. 1.7, the differential rate, with respect to  $E_R$ ,  $dR/dE_R$  for all WIMP velocities is given by,

$$\frac{dR}{dE_R} = \frac{\rho_0 N_n}{m_\chi} \int_{v_{min}}^{v_{max}} v f(v) \frac{d\sigma}{dE_R} dv \quad (1.8)$$

WIMPs are non-relativistic i.e. they have velocities  $O(10^{-3}c)$ . Assuming non-relativistic kinematics, recoil energy can be given for WIMP-nucleus elastic scattering with scattering

angle  $\theta$  in the centre of mass frame,

$$E_R = \frac{\mu_n^2 v^2}{m_n} (1 - \cos \theta) \quad (1.9)$$

where,  $\mu_n = \frac{m_\chi m_n}{m_\chi + m_n}$  is the WIMP-nucleus reduced mass,  $m_n$  is the mass of nuclei. The minimum velocity to induce a certain  $E_R$  can be written from Eq. 1.9.

$$v_{min} = \sqrt{\frac{m_n E_R}{2\mu_n^2}} \quad (1.10)$$

### Spin-independent interaction cross-section

Since the nature of the DM is unknown, a more general approach is taken to compute the interaction cross-section. We categorize WIMP-nuclei interaction into two types: spin-independent (SI) and spin-dependent (SD). We will be discussing only the SI interaction.

The cross-section is usually expressed in terms of momentum transferred in the scattering process,  $q^2 = 2m_n E_R$ . In the limit  $q \rightarrow 0$ , for a nucleus (A, Z), the cross-section is given by,

$$\left. \frac{d\sigma^{SI}}{dq^2} \right|_{q \rightarrow 0} = \frac{1}{\pi v^2} [f_p Z + f_n (A - Z)]^2 \quad (1.11)$$

The cross-section in the zero momentum limit is defined as  $\sigma_0^{SI}$ .

$$\sigma_0^{SI} = \int_0^{4\mu_n^2 v^2} \left. \frac{d\sigma_{SI}}{dq^2} \right|_{q \rightarrow 0} dq^2 = \frac{4\mu_n^2}{\pi} [f_p Z + f_n (A - Z)]^2 \quad (1.12)$$

where  $f_p$  and  $f_n$  are the functions of couplings for proton and neutron, respectively. As the recoil energy increases,  $q > 0$ , the WIMP starts to probe the internal structure of the nucleus. A nuclear form factor  $F_{SI}(q)$  needs to be multiplied to introduce this.

$$\frac{d\sigma^{SI}}{dq^2} = \frac{1}{\pi v^2} [f_p Z + f_n (A - Z)]^2 F_{SI}^2(q) = \frac{1}{4\mu_n^2 v^2} \sigma_0^{SI} F_{SI}^2(q) \quad (1.13)$$

$$\frac{d\sigma^{SI}}{dE_r} = \frac{m_n}{2\mu_n^2 v^2} \sigma_0^{SI} F_{SI}^2(q) \quad (1.14)$$

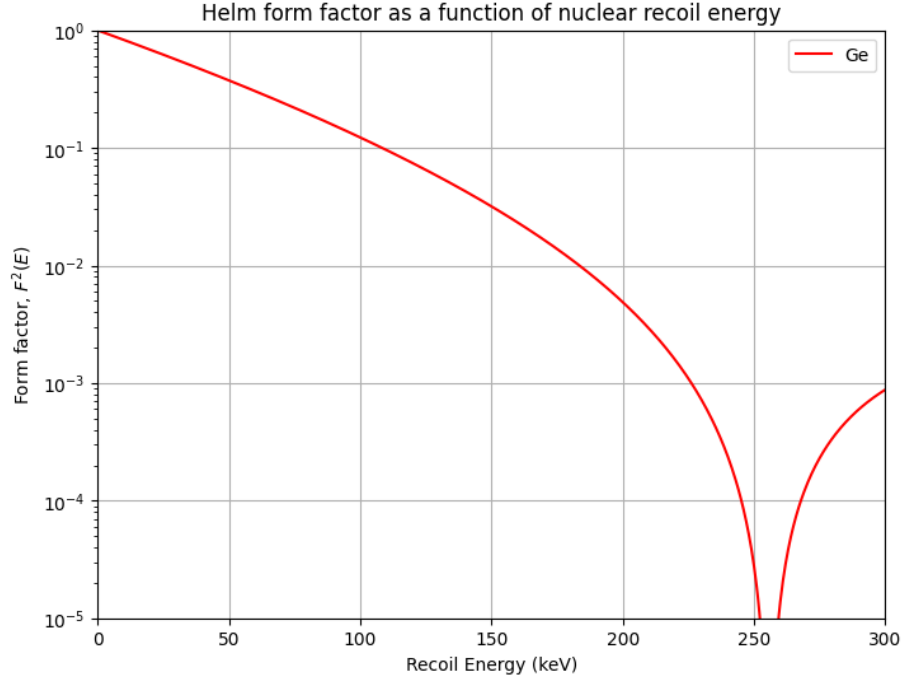


FIGURE 1.8: Helm factor as a function of nuclear recoil energy for germanium target.

### Helm form factor

There are several analytical and theoretical models for the form factor; the one which is mostly used is the Helm form factor [31, 32].

$$F_{SI}(q) = 3 \frac{\sin(qr_n) - qr_n \cos(qr_n)}{(qr_n)^3} e^{-\frac{1}{2}(qs)^2} \quad (1.15)$$

where,  $r_n$  is a measure of the nuclear radius, and  $s$  is a measure of the nuclear skin thickness.

These values are given by,

$$r_n^2 = c^2 + \frac{7}{3}\pi^2 a^2 - 5s^2 \quad (1.16)$$

where  $c \simeq 1.23A^{1/3} - 0.60$  fm,  $s \simeq 0.9$  fm and  $a \simeq 0.52$  fm. The  $F_{SI}^2(q)$  function for germanium target nuclei is shown in Fig. 1.8. After inserting Eq. 1.14 in Eq. 1.8, the

differential event rate for SI WIMP-nucleon interaction can be given as,

$$\frac{dR}{dE_R} = \underbrace{\frac{N_n m_n}{2m_\chi \mu_n^2}}_{\text{Detector}} \cdot \underbrace{[\sigma_0^{SI} F_{SI}^2(E_R)]}_{\text{Nuclear and Particle}} \cdot \rho_0 \underbrace{\int_{v_{min}}^{\infty} \frac{f(v)}{v} dv}_{\text{Astrophysics}} \quad (1.17)$$

### Standard Halo model

The integral part in the Eq. 1.17 refers to the information about the Standard Halo model (SHM) for the WIMP velocity distribution and can be written as,

$$I(E_R) = \frac{\sqrt{\pi} v_0}{2} \int_{v_{min}}^{\infty} \frac{f(v)}{v} dv \quad (1.18)$$

where  $v_0$  is the velocity of the solar system around the centre of the Milky Way. According to the SHM, the WIMP velocity distribution follows the Maxwellian velocity distribution function, which is,

$$f(v) = \frac{4v^2}{v_0^3 \sqrt{\pi}} e^{-\frac{v^2}{v_0^2}} dv \quad (1.19)$$

Solving the integral in Eq. 1.18 gives,

$$I(E_R) = e^{-\frac{v_{min}^2}{v_0^2}} \quad (1.20)$$

### Differential rate equation

Plugging Eq. 1.20 and 1.10 back into Eq. 1.17 gives

$$\frac{dR}{dE_R} = \frac{N_n m_n}{2m_\chi \mu_n^2} \cdot \sigma_0^{SI} F_{SI}^2(E_R) \cdot \rho_0 \frac{2}{\sqrt{\pi} v_0} e^{-\frac{E_R m_n}{2\mu_n^2 v_0^2}} \quad (1.21)$$

Equation 1.21 emphasizes that the differential rate decreases exponentially with the recoil energy and how it is crucial to have detectors with low energy threshold to search for the WIMP signals. Figure 1.9 presents the differential rate vs. the recoil energy for the germanium detector as calculated using Eq. 1.21 and 1.15. The figure has been plotted for different WIMP masses and an SI cross-section,  $\sigma = 10^{-44} \text{ cm}^2$ . Experiments measure



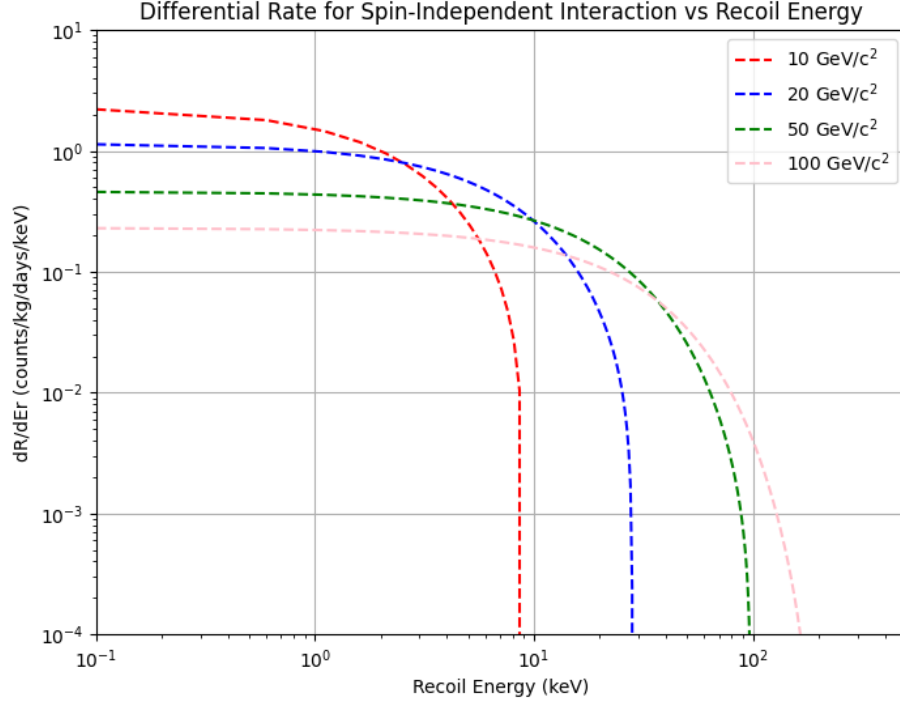


FIGURE 1.9: The differential rate, measured in counts/kg.days.keV, is calculated for spin-independent WIMP-nucleon elastic scattering with a cross-section value of  $\sigma_0^{SI} = 10^{-44} \text{ cm}^2$ . Various WIMP masses are considered, and the target is germanium.

the number of events,  $N$ , occurring within a specified recoil energy range. Utilizing this information, the event rate,  $dR/dE_R$ , can be calculated, providing details about the left-hand side (LHS) in Equation 1.21. On the right-hand side (RHS) of Equation 1.21, all relevant information is known except for the dark matter mass,  $m_\chi$ , and the cross-section,  $\sigma_0^{SI}$ . Consequently, a parameter space emerges, encapsulating these two unknowns—the DM-nucleon cross-section and the DM mass. This parameter space is commonly referred to as the Exclusion Plot in the context of direct DM search experiments. An exclusion curve is constructed in the DM-nucleon cross-section vs. DM mass parameter space by comparing the observed total number of events in the energy range with the expected backgrounds and expected DM rate from Equation 1.21. This curve outlines regions where certain DM masses are excluded based on experimental observations.

### 1.3.2 Direct detection experiments

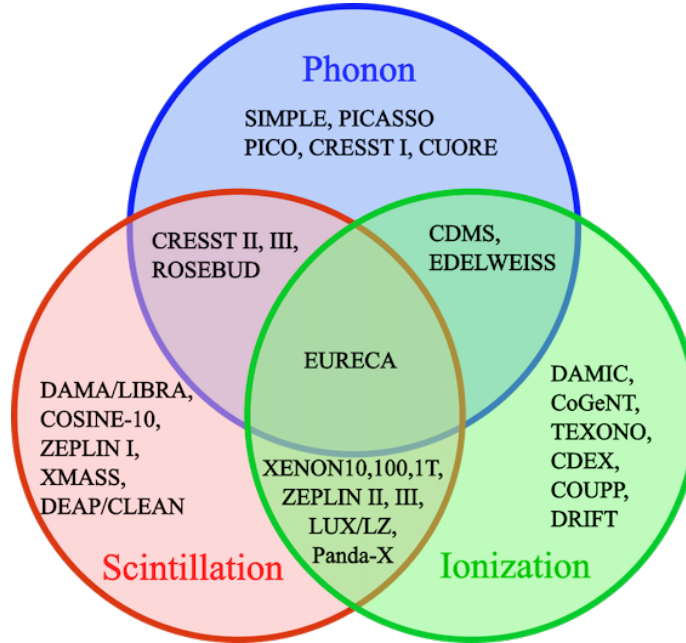


FIGURE 1.10: Summary of direct detection experiments based on the measurement of three types of signals: phonons (heat), scintillation (light) and ionization (charge) caused by the recoil energy transfer by the interacting particles.

Experiments utilize three distinct signals associated with the recoil energy of target nuclei interacting with DM particles. (i) Phonon signals arise from the interaction as a dark matter particle collides with a nucleus, generating collective vibrational modes or phonons in the crystal lattice of the target material. Cryogenic detectors then measure the resulting temperature changes, allowing for the quantification of the energy deposited during the interaction. (ii) An ionization signal is generated when DM particles collide and ionize the target atoms by knocking off electrons. This process results in the generation of ionization signals, which can be detected by sensitive detectors, such as ionization chambers or semiconductor detectors. (iii) Scintillation signals involve the emission of photons when atoms in the target material return to their ground state after being excited by

the interaction with a dark matter particle. These emitted photons constitute scintillation light, which is detected using photodetectors. Simultaneous measurement of phonons and ionization or phonons and light enhances the capability of these experiments by enabling one to discriminate between different incident particles. Figure 1.10 shows the summary of direct detection experiments based on different recoil energy signals. A more detailed discussion on the ongoing experiments and their current status are presented in section 1.5.1.

## 1.4 Neutrino

The second type of rare event under consideration involves the interactions between atomic nuclei and the neutrino ( $\nu$ ). This particle is not only rare, but its interactions with ordinary matter are also rare.

In 1930, Wolfgang Pauli first proposed the existence of the  $\nu$  as a solution to the missing energy conservation during  $\beta$  decay where an electron ( $e^-$ ) and antineutrino ( $\bar{\nu}$ ) is emitted in decay of a neutron ( $n^0$ ) to proton ( $p^+$ ) [33]:

$$n^0 \rightarrow p^+ + e^- + \bar{\nu}_e \quad (1.22)$$

Pauli postulated that the  $\nu$  would be a nearly massless spin-1/2 and charge-neutral particle with a very small magnetic moment. In 1934, Enrico Fermi further developed the theory of  $\nu$ , providing a mathematical framework for their description. He coined the term “neutrino”, which means “little neutral one” in Italian. The experimental detection of neutrinos proved challenging due to their elusive nature. The first successful detection occurred in 1956 by Frederick Reines and Clyde Cowan at the Savannah River Plant in South Carolina. They detected antineutrinos produced in the inverse beta decay (IBD:  $\bar{\nu}_e + p^+ \rightarrow n^0 + e^-$ ) at a nuclear reactor using a large liquid scintillator detector [34]. This experiment marked the

first successful detection of neutrinos, and efforts of several experiments solidified their position in SM [35].

According to the SM, the  $\nu$ s are leptons and have three flavours corresponding to the three charged leptons: electron ( $\nu_e$ ), muon ( $\nu_\mu$ ) and tau ( $\nu_\tau$ ). They were found to be charge neutral and spin-1/2, as Pauli predicted. It was thought that they were massless. However, several experiments later observed that neutrinos are not strictly confined to a single flavour; they can change from one flavour to another as they propagate through space. This transition between the flavours is known as “Neutrino oscillation”. Ray Davis Jr. and John N. Bahcall conducted experiments in the 1960s to measure solar neutrinos. The observed number was significantly lower than predicted, leading to the “Solar Neutrino Problem” [36]. The theory of neutrino oscillations later resolved this mystery. In 1998, the Super-Kamiokande experiment in Japan provided compelling evidence for neutrino oscillations [37]. Neutrino oscillation implies that neutrinos have non-zero masses and puts a question mark on the SM prediction. Thus, precise measurement of neutrino properties is essential to check if the SM predictions are correct or if we need new physics beyond SM.

### 1.4.1 Coherent Elastic Neutrino Nucleus Scattering ( $\text{CE}\nu\text{NS}$ )

Daniel Z. Freedman was the first to explain coherent elastic neutrino-nucleus scattering ( $\text{CE}\nu\text{NS}$ ) as a process within the SM [38]. The interaction between a neutrino and a nucleus during scattering relies on the non-trivial interplay between the neutrino and the individual nucleons. However, if the momentum transfer between the neutrino and the nucleus is small, it does not reveal the internal structure of the nucleus. Consequently, the neutrino scatters off the nucleus as a whole. This quantum mechanical effect leads to a coherent increase in the scattering cross-section, which roughly scales with the square of the neutron number in the target nucleus. As a result, the resulting scattering cross-section is much

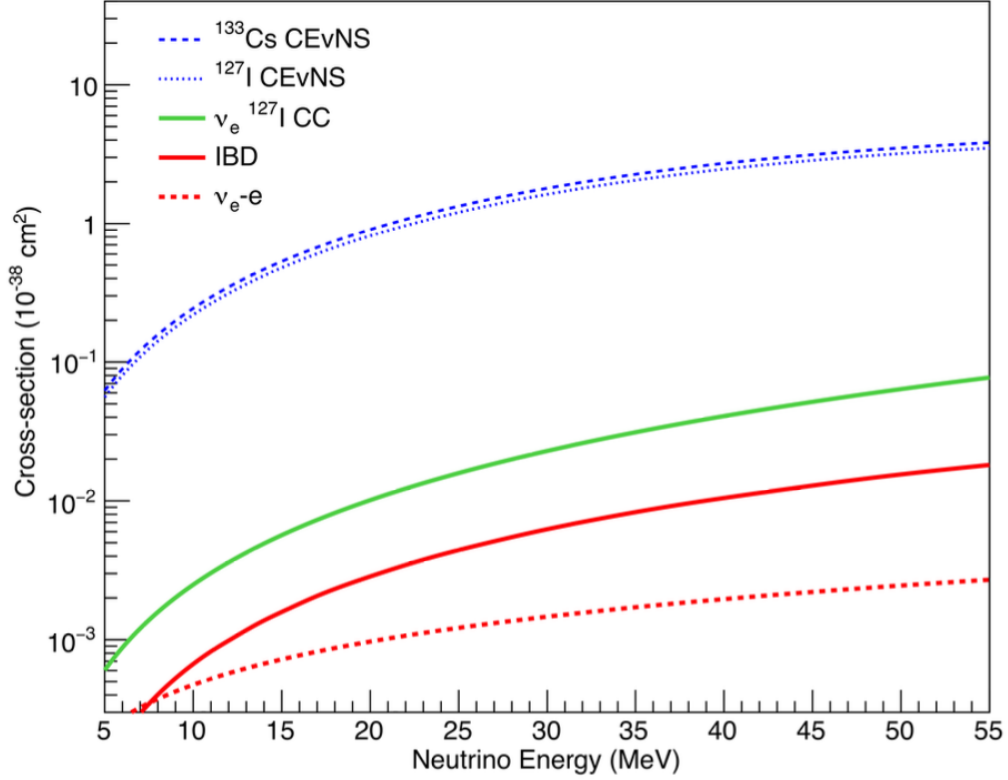


FIGURE 1.11: The total cross-section for CE $\nu$ NS (blue) is compared to other neutrino couplings. Cross-sections from charged-current (CC) interaction with iodine (green), inverse beta decay (IBD) (red), and neutrino-electron scattering (dotted red) are shown. CE $\nu$ NS exhibits the largest cross-section, surpassing any charged-current interaction for incoming neutrino energies below 55 MeV. The figure is adapted from Ref. [39].

larger, by several orders of magnitude, compared to other neutrino-nucleus couplings like IBD. Figure 1.11 shows the total cross-section for CE $\nu$ NS and other neutrino couplings. It is evident that for incoming neutrino energies below 55 MeV, CE $\nu$ NS (blue) provides the largest cross-section when compared with the cross-sections from charged-current (CC) interaction with iodine (green), IBD (red), and neutrino-electron scattering (dotted red).

### Cross-section

The spin-independent differential cross-section of CE $\nu$ NS process for incident neutrino

energy  $E_\nu$  and recoil energy  $T$  is [30],

$$\frac{d\sigma_{\nu-N}}{d\cos\phi} = \frac{G_F^2}{8\pi} [Z(4\sin^2\Theta_W - 1) + N]^2 E_\nu^2 (1 + \cos\phi) \quad (1.23)$$

where  $G_F$  is the Fermi coupling constant,  $Z$  and  $N$  are the number of proton and neutrons in the target nucleus, respectively,  $\sin^2\Theta_W$  is the weak mixing angle,  $\phi$  is the scattering angle. For simplicity, the contributions from axial vector currents and radiative corrections beyond are ignored in Eq. 1.23. For small momentum transfer,  $\sin^2\Theta_W = 0.23867 \pm 0.00016 \approx \frac{1}{4}$  [40]. To simplify Eq. 1.23, we constrain the contributions from proton coupling up to first-order only. In experiments where the only observable outcome is the energy deposition in the form of a nuclear recoil in the detector, it is advantageous to express the differential cross-section as a function of  $T$  carried by the target nucleus of mass  $M$ .

$$\frac{d\sigma_{\nu-N}}{dT} = \frac{G_F^2 M}{4\pi} N^2 \left(1 - \frac{MT}{2E_\nu^2}\right) \quad (1.24)$$

Equation 1.24 illustrates that the CE $\nu$ NS cross-section is directly proportional to  $N^2$ . The main challenge in a CE $\nu$ NS measurement is that the only detectable signal is a very low-energy nuclear recoil from the target nucleus. The energy of the recoiling nucleus ranges from  $0 \leq T \leq T_{max} = \frac{2E_\nu^2}{M+2E_\nu}$ . An example of the detector threshold requirement is a  $\sim 30$  MeV neutrino scattering off a heavy nucleus such as argon,  $T_{max} \simeq 50$  keV.

### Motivation

Even though the initial theories regarding the CE $\nu$ NS process emerged more than 40 years ago, its discovery only occurred recently through the efforts of the COHERENT collaboration, utilizing a CsI[Na] target [39]. A precise measurement of CE $\nu$ NS cross-section becomes crucial for DM search experiments as it faces an unavoidable CE $\nu$ NS background from astrophysical neutrinos, like those from the sun or the diffuse supernova neutrino

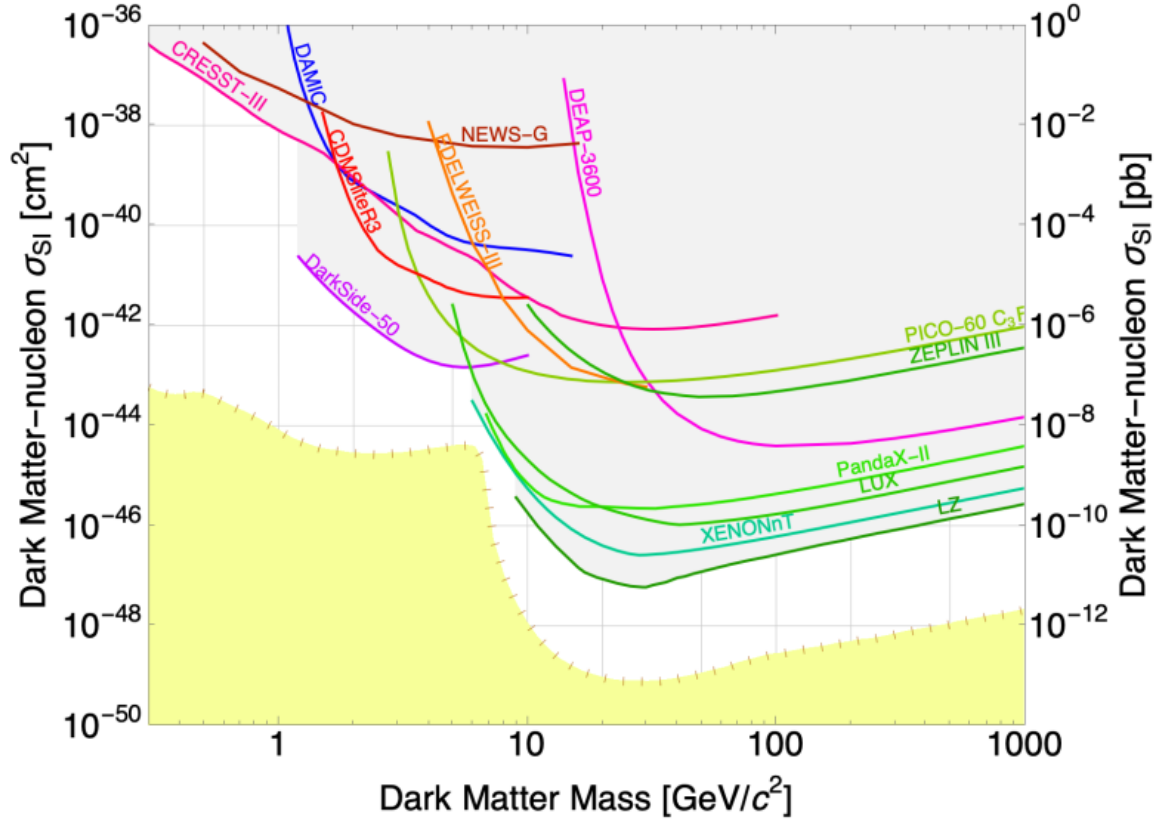


FIGURE 1.12: The outcomes of various dark matter search experiments are illustrated in the parameter space of DM-nucleon versus DM mass. The area above each solid curve, associated with a specific experiment, has been ruled out. The region below these solid curves remains unexplored. The neutrino floor, described in the text, is represented by the brown dashed line. This delineates the parameter space region where a DM signal cannot be distinguished from CE $\nu$ NS. The figure is created using Ref. [41]

background (DSNB). Since both CE $\nu$ NS and WIMP scattering produce a similar low-energy nuclear recoil signal, distinguishing between them is impossible. This challenge forces potential WIMP discoveries to rely on innovative approaches like directional recoil measurements. Figure 1.12 illustrates the “neutrino floor”, representing the challenging limit for WIMP discovery in future DM experiments, assuming an SM CE $\nu$ NS cross-section. The figure also showcases the recent best limits on the WIMP-nucleus scattering cross-section from various dark matter experiments.

### Searches at reactor

Nuclear reactors play a significant role in neutrino science, being the origin of the first-ever detected neutrinos. Recent proposals aim to detect  $\text{CE}\nu\text{NS}$  using these reactors, as they naturally produce substantial fluxes of electron antineutrinos, around  $2 \times 10^{20} \nu/\text{sec}$  per GW reactor power (compared to about  $3.5 \times 10^{15} \nu/\text{sec}$  at ESS) [42]. The high fluxes provide an opportunity for experiments with high statistics in a relatively short time. Moreover, characterizing ambient environmental backgrounds is straightforward, as data can be collected during reactor ON and OFF. These factors make nuclear reactors an attractive source for  $\text{CE}\nu\text{NS}$  searches.

## 1.5 State-of-the-art detectors in rare event searches and their current status

### 1.5.1 Direct Dark matter searches

In the current landscape of DM research, multiple direct detection experiments are actively underway (shown in Fig. 1.10), each employing unique approaches and cutting-edge technologies. This section provides a concise overview of some state-of-the-art detectors utilized in leading experiments within this field.

#### XENON detectors

XENON is a pioneering large size experiment searching for dark matter at Gran Sasso Lab in Italy. It uses liquid and gaseous xenon in a special chamber. When particles hit xenon, they create light (S1 signal) and ionization electrons (S2 signal). Photomultiplier tubes detect these signals. S1 tells about energy, and S2 helps find ionization electrons. The



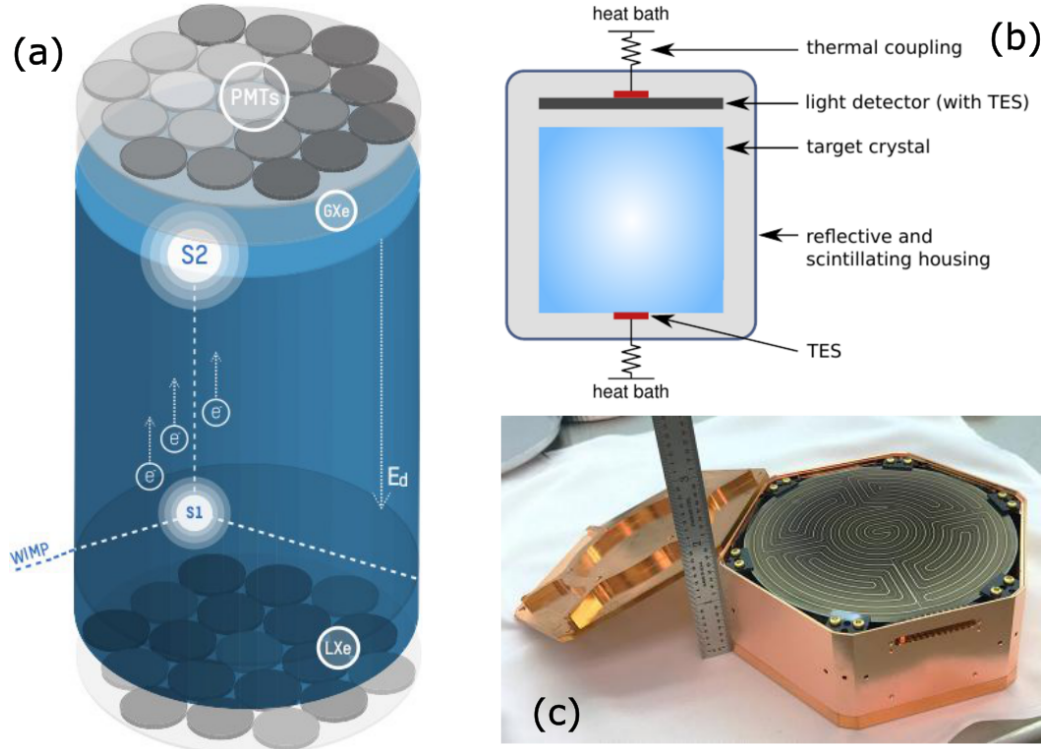


FIGURE 1.13: (a) Schematic of XENON TPC detector showing the detection principle. The top section of the detector contains a gaseous phase (GXe), while the bottom has a liquid phase (LXe). PMTs positioned at the top and bottom collect light signals. An electric field is applied to gather electrons from the liquid phase. (b) Standard CRESST module detector design. Energy deposition generates phonons, detected by the TES on the target crystal ( $\text{CaWO}_4$ ), and photons, collected by the light detector. Both detectors have a weak coupling to a heat bath at  $T_0 \sim 10$  mK. (c) SuperCDMS SNOLAB iZIP detector showing interleaved ionization and phonon sensors on the surface.

schematic of XENON TPC detector setup is shown in Fig. 1.13(a). The setup can detect signals from a single electron. The precise measurement and correlation of the S1 signal and S2 signal play a crucial role in distinguishing DM signals from background noise. XENONnT is the most recent version of the XENON1T experiment. While XENON1T utilized 3.2 tons of ultra radio-pure liquid xenon, featuring a TPC with dimensions of 1 m in diameter and 1 m in height [43], XENONnT will employ over 8 tons of liquid xenon, and its TPC will have a diameter and height of around 1.4 m [44]. LUX-ZEPLIN (LZ) [45], PandaX [46] represent other experiments, scaling up the use of liquid xenon for enhanced

sensitivity and precision in capturing potential DM signals.

### **Cryogenic Rare Event Search with Superconducting Thermometers (CRESST)**

CRESST is another leading experiment for DM detection, located at Gran Sasso National Laboratory in Italy. The detector consists of calcium tungstate ( $\text{CaWO}_4$ ) crystals arranged in an array, each equipped with a light detector and a superconducting thermometer, mainly a Transition-Edge Sensor (TES). Fig. 1.13(b) shows the CRESST detector module. When a particle interacts with the crystal, it imparts energy to the lattice, triggering both scintillation and phonon signals. Scintillation light, emitted as a result of the energy deposition, is detected by highly sensitive light detectors operating at TESs. Simultaneously, the deposited energy generates vibrations, or phonons, which propagate through the crystal lattice and are measured by TESs. Information from both scintillation and phonon channels enhances discrimination between DM signals and background noise, making the CRESST detector a powerful tool in the search for DM particles. The most recent upgrade of the CRESST experiment is CRESST III, featuring a cuboid-shaped detector with dimensions of  $20 \times 20 \times 10 \text{ mm}^3$ , resulting in a mass of approximately 25 g [47]. The light detectors in this setup are typically constructed from a thin sapphire wafer with a layer of  $\text{SiO}_2$ .

### **Super Cryogenic Dark Matter Search (SuperCDMS)**

SuperCDMS employs germanium and silicon crystals as target materials, operating at a few milliKelvin temperatures to minimize thermal noise and enhance sensitivity to low-energy particle interactions. When a dark matter particle interacts with the crystal nuclei, it generates ionization and phonon signals. Utilizing Interleaved Z-sensitive Ionization and Phonon (iZIP) sensors positioned across the detector surface allows for the simultaneous collection of ionization and phonon signals. This dual-readout strategy is valuable

for effective background discrimination. The future SuperCDMS SNOLAB in Sudbury, Canada, is a leading experiment for low-mass dark matter detection. Fig. 1.13(c) shows the cylindrical iZIP detector with a diameter of 100 mm and a thickness of 33 mm [48] will be operated in this experiment.

Other experiments contributing to this global effort include DarkSide experiment [49], which employs liquid argon as its detection medium, with a focus on minimizing background signals to improve the discernment of dark matter interactions, DEAP [50], which also utilizes liquid argon, and DAMIC [51], which employs charge-coupled devices for detection. The COSINE experiment [52] utilizes NaI crystals to explore potential dark matter signals, while EDELWEISS [53] employ cryogenic bolometer detectors. Figure 1.12 shows the experimental reach for all these direct detection experiments.

### 1.5.2 $\text{CE}\nu\text{NS}$ searches at reactor

Numerous experiments are actively pursuing  $\text{CE}\nu\text{NS}$  at nuclear reactors, demonstrating a diverse range of approaches. Experiments like MINER [54] and RICOCHET [55] utilize research reactors as their neutrino sources, while others, including CONNIE [56], CONUS [57], Dresden-II [58], NUCLEUS [59], NuGeN [60], RED-100 [61] employ commercial power reactors, benefitting from their higher thermal power output. While power reactors produce more neutrinos, research reactors offer advantages for experiments because of their proximity to the reactor core. However, this proximity also increases the uncertainty of reactor-induced backgrounds. The detector technologies used in these experiments share similarities with those employed in DM detection.

#### **Coherent Neutrino Nucleus Interaction Experiment (CONNIE)**

CONNIE experiment is located at the Angra Nuclear Power Plant in Brazil. It has a 3.8

GW reactor with a baseline distance of about 30 m. The experiment utilizes silicon charge-coupled devices (CCDs) featuring a two-dimensional array where the sensitive region is divided into millions of square pixels, each measuring  $15\ \mu\text{m} \times 15\ \mu\text{m}$ . This arrangement results in an area of a few tens of square centimeters with thicknesses of approximately  $650\ \mu\text{m}$ , providing detector masses equivalent to a few grams per device. CCDs are known for their high sensitivity to low-energy deposition. When particles hit the detector, they create  $e^-/h^+$  pairs. Electric fields move these charges across the array, where the charge packets are read out, amplified, and converted into a digital signal. This process enables precise imaging and detection.

CONUS, NUGen utilize a detector known as the “p-type point contact” (PPC) semiconductor detector. This detector consists of a semiconductor crystal made of germanium, kept at low temperatures and connected to high-voltage electrodes. This setup generates a large, nonuniform electric field within the crystal. Experiments such as MINER, NUCLEUS, and RICHOCHET utilize different detector technologies involving cryogenic calorimeters. These calorimeters are composed of low-temperature semiconductor crystals, similar to the technology used in DM detection experiments. RED-100 employs two-phase noble gas scintillators, while charge-coupled devices (CCDs) are employed in  $\text{CE}\nu\text{NS}$  searches at reactors.

## 1.6 Backgrounds in rare event searches

Rare event search experiments mainly deal with characterizing and reducing backgrounds. The sensitivity of an experiment lies in how large the background is and how well that can be removed. Some of the key methods to deal with backgrounds are discussed below.

1. **Background Reduction Strategies:** Experimental designs often incorporate strate-

gies to minimize background contributions, such as operating in underground laboratories, shielding, active vetoes, or selecting specific regions of interest. These measures aim to enhance the signal-to-background ratio and improve the experimental sensitivity. In Chapter 2, a more detailed discussion can be found on types of backgrounds and corresponding mitigation strategies.

2. **Background Modeling:** Modeling techniques are employed to predict and subtract background contributions from the observed data accurately. This involves using simulations, statistical methods, and detailed knowledge of the experimental setup.
3. **Detector Improvements:** Ongoing efforts focus on developing detectors with enhanced background rejection capabilities. This includes using advanced materials, improved shielding, and innovative detection technologies. In Chapter 2, we will be discussing a novel detector technology for cryogenic detectors that can tag and reject background events with  $> 90\%$  efficiency in the energy range  $< 100$  keV.
4. **Data Analysis Techniques:** Data analysis techniques are used to identify backgrounds. In Chapter 4, we will use data to estimate  $^{32}\text{Si}$  background in the CDMS II experiment. Machine learning methods, pattern recognition algorithms, or Bayesian analysis approaches are also used to identify background noise from data.

## 1.7 Preface to work in this thesis

The lack of a positive laboratory signal for GeV scale DM is a compelling reason for researchers to shift their focus towards investigating low-mass dark matter (LMDM). To explore the lower mass range of the parameter space, currently limited by existing detection technology, it becomes crucial to develop detectors that can detect nuclear recoils with a

low energy threshold. Due to the extremely weak interaction cross-sections ( $\sim 10^{-43} \text{ cm}^2$ ) of dark matter particles, these detectors should allow for the construction of large detector systems for detection in a reasonable amount of time. CE $\nu$ NS encounters similar challenges to LMDM detection and therefore necessitates using low threshold detectors. Thus, these experiments face significant challenges, primarily centred around (i) achieving detectors with large mass low recoil energy thresholds and (ii) comprehending and mitigating backgrounds. The subsequent chapters in this thesis will delve into both of these areas. A concise overview of some relevant works has been procluded here.

### 1.7.1 Cryogenic detectors with veto system

Cryogenic detectors are a popular choice for numerous rare event search experiments. DM search experiments such as SuperCDMS/CDMSLite and EDELWEISS utilize semiconductors, specifically germanium and silicon, as the primary detector materials [51, 53, 62]. The signals get lost amid significant background noise in these detectors, mostly from nearby radioactive materials. The key to improving experimental sensitivity lies in reducing this background effectively. One method of achieving this is by using active veto detectors. Chapter 2 explores the development of a new active veto detector that efficiently identifies background events. We will discuss the challenges in making it, the simulation setup, calibration, noise performance, and the results at the MINER experimental site.

### 1.7.2 Simultaneous measurement of phonon and light from $\text{Al}_2\text{O}_3$

To detect extremely low recoil energy, experiments prefer using detector materials with a lower atomic mass number, as indicated by Eq. 1.9, where  $E_R \propto \frac{1}{m_n}$ .  $\text{Al}_2\text{O}_3$  is an ideal choice for constructing a detector, unlike traditional materials like germanium or silicon. MINER, in addition to germanium and silicon will employ scintillating detector made up

of  $\text{Al}_2\text{O}_3$ . Also, NUCLEUS will use  $\text{Al}_2\text{O}_3$  in search for  $\text{CE}\nu\text{NS}$  [54, 59, 63, 64]. Some experiments also explore novel gas detectors employing mixtures such as Neon and  $\text{CH}_4$  or utilizing Diamond as the detector medium. Opting for scintillating detectors like  $\text{Al}_2\text{O}_3$  offers the advantage of sensitivity to both LMDM and  $\text{CE}\nu\text{NS}$ . Additionally, the simultaneous measurement of phonon and light from  $\text{Al}_2\text{O}_3$  aids in background discrimination. In Chapter 3, we will delve into the performance of a 100 g  $\text{Al}_2\text{O}_3$  detector, focusing on its most challenging aspect—measuring the produced light from  $\text{Al}_2\text{O}_3$ .

### 1.7.3 Background measurement for dark matter searches

The primary approach to reduce background interference in these experiments involves either passive or active shielding. In addition to operating at substantial depths underground, a passive, multi-layer hermetic shield proves effective in significantly lowering the rates of background particles, particularly gammas and neutrons. However, these measures fail to address in-situ backgrounds inherent in the detector material. These backgrounds arise from cosmogenic activation, giving rise to isotopes like  $^{32}\text{Si}$  and  $^3\text{H}$ . In particular,  $^{32}\text{Si}$  poses a significant concern for silicon detectors in rare event search experiments. DAMIC has already measured the  $^{32}\text{Si}$  background rate in their silicon CCD detectors [65], revealing its potential impact on the upcoming SuperCDMS SNOLAB experiment [48]. Therefore, a precise measurement becomes crucial. Chapter 4 will explore an ongoing analysis of estimating  $^{32}\text{Si}$  backgrounds for the CDMS II experiment.

This thesis delves into the aforementioned aspects concerning rare event searches. In the last chapter, there is a summary and a discussion of future perspectives based on the work done in this thesis.

## Bibliography

- [1] Andrew Liddle. *An Introduction to Modern Cosmology, Second Edition*. Wiley, 2003.
- [2] N. Aghanim et al. “Planck 2018 results. VI. Cosmological parameters”. *Astron. Astrophys.* 641 (2020). arXiv: [1807.06209 \[astro-ph.CO\]](#).
- [3] F. Zwicky. “Die Rotverschiebung von extragalaktischen Nebeln”. *Helv. Phys. Acta* 6 (1933), p. 110–127.
- [4] Yoshiaki Sofue and Vera Rubin. “Rotation curves of spiral galaxies”. *Ann. Rev. Astron. Astrophys.* 39 (2001), p. 137–174. arXiv: [astro-ph/0010594](#).
- [5] Albert Einstein. “Lens-Like Action of a Star by the Deviation of Light in the Gravitational Field”. *Science* 84 (1936), p. 506–507.
- [6] R. Hurt (IPAC/Caltech)/The GraL Collaboration. *Gaia Satellite*. 2021. URL: <https://sci.esa.int/web/gaia/-/lensing-explained>.
- [7] Peter Schneider, Jürgen Ehlers, and Emilio E. Falco. *Gravitational Lenses*. 1992.
- [8] Richard Massey, Thomas Kitching, and Johan Richard. “The dark matter of gravitational lensing”. *Rept. Prog. Phys.* 73 (2010), p. 086901. arXiv: [1001.1739 \[astro-ph.CO\]](#).
- [9] Chandra X ray Observatory. *NASA Finds Direct Proof of Dark Matter*. URL: [https://chandra.harvard.edu/photo/2006/1e0657/..](https://chandra.harvard.edu/photo/2006/1e0657/)
- [10] Douglas Clowe et al. “A Direct Empirical Proof of the Existence of Dark Matter\*”. *The Astrophysical Journal* 648 (2006), p. L109.
- [11] Volker Springel et al. “Simulating the joint evolution of quasars, galaxies and their large-scale distribution”. *Nature* 435 (2005), p. 629–636. arXiv: [astro-ph/0504097](#).
- [12] Volker Springel, Carlos S. Frenk, and Simon D. M. White. “The large-scale structure of the Universe”. *Nature* 440 (2006), p. 1137. arXiv: [astro-ph/0604561](#).
- [13] Gianfranco Bertone and Tim Tait M. P. “A new era in the search for dark matter”. *Nature* 562 (2018), p. 51–56. arXiv: [1810.01668 \[astro-ph.CO\]](#).



- [14] Jonathan L. Feng. “Dark Matter Candidates from Particle Physics and Methods of Detection”. *Ann. Rev. Astron. Astrophys.* 48 (2010), p. 495–545. arXiv: [1003.0904 \[astro-ph.CO\]](#).
- [15] Bernard Carr, Florian Kuhnel, and Marit Sandstad. “Primordial Black Holes as Dark Matter”. *Phys. Rev. D* 94 (2016), p. 083504. arXiv: [1607.06077 \[astro-ph.CO\]](#).
- [16] A. Boyarsky et al. “Sterile neutrino Dark Matter”. *Prog. Part. Nucl. Phys.* 104 (2019), p. 1–45. arXiv: [1807.07938 \[hep-ph\]](#).
- [17] R. D. Peccei and Helen R. Quinn. “CP Conservation in the Presence of Instantons”. *Phys. Rev. Lett.* 38 (1977), p. 1440–1443.
- [18] Gerard Jungman, Marc Kamionkowski, and Kim Griest. “Supersymmetric dark matter”. *Phys. Rept.* 267 (1996), p. 195–373. arXiv: [hep-ph/9506380](#).
- [19] Antonio Boveia and Caterina Doglioni. “Dark Matter Searches at Colliders”. *Ann. Rev. Nucl. Part. Sci.* 68 (2018), p. 429–459. arXiv: [1810.12238 \[hep-ex\]](#).
- [20] Marcello Campajola. “Dark Sector first results at Belle II”. *Phys. Scripta* 96 (2021), p. 084005. arXiv: [2208.01101 \[hep-ex\]](#).
- [21] O. Adriani et al. “Cosmic-Ray Positron Energy Spectrum Measured by PAMELA”. *Phys. Rev. Lett.* 111 (2013), p. 081102. arXiv: [1308.0133 \[astro-ph.HE\]](#).
- [22] L. Accardo et al. “High Statistics Measurement of the Positron Fraction in Primary Cosmic Rays of 0.5–500 GeV with the Alpha Magnetic Spectrometer on the International Space Station”. *Phys. Rev. Lett.* 113 (2014), p. 121101.
- [23] M. G. Aartsen et al. “Search for neutrinos from decaying dark matter with IceCube”. *Eur. Phys. J. C* 78 (2018), p. 831. arXiv: [1804.03848 \[astro-ph.HE\]](#).
- [24] M. Ackermann et al. “Dark Matter Constraints from Observations of 25 Milky Way Satellite Galaxies with the Fermi Large Area Telescope”. *Phys. Rev. D* 89 (2014), p. 042001. arXiv: [1310.0828 \[astro-ph.HE\]](#).
- [25] H. Abdallah et al. “Search for  $\gamma$ -Ray Line Signals from Dark Matter Annihilations in the Inner Galactic Halo from 10 Years of Observations with H.E.S.S.” *Phys. Rev. Lett.* 120 (2018), p. 201101. arXiv: [1805.05741 \[astro-ph.HE\]](#).

- [26] Rebecca K. Leane. “Indirect Detection of Dark Matter in the Galaxy”. In: *3rd World Summit on Exploring the Dark Side of the Universe*. 2020, p. 203–228. arXiv: [2006.00513 \[hep-ph\]](#).
- [27] Marc Schumann. “Direct Detection of WIMP Dark Matter: Concepts and Status”. *J. Phys. G* 46 (2019), p. 103003. arXiv: [1903.03026 \[astro-ph.CO\]](#).
- [28] J. D. Lewin and P. F. Smith. “Review of mathematics, numerical factors, and corrections for dark matter experiments based on elastic nuclear recoil”. *Astropart. Phys.* 6 (1996), p. 87–112.
- [29] Mark W. Goodman and Edward Witten. “Detectability of Certain Dark Matter Candidates”. *Phys. Rev. D* 31 (1985). Ed. by M. A. Srednicki, p. 3059.
- [30] A. Drukier and Leo Stodolsky. “Principles and Applications of a Neutral Current Detector for Neutrino Physics and Astronomy”. *Phys. Rev. D* 30 (1984), p. 2295.
- [31] Gintaras Duda, Ann Kemper, and Paolo Gondolo. “Model Independent Form Factors for Spin Independent Neutralino-Nucleon Scattering from Elastic Electron Scattering Data”. *JCAP* 04 (2007), p. 012. arXiv: [hep-ph/0608035](#).
- [32] Richard H. Helm. “Inelastic and Elastic Scattering of 187-Mev Electrons from Selected Even-Even Nuclei”. *Phys. Rev.* 104 (1956), p. 1466–1475.
- [33] Marino A.D. Franklin A.D. *Are There Really Neutrinos?: An Evidential History*. CRC Press, 2020.
- [34] F. Reines and C. L. Cowan. “Detection of the free neutrino”. *Phys. Rev.* 92 (1953), p. 830–831.
- [35] C. L. Cowan et al. “Detection of the free neutrino: A Confirmation”. *Science* 124 (1956), p. 103–104.
- [36] John N. Bahcall and R. Davis. “Solar Neutrinos - a Scientific Puzzle”. *Science* 191 (1976), p. 264–267.
- [37] Y. Fukuda et al. “Evidence for oscillation of atmospheric neutrinos”. *Phys. Rev. Lett.* 81 (1998), p. 1562–1567. arXiv: [hep-ex/9807003](#).
- [38] Daniel Z. Freedman. “Coherent Neutrino Nucleus Scattering as a Probe of the Weak Neutral Current”. *Phys. Rev. D* 9 (1974), p. 1389–1392.

- [39] D. Akimov et al. “Observation of Coherent Elastic Neutrino-Nucleus Scattering”. *Science* 357.6356 (2017), p. 1123–1126. arXiv: [1708.01294 \[nucl-ex\]](#).
- [40] Jens Erler and Michael J. Ramsey-Musolf. “The Weak mixing angle at low energies”. *Phys. Rev. D* 72 (2005), p. 073003. arXiv: [hep-ph/0409169](#).
- [41] Super Cryogenic Dark Matter Search. *Dark Matter Limit Plotter*. 2023.
- [42] Th. A. Mueller et al. “Improved Predictions of Reactor Antineutrino Spectra”. *Phys. Rev. C* 83 (2011), p. 054615. arXiv: [1101.2663 \[hep-ex\]](#).
- [43] E. Aprile et al. “First Dark Matter Search Results from the XENON1T Experiment”. *Phys. Rev. Lett.* 119 (2017), p. 181301. arXiv: [1705.06655 \[astro-ph.CO\]](#).
- [44] E. Aprile et al. “First Dark Matter Search with Nuclear Recoils from the XENONnT Experiment”. *Phys. Rev. Lett.* 131 (2023), p. 041003.
- [45] J. Aalbers et al. “First Dark Matter Search Results from the LUX-ZEPLIN (LZ) Experiment”. *Phys. Rev. Lett.* 131 (2023), p. 041002. arXiv: [2207.03764 \[hep-ex\]](#).
- [46] Yue Meng et al. “Dark Matter Search Results from the PandaX-4T Commissioning Run”. *Phys. Rev. Lett.* 127 (2021), p. 261802. arXiv: [2107.13438 \[hep-ex\]](#).
- [47] G. Angloher et al. “Results on sub-GeV dark matter from a 10 eV threshold CRESST-III silicon detector”. *Phys. Rev. D* 107 (2023), p. 122003.
- [48] R. Agnese et al. “Projected Sensitivity of the SuperCDMS SNOLAB experiment”. *Phys. Rev. D* 95 (2017), p. 082002. arXiv: [1610.00006 \[physics.ins-det\]](#).
- [49] P. Agnes et al. “Search for low-mass dark matter WIMPs with 12 ton-day exposure of DarkSide-50”. *Phys. Rev. D* 107 (2023), p. 063001. arXiv: [2207.11966 \[hep-ex\]](#).
- [50] R. Ajaj et al. “Search for dark matter with a 231-day exposure of liquid argon using DEAP-3600 at SNOLAB”. *Phys. Rev. D* 100 (2019), p. 022004. arXiv: [1902.04048 \[astro-ph.CO\]](#).
- [51] A. Aguilar-Arevalo et al. “Results on low-mass weakly interacting massive particles from a 11 kg-day target exposure of DAMIC at SNOLAB”. *Phys. Rev. Lett.* 125 (2020), p. 241803. arXiv: [2007.15622 \[astro-ph.CO\]](#).
- [52] G. Adhikari et al. “Three-year annual modulation search with COSINE-100”. *Phys. Rev. D* 106 (2022), p. 052005. arXiv: [2111.08863 \[hep-ex\]](#).

- [53] L. Hehn et al. “Improved EDELWEISS-III sensitivity for low-mass WIMPs using a profile likelihood approach”. *Eur. Phys. J. C* 76 (2016), p. 548. arXiv: [1607.03367 \[astro-ph.CO\]](#).
- [54] G. Agnolet et al. “Background Studies for the MINER Coherent Neutrino Scattering Reactor Experiment”. *Nucl. Instrum. Meth. A* 853 (2017), p. 53–60. arXiv: [1609.02066 \[physics.ins-det\]](#).
- [55] Ricochet Collaboration et al. *Ricochet Progress and Status*. 2021. arXiv: [2111.06745 \[physics.ins-det\]](#).
- [56] Alexis Aguilar-Arevalo et al. “Exploring low-energy neutrino physics with the Coherent Neutrino Nucleus Interaction Experiment”. *Phys. Rev. D* 100 (2019), p. 092005. arXiv: [1906.02200 \[physics.ins-det\]](#).
- [57] H. Bonet et al. “Constraints on elastic neutrino nucleus scattering in the fully coherent regime from the CONUS experiment”. *Phys. Rev. Lett.* 126 (2021), p. 041804. arXiv: [2011.00210 \[hep-ex\]](#).
- [58] J. Colaresi et al. “First results from a search for coherent elastic neutrino-nucleus scattering at a reactor site”. *Phys. Rev. D* 104 (2021), p. 072003. arXiv: [2108.02880 \[hep-ex\]](#).
- [59] V. Wagner et al. “Exploring CE $\nu$ NS of reactor neutrinos with the NUCLEUS experiment”. *J. Phys. Conf. Ser.* 2156 (2021), p. 012118.
- [60] I. Alekseev et al. “First results of the  $\nu$ GeN experiment on coherent elastic neutrino-nucleus scattering”. *Phys. Rev. D* 106 (2022), p. L051101. arXiv: [2205.04305 \[nucl-ex\]](#).
- [61] D. Yu Akimov et al. “First ground-level laboratory test of the two-phase xenon emission detector RED-100”. *JINST* 15 (2020), P02020. arXiv: [1910.06190 \[physics.ins-det\]](#).
- [62] I. Alkhatib et al. “Light Dark Matter Search with a High-Resolution Athermal Phonon Detector Operated Above Ground”. *Phys. Rev. Lett.* 127 (2021), p. 061801. arXiv: [2007.14289 \[hep-ex\]](#).
- [63] Wei Eng Ang, Shikha Prasad, and Rupak Mahapatra. “Coherent elastic neutrino nucleus scatter response of semiconductor detectors to nuclear reactor antineutrinos”. *Nucl. Instrum. Meth. A* 1004 (2021), p. 165342.

- [64] R. Strauss et al. “The  $\nu$ -cleus experiment: Gram-scale cryogenic calorimeters for a discovery of coherent neutrino scattering”. *J. Phys. Conf. Ser.* 1342 (2020). Ed. by Ken Clark et al., p. 012132.
- [65] A. Aguilar-Arevalo et al. “Measurement of radioactive contamination in the high-resistivity silicon CCDs of the DAMIC experiment”. *Journal of Instrumentation* 10 (2015), p. 08014.

# Active veto detector

## Contents

2.1	Types of backgrounds . . . . .	40
2.2	Detector technology . . . . .	47
2.3	Results . . . . .	54
2.4	Improvement in background reduction with $4\pi$ veto coverage . . . . .	62
2.5	Summary and outlook . . . . .	66

Understanding the impact of backgrounds on the experiments searching for rare events is crucial. Not identifying and considering backgrounds can contaminate signal rates and lead to inaccurate conclusions about WIMP characteristics. Figure 1.9 from Chapter 1 shows that WIMPs in the mass range 10-100 GeV/c<sup>2</sup> induce recoil energy in the  $O(10^2)$  keV or less, with a scattering event rate in the  $O(10^{-2})$  events kg<sup>-1</sup> keV<sup>-1</sup> day<sup>-1</sup> which is significantly below standard background rates. To mitigate this, experiments are operated in low background environments through careful location selection, like in underground laboratories, with shielding and methods to distinguish between WIMP and background events. Detectors play a crucial role in identifying and discriminating against background

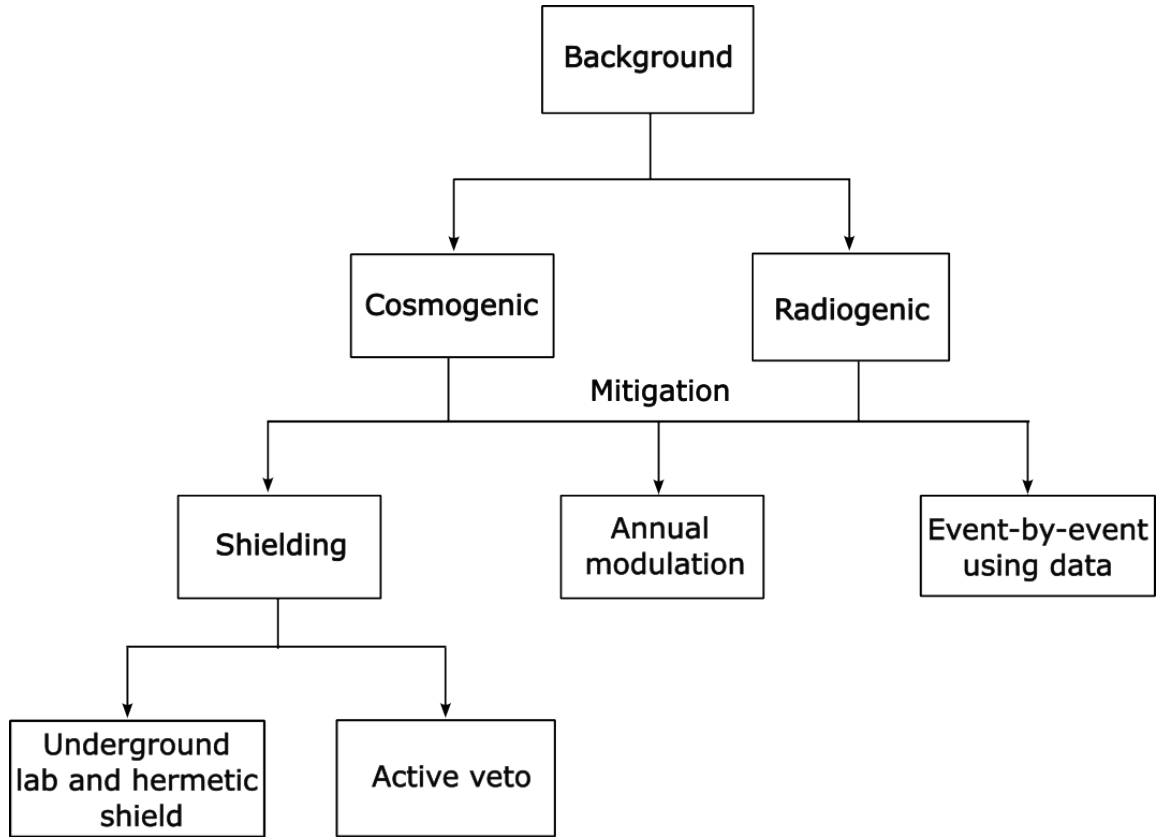


FIGURE 2.1: A summary of common backgrounds in rare event search experiments and corresponding mitigation strategies.

events individually or searching for modulation signatures within well-known backgrounds.

## 2.1 Types of backgrounds

Common backgrounds for rare event search experiments can be categorized into two types: cosmogenic and radiogenic. The following section provides a brief overview of the origin of these backgrounds and the mitigation strategies for any rare event search experiment. Figure 2.1 helps to understand the types of backgrounds and their possible mitigation procedures.

## Cosmogenic

Cosmic rays are high-energy particles, primarily protons and atomic nuclei, originating from various sources in the universe. When cosmic rays enter the Earth's atmosphere, they interact with air molecules, producing secondary particles like pions which mostly decay to high-energy muons. These muons can travel through substantial amounts of material, like Earth's crust, before creating lower-energy secondary particles. Among them, secondary neutrons pose a challenge as they scatter from detector nuclei, mimicking the WIMP signal. In addition, cosmic rays can also induce formation of radioactive isotopes in detector materials. These internal isotopes are unavoidable, but efforts are made to minimize their presence.

## Radiogenic

These background sources originate from radioactive isotopes in materials surrounding the detectors, such as shielding materials like lead and copper. Radioactive decays give rise to the emission of  $\gamma$  rays,  $\beta$  particles, or neutrons. Based on their production, these radiogenic sources can be classified into three categories [1]:

1. **Primordial sources:** Isotopes with half-lives exceeding  $10^9$  years have been present in Earth's ores since its formation. Despite purification attempts, traces of these isotopes, including  $^{232}\text{Th}$ ,  $^{238}\text{U}$ , and  $^{40}\text{K}$ , persist in shielding materials. Neutrons primarily originate from  $^{232}\text{Th}$  and  $^{238}\text{U}$ , undergoing spontaneous fission and producing  $^{222}\text{Rn}$  and  $^{210}\text{Pb}$  during decay. The half-life of  $^{210}\text{Pb}$  is 22 years. Fission yields alpha particles and neutrons, while the decay of  $^{222}\text{Rn}$  and  $^{210}\text{Pb}$  contributes to most  $\gamma$ -rays and  $\beta$ -particles.
2. **Anthropogenic:** The fission product  $^{137}\text{Cs}$  is a common byproduct of  $^{235}\text{U}$  in nuclear reactors. Being water-soluble, it easily spreads and is found in various materials,



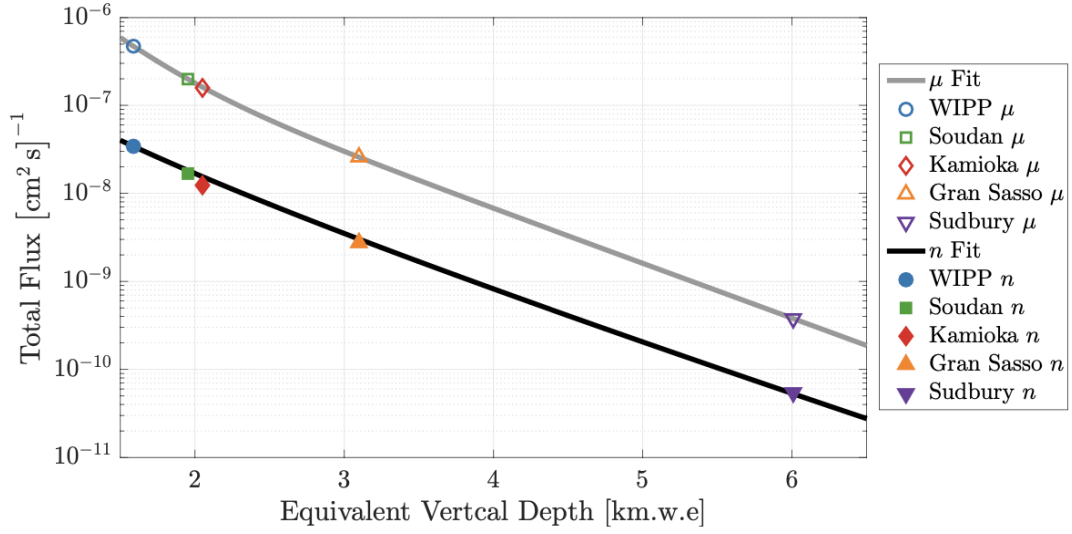


FIGURE 2.2: Cosmic muon and neutron fluxes at different underground laboratories with varying overburden depths. The muon flux data points are obtained through measurements, whereas neutron flux data points are computed using simulations and the measured muon fluxes. The depth is expressed in km-water-equivalent. Each data set is fitted with models, and both data and fits are sourced from [1, 3].

emitting  $\beta$ -particles and  $\gamma$ -rays that contribute to backgrounds.

3. **Isotopes from cosmic rays:** Cosmic rays can induce the formation of radioactive isotopes in materials. Dominant cosmogenic isotopes include tritium ( $^3\text{H}$ ) in Ge detectors [2] and both  $^3\text{H}$  and  $^{32}\text{Si}$  in Si detectors. All these isotopes are radioactive and produce  $\beta$ -particles and  $\gamma$ -rays.  $^{32}\text{Si}$  background and the estimation of its decay rate from data will be discussed in Chapter 4.

### 2.1.1 Mitigation strategies

There are three strategies to distinguish WIMP scatters from remaining background signals.

#### Shielding

To mitigate cosmogenic backgrounds, these experiments are often conducted in under-

ground laboratories. Muons deposit around  $O(1 \text{ MeV})$  energy in detectors, exceeding the typical WIMP range, but they can be filtered out by setting an appropriate energy range for WIMP searches. However, secondary neutrons, with enough energy to penetrate shielding, create recoils suitable for a WIMP search, contributing to a significant background. This background can be reduced by using deeper underground laboratories. Figure 2.2 shows muon (based on the measurements) and neutron fluxes (based on the simulation and muon flux measurements) at different overburden depths for various laboratories. The SuperCDMS SNOLAB is located at Sudbury. In spite of operating in deep underground labs, passive shielding is required to protect these experiments from surrounding radiation. Materials with high electron density, like Lead and Copper, effectively shield electromagnetically interacting particles. On the other hand, hydrogenous materials such as Polyethylene or water effectively shield neutrons. However, the small amounts of radiation present in the shielding can transform the shielding into a source of backgrounds. Unfortunately, the reduction of these backgrounds is ineffective for only passive shielding. One way to reduce this background is by applying active shielding. Active shielding is one which can identify backgrounds and reject them. Muon veto systems are an example of active shielding in which detectors are strategically placed around the experimental setup to identify and reject events caused by cosmic ray muons. Most dark matter experiments employ muon veto systems, typically using plastic or liquid scintillators [4, 5]. Other examples of active veto systems, such as the active neutron veto system in XENON and LUX experiments, are employed to detect and identify neutrons [6–8]. In the upcoming Section 2.1.2, we will discuss the impact of radiogenic backgrounds on the upcoming SuperCDMS SNOLAB experiments and the performance of a novel active veto detector designed explicitly for mitigation purposes. The detector is instrumented in the immediate vicinity of the target detector, enabling the rejection of radiogenic backgrounds efficiently.

### Modulation signal

Some experiments look for WIMPs by observing their astrophysical modulation signatures, either annually or daily. Annual modulation results from the Earth's orbit around the Sun within the Milky Way, causing variations in the Earth's velocity relative to the galactic frame and, consequently, a detectable modulation in WIMP flux. Daily modulation relies on changes in WIMP flux as the Earth rotates on its axis, leading to variations in the direction of WIMP-induced recoils. Detecting such modulations requires a large sample of WIMP recoils and well-characterized, stable backgrounds.

The DAMA collaboration claims WIMP detection with significance  $> 8\sigma$  based on over a decade of annual modulation observed in the recoil spectrum of its NaI crystals [9]. However, other experiments have cast doubt on this interpretation, as a standard WIMP explanation of DAMA's modulation signal has been ruled out. The CoGeNT collaboration also reports a  $2.8\sigma$  annual modulation signal, but with a phase different from the expected modulation phase by  $4\sigma$  [10].

### Event-by-event discrimination

Event-by-event discrimination is a powerful tool that enables experiments to distinguish between the different types of particle interactions. As discussed earlier, the direct detection method is based on the measurement of three types of signals: phonons, ionization, and scintillation (shown in Fig. 1.10). It exhibits distinct responses to different interactions, enabling the discrimination of each event as either electron recoil (ER) or nuclear recoil (NR). WIMPs and neutrinos scatter within keV ranges as NRs, while most backgrounds scatter as ERs. For example, the creation of quanta involves different energy thresholds: a few meV per phonon, approximately 10 eV per charge carrier in ionization, and around

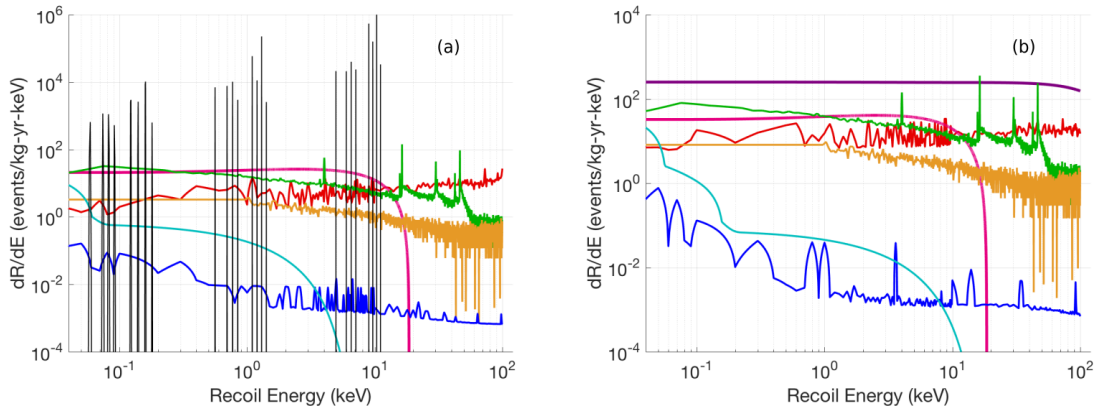


FIGURE 2.3: A Monte Carlo simulation is performed to estimate the expected background rate for SuperCDMS SNOLAB experiment. In the figures it is shown in units of events/kg·yr·keV as a function of recoil energy. (a) and (b) represent background rate in germanium and silicon detector respectively.  $^3\text{H}$  (pink) in germanium and  $^{32}\text{Si}$  (purple) in silicon are the main contributors to the backgrounds. The remaining relevant backgrounds are Compton scatters from gamma rays (curve in red), surface betas (curve in green), decay daughters of  $^{222}\text{Rn}$  (curve in orange), neutrons (curve in blue), and coherent elastic neutrino-nucleus scattering (curve in cyan). The black lines indicate the activation lines in germanium from the electron capture process [16].

100 eV per scintillation photon [11]. These different energy thresholds result in distinct responses to different types of particle interactions. The ratios between the responses to different signals serve as discriminators for the type of event that occurred. Several experiments are designed to measure two signals simultaneously to avail event-by-event background discrimination [12–15].

### 2.1.2 Impact of radiogenic backgrounds on SuperCDMS SNOLAB

The upcoming SuperCDMS SNOLAB experiment will be situated about 2 km underground in Sudbury, Ontario, Canada, within the SNOLAB facility—the rock overburden at SNOLAB shields against cosmic-ray secondaries, equivalent to 6010 meters of water [16]. SuperCDMS SNOLAB will utilize a combination of silicon (Si) and germanium (Ge) detectors, offering complementary capabilities, especially in the search for sub-GeV dark

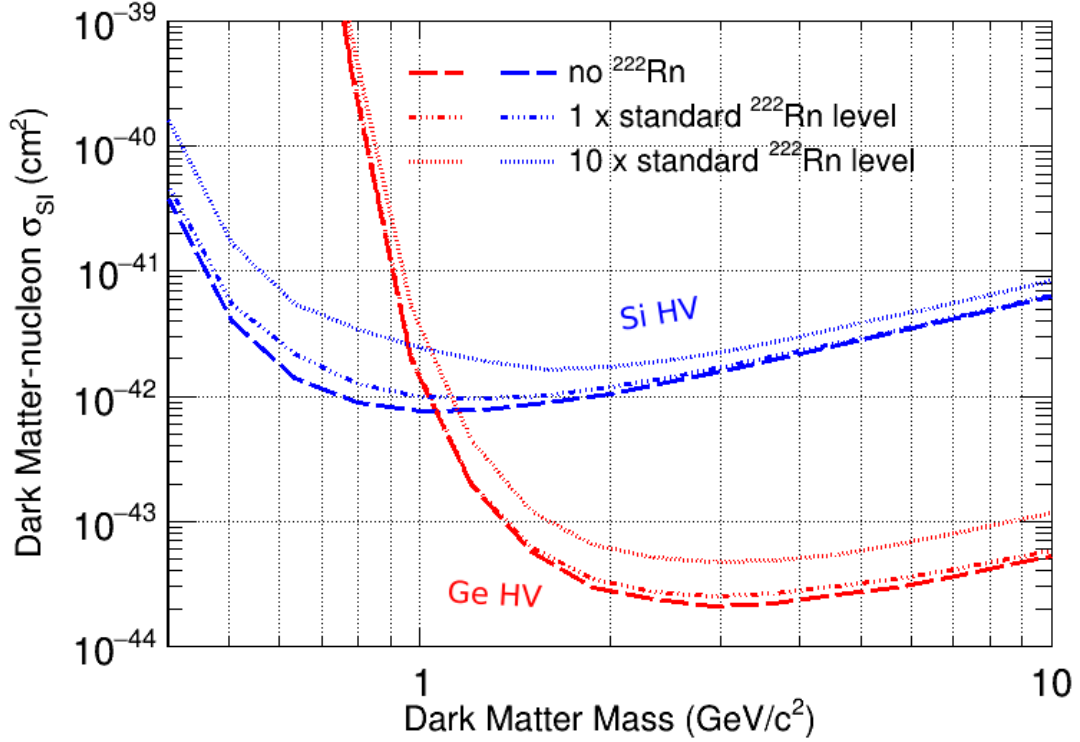


FIGURE 2.4: The sensitivity projection of the SuperCDMS SNOLAB direct detection dark matter experiment demonstrates variations in limits due to different levels of  $^{222}\text{Rn}$  contamination. The blue and red lines represent contamination in the silicon and germanium detectors. The lines vary for no contamination (dashed line), standard contamination (dash-dotted line), and contamination 10 times higher than usual (dotted line), with the standard contamination level set at  $50 \text{ nBq/cm}^2$  [16]. The figure is taken from [17].

matter. These detectors are cylindrical crystals with diameters of 100 mm and a thickness of 33.3 mm. Each Ge(Si) crystal weighs 1.39 (0.61) kg. The detectors will be operating in both high voltage (HV) and iZIP modes. In HV mode, they can be operated at a very low threshold. iZIP mode, on the other hand, enables event-by-event discrimination, a capability that HV mode lacks. The reduction of backgrounds for HV detectors is a challenge in itself. The three concerning background sources for the SuperCDMS SNOLAB experiment are (i) Compton scatters from the gamma rays, (ii) surface betas from surrounding materials, and (iii) recoils from the decay radiation of  $^{210}\text{Pb}$  and its progeny existing on the detector surfaces from radon exposure [18].

Figure 2.3 shows the MC simulation of the expected background rate as a function of recoil energy for both Ge and Si detectors in the SuperCDMS SNOLAB experiment. To understand the impact of these backgrounds, we calculate the expected sensitivity based on the background spectra after applying analysis threshold and cuts. By simulating events from the total background spectrum, considering the experimental exposure and background normalization, we estimate the expected spectrum for a given DM particle mass. Applying efficiency adjustments, we use Optimal Interval calculation to determine a 90% C.L. exclusion cross-section [19]. This process is repeated across the mass range of interest to create exclusion curves from single background simulations. The median 90% C.L. exclusion cross-section provides the sensitivity for each DM mass. Figure 2.4 shows the expected sensitivity curve for Ge and Si HV detectors, varying the  $^{222}\text{Rn}$  background contamination. It indicates that the sensitivity improves significantly in the absence of  $^{222}\text{Rn}$  background, compared to the 10 times of  $^{222}\text{Rn}$  for both Silicon (blue curves) and Germanium (red curves) HV detectors. Thus, it is crucial to reject these background sources to enhance the experimental sensitivity effectively. The motivation for instrumenting the novel active veto detector is to eliminate these background sources. The following section will delve into the detection principle, followed by the discussion of fabrication challenges and performance of the active veto detector.

## 2.2 Detector technology

The active veto detector system comprises a cylindrical target detector surrounded by a donut-shaped veto detector made of Ge. When a particle scatters in the detector, one part of the deposited energy liberates  $e^-/h^+$  pairs or ionization energy. The average energy required to create a  $e^-/h^+$  in Ge/Si is  $\epsilon_\gamma = 3.0/3.8$  eV [20]. Another part of the deposited

energy is used to create phonons. For ERs, most of the deposited energy goes into creating  $e^-/h^+$  pairs and a very small part is used to generate phonons. For NRs, we see the opposite. The ratio of ionization energy to the total recoil energy is defined as Ionization yield, which provides event-by-event discrimination. A voltage bias is applied across the detector surface to drift the  $e^-/h^+$  pairs to the surface where sensors are placed. Depending on the applied bias voltage, detectors are operated in two modes: (i) iZIP mode, where we measure both ionization and phonons energy, and (ii) HV mode, where only phonons are measured. In this chapter, our discussion will focus on phonon collection. Further details on ionization energy will be explored in Chapter 4.

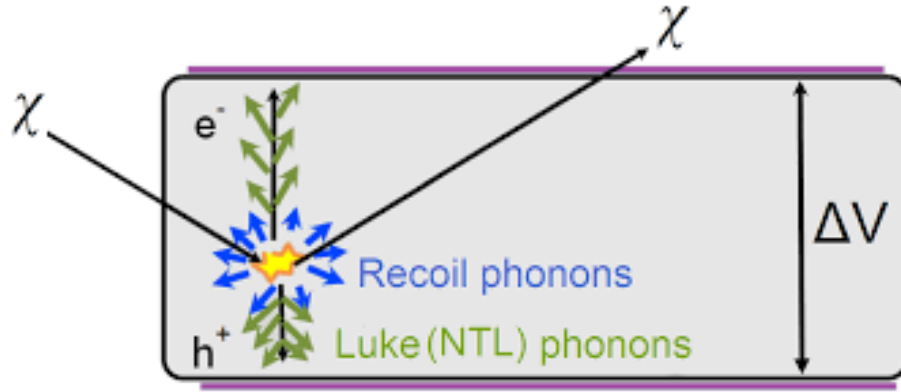


FIGURE 2.5: A detector schematic showing the phonon generation from a particle interaction. Primary recoil phonons are shown in blue. Green represents NTL phonons generated as electrons and holes drift towards the surface due to the applied bias voltage ( $\Delta V$ ).

### 2.2.1 Phonons

Particle interaction can generate three types of phonons. These are discussed below:

#### Primary phonons

The phonons generated by the initial scatter are specifically termed “primary” phonons. These primary phonons hold information regarding position, energy, and timing. The

energy from primary recoil phonons denoted as  $E_P$ .

### Relaxation phonons

These phonons are generated when the  $e^-/h^+$  pairs drift to the surface and relax back to the Fermi level, releasing energy ( $E_{relax}$ ) in the form of phonons.

### Neganov-Trofimov-Luke phonons

Neganov-Trofimov-Luke (NTL) phonons are produced by drifting  $e^-/h^+$  pairs through the crystal [21, 22]. As they move across the lattice sites, a portion of their energy is transferred to the lattice, generating phonons. This energy is denoted as  $E_{NTL}$ . Figure 2.5 shows a schematic to understand the phonon creation and propagation in the detector. Considering all three contributions to the total phonon energy,  $E_t$  is calculated as:

$$E_t = E_P + E_{relax} + E_{NTL} = E_R + E_{NTL} = E_R + eN_{e/h}V_b \quad (2.1)$$

where  $E_R$  is the total recoil energy,  $N_{e/h}$  is the total number of  $e^-/h^+$  pairs in the surface,  $V_b$  is the applied bias voltage,  $e$  is the electronic charge. Equation 2.1 indicates that applying a bias voltage can proportionally amplify a very small recoil energy ( $E_R$ ). This amplification is known as NTL gain, which enhances the signal-to-noise ratio, which is particularly beneficial for improving the performance of low-threshold detectors.

### 2.2.2 Phonon detection

The phonon sensors utilize Transition Edge Sensors (TES) technology [24], incorporating two superconducting materials, Aluminum (Al) and Tungsten (W), arranged on the detector's surface through photolithography, as illustrated in Fig. 2.6 [25]. The W layer is positioned above the Al layer, and their respective transition temperatures ( $T_c$ ) are approximately 1.2 K for Al and around 80 mK for W [26]. The detector operates at a sufficiently



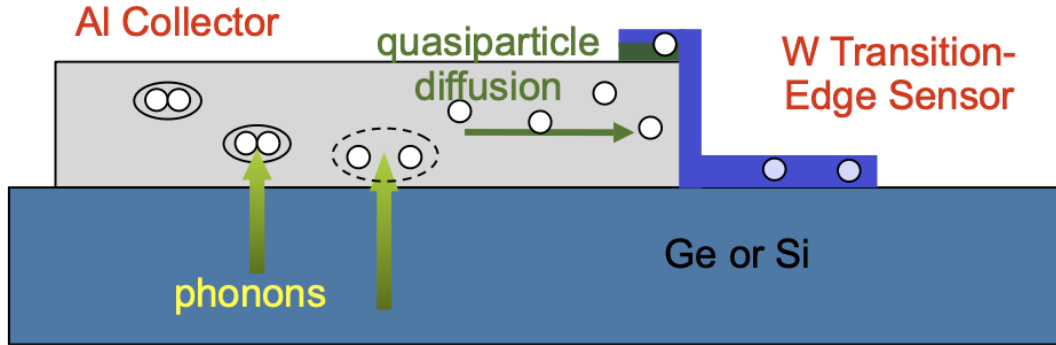


FIGURE 2.6: A schematic of TES collecting phonons at the surface of the detector. After entering the Al absorber, phonons break Cooper pairs and produce quasiparticles. They diffuse through Al and are trapped in the W [23].

low temperature to ensure that both Al and W are in a superconducting state, with W maintained near the edge of its transition temperature.

The Al layer serves as the first layer to absorb incoming phonons. Suppose the energy of the phonons exceeds the superconducting band gap of Al, around  $340 \mu\text{eV}$ . In that case, it leads to breaking Cooper pairs within the Al layer, resulting in the generation of quasiparticles. Phonons with energy less than  $340 \mu\text{eV}$  are considered inefficient for detection and are lost.

The quasiparticles then diffuse into the overlying W layer, which possesses a lower superconducting band gap energy of approximately  $80 \mu\text{eV}$  compared to Al. They further break up Cooper pairs in the W layer, thereby concentrating the phonon energy in the quasiparticles. These quasiparticles, now trapped in the W layer, induce a heating effect, causing the W to transition from a superconducting to a normal state. The circuit's sharp change in resistance, and consequently current, is utilized to convert the signal from phonon energy to an electronic signal.

The W layer is biased at 0 V (ground). The increase in temperature of W, induced by a phonon signal, results in a decrease in Joule heating. This, in turn, causes the TES to cool

back to its operating point. This intricate process is known as the electrothermal feedback loop.

### 2.2.3 Detector geometry and channel layout

The active veto detector has a shape of a donut. It has a mass of  $\sim 500$  g, having an inner and outer diameter of 28 mm and 76 mm, respectively, and 25 mm thickness. Figure 2.7(a) shows the donut-shaped veto detector inside a copper casing. Dotted points on the surface of the detector represent the phonon sensors patterned photolithographically. There are thousands of phonon sensors, which are further divided into two channels: outer and inner. In Fig. 2.7(b), the outer channel is shown in green, whereas the remaining sensors of the inner channels (blue, pink, and orange) were wired together in parallel to create one large inner channel. The inner target detector of the veto system is shown in Fig. 2.7(c). The detector is mounted in a copper nest, which helps to suspend the target detector inside the donut veto. In section 2.2.4, we will discuss the fabrication challenges and motivation for this design. After placing the inner detector nest inside the veto, the combined veto system is depicted in Figure 2.7(d), sharing the same diameter (76 mm) and thickness (25 mm) as the SuperCDMS detectors.

### 2.2.4 Fabrication challenges and signal readout

The veto detector has been developed at the test facility in Texas A&M University by the Texas A&M group. There are three main challenges to overcome in fabricating and mounting such a unique detector arrangement.

1. **Circuit design:** Patterning the circuit on the surface of an annular detector presents a challenge in the fabrication process. The usual method involves applying a photosensitive chemical called photoresist by spinning the substrate rapidly. However,

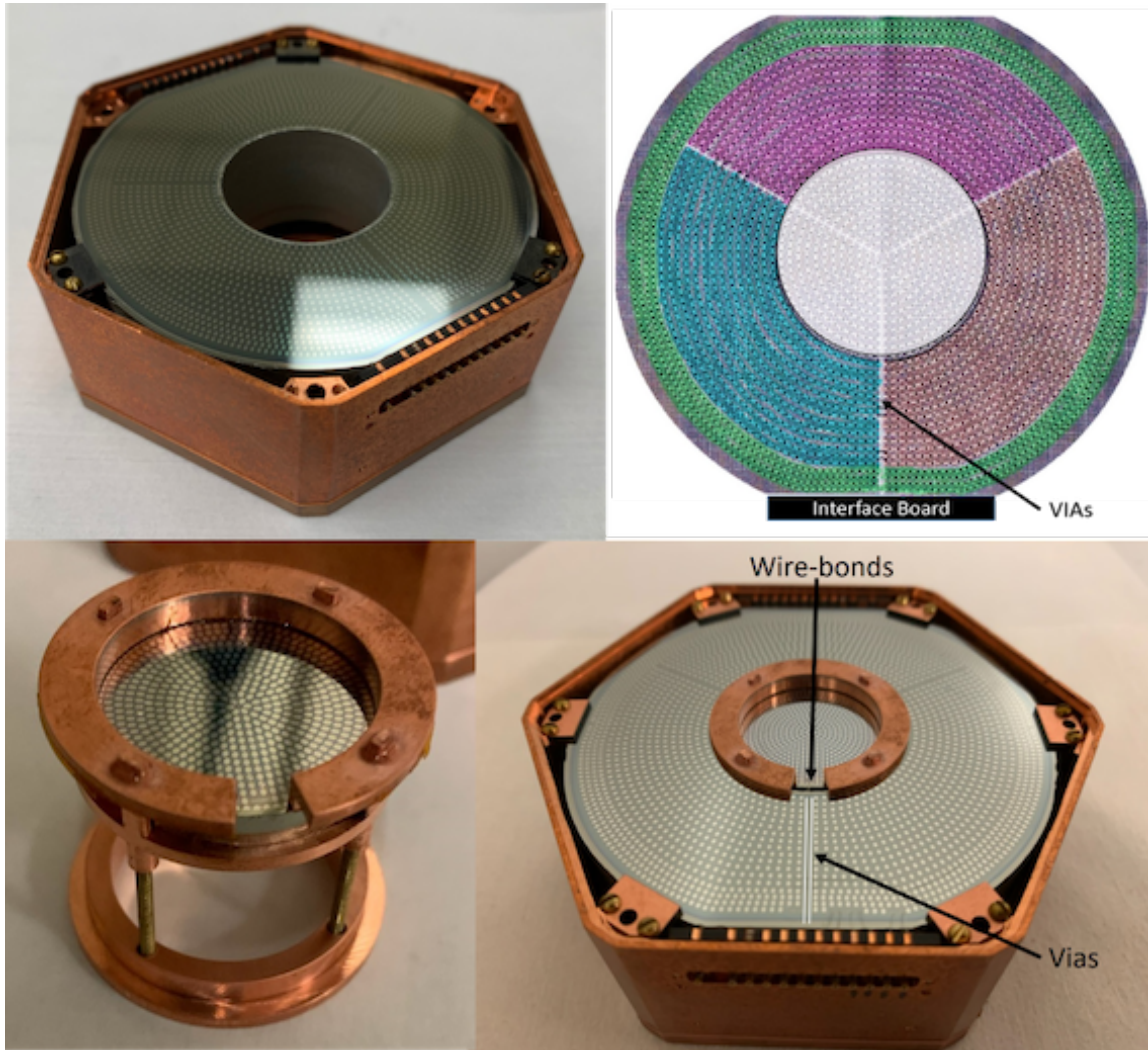


FIGURE 2.7: (a) The veto detector is in a copper cage, ready for wire bonding and cryogenic testing. (b) A picture showing the sensor's arrangement, with the inner part missing in the core drill region. Aluminium lines (vias) help wire the inner detector using standard interface boards. The “outer” channel is in green, while the other sensors of the “inner” channels (blue, pink, and orange) are connected to make one big inner channel. (c) The copper nest holds the inner detector, hanging it inside the veto while keeping them well connected for thermal conductivity. (d) The inner detector nest is inside the veto detector, making the whole setup 76 mm wide and 25 mm thick [17].

concerns arise when dealing with a substrate with a large hole in the centre, as this may lead to uneven film thickness and, consequently, irregular circuit patterns. To address this challenge, a core-drilling method is employed by TAMU in detector fab-

rication [25]. This method, outlined in their process, does not compromise crystal response, and it is done before patterning the detector circuit.

2. **Mounting the inner detector:** Making an internal veto detector is problematic because it physically separates the inner detector from its housing. Even though this helps in shielding the detector from radiation, it creates a challenge for mounting. The design we chose for this setup is like a nest. It is made of an upper copper two-piece cage that holds the inner detector. The pieces are connected with vertical ribs that press against the inner detector when it's installed. We used epoxy to glue the pieces together, creating good thermal contact between the nest and the inner detector. A lower ring squeezes the veto detector to complete the cooling process, ensuring good thermal contact (see in subsection 2.3.2).
3. **Connection to readout:** We also needed a way for wires to connect the inner and veto detectors. We achieved this by using aluminium connections on the veto detector to read signals from the inner detector. This is done through the interface board, where the detectors are wired to external electronics. Because of this, there are two aluminium lines on the mask/circuit that extend from the interface board to the centre of the detector. This is seen in Fig. 2.7(d). The signals are read out using a Superconducting Quantum Interference Device (SQUID) based on front-end amplifiers.

A potential area for future work is that, although these masks were initially created for standard detector dimensions and wiring setups, the modifications made in this study further diverge them from the optimal configuration. The elimination of sensors and wiring channels in parallel has an impact on the electrical characteristics of the channels, potentially causing a notable decrease in performance. Consequently, forthcoming efforts

will focus on developing custom masks, especially for these geometries, presenting a distinct pathway for improvement.

### 2.2.5 Veto technique

The backgrounds are mainly multiple scatter events. DM or a neutrino rarely interact with a single detector and deposits energy. So, signals are considered as single scatter (SS) particles. The design of the active veto detector is such that it would tag and reject multiple scatter (MS) events, i.e. the events that will deposit energy both in the active veto and inner target detector. Three conditions need to be satisfied simultaneously to select SS events: (i) deposited energy should be above the noise level of the target, (ii) deposited energy in the veto should be below or equal to the noise level of the veto detector, and (iii) time between two interacts should be in the coincidence time window of the DAQ which is of the order of few milliseconds. SS events distribution measured by the veto system has been discussed in section [2.4](#).

## 2.3 Results

With a successfully fabricated and mounted veto and inner detector module, the detector has been tested in the test facility as well as in the Mitchell Institute of Neutrino Experiment at Reactor (MINER) experimental site. MINER is an experiment located at Texas A&M University, USA, looking for Coherent Elastic Neutrino Nucleus Scattering ( $\text{CE}\nu\text{NS}$ ) cross-section using reactor neutrinos [[27](#)]. The experiment is currently under development. A more detailed discussion of the MINER experiment can be found in Chapter [3](#), including its scientific objectives and its current status. This section delves into the performance assessment of the prototype detector, emphasizing key aspects:

- Effective cooling of both detectors to operational temperatures.
- Achievement of low energy baseline resolution for the veto ( $\sim 1$  keV) and inner detector ( $\sim 100$  eV).
- Background reduction through coincident event tagging using the veto to restrict inner detector data to “single scatters”.

This section will start with the experimental data and analysis framework. We will then discuss the test results of the active veto detectors at both the test facility and the MINER experimental site. A GEANT4-based simulation with a similar detector geometry has been compared with the experimental result, showing excellent agreement. We also provide a way for improvement with a  $4\pi$  veto system with the active veto. Finally, we will conclude the section with a summary and outlook for the presented work.

### 2.3.1 Experimental setup and analysis framework

The experimental setup consists of the veto detector kept inside a copper case (shown in Fig. 2.5), which is then mounted within the BlueFors LD400 pulse-tube-based  $^3\text{He}$ - $^4\text{He}$  dilution refrigerator provided by NISER. This refrigerator is crucial for lowering the temperature of the detector to a few mK. Additionally, the experimental setup includes a data acquisition (DAQ) system and readout electronics for signal readout. Calibration sources are placed on the bare and polished surfaces of the detector. These sources are enclosed within a copper source holder featuring a narrow slit. The design allows for the adjustment of the event rate from the source by optimizing the slit width to achieve the desired value. This setup enables the creation of a focused, collimated beam of particles passing through and targeting the detector region. Figure 2.8 shows the images of the experimental setup at the test facility and the MINER experimental site. To reduce huge backgrounds at the



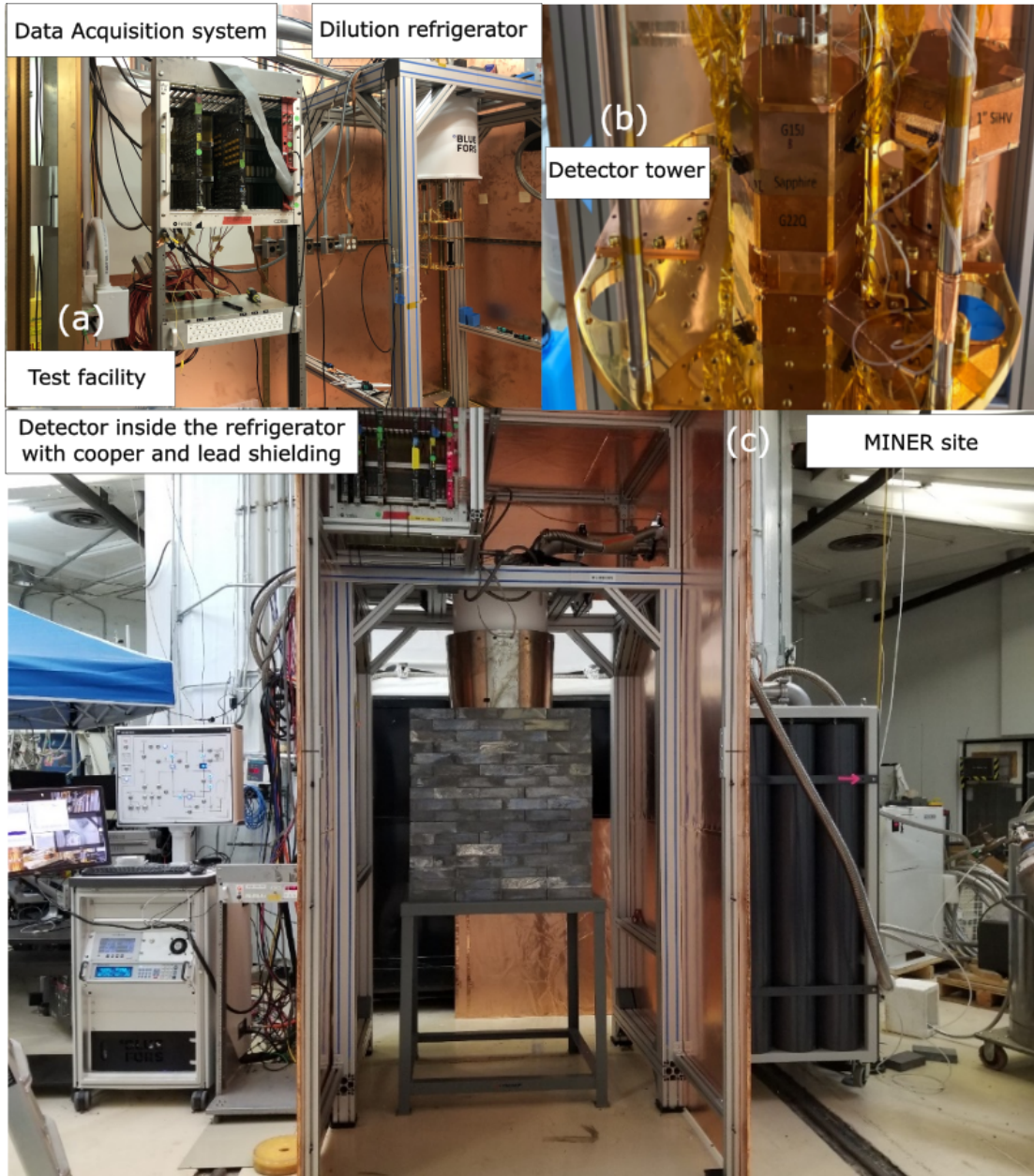


FIGURE 2.8: (a) Image of the testing facility, showing the dilution refrigerator on the right and the DAQ system on the left. The detector tower mounted on the refrigerator can be seen in (b). (c) Experimental site at MINER with primary Lead and Cooper shielding.

experimental site, primary shieldings, including Lead bricks, are provided as shown in Fig. 2.8(c).

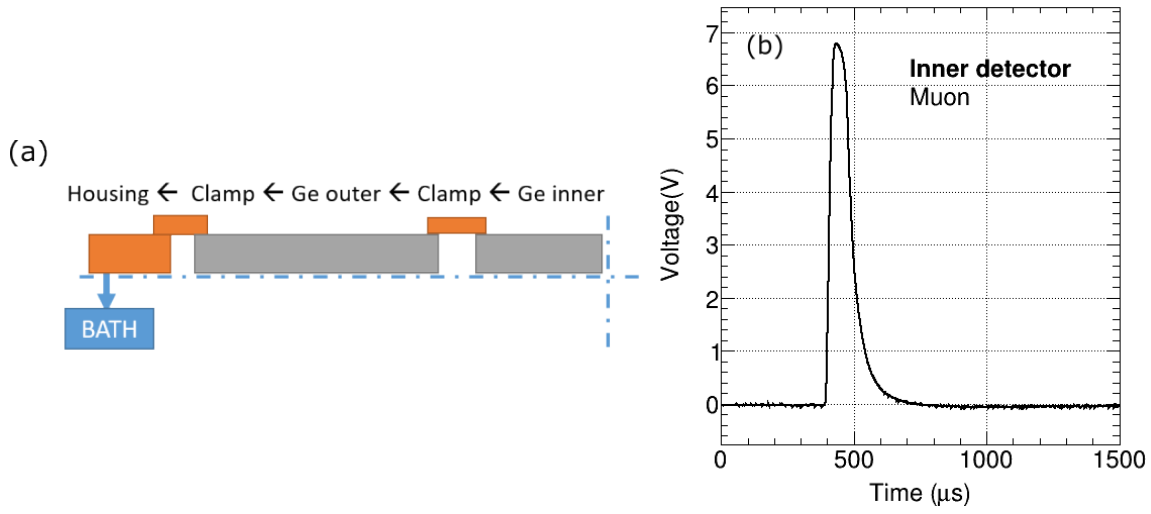


FIGURE 2.9: (a) Illustration showing the thermal conduction path from the inner detector to the refrigerator (bath). Dashed lines with dots denote planes of symmetry. Copper is represented in orange, and germanium is in gray. (b) A typical muon pulse in the inner target detector is shown as voltage vs time, indicating quick thermal recovery. The gain was minimized to prevent saturation of the digitizer by the muon pulses [17].

### 2.3.2 Thermal performance

As mentioned earlier, ensuring the effective cooling of the inner detector at a very low temperature (around tens of mK) is crucial. We introduced an outer veto between the inner detector and the cooling power (shown in Fig. 2.9(a)), which adds complexity due to multiple thermal impedances and coupling vibration. To qualitatively investigate the thermalization of the inner detector, we examined the thermal recovery times following high-energy depositions in the inner detector. We used cosmic muons for this, and they are expected to deposit about 3.3 MeV of energy into the inner detector. If the cooling is not sufficient, it will take a long time for the temperature to go back to normal, especially if the temperature is too high and close to the point where the sensors stop working well. Figure 2.9(b) shows an example of a muon pulse in the inner detector. We calculate the risetime and falltime of the muon pulse. The rise time is the time it takes for a pulse to



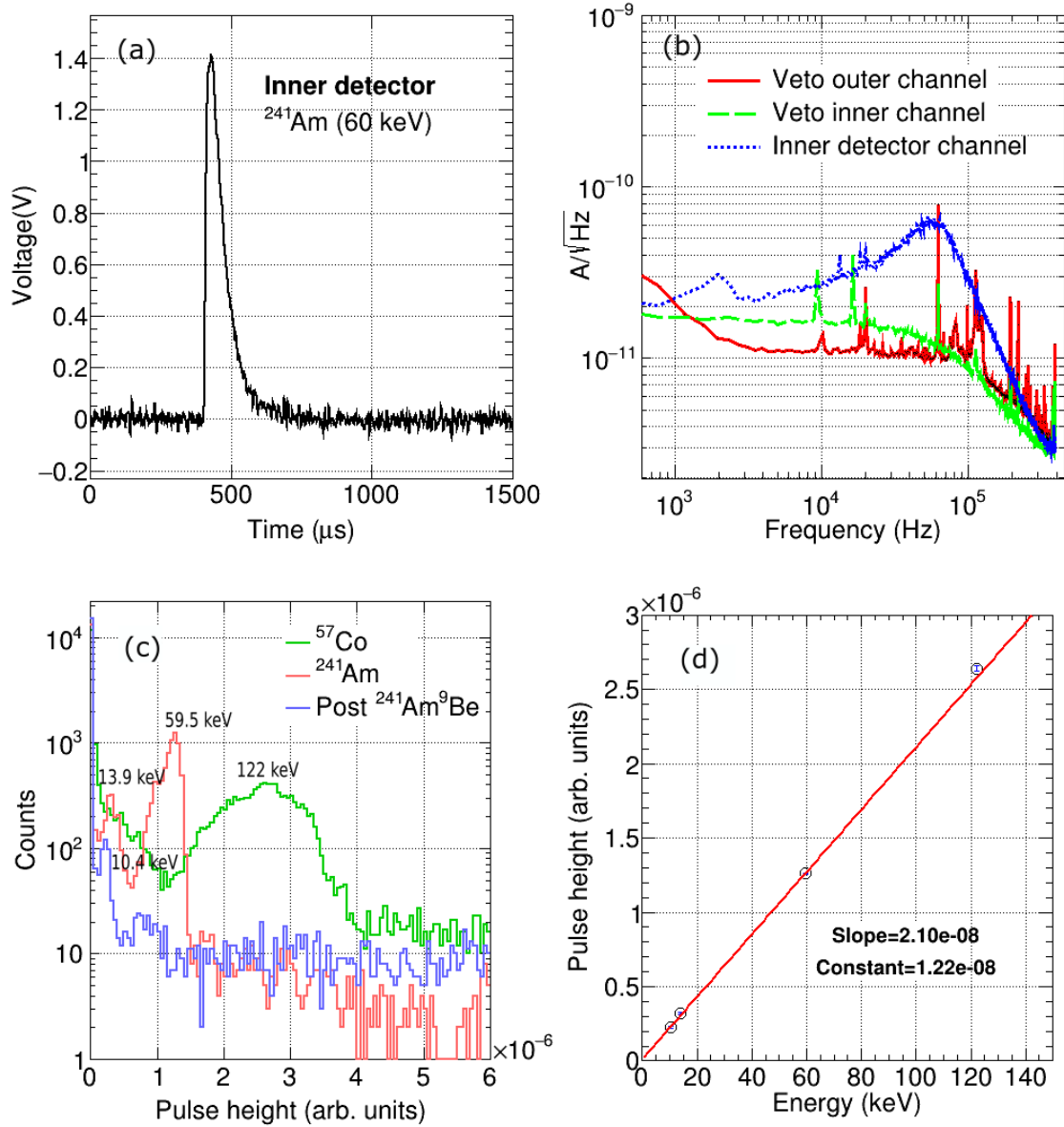


FIGURE 2.10: (a) A typical 60 keV pulse from the inner detector. (b) The noise PSD of inner and outer channels of the active veto detector and the inner detector channel. The noise in inner detector channel behaves differently from veto detector channels due to the application of higher bias voltage on the Quasiparticle-trap-assisted Electrothermal-feedback Transition-edge-sensors (QET) electronics. (c) In the inner target detector, the  $^{241}\text{Am}^9\text{Be}$  source produces a 10.4 keV germanium activation peak, 13.9 keV and 59.5 keV peaks from the  $^{241}\text{Am}$  source, and a 122 keV peak from the external  $^{57}\text{Co}$  source. The spread in the 122 keV peak is due to the external placement of the  $^{57}\text{Co}$  source, while the  $^{241}\text{Am}$  source is internal. Gaussian and linear functions are used for fitting the visible gamma energy peaks. (d) The mean of the gamma energy peaks in arbitrary units is plotted against the energy in keV, confirming the linearity of the energy scale up to 122 keV [17].

go from 10% to 90% of its peak value during the rising time of the pulse, while fall time is the duration for the pulse to go from 90% to 10% of its peak value during the fall time of the pulse. We find that the muon pulse has a risetime of  $\sim 20 \mu\text{s}$  and falltime of  $\sim 90 \mu\text{s}$ , which means it cools down quickly. This suggests that the thermalization of the inner detector is achieved.

### 2.3.3 Calibration

To calibrate the energy scale, we use an external  $^{57}\text{Co}$  and internal  $^{241}\text{Am}$  sources to illuminate the veto detector.  $^{57}\text{Co}$  source is characterized by 122 keV gammas while  $^{241}\text{Am}$  source has multiple energy lines, among them 13.9 keV and 59.5 keV gammas have higher intensity. These known energy sources are used to calibrate the inner target and the veto detector. To extract energy from raw pulses, a pulse template fitting algorithm known as the “Optimal Filter (OF)” is used [28]. It takes three inputs: (i) raw data, (ii) pulse template and (iii) noise Power Spectral Density (PSD). In Fig. 2.10(a), an example of a 60 keV pulse from the  $^{241}\text{Am}$  source in the inner detector is shown. To make a pulse template, we averaged over all such good pulses. Noise data is generated with random triggers, which are also used to study the noise performance of the detectors. From the noise data, specific noise traces were selected, and PSD was obtained. PSD describes the power distribution in a signal (or in a noise) into components of different frequencies. Figure. 2.10(b) shows the PSD of inner and veto detectors. The OF method fits the template to the pulse and determines the pulse amplitude from the best-fit result. Then, the OF amplitude distribution for the entire dataset was calibrated using the known gamma energies. The pulse height distribution, measured in arbitrary units, is presented in Fig. 2.10(c) for the internal  $^{241}\text{Am}$ , and external  $^{57}\text{Co}$  and  $^{241}\text{Am}^9\text{Be}$  sources. Notable peaks, such as the 10.4 keV germanium activation peak, 13.9 keV and 59.5 keV peaks from  $^{241}\text{Am}$ , and a 122 keV peak from  $^{57}\text{Co}$ ,

are visible in the inner detector. Furthermore, the linearity of the energy scale was validated up to 122 keV, as demonstrated in Fig. 2.10(c). The mean of the distribution is obtained by fitting the gamma peaks with a Gaussian. The error in the blue marker with each data point represents statistical error from the Gaussian fit.

### 2.3.4 Baseline resolution

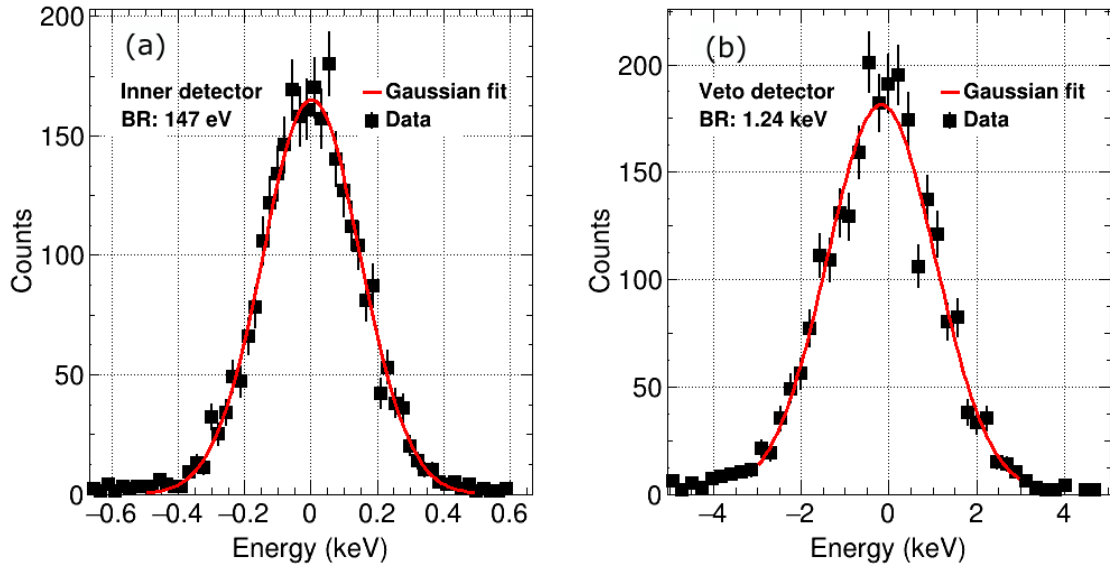


FIGURE 2.11: (a) The measured baseline resolution for the inner detector is 147 eV [17]. (b) The veto detector exhibits a baseline resolution of 1.24 keV when coupled with the inner detector. The error bars on the data points represent statistical uncertainties.

We measured the baseline resolution to assess the signal-to-noise (S/N) performance of the veto detector. Electronic noise stands out as a significant noise source in the detector, causing a poor S/N ratio. To obtain the baseline resolution, we process the raw noise data using the OF method, which, as an output, gives noise energy distribution in the OF unit. The baseline resolution is defined as the  $1\sigma$  width of the calibrated noise energy distribution, calculated by a Gaussian fit to the data. The results can be seen in Fig 4.18.

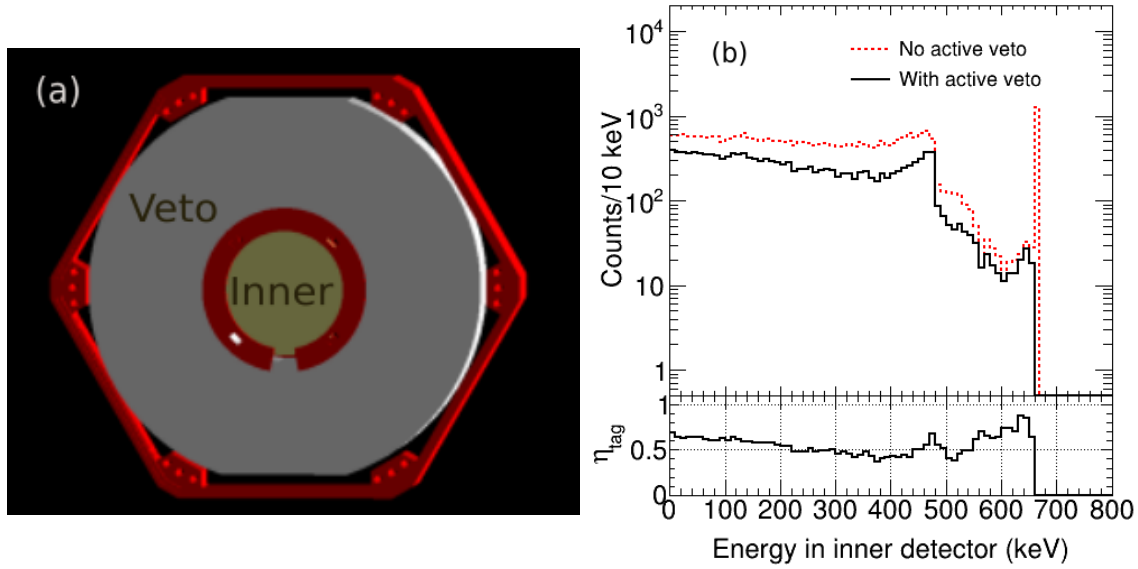


FIGURE 2.12: (a) An image of an active veto detector with an inner target detector used in the simulation. (b) Simulated energy deposition spectrum (upper panel) for a  $^{137}\text{Cs}$  source and tagging efficiency ( $\eta_{tag}$ ) (lower panel) as a function of energy deposition in the inner detector. The red dashed line in the figure shows the energy deposition spectrum in the inner detector before tagging, while the solid black line represents after tagging with the veto. It indicates that  $\eta_{tag}$  of the veto detector is expected to be between 50%–80% [17].

The veto detector showed a baseline resolution of 1.24 keV, whereas the inner detector, located internally, demonstrated a finer baseline resolution of 147 eV. Due to its lower mass, the inner detector showed better S/N performance than the veto detector. A conservative energy threshold for the veto detector, set at  $5\sigma$ , corresponds to approximately 6 keV, well below the 10 keV energy threshold found sufficient in simulations performed in GEANT4. In the next section, we will discuss the result of the veto detector from the simulation and compare it with the result from the test facility and the MINER site.

### 2.3.5 Test facility: simulation vs. experiment

We performed a simulation using GEANT4 [29] to tag Compton scatter events with the annular veto and the inner target detector. The simulation consists of an isotropic point

source of  $^{137}\text{Cs}$  placed 50 cm away from the centre of the detector along the detector plane. Figure 2.12(a) illustrates the GEANT4 model of the veto detector with the inner target.

We defined the tagging efficiency, denoted as  $\eta_{tag}$ , as the ratio of events depositing energy in both the inner and veto detectors to the total number of events depositing energy in the inner detector. Figure 2.12(b) presents the simulation results, where the upper panel displays the distribution of energy deposition in the inner detector, and the lower panel shows  $\eta_{tag}$  as a function of energy deposition in the inner detector. According to the figure, we expect  $\eta_{tag}$  by the veto to be between 50% to 80%.

To validate the capability of tagging and vetoing Compton scatter events, an experiment was performed at the Texas A&M University test facility. In this experiment, 662 keV gamma rays from a  $^{137}\text{Cs}$  source were directed towards the active veto detector. The comparison between the simulated and experimental results is depicted in Fig. 2.13(a) and Fig. 2.13(b), respectively. In the simulation, a 662 keV gamma band was observed to be shared between the inner and veto detectors. However, a sharp gamma line is visible as the detector resolution was not considered in the simulation. In contrast, the experimental data exhibit a smeared distribution due to the detector resolution, as illustrated in Fig. 2.13(b). Both sets of results are qualitatively consistent with each other. To ensure accuracy, a threshold of 70 keV was applied in the experimental data to eliminate events at 60 keV originating from an internal  $^{241}\text{Am}$  source.

## 2.4 Improvement in background reduction with $4\pi$ veto coverage

While the veto system with the inner target is capable of vetoing Compton scatter events effectively, further improvement is done with  $4\pi$  veto coverage. This is done by placing

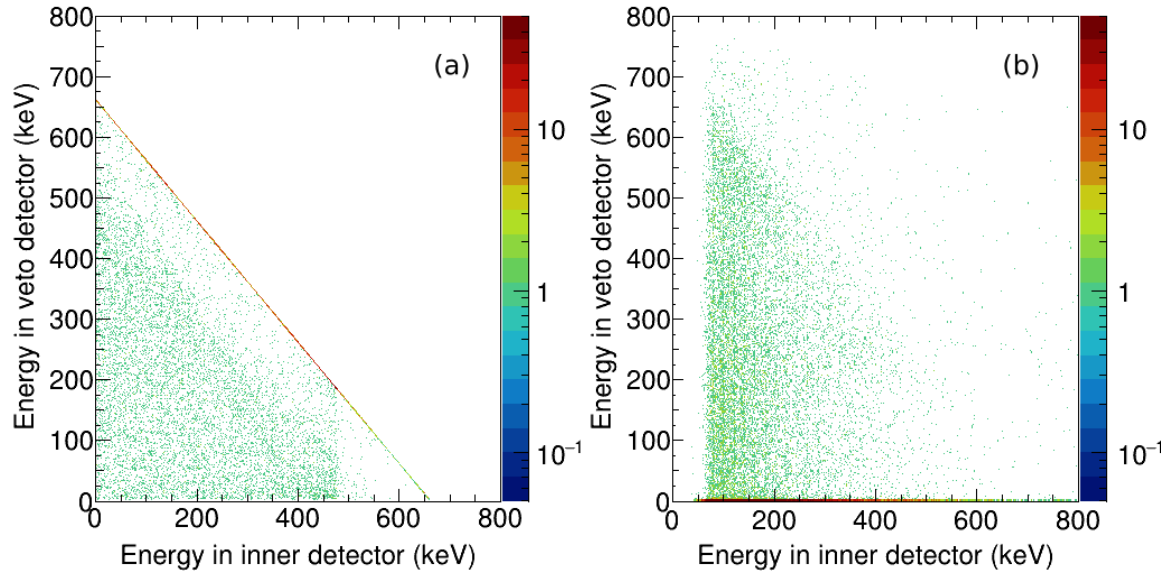


FIGURE 2.13: (a) and (b) show the distribution of shared energy between the veto detector (on the X-axis) and the inner detector (on the Y-axis) from simulation of  $^{137}\text{Cs}$  source and experimental data, respectively. Compton scatter events are tagged via coincidence [17]. Color code represents the number of events.

the veto and inner target between two germanium detectors with similar dimensions.

### 2.4.1 MINER: simulation vs. experiment

A simulation is performed with expected radiogenic background sources for SuperCDMS SNOLAB. The background sources are mainly from the decay daughters of U, Th and  $^{40}\text{K}$ . We have applied an analysis threshold of 10 keV. The GEANT4 simulation utilized a Computer-Aided Design (CAD) software representation of the detector stack, as shown in Fig. 2.14(a). The results, shown in Fig. 2.14(b), indicate an increase in  $\eta_{tag}$  by placing the active veto detector with the germanium inner detector between two other germanium detectors. The black solid histogram shows the energy deposition in the inner detector without any veto being taken into account. The red dotted histogram indicates energy deposition when only the active veto is considered. The lower panel indicates that  $\eta_{tag}$  has

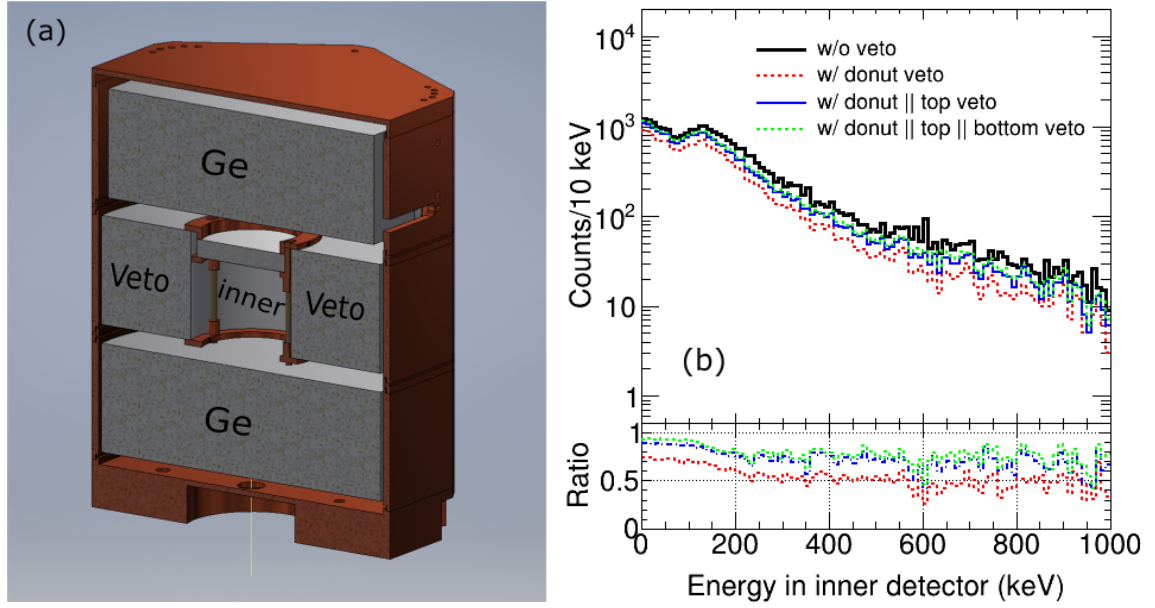


FIGURE 2.14: (a) A cross-sectional view of the detector stack in CAD used in simulations, consisting of an inner target detector made of germanium and silicon. The inner germanium and silicon detectors have a 25 mm diameter and are placed within an annular germanium veto detector with a 76 mm outer diameter and 28 mm inner diameter. These modules are sandwiched between two 76 mm diameter and 25 mm thick germanium detectors. (b) Simulated energy deposition spectrum (upper panel) and  $\eta_{tag}$  (lower panel) are depicted for germanium inner detectors. The black histogram shows the energy deposition distribution in the inner detector without any veto consideration. The red dotted, blue solid, and green dotted distributions represent energy deposition in the inner detector when tagged with the active veto only, with the active veto and top germanium detector, and with the veto, top, and bottom germanium detectors, respectively. At low energies ( $< 100$  keV), exceeds 70% with only the active veto and increases to  $> 90\%$  when including top and bottom germanium detectors, as explained in (a) [17].

the lowest limits, particularly below 100 keV at around 70%. The blue solid histogram shows energy deposition when both the active veto and the top germanium detector are involved. This results in an increase of  $\eta_{tag}$  as shown in the lower panel. Finally, the green dotted histogram represents the energy distribution when the veto, top, and bottom germanium detectors are all considered. This arrangement provide maximum  $\eta_{tag}$  which is  $> 90\%$  in the low-energy ( $< 100$  keV) region of interest.

After gaining confidence from the simulation, the active veto detector with  $4\pi$  veto

## 2.4. IMPROVEMENT IN BACKGROUND REDUCTION WITH $4\pi$ VETO COVERAGE 65

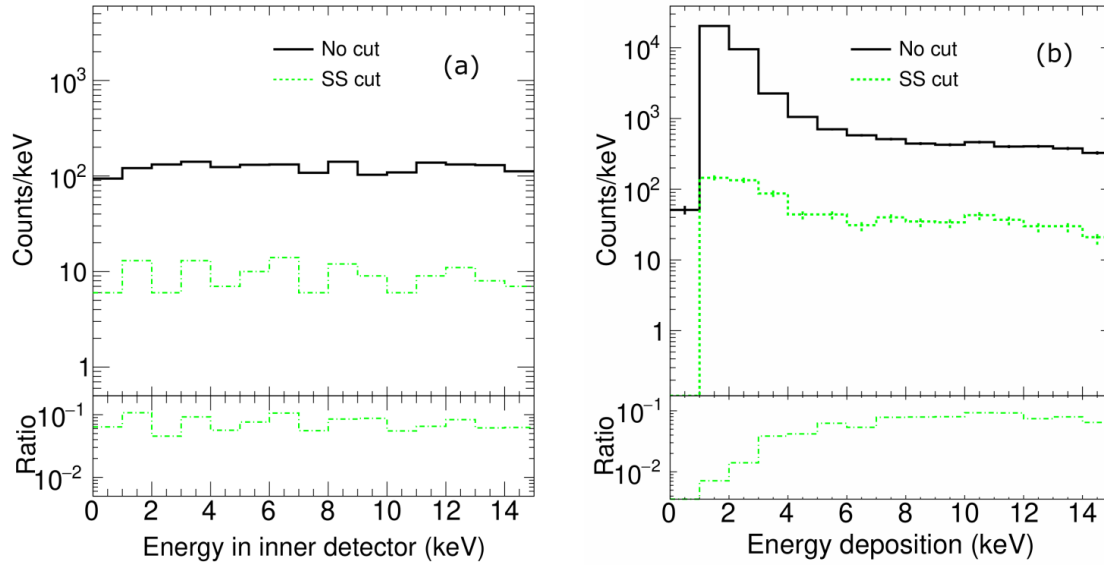


FIGURE 2.15: (a) Simulated background spectra (upper panel) in the inner detector using expected background sources for SuperCDMS SNOLAB, and (b) Background spectra measured by the inner detector (upper panel) at the MINER experimental site with and without a single scatter cut. In both (a) and (b), the black histogram indicates the total energy deposition measured in the inner detector. In contrast, the green histogram represents the energy deposition by single scatter events in the inner detector (upper panel). The lower panel shows the ratio of these two histograms, which measure background reduction.

coverage underwent in-situ characterization at the MINER experimental site. The configuration of the detector tower inside the dilution fridge at the MINER site is shown in Fig. 2.13(a). This setup includes an inner and annular veto detector pair positioned between two 76 mm diameter and 25 mm thick germanium detectors. The error bars on the data points represent statistical uncertainties. Using this detector arrangement, we estimated the energy deposition of single scatter (SS) events in the inner target detector. In the analysis, events with energy deposition above the threshold in the inner detector and energy deposition consistent with noise in the other detectors were considered as single scatter events. The simulated energy deposition of these single scatter events from SuperCDMS SNOLAB backgrounds is presented in Fig. 2.15(a). With no cut applied, we fit the simulated data



points with a straight line, yielding a background rate of 122 counts/keV in the energy range of 5 keV to 15 keV. With the SS cut, the background rate is reduced to 9 counts/keV in the same energy range. The simulation suggests that the veto system can reduce the rate by more than 10 times. To validate these results, experimental measurements with a similar detector arrangement were conducted at the MINER site. The measured background spectrum at the reactor site without and with the SS cut is shown in Fig. 2.15(b). We observe a similar reduction in experimental data, except at energies below 5 keV. In the simulation, we have not considered any internal background sources, unlike in the experiment, where backgrounds from the detector housing and nearby materials are present in the experimental data. The annular active veto efficiently removes such low-energy electron recoil background events and reduces the ratio predicted by the simulation. To quantify the reduction, we fit the spectra with a straight line. Without any cut, the background rate is approximately 443 counts/keV. After applying the SS cut, the measured background rate is 33 counts/keV in the energy range between 5 and 15 keV. This agrees well with the simulation, demonstrating an order-of-magnitude reduction in the background.

Hence, the  $4\pi$  veto coverage has proven effective in substantially reducing backgrounds, both in the simulation and in the data collected at the MINER site.

## 2.5 Summary and outlook

In this chapter, we discuss the characterization of a newly developed phonon-mediated veto detector prototype made of germanium. The detector shows an excellent reduction of the ambient radiogenic backgrounds, dominantly gamma radiation. We detail the fabrication process of the detector and the methodology employed in its mounting, addressing various challenges inherent in the design and setup. The thermalization of the detector is confirmed

through the study of muon data. The veto detector achieves a baseline resolution of 1.24 keV, providing an energy threshold of  $\sim 6$  keV. We also show the agreement between the simulated response of the veto detector and the experimental results. Implementing a  $4\pi$  veto coverage has proven highly effective, significantly reducing backgrounds at the MINER site. The detector can reject three primary background sources: surface betas,  $^{210}\text{Pb}$ , and Compton scatters that are expected to limit the sensitivity of the SuperCDMS SNOLAB experiment. The simulation and data analysis are carried out without applying bias voltage to either of the detectors, measuring the actual recoil energy deposited by the particle in both detectors. Operating the detectors at a higher voltage amplifies the phonon signals linearly through the Neganov–Trofimov–Luke (NTL) effect. This enhancement improves the signal-to-noise (S/N) ratio and opens up possibilities to investigate lower energy regions (in the eV scale) in future studies. Plans are also underway to fabricate a veto detector with a silicon inner detector. With an impressive background rejection efficiency of up to 90%, the active veto detector stands out as a highly promising candidate for both DM searches and  $\text{CE}\nu\text{NS}$  experiments.

## Bibliography

- [1] Mark David Pepin. “Low-Mass Dark Matter Search Results and Radiogenic Backgrounds for the Cryogenic Dark Matter Search”. PhD thesis. Minnesota U., 2016.
- [2] R. Agnese et al. “Production Rate Measurement of Tritium and Other Cosmogenic Isotopes in Germanium with CDMSlite”. *Astropart. Phys.* 104 (2019), p. 1–12. arXiv: [1806.07043 \[physics.ins-det\]](#).
- [3] Dongming Mei and A. Hime. “Muon-induced background study for underground laboratories”. *Phys. Rev. D* 73 (2006), p. 053004. arXiv: [astro-ph/0512125](#).
- [4] B. Schmidt et al. “Muon-induced background in the EDELWEISS dark matter search”. *Astroparticle Physics* 44 (2013), p. 28–39.

- [5] Klemens Rottler. “Muons in the CRESST Dark Matter Experiment”. PhD thesis. U. Tübingen, 2014.
- [6] Alex Wright et al. “A highly efficient neutron veto for dark matter experiments”. *Nuclear Instruments and Methods in Physics Research Section A: Accelerators, Spectrometers, Detectors and Associated Equipment* 644 (2011), p. 18–26.
- [7] Bruno Cimmino. “Dark matter search: the Neutron Veto in the XENONnT Detector Upgrade”. PhD thesis. Naples U., Università degli Studi di Napoli Federico II, Università’ Di Napoli, Naples U., 2020.
- [8] Kirill Pushkin. “Direct search for WIMP dark matter particles with the LUX-ZEPLIN (LZ) detector”. *Nuclear Instruments and Methods in Physics Research Section A: Accelerators, Spectrometers, Detectors and Associated Equipment* 936 (2019). *Frontier Detectors for Frontier Physics: 14th Pisa Meeting on Advanced Detectors*, p. 162–165.
- [9] R. Bernabei et al. “New results from DAMA/LIBRA”. *Eur. Phys. J. C* 67 (2010), p. 39–49. arXiv: [1002.1028 \[astro-ph.GA\]](#).
- [10] C. E. Aalseth et al. “Search for an Annual Modulation in a P-type Point Contact Germanium Dark Matter Detector”. *Phys. Rev. Lett.* 107 (2011), p. 141301. arXiv: [1106.0650 \[astro-ph.CO\]](#).
- [11] Jeffrey Peter Filippini. “A Search for WIMP Dark Matter Using the First Five-Tower Run of the Cryogenic Dark Matter Search”. PhD thesis. University of California, Berkeley, 2008.
- [12] Z. Ahmed et al. “Dark Matter Search Results from the CDMS II Experiment”. *Science* 327 (2010), p. 1619–1621. arXiv: [0912.3592 \[astro-ph.CO\]](#).
- [13] E. Armengaud et al. “Final results of the EDELWEISS-II WIMP search using a 4-kg array of cryogenic germanium detectors with interleaved electrodes”. *Phys. Lett. B* 702 (2011), p. 329–335. arXiv: [1103.4070 \[astro-ph.CO\]](#).
- [14] G. Angloher et al. “Commissioning Run of the CRESST-II Dark Matter Search”. *Astropart. Phys.* 31 (2009), p. 270–276. arXiv: [0809.1829 \[astro-ph\]](#).
- [15] E. Aprile et al. “Dark Matter Results from 100 Live Days of XENON100 Data”. *Phys. Rev. Lett.* 107 (2011), p. 131302. arXiv: [1104.2549 \[astro-ph.CO\]](#).

- [16] R. Agnese et al. “Projected Sensitivity of the SuperCDMS SNOLAB experiment”. *Phys. Rev. D* 95 (2017), p. 082002. arXiv: [1610.00006 \[physics.ins-det\]](#).
- [17] M. Chaudhuri et al. “A novel active veto prototype detector with an inner target for improved rare event searches”. *Nucl. Instrum. Meth. A* 1039 (2022), p. 167150. arXiv: [2202.11004 \[physics.ins-det\]](#).
- [18] Robert Agnese et al. “Energy loss due to defect formation from 206Pb recoils in SuperCDMS germanium detectors”. *Applied Physics Letters* 113 (2018).
- [19] S. Yellin. “Finding an upper limit in the presence of unknown background”. *Phys. Rev. D* 66 (2002), p. 032005. arXiv: [physics/0203002](#).
- [20] F. E. Emery and T. A. Rabson. “Average Energy Expended Per Ionized Electron-Hole Pair in Silicon and Germanium as a Function of Temperature”. *Phys. Rev.* 140 (1965), A2089–A2093.
- [21] Neganov, B. S. and Trofimov, V. N. and Stepankin, V. “Application of ionization to heat conversion to the light absorption spectra measurement in silicon at 1 K through adiabatic calorimetry”. *Journal of Low Temperature Physics* 93 (1993), 417–422.
- [22] P.N. Luke et al. “Calorimetric ionization detector”. *Nuclear Instruments and Methods in Physics Research Section A: Accelerators, Spectrometers, Detectors and Associated Equipment* 289 (1990), p. 406–409.
- [23] Zeeshan Ahmed. “A Dark Matter Search Using The Final CDMS II Dataset And a Novel Detector of Surface Radiocontamination”. PhD thesis. California Institute of Technology, Pasadena, California, 2012.
- [24] K. D. Irwin et al. “A quasiparticle-trap-assisted transition-edge sensor for phonon-mediated particle detection”. *Rev. Sci. Instrum.* 66 (1995), p. 5322.
- [25] A. Jastram et al. “Cryogenic Dark Matter Search Detector Fabrication Process and Recent Improvements”. *Nucl. Instrum. Meth. A* 772 (2015), p. 14–25. arXiv: [1408.0295 \[physics.ins-det\]](#).
- [26] Ritoban Basu Thakur. “The Cryogenic Dark Matter Search low ionization-threshold experiment”. PhD thesis. University of Illinois at Urbana-Champaign, 2015.

- [27] G. Agnolet et al. “Background Studies for the MINER Coherent Neutrino Scattering Reactor Experiment”. *Nucl. Instrum. Meth. A* 853 (2017), p. 53–60. arXiv: [1609.02066 \[physics.ins-det\]](#).
- [28] Sunil Ramanlal Golwala. “Exclusion limits on the WIMP nucleon elastic scattering cross-section from the Cryogenic Dark Matter Search”. PhD thesis. University of California, Berkeley, 2000.
- [29] S. Agostinelli et al. “Geant4—a simulation toolkit”. *Nuclear Instruments and Methods in Physics Research Section A: Accelerators, Spectrometers, Detectors and Associated Equipment* 506 (2003), p. 250–303.

---

# Low-threshold detectors for $\text{CE}_\nu\text{NS}$

## search at MINER

---

### Contents

3.1	MINER . . . . .	71
3.2	Simultaneous detection of phonon and light in sapphire . . . . .	84
3.3	Analysis and Result . . . . .	87
3.4	Detector performance at NSC . . . . .	95
3.5	Current status of MINER . . . . .	104
3.6	Summary . . . . .	104

---

## 3.1 MINER

The Mitchell Institute Neutrino Experiment at Reactor (MINER) is currently running at the Nuclear Science Center (NSC) at Texas A&M University in the USA [1]. The primary objective of MINER is to measure the cross-section of Coherent Elastic Neutrino Nucleus

Scattering ( $CE\nu NS$ ) precisely by utilizing the huge neutrino flux generated by the 1 MW reactor. The reactor itself is a TRIGA (Training, Research, Isotopes, General Atomics) pool reactor featuring a core with low-enriched Uranium (approximately 20%  $^{235}\text{U}$ , LEU) and operates at a standard power of 1 MW. Detailed information about the MINER reactor can be found in Table 3.1. The facility has the advantage of having a movable core. It provides access to deploy detectors as close as 1 m from the reactor core. This also allows a varying distance from the neutrino source to the detector. The neutrino spectrum from

TABLE 3.1: MINER reactor details

Reactor fuel	$^{235}\text{U}$ (20%, LEU)
Reactor power	1 MW
Energy per $^{235}\text{U}$ fission	200 MeV
Neutrino yield per fission	$\sim 6$
Neutrino energy per fission	1.5 MeV
Neutrino flux at 1 m from core	$\sim 10^{12} \text{ cm}^{-2}\text{s}^{-1}$

the reactor [2] is depicted in Fig. 3.1, where the blue dotted vertical line indicates the energy threshold for the Inverse Beta Decay (IBD) process. Notably, a significant portion of the neutrino flux is below this threshold, making their detection feasible through the  $CE\nu NS$  process. Detecting this low-energy neutrino necessitates detectors with a low recoil energy threshold, typically around 100 eV. This emphasis on low recoil energy thresholds is crucial for studying the lower end of the neutrino energy spectrum [3]. In addition to measuring  $CE\nu NS$ , MINER can search for sterile neutrinos [4]. If sterile neutrinos exist, they might mix with standard neutrinos, oscillating between different neutrino flavours, including sterile neutrinos. The experiment can measure the energy spectrum of emitted neutrinos at varying distances, as close as 1 m. Theory predicts that if they have a mass difference of  $\sim 1$  eV, effects could be observed over short baselines [5]. Deviations from

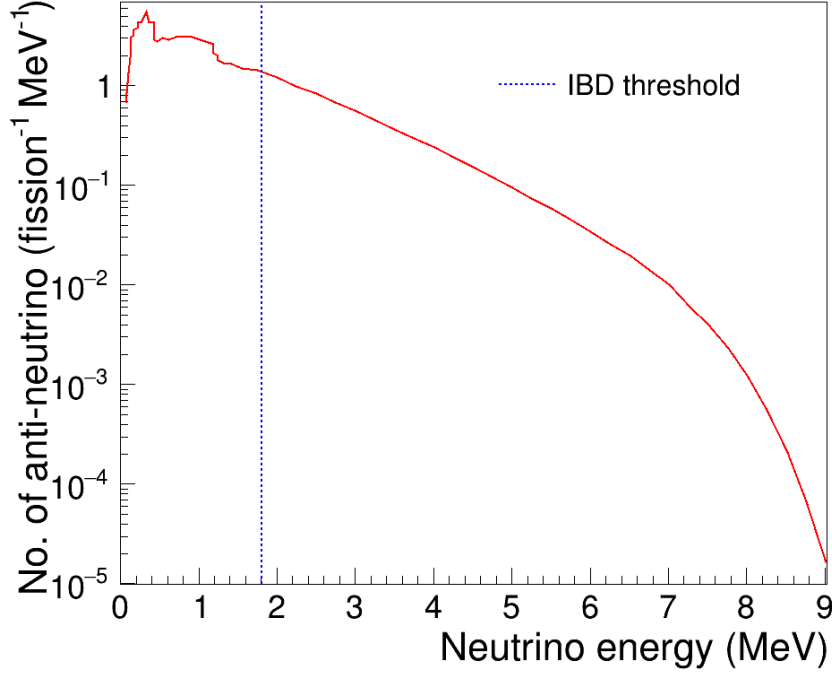


FIGURE 3.1: Reactor neutrino spectrum, where on the horizontal axis, we have neutrino energy measured in MeV, and on the vertical axis, it shows the anti-neutrino flux per fission per MeV. The dashed blue line indicates the Inverse Beta Decay (IBD) threshold.

the expected spectrum, such as a deficit of events at specific energy ranges, could be the experimental signature of sterile neutrino oscillations.

MINER will also search for axions/axion-like particles (ALPs) produced from the scattering of photons from the reactor material via Primakoff and Compton-like processes [6]. These axions/ALPs directly interact with the detectors through inverse Primakoff and inverse Compton-like processes, producing photons or electron-positron pairs. The axions/ALPs signature can be experimentally probed by measuring the excess photons in the detectors.



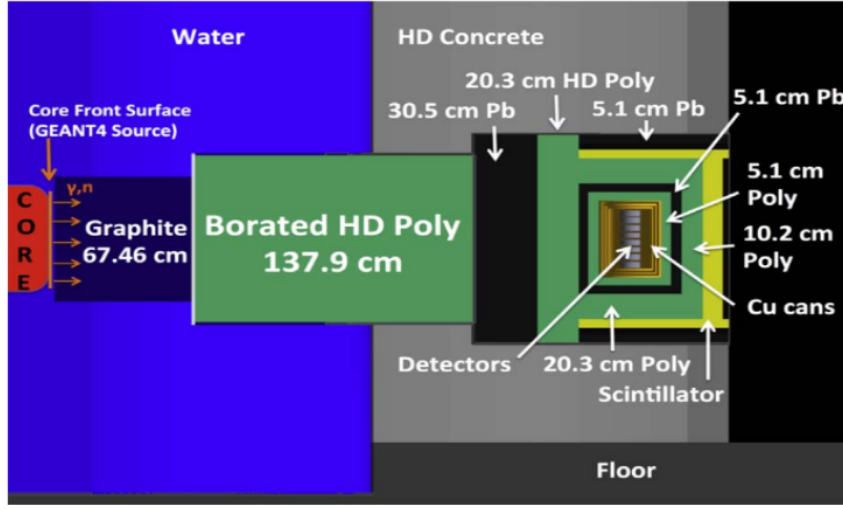


FIGURE 3.2: The GEANT4 geometry model of the experimental cavity with an initial shield design. Various materials are shown in different colours: Blue for water, Dark Blue for graphite, Green for 5% Borated polyethylene, Light Gray for high-density (HD) concrete, Dark Gray for Lead, Gold for Copper, and Yellow for Plastic Scintillator. Inside the copper, small disks represent germanium and silicon detectors [1].

### 3.1.1 Proposed experimental setup

Fission processes in the reactor produce significant gamma rays and neutrons near the core. The NSC pool-type reactor is encased in high-density concrete (approximately  $3.5 \text{ g/cm}^3$ ), acting as a shield against these intense neutron and gamma fluxes. Using an MCNP reactor core model [7], the neutron energy spectrum is calculated, including  $5.8 \times 10^{11} \text{ cm}^{-2}\text{s}^{-1}$  fast neutrons with kinetic energy  $> 100 \text{ keV}$  and  $7.7 \times 10^{12} \text{ cm}^{-2}\text{s}^{-1}$  thermal neutrons with kinetic energy  $> 0.625 \text{ eV}$  [1]. Fast neutrons are converted to thermal neutrons through a moderator, and then thermal neutrons are shielded using a neutron absorber like boron. Similarly, a gamma spectrum was simulated with a flux of  $9.0 \times 10^{11} \text{ cm}^{-2}\text{s}^{-1}$ , and high-density materials like lead were employed to shield against these gamma rays. A preliminary shielding design was incorporated into the GEANT4 geometry model to evaluate the expected background in the experimental setup. The shielding materials

included 1.38 m of high-density borated (5%) polyethylene for neutron shielding and 30.5 cm of lead for gamma shielding. Additional lead and polyethylene were added to minimize backgrounds from secondary particles, such as neutrons from  $(\gamma, n)$  reactions and gammas released from neutron captures in the shielding materials. The primary shielding design is shown in Fig. 3.2 using initial estimates based on GEANT4 geometry models. An active muon veto setup (yellow panel in Fig. 3.2) is implemented to reject cosmogenic muons. The movable core has an additional advantage for understanding and reduction of backgrounds.

### 3.1.2 MINER detectors

Detecting low-energy neutrinos requires detectors with a low recoil energy threshold. Neutrinos have an extremely small mass. Assuming  $m_\chi \ll m_n$  in Eq. 1.9 from Chapter 1 implies  $E_R \propto \frac{1}{m_n}$ . The lower the atomic mass, the more sensitive the detector is to lower nuclear recoil energies. Figure 3.3 shows the maximum recoil energy based on neutrino energy for different target masses (solid lines). Aluminum (Al), oxygen (O), and silicon (Si) exhibit the maximum recoil energy due to their lower atomic mass.

Additionally, the Standard Model predicts that in coherent scattering processes, the interaction cross-section is enhanced by a factor of  $N^2$ , where  $N$  is the number of neutrons in the target nucleus, in contrast to Inverse Beta Decay (IBD) [8]. The interaction cross-section, as a function of neutrino energy (dash-dotted lines), is depicted in the same Fig. 3.3, plotted on the right Y-axis for Al, O, and Si target materials. It is observed that the cross-section for Al, O, and Si through CE $\nu$ NS is two orders of magnitude higher than IBD.

The key considerations for constructing detectors to search for CE $\nu$ NS using reactor neutrinos are as follows:

1. Detectors should have a low-energy threshold ( $\sim 100$  eV), meaning they are made of elements with lower atomic numbers.
2. Detectors should be massive to increase the interaction rate with the target nuclei.
3. They should possess event-by-event background discrimination capability.

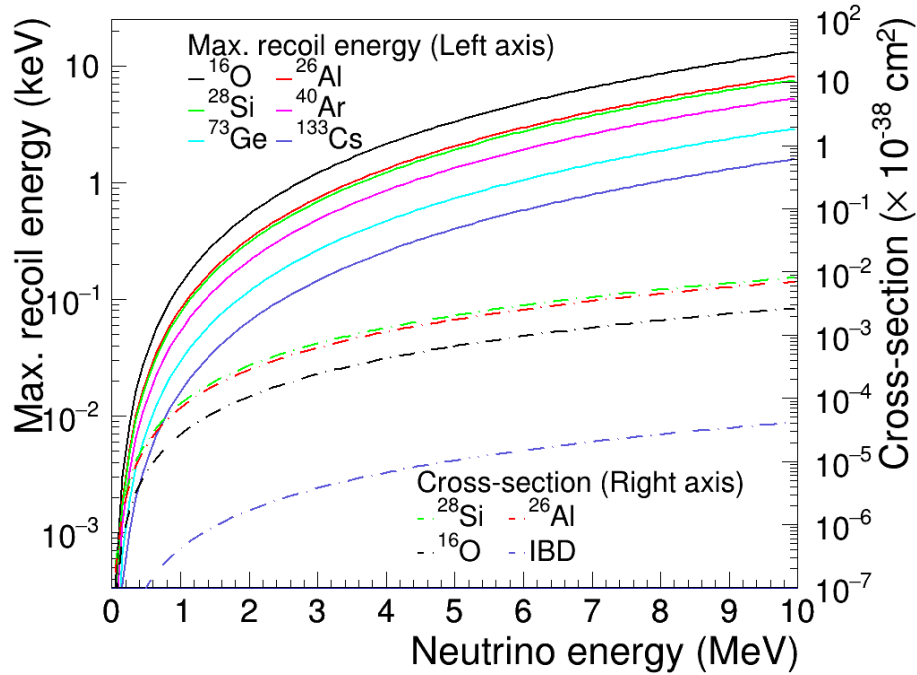
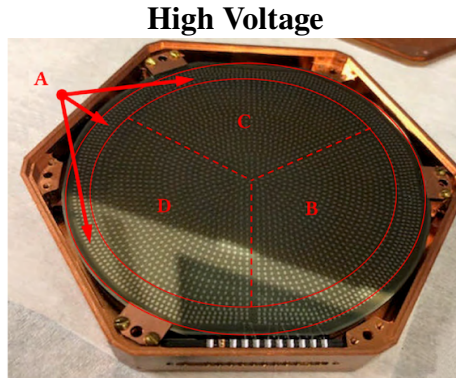


FIGURE 3.3: The left axis shows the maximum recoil energy in keV versus neutrino energy in MeV, where Al and O indicate higher recoil energy. On the right axis, the cross-section versus neutrino energy is shown. The blue dash-dotted line represents the cross-section for IBD, while the upper curves represent the cross-section for Al, O, and Si through CE $\nu$ NS, two orders of magnitude higher than IBD.

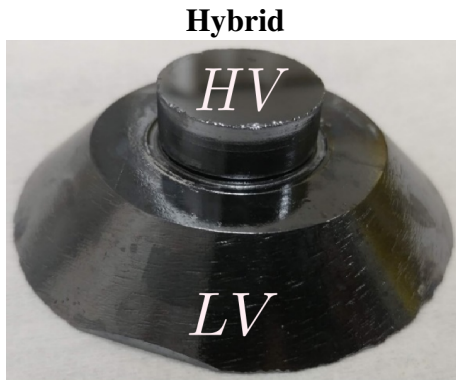
To achieve this goal, we have developed several low-threshold cryogenic detectors utilizing novel technology for the MINER experiment [9–12]. These detectors primarily consist of germanium, silicon, and sapphire. After fabricating and testing these detectors at the test facility at Texas A&M University, they were prepared for deployment for MINER test runs at the NSC

The following sections will discuss the development of the three most promising novel low-threshold cryogenic detectors for the MINER experiment and their performance in the reactor environment at the NSC.

TABLE 3.2: Detectors developed for MINER experiment



<b>Material</b>	Si
<b>Mass (g)</b>	~ 100
<b>Dimension in cm (Diameter, thickness)</b>	7.5, 1
<b>Bias voltage (V)</b>	0 - 320
<b>No. of channels</b>	4 (A, B, C, D)
<b>Features</b>	Single $e^-$ sensitivity



<b>Material</b>	Si
<b>Mass (g)</b>	~ 112
<b>Dimension in cm (Diameter, thickness)</b>	Bottom: 7.6 and top: 2.5, 2.5
<b>Bias voltage (V)</b>	12
<b>No. of channels</b>	1 (top), 4 (A, B, C, D) (bottom)
<b>Features</b>	Background discrimination



<b>Material</b>	$\text{Al}_2\text{O}_3$
<b>Mass (g)</b>	~ 100
<b>Dimension in cm (Diameter, thickness)</b>	7.6, 0.4
<b>Bias voltage (V)</b>	0
<b>No. of channels</b>	4 (A, B, C, D)
<b>Features</b>	~ 100 eV scale threshold

**Silicon High Voltage (HV) detector**

A novel phonon-mediated Si detector of  $\sim 100$  g utilizing a new interface architecture has been developed at Texas A&M University [13]. The detector operates in HV mode; hence, it is called an HV detector. The detector technology is explained earlier in Section 2.2 from Chapter 2. During testing in the test facility, the detector achieves an excellent baseline resolution of  $\sim 1$  e $^-$ /h $^+$  pair while maintaining a leakage current on the order of  $10^{-16}$  A. This performance was achieved by implementing a contact-free interface architecture and removing an amorphous-Si layer. Previously, a leakage current between the crystal surface and metal electrode limited the S/N performance at higher voltages. In this method, a  $\sim 600$   $\mu$ m vacuum gap between the crystal-metal interface reduces leakage current effectively. Additionally, the phonon absorption efficiency is improved by removing the amorphous Si-layer. The HV detector is shined with LASER photons for different voltages applied starting from 0 V to 320 V. Figure 3.4(a) shows a linear increase of LASER phonon signal amplification as the bias voltage rises, reaching up to 240 V, leading to an improvement in the S/N ratio. Baseline resolution is calculated in units of e $^-$ /h $^+$  pair across all the voltages and shown in Fig. 3.4(b). To understand the behaviour of baseline resolution with the voltages, the data points are fitted with a function for noise (N) and signal (S) defined as:

$$N = \sqrt{N_0^2 + (V_b b)^2} \quad (3.1)$$

$$S = S_0 + \frac{S_0 q V_b G}{\epsilon} \quad (3.2)$$

In this context,  $N_0$  represents the noise at 0 V,  $V_b$  is the applied bias voltage,  $b$  signifies the noise associated with the leakage current,  $S_0$  stands for the normalized mean laser amplitude at 0 V,  $q$  denotes the charge of an electron,  $G$  is a dimensionless factor incorporating the impact of the gap between the detector and the electrode, and  $\epsilon$  indicates the average energy needed to generate an e $^-$ /h $^+$  in Si. The lowest baseline resolution obtained was  $0.83^{+0.03}_{-0.34}$

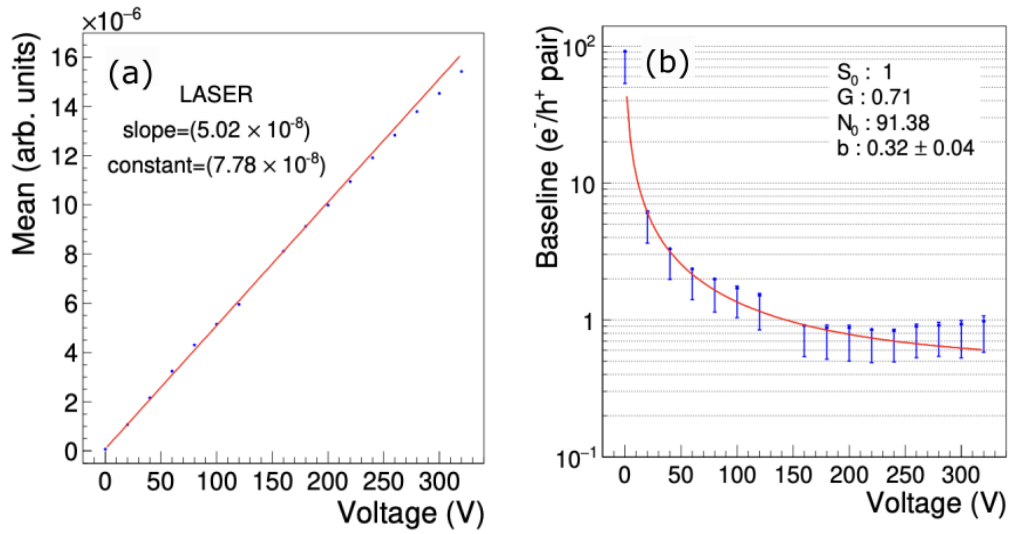


FIGURE 3.4: (a) The mean value of laser energy distributions in arbitrary units across various voltages ranging from 0 V to 320 V. The red line represents a straight line fitted to the data points, and the corresponding fit parameters are also provided. The statistical errors (equivalent to the size of the markers) are shown with each data point. (b) Baseline resolution in units of  $e^-/h^+$  pair units as a function of voltage. The data points are fit to a functional form  $N/S$  where  $N$  and  $S$  are defined in Eq.3.1 and Eq.3.2. Figures are taken from [13].

$e^-/h^+$  pairs at 240 V bias. This unique characteristic allows the detector to operate at a very low energy threshold, which proves advantageous for searches related to  $CE\nu NS$  and DM.

### Hybrid detector

Hybrid is another novel phonon-mediated Si detector developed in Texas A&M University, which has event-by-event discrimination ability at low energies [10]. The detector is a combination of both iZIP and HV detectors. Hence, it is called a Hybrid detector. The detector has a conical shape where the top and bottom surface have a diameter of 2.5 cm and 7.6 cm, respectively, as described and shown in the middle column of Table 3.2. Due to its geometry, the electric field intensity is higher at the top (HV region) and lower at the bottom (LV region). These two regions are separated by a narrow channel, which allows charge transport and constrains phonon transport from LV to HV. Since the crystal volume

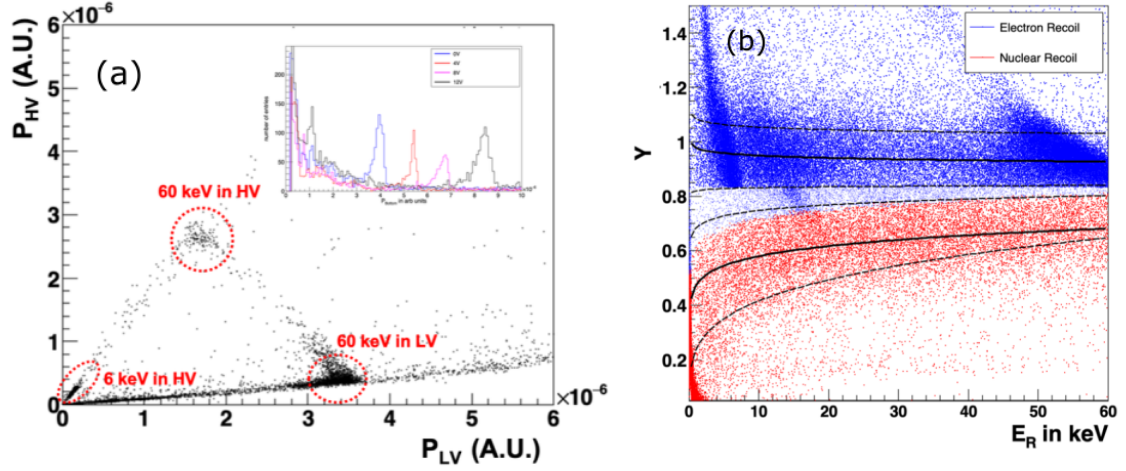


FIGURE 3.5: (a) The sharing of phonon energy in the HV and LV phonon channels at a 0 V bias is shown. This is crucial for determining key phonon transport parameters in this hybrid detector. (b) From the  $^{252}\text{Cf}$  calibration source, a distinct separation is seen between the NR (red points) and ER (blue points) events. Figures are sourced from [10].

is larger at the bottom, most interactions occur in the LV region where recoiling phonons are sensed ( $P_{LV}$ ). In contrast, the HV region senses NTL phonons due to the movement of charges ( $P_{HV}$ ). The ratio,  $Y = \frac{P_{HV}}{P_{LV}}$ , of the measured phonon energy in HV to the LV region will act as a discriminator of electron recoil (ER) and nuclear recoil (NR) in the hybrid detector. Figure 3.5(a) shows the distribution of phonon energy among the HV and LV phonon channels at 0 V bias. Two distinct populations of events distributed along two lines that cross the origin correspond to events in either HV or LV regions. The points distributed along the diagonal that connects the two 60 keV populations correspond to the 60 keV photons in the transition region between the HV and the LV regions. The discriminator,  $Y$ , is plotted using  $^{252}\text{Cf}$  calibration source. We see a clear separation between the NR (red points) and ER (blue points) in Fig. 3.5(b).



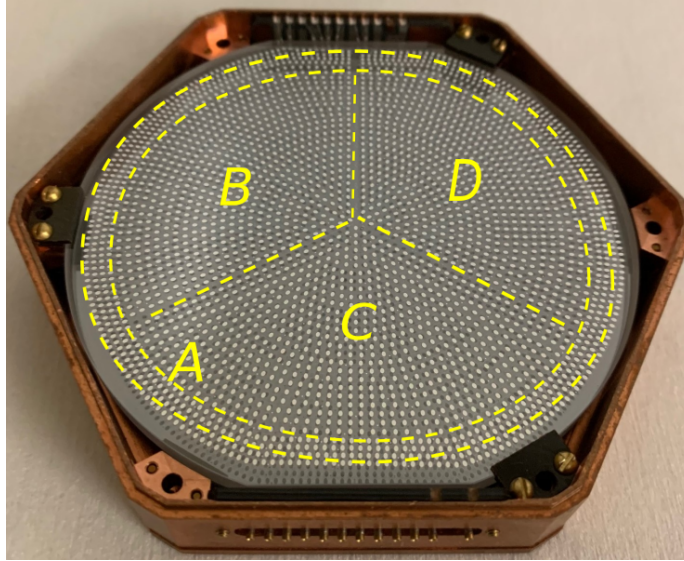


FIGURE 3.6: The 100 g sapphire detector, with a diameter of 7.6 cm and a thickness of 0.4 cm, used in this work, is kept inside a copper casing. The phonon sensors comprise approximately 1000 TESs, organized into four groups of around 250 sensors each. These groups are independently read out, forming four channels (A, B, C, and D). This arrangement enables the reconstruction of interaction positions in the detector by examining the relative amplitudes among the separate channels.

### Sapphire ( $\text{Al}_2\text{O}_3$ ) detector

The chemical composition of sapphire made it an excellent candidate for low-threshold detectors. A 100 g sapphire ( $\text{Al}_2\text{O}_3$ ) scintillation detector was fabricated and tested at Texas A&M University test facility [12]. This thesis focuses on the performance of this sapphire detector.

Particles interacting with this detector generate phonons and scintillation light. These phonons are sensed by Transition-Edge-Sensors (TESs) placed on the surface of the detector, organized into 4 independent groups or channels. Figure 3.6 shows the detector picture with the 4-channel configuration. The specifications of this detector are also listed in the last column of Table 3.2. One advantage of having a sapphire detector is the enhanced phonon transmission between the Al substrate and the Al phonon absorber within TES sensors. This improvement is due to the absence of an amorphous silicon layer,



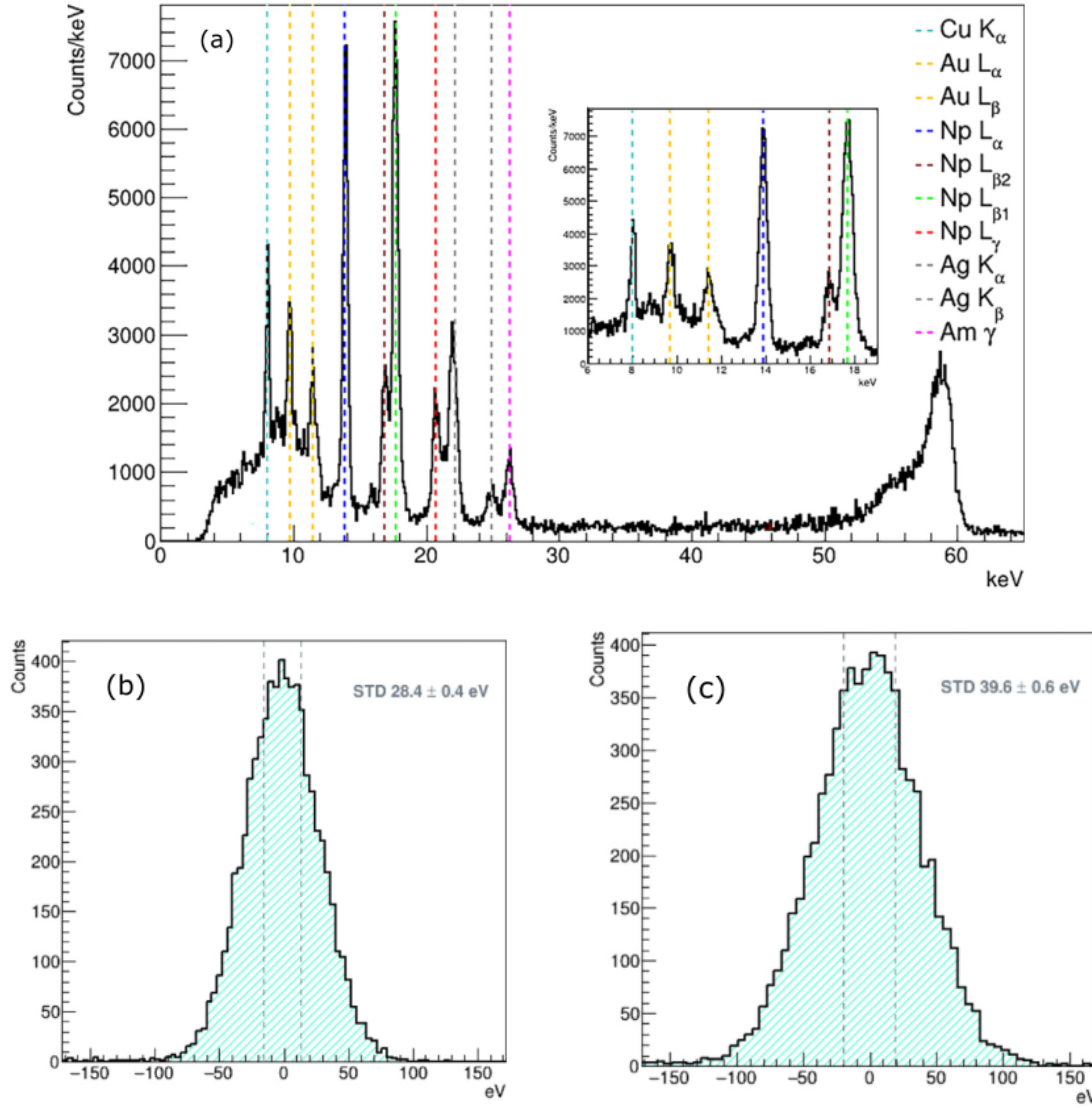


FIGURE 3.7: (a) Deposited energy distribution on the sapphire detector, calibrated with the 13.9 keV line (blue). Various dotted lines denote X-ray peaks from  $^{241}\text{Am}$  source and decay products from gold and silver present in  $^{241}\text{Am}$  source. The 59.5 keV gamma from  $^{241}\text{Am}$  source is slightly lower due to the non-linear detector response in this energy range. (b) The distribution of noise amplitude for a single channel (channel D) of sapphire. The standard deviation (STD) of the fitted Gaussian distribution, representing baseline resolution, is  $28.4 \pm 0.4$  eV. (c) For summed over all channels, the baseline resolution is measured at  $39.6 \pm 0.6$  eV. The figures are sourced from [12].

commonly found in CDMS-style detectors, which protects the substrate surface from Al and W (tungsten) etchants. Instead, Al is directly deposited onto sapphire, resulting in

improved phonon transmission compared to other silicon or germanium detectors.

The detector is shined with a  $^{241}\text{Am}$  source with several X-ray and gamma lines [14]. The source is placed near channel D of the detector (see Fig. 3.6). Figure 3.7(a) shows the measured energy spectrum. To calibrate the spectrum, we use the known energy line at 13.9 keV ( $L_\alpha$ ). Consequently, we identify X-ray lines at 16.9 keV ( $L_{\beta_2}$ ), 17.7 keV ( $L_{\alpha_1}$ ), 20.7 keV ( $L_\gamma$ ) from  $^{239}\text{Np}$ , and gammas at 26.3 keV and 59.5 keV from the nuclear decay of  $^{241}\text{Am}$ . Additionally, small peaks are observed, likely representing Np  $L_\eta$  (15.9 keV) and Np  $L_{\beta_6}$  (16.1 keV). The standard procedure for producing a  $^{241}\text{Am}$  radioactive source involves mixing americium dioxide  $\text{AmO}_2$  with gold and then coating it with a thin layer of gold and silver [15]. Two lower energy peaks in the spectrum align well with X-ray lines from gold — Au  $L_\alpha$  (9.7 keV) and Au  $L_\beta$  (11.4 keV). We suspect that Np  $L_l$  (11.9 keV), with relatively low intensity, is concealed beneath the identified Au  $L_\beta$  peak. Furthermore, we believe the detector detects X-rays from silver, with two peaks in the spectrum corresponding to Ag  $K_\alpha$  (22.16 keV) and  $K_\beta$  (24.94 keV). Additionally, we observe energy lines at 8.05 keV and 8.91 keV from Cu  $K_\alpha$  and Cu  $K_\beta$ , originating from the copper source holder. The low-energy peaks in the distribution closely match the expected energies for the  $^{241}\text{Am}$  source, copper, gold, and silver (indicated by dotted lines in Fig. 3.7(a)), suggesting that the detector's response is linear up to 30 keV. There is a slight saturation effect observed at 59.5 keV events, with the corresponding peak (mean value) slightly lower.

Baseline resolution is calculated to check the noise performance. It shows a baseline resolution of  $39.6 \pm 0.6$  eV when all four channels are combined, while the single channel baseline resolution was  $28.4 \pm 0.4$  eV, and the errors associated with these values arise from statistical uncertainties. This is the lowest baseline resolution for a 100 g scale cryogenic detector. Another advantage is its ability to distinguish events at lower recoil energies on an event-by-event basis. This is achieved by simultaneously measuring phonons and light

from a sapphire crystal.

In this thesis, we demonstrated two low-threshold detector technologies utilizing Si HV and sapphire, with the goal of creating a low-threshold detector system with a large mass. This system concurrently measures athermal phonons in a sapphire detector and detects scintillation light from the same detector using an adjacent Si HV detector. Due to their difference in scintillation light yield, this detector system offers the potential for distinguishing between different types of events (ER and NR) on an event-by-event basis. Although smaller detectors have previously demonstrated simultaneous phonon and light detection, this system is specifically designed for a large detector mass with high amplification to address the challenge of limited scintillation light.

## **3.2 Simultaneous detection of phonon and light in sapphire**

Besides phonons, a small amount of the energy deposited in the detector is released as scintillation light [16]. Detecting such low amounts of light necessitates a highly sensitive detector for effective background discrimination at lower recoil energies. Previous experiments, like CRESST, have successfully demonstrated the simultaneous detection of phonons and light using a combination of CaWO<sub>4</sub> and Si sensors [17]. Our tungsten TES employs aluminium fins to absorb phonons from the sapphire crystal substrate, generating quasi-particles. This pairing of the sapphire particle absorber and the Al phonon absorber is expected to offer a low threshold due to the lower atomic number of Al and O in sapphire, as well as good crystal matching for phonons produced by both absorbers.

To address the challenge of detecting scintillation light, we pair our sapphire detector with the Si HV [18]. In the following sections, we will present the results of the Sapphire-Silicon

detector system for detecting both phonons and scintillation light. The anticipated linearity of the amplified photon signal with the applied voltage in the Si HV detector is illustrated.

### 3.2.1 Phonon-light measurement

When particles interact in the sapphire detector, they produce photons with a wavelength of around 325 nm [19]. When absorbed by the Si detector, these photons generate phonons and  $e^-/h^+$  pairs. For instance, the sapphire detector's light yield for 60 keV photons from  $^{241}\text{Am}$  is about  $10\% \pm 3\%$  [20]. Applying a bias voltage across the Si detector can enhance the detected signal. Amplification of phonon signal is earlier discussed in Chapter 2 in Section 2.2. The drifting  $e^-/h^+$  pairs in Si generate additional phonons, amplifying the phonon signal. This amplification, known as the NTL gain, is represented by the equation  $g_{\text{NTL}} = 1 + eV/\epsilon$ , where  $V$  is the applied voltage,  $e$  is the electronic charge, and  $\epsilon$  is the average energy needed to create an  $e^-/h^+$  pair in Si. The NTL gain is directly proportional to the applied voltage  $V$ .

### 3.2.2 Experimental setup and data set

The Texas A&M group developed sapphire and Si detectors weighing 100 g. The sapphire one is 76 mm in diameter and 4 mm thick, while the Si one is also 76 mm in diameter but 10 mm thick. These detectors are combined as a module and placed in a BluFors dilution refrigerator, which uses cryocoolers to maintain a base temperature of about 8 mK. The setup is illustrated in Fig. 3.8, with the sapphire and Si HV detectors shown in orange and cyan. There is a 2 mm gap between them. TES arrays on one face of each detector are used for phonon signal readout and are divided into 4 independent groups (A, B, C, D). The phonon signal is read out by standard CDMS electronics [21], with a SQUID amplifying the signal initially and further amplification by a front-end board outside the

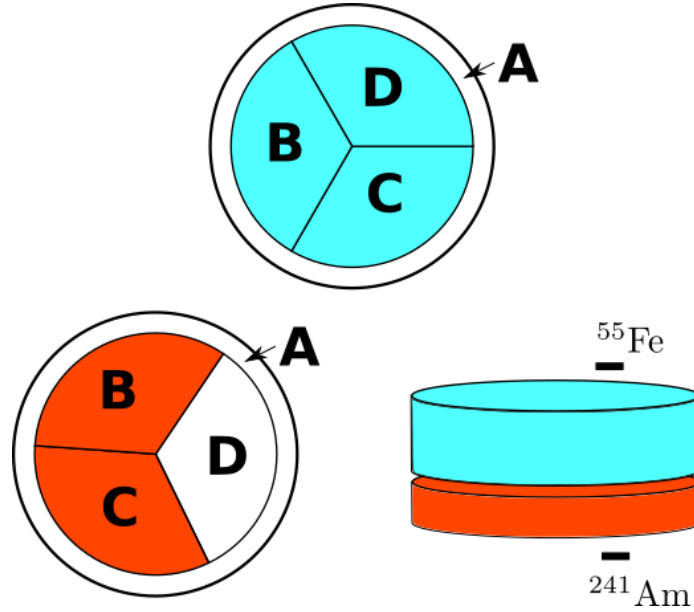


FIGURE 3.8: Diagram of the detector setup in the dilution refrigerator, featuring Si HV and sapphire detectors in cyan and orange, respectively. The detectors are paired to form a module. When a particle interacts with the sapphire, it produces two signals: phonons (read by a TES on the top surface of the sapphire) and photons (collected by the Si detector, also equipped with a TES). Each TES at the surface of both the detectors has four independent readout channels—outer channel A and inner channels B, C, and D. During this run, channel D is not used due to SQUID readout electronics limitations. Calibration involves two known energy sources: an  $^{55}\text{Fe}$  source atop the Si detector and an  $^{241}\text{Am}$  source beneath the sapphire detector [18].

cryostat, feeding into a PicoScope digitizer. The sampling window for each event is 2 ms long, with approximately 2000 sample points ( $1\ \mu\text{s}$  sampling rate). Initially, a small dataset without any trigger condition is taken to determine the average noise level. During data collection with known sources, a trigger is set around  $500\ \mu\text{s}$  to include noise, recording signal events close to the threshold. Fig. 3.9 illustrates an exemplary pulse with the trigger point indicated.

To calibrate the Si detector, an  $^{55}\text{Fe}$  gamma source is placed on top, and an  $^{241}\text{Am}$  source is placed at the bottom of the sapphire detector. The  $^{241}\text{Am}$  emits alpha particles with 5 MeV energy. In our experiment, we shielded these particles because they can deposit energy in both detectors and might get mixed up with 6 keV events due to early saturation of

the detector channels. The light produced in the sapphire is collected in the Si HV detector using coincidence techniques. To enhance the light input in the Si HV, we use a reflector. This way, the emitted light from sapphire is reflected onto the Si HV. In this experimental setup, no reflector is utilized. The Si HV detector operates with a bias voltage of up to 100 V to study the NTL gain of the light output from the sapphire.

### 3.3 Analysis and Result

The raw data acquired from the DAQ contains the information of each event in the form of a voltage as a function of time. Because the recorded pulses can be either signal or noise, an anomaly detection (AD) technique is used to improve the data quality during pulse filtration in the data analysis. In this work, we used a combination of two algorithms, namely t-SNE [22] and DBSCAN [23], to organize our data. The process involves using t-SNE, which stands for t-distributed stochastic neighbourhood embedding, to transform the data from a higher dimensional space to a lower one while keeping similar events together. This unsupervised machine learning technique identifies overall trends and patterns without prior knowledge of the data [24]. The output from t-SNE is fed into the DBSCAN algorithm. DBSCAN, short for Density-based spatial clustering of application with noise, is a clustering method that groups data based on their spatial information and relative distance. The resulting groups are referred to as clusters. In this analysis, the shape of the pulses from channels of the sapphire detector is characterized by a 23-dimensional vector that we call a feature vector. Using the feature vector, we represent each event in 23 dimensions. Each variable of the feature vector is calculated from a pulse and can be understood by Fig. 3.9. The variables are Pre-pulse standard deviation (STD), Post-pulse STD, Max time, Min time, Peak, Max tail, risetime, falltime, Widths at 10%, 50%, and

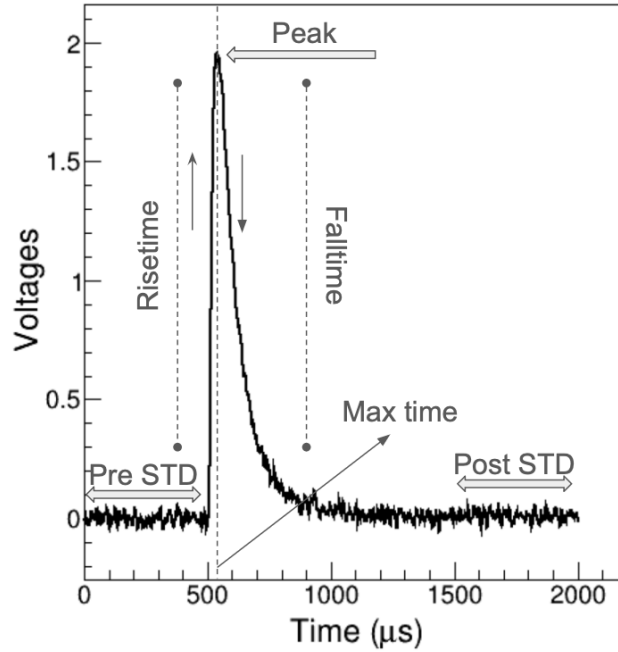


FIGURE 3.9: The t-SNE and DBSCAN input variables are computed using a typical pulse, presented as a voltage variation over time. The parameters extracted include pre-pulse and post-pulse STD (standard deviation) from the first 500  $\mu s$  and last 256  $\mu s$  of pulse amplitude. Other features involve the pulse's peak amplitude, the times of its maximum and minimum amplitudes, the maximum of the last 256  $\mu s$  (max tail), the rise time (time taken for 10% to 90% of the peak from the rising side), and the fall time (time taken for 90% to 10% of the peak from the decay side). Additionally, we calculate the full width at 10%, 50%, and 90% of the pulse amplitude.

90% of the Peak value and Max STD. The total feature vector contains all these variables calculated for all the channels of sapphire. Pre-pulse and post-pulse STDs indicate pulse height variation at the start and end, helping classify good pulses. A  $3\sigma$  deviation from the noise baseline distinguishes pulses from noise. Higher Post-pulse STD value identifies high-energy saturated pulses and discriminates against pile-up events also. Examples of a good pulse, saturated pulse and pile-up pulse are shown in Fig. 3.10(a). Max time, Min time, and Peak aid in classifying pulses based on timing and amplitude. Peak value can occur at any time for pile-up pulses, saturated pulses and ringing pulses (see Fig. 3.10(a)). Max tail helps spot long-tail saturated pulses. Rise time, fall time, and full widths at 10%,

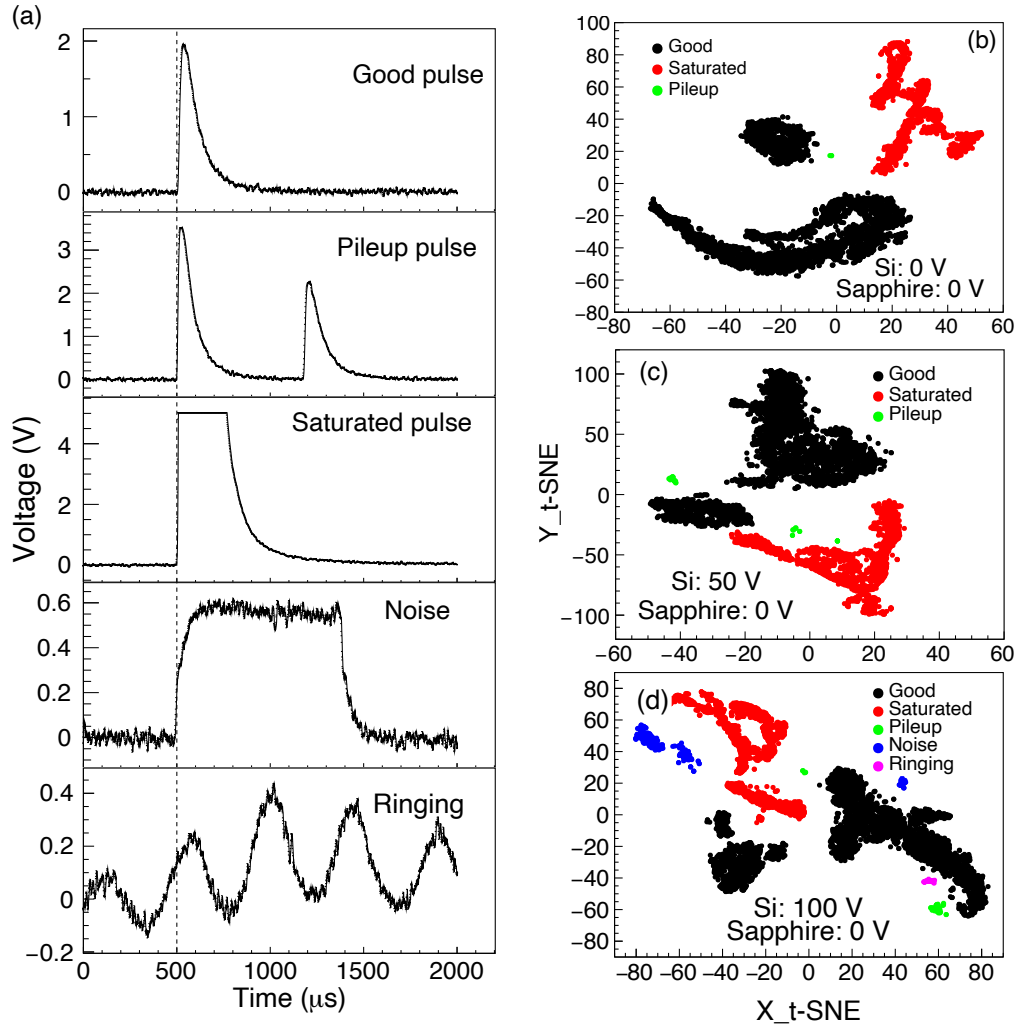


FIGURE 3.10: (a) Examples of a typical good pulse, pileup pulse, saturated pulse, noise, and ringing pulse are presented for the 100 V dataset. The voltage is plotted against time in microseconds. (b), (c) and (d) depict t-SNE and DBSCAN response plots, where the X and Y axes represent the t-SNE x and t-SNE y axes. The data in 2-dimensional t-SNE space is displayed after clustering with three different voltages: 0 V, 50 V, and 100 V, respectively. In (b) and (c), black, red, and green represent good, saturated, and pileup events, respectively. In (d), we include typical noise and ringing events indicated by blue and pink markers, respectively. Good events (black) are selected for further data analysis across all three voltage datasets. The figure is taken from [18].

50%, and 90% of pulse amplitude assist in distinguishing ringing and noise pulses. Max SD characterizes the distribution of time instances where the Peak value occurs in different channels, expecting slight variations. We reduced the 23-dimensional feature vector to 2



dimensions using t-SNE and then applied DBSCAN to cluster the data. In Fig.3.10 (b), (c), and (d), we display distinct clusters in the 2D t-SNE space for three bias voltages on the Si detector. We analyze DBSCAN-generated clusters, categorizing them into saturated pulses, good pulses, piled-up pulses, ringing, and noise. Multiple clusters may contain good pulses; for instance, at 0 V, two clusters with good pulses were observed, differing in amplitude. We merged them as both represented good pulses, depicted in Fig.3.10(b) with black colour. Saturated pulses are in red, pile-ups are in green, noise is in blue, and ringing is in magenta. Fig.3.10(a) provides examples of a typical good pulse, pile-up pulse, saturated pulse, noise, and ringing. Further analysis focuses on events from clusters representing good pulses.

### 3.3.1 Processing raw data with Optimal filter (OF) method

We used the Optimal Filter (OF) algorithm [25, 26] for pulse template fitting to extract energy information from filtered raw traces. Noise power spectral density (PSD) is calculated from a dataset with random triggers. The OF algorithm is applied to the raw data, fitting pulses in the frequency domain to determine pulse amplitude via the best  $\chi^2$  fit values. The amplitude, directly proportional to pulse energy, is calibrated using known energy sources. The random-triggered dataset measures noise and helps calculate baseline resolution for the detectors.

### 3.3.2 Calibration of Si HV

We first calibrate and check the noise performance of Si HV using 6 keV gamma rays from the  $^{55}\text{Fe}$  source. Three bias voltages were used: 0 V, 50 V, and 100 V. In Fig.3.11(a), the noise performance is displayed through the Power Spectral Density (PSD) of three inner channels (B, C, and D) of the Si HV detector. The green curve represents channel B biased

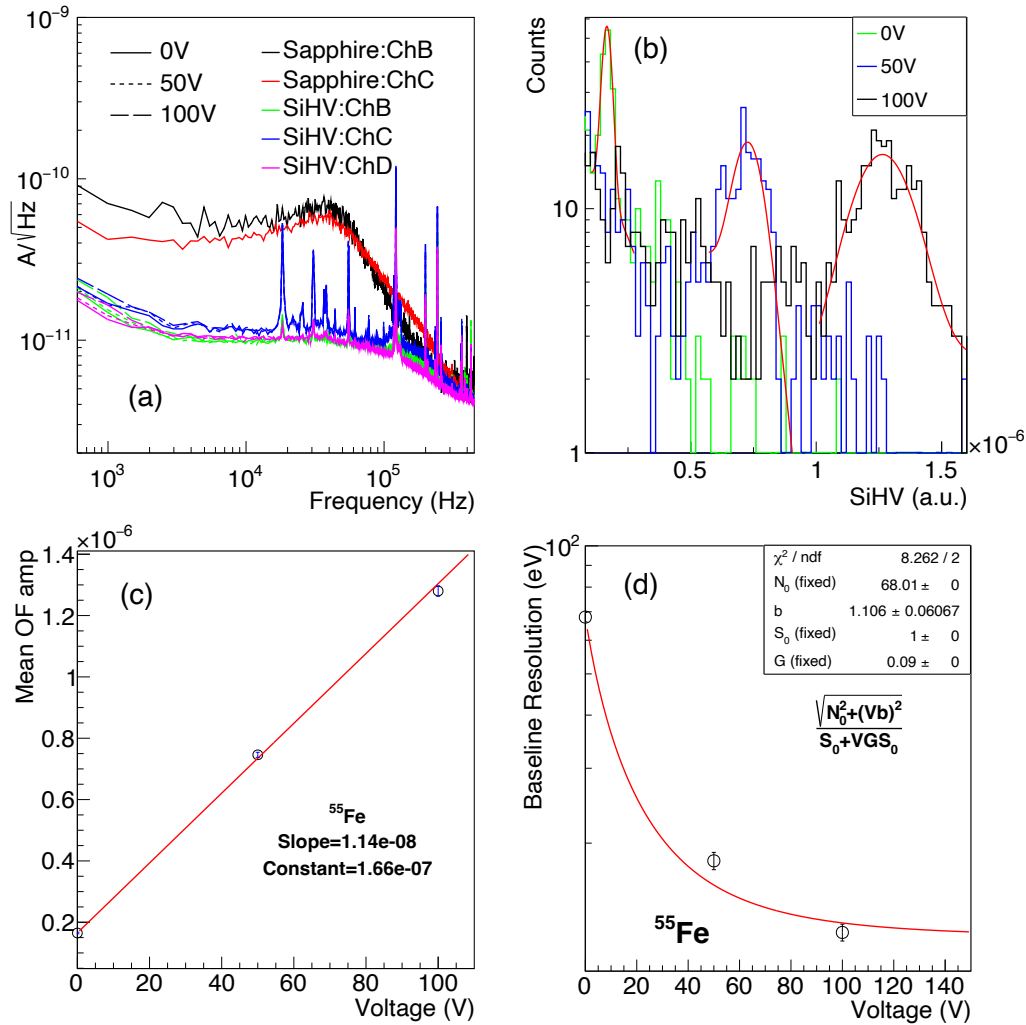


FIGURE 3.11: (a) Phonon noise power spectral density (PSD) depicts current amplitude in  $A/\sqrt{\text{Hz}}$  plotted against frequency in Hz. The PSD for two sapphire channels at 0 V is shown in black and red solid curves. For the Si HV detector, PSD for three channels is shown in green, blue, and pink with solid, dotted, and dashed lines corresponding to 0 V, 50 V, and 100 V, respectively. (b) 6 keV peaks from the  $^{55}\text{Fe}$  source in the Si HV detector at 0 V, 50 V, and 100 V are represented by green, blue, and black lines, respectively, along with Gaussian fits shown in red. (c) The mean of the peak in the OF unit is plotted with the applied voltages (0 V, 50 V, and 100 V), revealing a linear amplification of the phonon signal in the experimental data. (d) Baseline resolution in eV is plotted against applied voltages, showing statistical errors with the data points. The lowest baseline resolution value is  $12.33 \pm 0.56$  eV at 100 V, indicating an improvement in the S/N ratio with higher voltages. The data points are fit to a functional form  $N/S$  where  $N$  and  $S$  are defined in Eq. 3.1 and Eq. 3.2. The figure is sourced from [18].

at 0 V (solid line), 50 V (dotted line), and 100 V (dashed line), while blue and pink represent channels C and D, respectively. The same figure also shows the PSD of sapphire channels in black and red solid curves. The PSD distribution of Si HV exhibits a peaky feature due to higher bias voltages, causing an increase in noise at higher frequency regions.

In Fig.3.11(b), the 6 keV gamma peak from the  $^{55}\text{Fe}$  source is identified in Si HV for three different voltages, and the measured spectra are fitted with a Gaussian curve shown in red.

To confirm the linearity of the NTL phonons with applied voltages, the mean value of the distribution is plotted as a function of bias voltage in Fig.3.11(c). As expected, the NTL amplification of the 6 keV events is linearly proportional to the applied voltages, represented by the straight line in the figure. The error bars associated with the data points are statistical. The baseline resolution, calculated using randomly triggered data for all three voltages, is shown in Fig.3.11(d) as a function of voltage, with the lowest achieved baseline resolution being 12 eV. This distribution follows similar trends for the Si HV detector in Fig. 3.4(b).

### 3.3.3 Amplification of light in Si detector

In this part, we explore how the scintillation light from sapphire is amplified by Si HV detector, focusing only on events where both detectors detect signals. We use a  $^{241}\text{Am}$  source emitting 60 keV gammas to illuminate the sapphire detector.

When a 60 keV gamma is absorbed in the sapphire, it generates phonons and scintillation light. On average, only 10% of the incident gamma's energy is converted into light [20]. The TES on the sapphire detector measures phonons, while the TES on the Si HV detector detects only the photons reaching the Si detector. To estimate the light reaching Si HV, we considered three main factors causing light loss from sapphire:

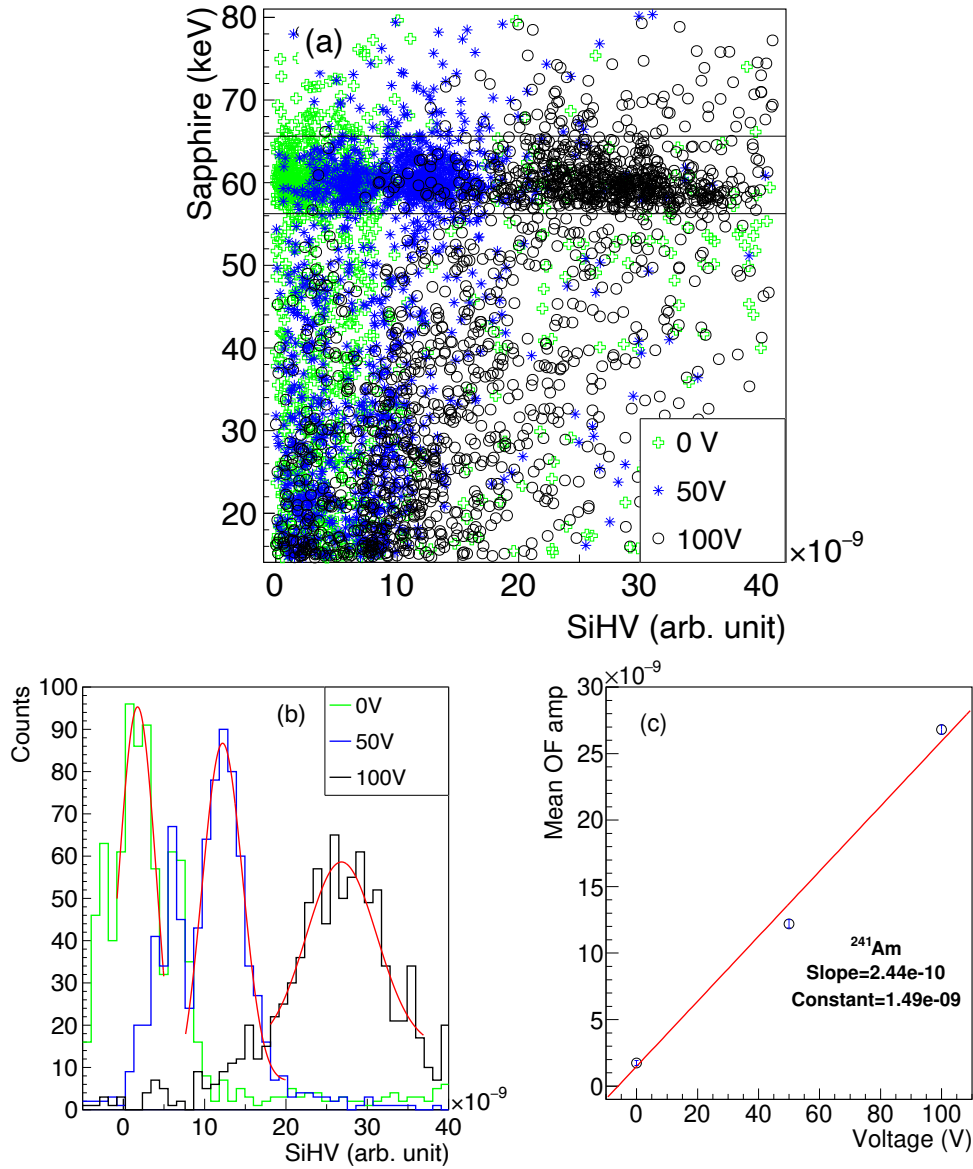


FIGURE 3.12: (a) The correlation plot showing the relationship between phonon energy measured in sapphire (on the Y-axis) and light output measured in the Si HV detector (on the X-axis) at three different voltages. The light output from 60 keV events originating from an  $^{241}\text{Am}$  source in the sapphire detector is amplified in the Si HV detector. Figure (b) showcases the projected 60 keV events (depicted by black lines) in the Si HV detector, exhibiting the amplified light at different voltages. In (c), the linearity of the amplified light as a function of voltage is demonstrated, with statistical errors associated with the data points. The figure reference is [18].

1. Geometrical acceptance: Not all light from sapphire reaches Si HV due to the geometry. A Monte Carlo simulation indicates that only 40% of photons from sapphire will reach Si HV.
2. Si HV mask: The high-voltage phonon mask on the Si HV detector covers 90% of the surface facing the sapphire detector, further reducing light entry.
3. Light absorption: Light falling on Si gets absorbed while passing through the material. Silicon has a reflectivity of about 56% [27, 28]. Thus, approximately 44% of light will be absorbed in Si.

We have considered these three main losses that limit the light collection in Si HV. The effective light collection is expected to be around 2%.

Scintillation photons of approximately 6 keV (10% of 60 keV gammas) hit the Si detector, creating phonon signals. The amplification of the light signal in the Si detector is observed through coincident events with the sapphire detector. Fig.3.12(a) illustrates the correlation between the sapphire and Si detectors, demonstrating the amplification of light output from 60 keV events in sapphire in the Si detector under applied voltages.

Fig.3.12(b) displays the coincidence of 60 keV events in the Si detector, showcasing light amplification at different voltages. The measured light in the Si HV detector, converted to energy using the detector's calibration factor, matches the expected 2% after accounting for all losses. Fig.3.12(c) illustrates the linearity of the amplified light output in the Si detector by plotting the mean of the projected event distribution with respective voltages.

### 3.3.4 Section summary

In this section, we show how we can simultaneously detect phonons and scintillation light in a system that consists of a sapphire and a Si HV detector. Even without using any

reflector in the experiment, we were able to measure 2% of the total light generated in the sapphire. This result aligns well with the expected value, accounting for all the losses.

The Si HV detector achieves the lowest energy threshold of 36 eV (3 times the baseline resolution) at 100 V. Since the Si HV detector can operate at voltages up to 240 V, our future work aims to reduce the energy threshold further by applying higher voltages. We also plan to enhance light collection efficiency by using a reflective detector housing and a Si HV detector with a custom phonon mask design, covering less Si HV detector surface area for maximum light collection efficiency.

In summary, this type of detector system holds promise for applications searching for low-mass dark matter and  $\text{CE}\nu\text{NS}$ , where detecting low-energy recoils with active background discrimination is crucial.

## 3.4 Detector performance at NSC

After being developed and tested at the test facility, all these detectors are placed in the reactor environment at NSC to study noise and background for the MINER experiment. Various test runs have been conducted with Si HV, Hybrid, Sapphire, and active Veto detectors. The upcoming sections will discuss some noteworthy results from Si HV and Sapphire detectors from MINER test run 28 and run 34.

### 3.4.1 Experimental setup at NSC

In the MINER experimental setup, the detectors are installed within a BlueForts dilution refrigerator, which maintains a base temperature of  $\sim 8$  mK. This refrigerator is positioned 4 meters away from the MINER reactor at NSC. The detectors are kept in copper housing with an additional shielding arrangement, including a 4-inch layer of lead, a 2 mm thick

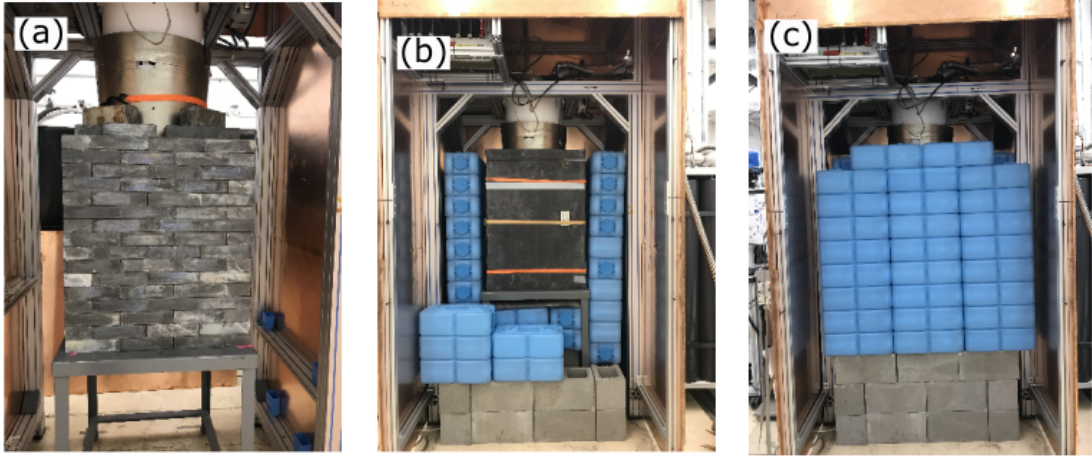


FIGURE 3.13: (a) A shielding with a 4-inch layer of Lead bricks surrounding the refrigerator, effectively blocking external gamma radiation. (b) A 2 mm thick layer of borated rubber serves as an additional shielding component after Lead shielding. (c) Shows another additional layer of 8-inch thick water bricks.

borated rubber sheet, and an 8-inch layer of water bricks. The experimental setup with shielding is shown in Fig. 3.13. This setup uses a 14-channel CAEN digitizer for collecting data. During run 28, we studied Si HV and Hybrid detectors, whereas, in run 34, a tower comprising one low-threshold sapphire detector and two germanium detectors with a diameter of 7.6 cm and thickness of 2.5 cm is mounted. The experimental setup utilizes  $^{55}\text{Fe}$  and  $^{57}\text{Co}$  sources for calibration purposes.

### 3.4.2 Si HV detector

We tested the performance of the Si HV detector with a  $^{55}\text{Fe}$  gamma source of around 6 keV at the NSC reactor site while the reactor was off. We employed primary shielding with water and lead bricks inside a copper shielding. The Si HV detector was operated at six different voltages: 0 V, 50 V, 100 V, 150 V, 200 V, and 250 V. We selected 250 V as the maximum voltage because, as shown in Fig. 3.4(a), linearity is lost beyond 250 V.

### Analysis and results

We utilized the Optimum Filter (OF) method to extract information such as pulse amplitude by analyzing raw pulses over time. The analysis follows the steps discussed earlier, involving applying cuts on pulse parameters like rise time, fall time, baseline STD, max value, min value, and max tail, and selecting good events. A pulse template was created by averaging all the good pulses. Noise data was obtained using random triggers. In Figure 3.14, three

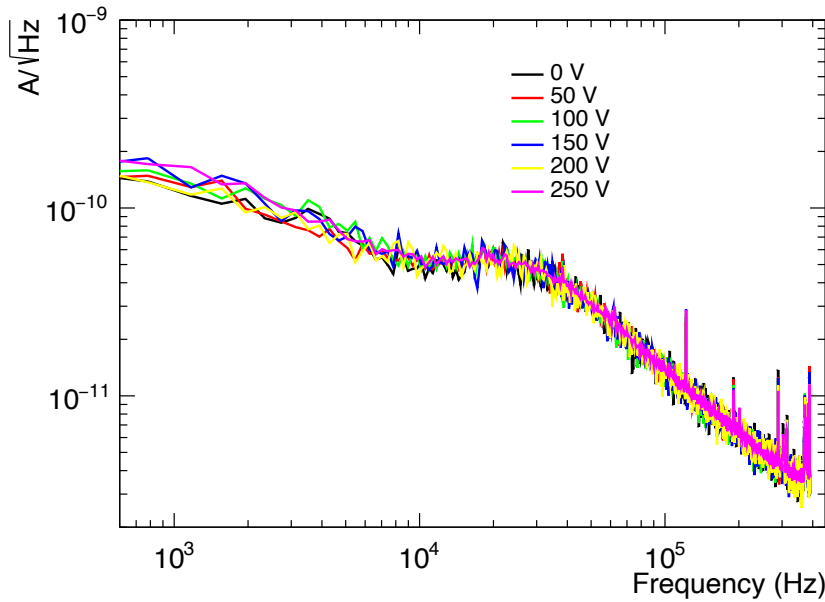


FIGURE 3.14: The TES current amplitude, measured in  $A/\sqrt{\text{Hz}}$ , is plotted against frequency for various voltages ranging from 0 V to 250 V. These plots represent the phonon noise PSDs. The noise performance across all the voltages is consistent.

inner channels (B, C, and D) of the detector were readout, while data from the outer channel A was excluded to eliminate unwanted surface events. We averaged the Power Spectral Density (PSD) of the noise data at each voltage and compared the noise PSD across all voltages for channel B in Figure 3.14. To identify 6 keV gamma events in the detector, we leveraged the phonon channel layout to create two variables—the X partition and Y partition—which estimate the location of sources on the detector in a system similar to X-Y



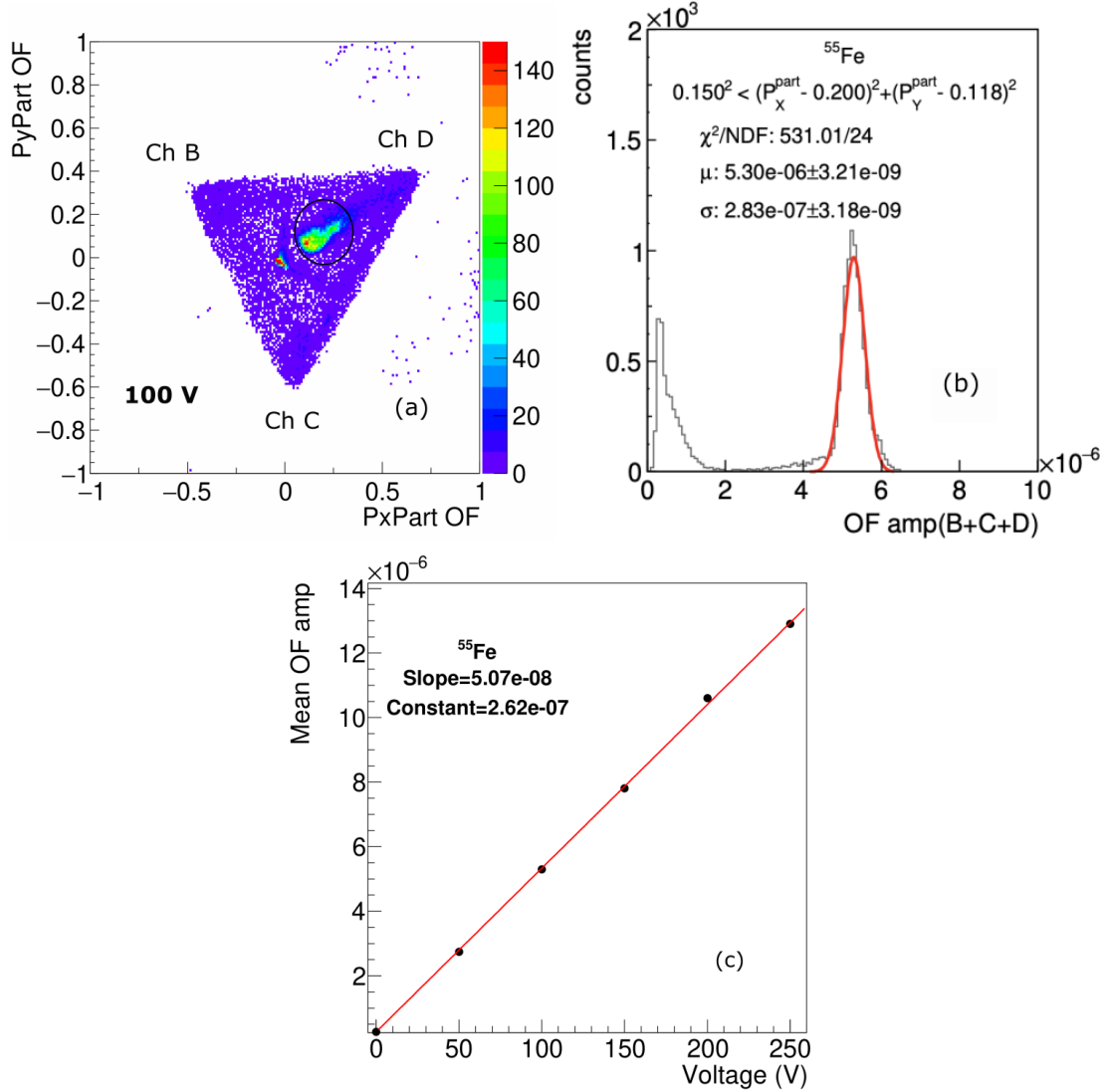


FIGURE 3.15: (a) The scatter plot showing the Y partition variable,  $PyPart$  versus the X partition variable,  $PxPart$ , indicating the positions of  $^{55}Fe$  events on channel D using Eq. 3.5 and Eq. 3.4. The colour palettes in this representation signify the number of events in each bin. (b) the pulse amplitude distribution from the OF method is presented, showcasing  $^{55}Fe$  peak fitted with a Gaussian distribution for 100 V data. (c) The mean value of phonon energy distributions in arbitrary units across various voltages ranging from 0 V to 250 V. The red line represents a straight line fitted to the data points, and the corresponding fit parameters are shown. The statistical errors (equivalent to the size of the markers) are shown with each data point [29].

Cartesian coordinates. These variables are defined as follows:

$$\text{X partition, } P_{xPart} = \frac{\cos 30^\circ \cdot pD + \cos 150^\circ \cdot pB + \cos 270^\circ \cdot pC}{pB + pC + pD} \quad (3.3)$$

$$\text{Y partition, } P_{yPart} = \frac{\sin 30^\circ \cdot pD + \sin 150^\circ \cdot pB + \sin 270^\circ \cdot pC}{pB + pC + pD} \quad (3.4)$$

Here,  $pB$ ,  $pC$ , and  $pD$  represent the phonon amplitudes of the event in channels B, C, and D, respectively. In Figure 3.15(a), a scatter plot of X and Y partition variables using 100 V data is shown, with the  $^{55}\text{Fe}$  source position visible as high-density blobs. To isolate the  $^{55}\text{Fe}$  peak, a circular cut is defined (shown in black), and a Gaussian function is fitted to the  $^{55}\text{Fe}$  peak after applying the cuts (Figure 3.15(b)). The error on this value is obtained from the errors on the Gaussian fits to the peak. Similarly, we identify the 6 keV gamma peak for all datasets with different voltages and fit it with a Gaussian. To determine the NTL gain, we plotted the mean of OF amp as a function of voltage (Figure 3.15(c)), showing a linear increase due to the NTL effect. We computed the baseline resolution across various voltages from the data obtained through random triggers. In Figure 3.16(a), the noise energy distribution is presented in terms of  $e^-/h^+$  pairs for 100 V data. The baseline resolution of the detector is determined by considering the  $1\sigma$  width of the distribution. We calculated the baseline resolution for all voltages and plotted it against voltage. The baseline resolution improves with increasing voltage, reaching its lowest point at around  $\sim 7 e^-/h^+$  pairs at 150 V.

In Figure 3.17, we compared the noise performance at NSC with data from the test facility. The noise level is higher at NSC than at the facility. Based on this observation, optimization at NSC was carried out for the best results.

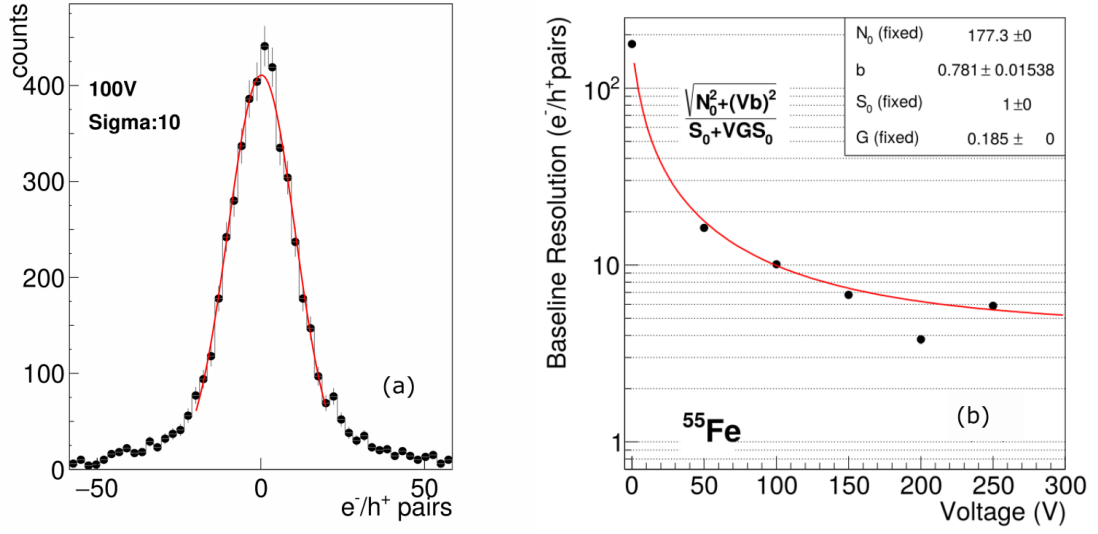


FIGURE 3.16: (a) The distribution of noise energy is shown in the  $e^-/h^+$  pair energy scale for the 100 V dataset. The sigma value from the Gaussian fit represents the baseline resolution of the detector. (b) Baseline resolution in units of  $e^-/h^+$  pair units as a function of voltage. The data points are fit to a functional form  $N/S$  where  $N$  and  $S$  are defined in Eq. 3.1 and Eq. 3.2 [29].

### 3.4.3 Sapphire detector

#### Calibration with $^{57}\text{Co}$ source

We positioned a 100 g sapphire detector at the MINER site alongside two germanium detectors, each weighing  $\sim 500$  g. The germanium detectors have a diameter of 7.6 cm and a thickness of 2.5 cm. A schematic of the detector tower is illustrated in Fig. 3.18(a). Organizing the detectors in a tower configuration allows us to investigate single scatter events in sapphire. All four channels of the sapphire detector are readout, while only the inner channels B and C are readout for the germanium detectors.

To assess the noise performance of the detector, we utilize noise data obtained from random triggers. In Fig. 3.18(b), the Power Spectral Density (PSD) distribution for both sapphire and germanium detector channels is displayed. We shine an external  $^{52}\text{Co}$  source emitting 122 keV gammas to the detector system. The summed spectrum of the four

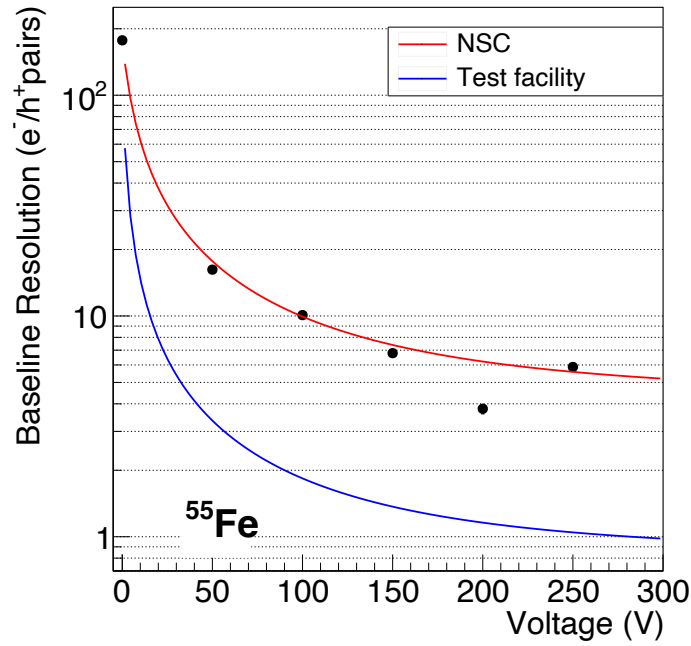


FIGURE 3.17: The noise performance is compared between NSC and the test facility at Texas A&M University. The noise level at NSC is much higher than at the test facility.

channels in the OF unit for the sapphire detector is shown in Fig. 3.18(c). The 122 keV gamma peak is observed with a spread due to the external placement of the  $^{57}\text{Co}$  source. The Compton edge of the 122 keV gamma comes at 39.43 keV and is visible in the summed spectrum. For calibration, we utilize the Compton edge, fitting the spectrum with a Compton edge function [30] to determine its value. The fitted function is:

$$F(E) = \alpha \cdot \text{erfc}\left[\frac{E - E_c}{\sqrt{2}\sigma}\right] + \beta \cdot \exp\left[-\frac{(E - E_c)^2}{2\sigma^2}\right] \quad (3.5)$$

where,  $E$  is the deposited energy,  $E_c$  is the measured Compton edge,  $\sigma$  is the boardening of edge.  $\alpha$  and  $\beta$  are the parameters defined here [30]. Figure.3.18(d) shows the Compton function fitted to the data with the parameter values.

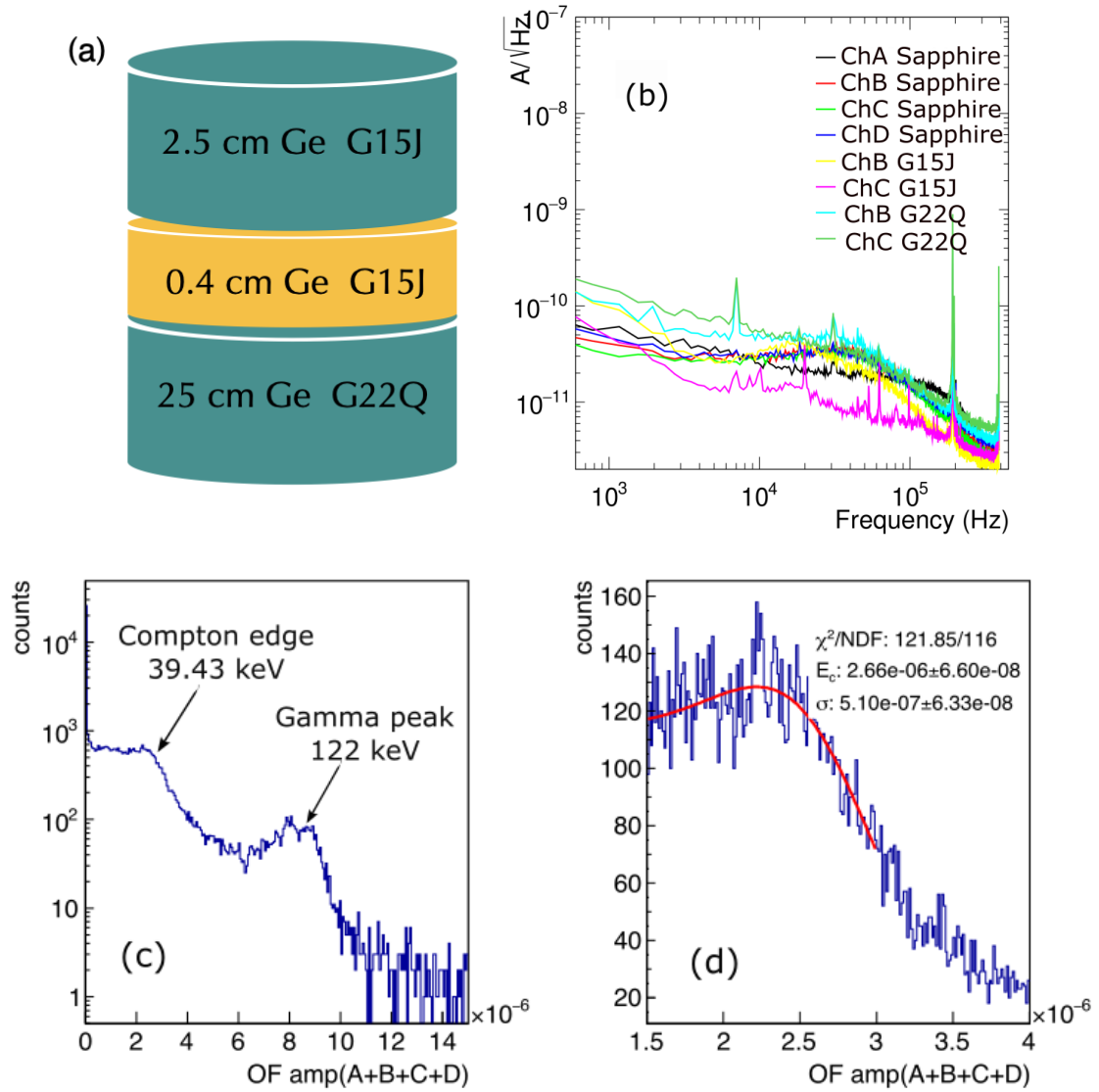


FIGURE 3.18: (a) A detector tower of low-threshold sapphire with two germanium detectors is placed at NSC. (b) The noise PSDs are shown for four sapphire channels (A, B, C, D) and two channels for each germanium detector. The noise level remains consistent across all detectors. (c) The distribution of phonon amplitudes, obtained through the OF method and summed over all four channels, is shown with  $^{57}\text{Co}$  source. We identify the gamma peak at 122 keV from a  $^{57}\text{Co}$  source, followed by a Compton edge at 39.43 keV. (d) A functional form is used to model the Compton edge at 39.43 keV, and the fitting parameters are provided.

### Al fluorescence

The sapphire detector is made of  $\text{Al}_2\text{O}_3$ . So, Al and O could be in-situ backgrounds for this detector as they show fluorescence. Also, Cu could be another background candidate as the

detector is kept in a Cu casing. During testing in the laboratory (non-reactor environment) with  $^{241}\text{Am}$  source, the detector provides a baseline resolution of  $28.4 \pm 0.4$  eV. Because of its excellent baseline resolution, we expect Al fluorescence at 1.49 keV. It is expected that Al fluorescence will be present in all the channels, mainly in the bulk of the detector.

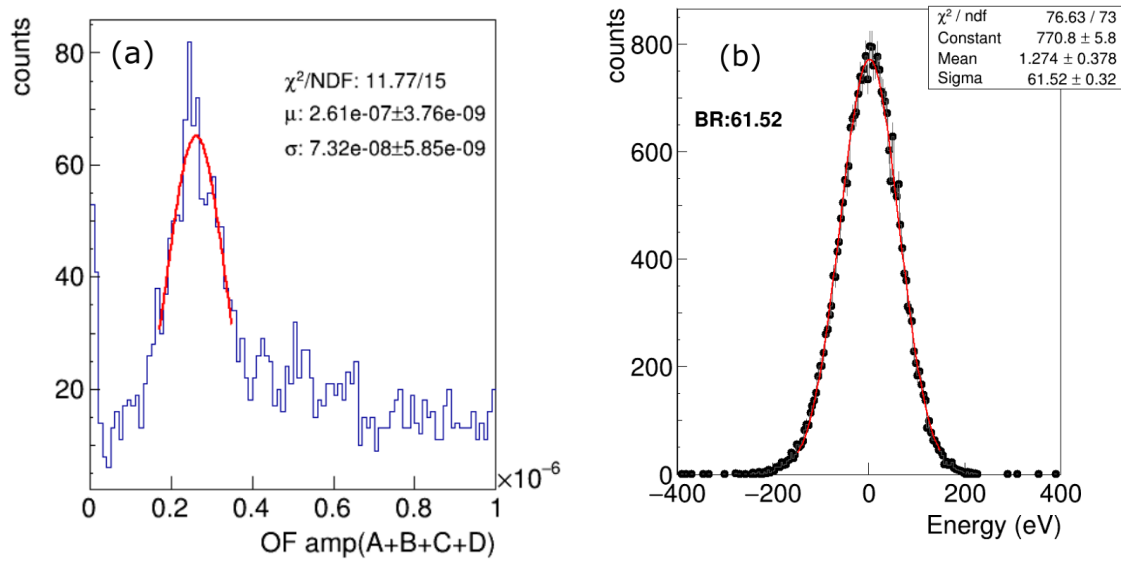


FIGURE 3.19: (a) The peak identified as Al fluorescence is shown and fitted using a Gaussian. (b) The baseline resolution of sapphire, summed over all channels, is measured at MINER and is  $\sim 61$  eV. This value is higher compared to the resolution at the test facility. The figures are taken from [31].

### Analysis and result

The good events are selected by considering events with good  $\chi^2$  values from the pulse template fit. We consider only single scatter events that share events that deposit energy in the sapphire detector but are consistent with noise in the top and bottom germanium detectors. Another cut is used to select only bulk events using partition variables for outer channel A. The variable is defined as the ratio of the amplitude in channel A to the sum of the amplitude in all the channels:  $\frac{A}{A+B+C+D}$ . Events with partition value  $< 0.15$

are selected. After applying these cuts, a prominent peak is found in individual sapphire channels and the combined spectrum. Figure. 3.19(a) shows the peak, which is considered an Al fluorescence peak in the combined spectrum at 1.49 keV, and it is fitted with a Gaussian (red line) for calibration. Using the calibration, we have calculated the baseline resolution using noise data taken with random triggers. A  $\sim 61$  eV baseline resolution is observed in the reactor environment and can be seen in Fig. 3.19(b). This is higher than a similar measurement with the sapphire detector at the test facility ( $\sim 28.4 \pm 0.4$  eV). This may be due to the different environmental conditions causing higher electronic noise.

### 3.5 Current status of MINER

The MINER experiment has transitioned from testing mode to a continuous experimental mode. We have set up a new 64-channel CAEN digitizer, enabling simultaneous readings from multiple detectors. Currently, we are testing a tower of five sapphire detectors using a triggerless mode that does not need threshold conditions. A dedicated software package for pulse extraction, offline analysis and increased data storage capacity has been installed to enhance data handling. Additionally, plastic scintillator veto panels are now placed around the detector setup to reduce background caused by muon-induced neutrons and other background sources.

### 3.6 Summary

MINER is an upcoming experiment aiming to measure  $CE\nu NS$  cross-section using reactor anti-neutrinos precisely. The experiment is currently under development at Texas A&M University, USA, utilizing several low-threshold detectors. Cryogenic detectors, mainly composed of silicon, germanium, and sapphire, are being developed at a test facility

located at Texas A&M University and then deployed and tested at the NSC in front of the reactor site. We have discussed the results of three newly developed phonon-mediated detectors and compared their performance at the test facility and the NSC.

The 100 g Si HV detector with contact-free geometry shows a single  $e^-/h^+$  pair resolution at the test facility. This detector has been positioned at the NSC and shows the lowest baseline resolution at  $\sim 7 e^-/h^+$  pairs. Meanwhile, the 100 g sapphire scintillation detector was developed in the test facility. A particle interacting with the detector can create phonons and light. The phonons are measured with TESs on the detector surface, showing the lowest single-channel baseline resolution of  $\sim 28.4 \pm 0.4$  eV. The measured phonon energy spectrum shows distinct calibration lines from the  $^{241}\text{Am}$  source. The sapphire detector is more sensitive than the silicon and germanium detectors due to its composition with lower atomic numbers and improved phonon collection efficiency.

In another study, by combining these low-threshold detectors, we have demonstrated two low-threshold detector technologies to develop a large-mass, low-threshold detector system. This system simultaneously measures the phonons in a sapphire detector while an adjacent Si HV detector detects the scintillation light from the sapphire detector. This technique can be utilized for event-by-event discrimination of ER and NR events. Even without using any reflector in the experiment, we were able to measure 2% of the total light generated in the sapphire. This result aligns well with the expected value, accounting for all the losses.

In the MINER experiment, a tower of three detectors, including a sapphire and two germanium detectors, has been characterized. We used a  $^{57}\text{Co}$  calibration source and identified the Compton edge at 39.43 keV and the gamma peak at 122 keV in the measured phonon energy distribution. We were also able to see the Al fluorescence peak after selecting single scatter and bulk events. The baseline resolution is quite high compared



to the test facility due to the reactor environment. The experiment is being upgraded from testing to continuous mode with a better DAQ system and improved data handling resources. Primary shielding is also optimized to minimize noise and background levels at the experimental site. All these low-threshold, Hybrid, and veto detectors will be deployed in tandem at MINER in the search for  $CE\nu NS$ .

## Bibliography

- [1] G. Agnolet et al. “Background Studies for the MINER Coherent Neutrino Scattering Reactor Experiment”. *Nucl. Instrum. Meth. A* 853 (2017), p. 53–60. arXiv: [1609.02066 \[physics.ins-det\]](#).
- [2] V. I. Kopeikin. “Flux and spectrum of reactor antineutrinos”. *Phys. Atom. Nucl.* 75 (2012), p. 143–152.
- [3] Wei Eng Ang, Shikha Prasad, and Rupak Mahapatra. “Coherent elastic neutrino nucleus scatter response of semiconductor detectors to nuclear reactor antineutrinos”. *Nucl. Instrum. Meth. A* 1004 (2021), p. 165342.
- [4] Bhaskar Dutta et al. “Sensitivity to Z-prime and nonstandard neutrino interactions from ultralow threshold neutrino-nucleus coherent scattering”. *Phys. Rev. D* 93 (2016), p. 013015. arXiv: [1508.07981 \[hep-ph\]](#).
- [5] Joachim Kopp, Michele Maltoni, and Thomas Schwetz. “Are There Sterile Neutrinos at the eV Scale?” *Phys. Rev. Lett.* 107 (2011), p. 091801. arXiv: [1103.4570 \[hep-ph\]](#).
- [6] James B. Dent et al. “New Directions for Axion Searches via Scattering at Reactor Neutrino Experiments”. *Phys. Rev. Lett.* 124 (2020), p. 211804. arXiv: [1912.05733 \[hep-ph\]](#).
- [7] T. Booth F. Brown J. Bull L. J. Cox J. Durkee J. Elson M. Fensin R. A. Forster J. Hendricks H. G. Hughes R. Johns B. Kiedrowski R. Martz S. Mashnik G. McKinney D. Pelowitz R. Prael J. Sweezy L. Waters T. Wilcox T. Zukaitis T. Goorley M. James. “Initial MCNP6 Release Overview”. *Nuclear Technology* 180 (2012), p. 298–315.

- [8] A. Drukier and Leo Stodolsky. “Principles and Applications of a Neutral Current Detector for Neutrino Physics and Astronomy”. *Phys. Rev. D* 30 (1984), p. 2295.
- [9] Nader Mirabolfathi et al. “Toward Single Electron Resolution Phonon Mediated Ionization Detectors”. *Nucl. Instrum. Meth. A* 855 (2017), p. 88–91. arXiv: [1510.00999 \[physics.ins-det\]](#).
- [10] H. Neog et al. “Phonon-mediated high-voltage detector with background rejection for low-mass dark matter and reactor coherent neutrino scattering experiments”. *Nucl. Instrum. Meth. A* 1033 (2022), p. 166707. arXiv: [2006.13139 \[physics.ins-det\]](#).
- [11] V. Iyer et al. “Large mass single electron resolution detector for dark matter and neutrino elastic interaction searches”. *Nucl. Instrum. Meth. A* 1010 (2021), p. 165489. arXiv: [2011.02234 \[physics.ins-det\]](#).
- [12] S. Verma et al. “Low-threshold sapphire detector for rare event searches”. *Nucl. Instrum. Meth. A* 1046 (2023), p. 167634. arXiv: [2203.15903 \[physics.ins-det\]](#).
- [13] Vijay Janardhana Iyer. “Development and calibration of semiconductor detectors for dark matter searches”. PhD thesis. Bhubaneswar, NISER, 2021.
- [14] E. Gatti and P. F. Manfredi. “Processing the Signals From Solid State Detectors in Elementary Particle Physics”. *Riv. Nuovo Cim.* 9N1 (1986), p. 1–146.
- [15] R Belanger, DW Buckley, and JB Swenson. *Environmental assessment of ionization chamber smoke detectors containing Am-241*. Tech. rep. Science Applications, Inc., La Jolla, CA (USA), 1979.
- [16] J. Amaré et al. “Light yield of undoped sapphire at low temperature under particle excitation”. *Appl. Phys. Lett.* 87 (2005), p. 264102.
- [17] M. Kiefer et al. “In-situ study of light production and transport in phonon/light detector modules for dark matter search”. *Nucl. Instrum. Meth. A* 821 (2016), p. 116–121. arXiv: [1503.07806 \[astro-ph.IM\]](#).
- [18] M. Chaudhuri et al. “Development of a large-mass, low-threshold detector system with simultaneous measurements of athermal phonons and scintillation light”. *Nucl. Instrum. Meth. A* 1053 (2023), p. 168374. arXiv: [2212.04342 \[physics.ins-det\]](#).

- [19] Yoshisuke Futami, Takayuki Yanagida, and Yutaka Fujimoto. “Optical, dosimetric, and scintillation properties of pure sapphire crystals”. *Japanese Journal of Applied Physics* 53 (2014), 02BC12.
- [20] J. Amaré et al. “Light yield of undoped sapphire at low temperature under particle excitation”. *Applied Physics Letters* 87 (2005), p. 264102. eprint: <https://doi.org/10.1063/1.2158518>.
- [21] D.A. Bauer et al. “The CDMS II Data Acquisition System”. *Nuclear Instruments and Methods in Physics Research Section A: Accelerators, Spectrometers, Detectors and Associated Equipment* 638 (2011), p. 127–133.
- [22] Laurens van der Maaten and Geoffrey Hinton. “Visualizing Data using t-SNE”. *Journal of Machine Learning Research* 9 (2008), p. 2579–2605.
- [23] Martin Ester et al. “A Density-Based Algorithm for Discovering Clusters in Large Spatial Databases with Noise”. *AAAI* (1996).
- [24] Arthur Zimek and Erich Schubert. “Outlier Detection”. In: *Encyclopedia of Database Systems*. Springer New York, 2017, p. 1–5.
- [25] Fink Caleb and Watkins Sam. *qetpy Documentation*. 2021.
- [26] Sunil Ramanlal Golwala. “Exclusion limits on the WIMP nucleon elastic scattering cross-section from the Cryogenic Dark Matter Search”. PhD thesis. University of California, Berkeley, 2000.
- [27] Martin A. Green. “Self-consistent optical parameters of intrinsic silicon at 300K including temperature coefficients”. *Solar Energy Materials and Solar Cells* 92 (2008), p. 1305–1310.
- [28] Martin A. Green and Mark J. Keevers. “Optical properties of intrinsic silicon at 300 K”. *Progress in Photovoltaics: Research and Applications* 3 (1995), p. 189–192. eprint: <https://onlinelibrary.wiley.com/doi/pdf/10.1002/pip.4670030303>.
- [29] Mouli Chaudhuri. “The Mitchell Institute Neutrino Experiment at Reactor (MINER)”. In: *Proceedings of the XXIV DAE-BRNS High Energy Physics Symposium, Jatni, India*. Ed. by Bedangadas Mohanty et al. Singapore: Springer Nature Singapore, 2022, p. 589–593.

- [30] M. J. Safari, F. Abbasi Davani, and H. Afarideh. “Differentiation method for localization of Compton edge in organic scintillation detectors” (2016). arXiv: [1610.09185 \[physics.ins-det\]](#).
- [31] Mouli Chaudhuri. “Characterization of Sapphire Detector for CE $\nu$ NS Search at MINER”. In: *Advanced Radiation Detector and Instrumentation in Nuclear and Particle Physics*. Ed. by Rajendra Nath Patra. Cham: Springer International Publishing, 2023, p. 97–102.



---

# $^{32}\text{Si}$ background estimation in CDMS II experiment

---

## Contents

4.1 Motivation . . . . .	112
4.2 $^{32}\text{Si}$ background measurement for CDMS II . . . . .	116
4.3 Summary and outlook . . . . .	153

---

The Cryogenic Dark Matter Search Experiment (CDMS) is a direct dark matter search experiment, aiming to detect nuclear recoils induced by Weakly Interacting Massive Particles (WIMPs) colliding with target nuclei while effectively rejecting all the background events [1–3]. Here, we focus on identifying dark matter (DM) interactions as signal events. The experiment also observes other particles such as gamma rays, beta particles, or neutrons, which are considered as background events. Mitigating these background events is crucial for the success of the experiment. In Chapter 2, we thoroughly explored various types of backgrounds and strategies to mitigate them. The primary approach involves im-

plementing passive or active shielding. Operating at substantial depths underground, along with employing a passive, multi-layer hermetic shield, effectively reduces background particle rates, particularly gamma rays and neutrons. However, these measures do not fully address in-situ backgrounds inherent in the detector material. These in-situ backgrounds stem from cosmogenic activation, leading to the production of isotopes such as  $^{32}\text{Si}$  and  $^3\text{H}$  in silicon (Si) detectors, and  $^3\text{H}$  in germanium (Ge) detectors. Furthermore, due to null results at higher DM mass ranges ( $>10 \text{ GeV}/c^2$ ) and interaction cross-sections exceeding  $10^{-41} \text{ cm}^2$ , most of experiments have shifted their focus to searching for DM at lower mass ranges ( $<10 \text{ GeV}/c^2$ ), where the nuclear recoil signal is below 10 keV and the event rate is very low (events per year) [4]. The backgrounds from the decay of  $^{32}\text{Si}$  has become a significant concern, posing a potential limitation on the DM sensitivity of future silicon-based detectors.

In this chapter, we delve into estimating one of the most concerning in-situ backgrounds for silicon detectors using CDMS II data. We begin by outlining the motivation behind this analysis in Section 4.1, followed by a concise overview of the CDMS II experiment in Section 4.2.1. We then detail the procedure for estimating the  $^{32}\text{Si}$  background in Section 4.2.3. Finally, we conclude with a summary and the current status of the analysis in Section 4.3.

## 4.1 Motivation

### 4.1.1 Presence of $^{32}\text{Si}$ isotope in Silicon detectors

The single-crystal high-purity silicon is quite popular among the detector material used in experiments searching for DM. The production of silicon is vastly done from mining in the terrestrial environment.  $^{32}\text{Si}$  can be present in the source material used for silicon detectors

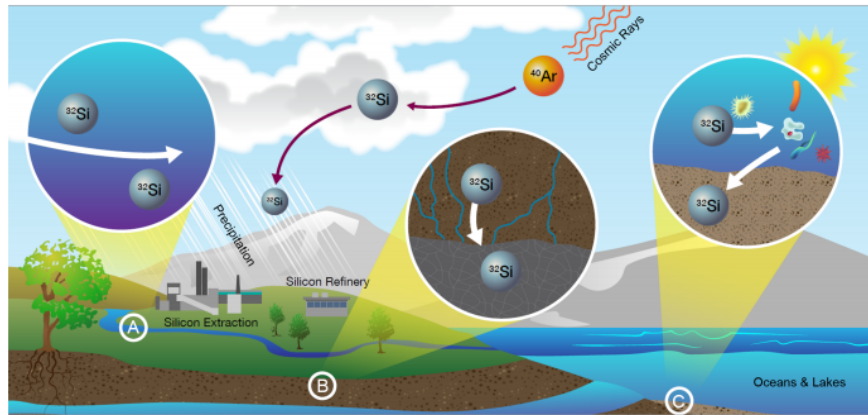


FIGURE 4.1: Cosmic rays interacting with  $^{40}\text{Ar}$  in the atmosphere create  $^{32}\text{Si}$ , which is transported to Earth through precipitation. This leads to the accumulation of  $^{32}\text{Si}$  in different ways into: A) streams and settling ponds used for silicon mining and refinement water; B) surface sands and near-surface silicon deposits; and C) oceans and lakes, where it can be carried by organisms and end up in sediments [5].

as  $^{32}\text{Si}$  is naturally found in the environment. It produced from the spallation of  $^{40}\text{Ar}$  by the cosmic rays in the Earth's atmosphere. These cosmogenically produced  $^{32}\text{Si}$  are then transported into the terrestrial environment via precipitation. It can then be accumulated in three different ways in the ore material. In Fig. 4.1, three different ways are shown as A, B and C and are also discussed below [5].

- A. Rainwater can carry  $^{32}\text{Si}$  into streams and ponds, which may then be utilized in the purification and processing of silicon crystals in industry.
- B.  $^{32}\text{Si}$  can also be carried to the surface sands (silica) or silicate rocks through precipitation, potentially serving as a source for silicon detectors.
- C.  $^{32}\text{Si}$  can mix into oceans and lakes. It is then transported into sediments by biological organisms.

$^{32}\text{Si}$  is found as an inherent impurity in Si detectors since their fabrication. It decays to  $^{32}\text{P}$  with half-lives of 153 years.  $^{32}\text{P}$  then beta decays to stable  $^{32}\text{S}$  and the half-lives is



14.27 days. These beta particles act as in-situ backgrounds for Si detectors.



The DAMIC collaboration reported their first measured specific radioactivity of  $^{32}\text{Si}$  in their Si detectors at  $80^{+110}_{-65}$  decays/kg-day [6]. The uncertainty on the estimated value is large. But their second measurement gave a rate of  $11.5 \pm 2.4$  decays/kg-day which is consistent within the errors of the previous value [7]. The reported activity variation is due to using different batches of Si detectors. So, the radioactivity level somewhat depends on the process or the source of Si from where the detectors are made. A more precise understanding is needed to measure the impurities in the detector material because there are not enough experiments done yet, and the ones that are done show different levels of contamination. Super Cryogenic Dark Matter Search SNOLAB (SuperCDMS SNOLAB) [8] which is the recent upgrade of CDMS II and SuperCDMS will use Si HV detectors and  $^{32}\text{Si}$  considered as a concerning background for this experiment. In the upcoming section we will understand the effect of  $^{32}\text{Si}$  background on sensitivity for the SuperCDMS SNOLAB experiment.

#### 4.1.2 Effect of $^{32}\text{Si}$ background on SuperCDMS SNOLAB sensitivity

The SuperCDMS SNOLAB is located in Sudbury, Ontario, Canada. In Chapter 2, we already discussed about SuperCDMS SNOLAB [8]. It will search for low mass DM using germanium (Ge) and silicon (Si) detectors. The detectors of each material will be of two types, high voltage (HV), and iZIP. The experiment site is  $\sim 2$  km underground which provides natural shielding from the high energy cosmic rays coming through the Earth's atmosphere.

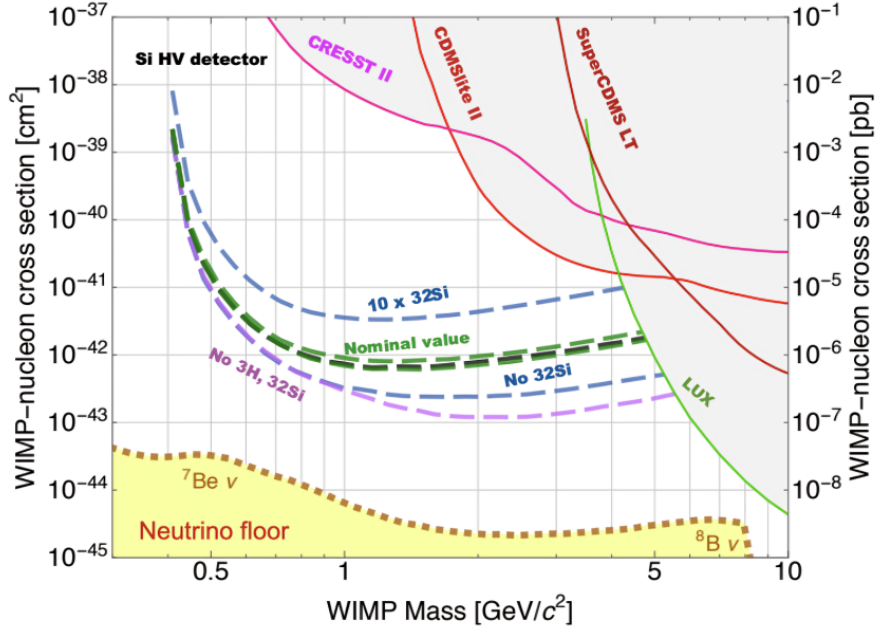


FIGURE 4.2: The projected sensitivity curves of the SuperCDMS SNOLAB experiment are shown in the DM-nucleon cross-section vs. DM mass parameter space for Si HV detector. The black dashed line represents the expected sensitivity using nominal values of  $^{32}\text{Si}$  and  $^3\text{H}$  in Si from literature. The blue dashed lines show sensitivity variations by adjusting the level of  $^{32}\text{Si}$  in Si HV from ten times its nominal value to zero. Similarly, the green dashed lines represent sensitivity variations by adjusting the level of  $^3\text{H}$  in Si from three times its nominal value to zero. The purple dashed line shows the sensitivity curve without the presence of any  $^3\text{H}$  and  $^{32}\text{Si}$  in the detector [8].

From what we have discussed in Section 2.1.2 of Chapter 2, we find that  $^{32}\text{Si}$  and  $^3\text{H}$  are the main sources of background in the Si HV detector (refer to Fig. 2.3(b)). Our main focus is on understanding the impact of  $^{32}\text{Si}$  background. Fig. 4.2 illustrates how variations in  $^{32}\text{Si}$  background affect the projected sensitivity of the SuperCDMS SNOLAB with Si detectors [8]. The black dashed line in Fig. 4.2 represents the expected sensitivity of the Si HV detector at SNOLAB in detecting DM with respect to the DM-nucleon cross section versus DM mass parameter space. This calculation relies on known production rates of  $^{32}\text{Si}$  in Si reported in existing literature. The blue dashed curve above the expected sensitivity projection depicts the sensitivity if we assume  $^{32}\text{Si}$  production to be 10 times

its standard value in literature. Conversely, the blue dashed curve below the expected sensitivity projection indicates the sensitivity of the Si detector in the absence of  $^{32}\text{Si}$  background. The purple dashed line shows the projected sensitivity assuming no  $^{32}\text{Si}$  or  $^3\text{H}$  background in Si. Figure 4.2 highlights the significance of precisely measuring the  $^{32}\text{Si}$  background rate in experiments employing Si detectors. This directly impacts the sensitivity of the experiments in detecting DM.

## 4.2 $^{32}\text{Si}$ background measurement for CDMS II

The CDMS experiment was one of the world's foremost direct dark matter search experiments. Its initial science run took place in 1996 at the Stanford Underground facilities (SUF) in California, USA. Since then, the experiment has undergone several upgrades. The CDMS run concluded in 2002, followed by the CDMS-II upgrade, which operated from 2003 to 2012 at the Soudan Underground Laboratory (SUL) in Minnesota. The subsequent upgrade was SuperCDMS, which ran from 2012 to 2015 at SUL in Soudan [9, 10]. These upgrades primarily focused on enhancing detector technology and payload, aiming to detect DM with a DM-nucleon cross-section of about  $10^{-42} \text{ cm}^2$  and a DM mass around  $8 \text{ GeV}/c^2$ . SuperCDMS SNOLAB represents the future of SuperCDMS, featuring significant enhancements in detector technology. Its science run is expected to commence in 2025. Our analysis utilizes CDMS-II data because this run employed the maximum number of Si detectors and provided sufficient statistical data for our analysis.

### 4.2.1 CDMS II experiment

The CDMS-II experiment took place at the SUL, situated 2341 feet underground on the 27th level of the mine. The surrounding rock provides an equivalent of 2090 meters

of water, shielding the experiment from cosmic rays. CDMS-II was deployed in stages, starting with an initial run (Run 118, October 2003 - January 2004) involving 6 detectors (1 tower) [11, 12]. This was followed by a subsequent run (Run 119, March 2004 - August 2004) utilizing 2 towers [13, 14], and finally, a series of six runs (Runs 123-128) with the complete payload of 5 towers [1, 15].

### Cryogenics

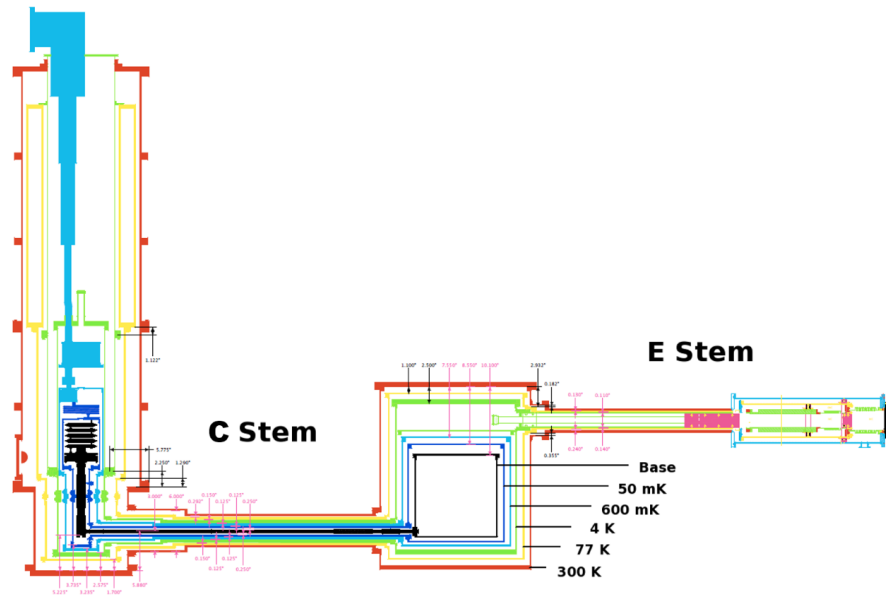


FIGURE 4.3: Diagram of the CDMS cooling setup with the dilution refrigerator and internal temperature levels were linked to the icebox via the C stem. The icebox contained six cans, maintained at different temperatures. The detector payload, although not visible, hung in the central can. Detector electronics were supplied from above the payload, connected at the 4 K stage through the E stem [16].

Figure 4.3 depicts the cross-sectional view of the icebox, fridge, and their connections [16]. The cryostat consisted of six cans at different temperatures (300 K, 77 K, 4 K, 600 mK, 50 mK, and 10 mK), connected via copper tubes to a Kelvinox 400-S dilution refrigerator. Nested tubes in the cold stem (C stem) penetrated the shielding, while read-out

cabling from detector electronics ran through nested tubes in the electronics stem (E stem). A Giffords-McMahon cryocooler on the E stem provided 1.5 W cooling power at 4 K which reduces live time loss during CDMS II experiments.

## Shielding

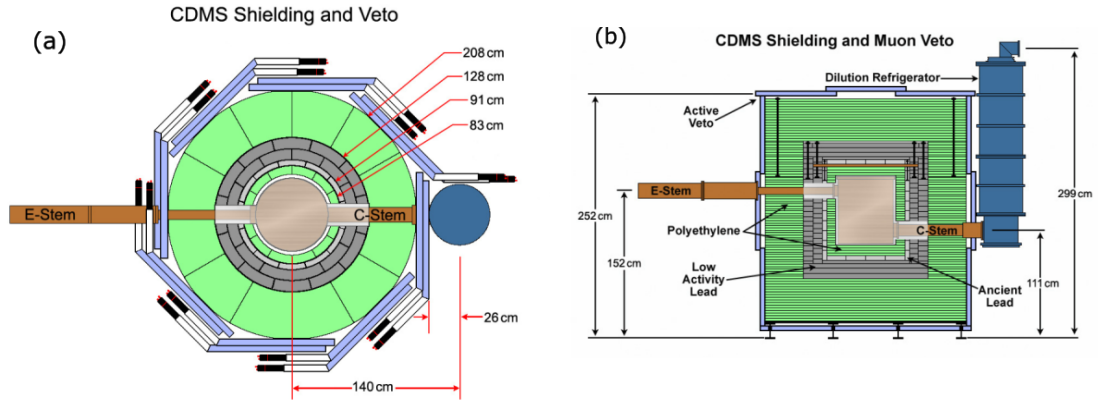


FIGURE 4.4: Diagrams showing the CDMS shielding viewed from above (a) and the side (b). The outer layer comprises muon veto scintillating panels (light blue) connected to photomultiplier tubes (white and black). Following layers include (from outermost to innermost): 40 cm of polyethylene (green), 18 cm of lead (dark grey), 4.5 cm of ancient lead (light grey), and 10 cm of polyethylene (green). The cryostat (light tan) provides an average of  $\sim 1.9$  cm of copper shielding. Also depicted are the E-stem and C-stem penetrations (brown) and the dilution refrigerator (dark blue) in relation to size and position [16].

The 713 m thick greenstone rock decreased the muon flux by a factor of  $5 \times 10^4$ . Despite this shielding, secondary particles from the remaining flux were still too high. An active muon veto layer, shown as blue rectangles with white photomultiplier tubes in Fig. 4.4, surrounded the experiment to further filter out cosmogenic backgrounds. Inside the veto panels, there were layers of neutron and gamma shielding made from 40 cm thick polyethylene. Electromagnetic particles, mainly gamma rays, were blocked by two layers of lead, providing 22.5 cm of shielding, with the inner 4.5 cm made of ancient lead, depleted of the isotope  $^{210}\text{Pb}$ , to minimize bremsstrahlung effects. A layer of polyethylene between

the lead shield and the cryostat offered 10 cm of neutron shielding. A thin mu-metal shield blocked magnetic fields that could interfere with detector electronics. The air layer between the mu-metal shield and the outermost cryostat was purged with "old air" to reduce radioactive  $^{222}\text{Rn}$  content, stored for at least two weeks for decay. The icebox cans added approximately 1.9 cm of additional gamma and beta shielding, with each can being 0.125 inches thick [16].

### Data type

A 'run' refers to a period when the cryogenics remain stable for data collection. Data sets, crucial for this thesis, spanned the final CDMS II runs, runs 125–128, known collectively as c58, conducted from 2006 to 2008. The primary data unit was a 'series', its length determined by the detector's ability to maintain adequate neutralization for capturing the charge signal. Neutralization was compromised after about 12 hours for CDMS-II [16].

Three main types of data were collected during CDMS II, two utilizing radioactive sources:

1. **Low-background/WIMP search:** These data, essential for determining scientific outcomes, searched for DM recoils amidst ambient background and signal events. This mode was predominantly used to maximize exposure to WIMP searches.
2.  **$^{133}\text{Ba}$  calibration:** Here, two  $^{133}\text{Ba}$  sources were positioned in source tubes extending along the E and C stems, ending at the cryostat's edge, within the polyethylene and lead shields. Decay of  $^{133}\text{Ba}$  to  $^{133}\text{Cs}$  via  $\gamma$  and conversion electron channels provided prominent energy peaks (356.0, 302.8, 383.8 and 276.4 keV) used for calibration and defining the electronrecoil (ER) band.

3.  **$^{252}\text{Cf}$  calibration:** In this data type, a single  $^{252}\text{Cf}$  source was alternately inserted between the source tubes. Primarily decaying by  $\alpha$  emission,  $^{252}\text{Cf}$  also underwent spontaneous fission, producing neutrons (with a most probable energy of  $\sim 1$  MeV) used for nuclear recoil (NR) calibration to define the NR band in the yield versus recoil energy plane.  $^{252}\text{Cf}$  data were sporadically collected to prevent neutron activation of the crystals.

### Detectors and towers

CDMS utilizes Si and Ge detectors for their sensitivity in searching for both low-mass and high-mass WIMPs. The detectors used in CDMS II are called Z-sensitive Ionization and Phonon (oZIP) detectors. Fig. 4.5(a) (left) displays a schematic of a ZIP detector, which is roughly cylindrical with four phonon sensors on one side and two charge channels on the other. Picture of an actual detector from a tower is shown in the right of Fig. 4.5(a). More specifications can be found in Table 4.1.

TABLE 4.1: CDMS-II detectors

Detector	Ge	Si
Number of detectors	19	11
Dimensions	Diameter: 7.6 cm, Width: 1 cm	Diameter: 7.6 cm, Width: 1 cm
Mass	$\sim 250$ g	$\sim 100$ g
Bias Voltage	3 V	4 V
Channels	Phonon: 4, Charge: 2	Phonon: 4, Charge: 2

These 30 detectors are arranged into five towers [T1-T5], each containing 6 detectors (shown on the left side of Fig. 4.5(b)). In the figure, cyan represents Ge detectors and yellow represents Si detectors. The standard naming convention for identifying a ZIP detector is T#Z, where # indicates the tower number and Z indicates the ZIP number in that tower.

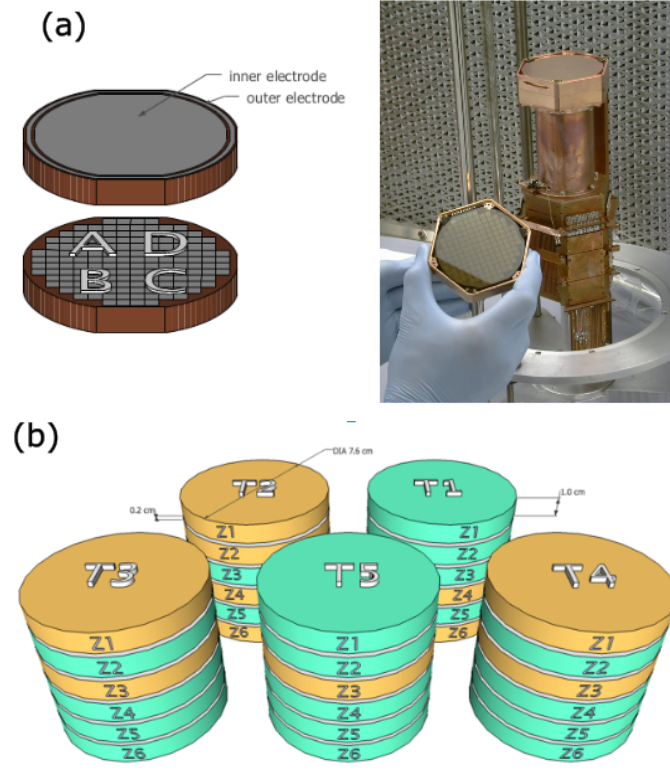


FIGURE 4.5: (a) Shows the type and position of ionization and phonon read-out channels for the oZIP detector (left). On the right, there is an image of a person holding an actual oZIP detector from a tower. (b) Illustrates the arrangement of ZIPs in CDMS-II. The detectors are identified by tower (T1-T5) and position within the tower (Z1-Z6). Different colors represent different types of detectors: aqua for germanium and beige for silicon. This tower arrangement into two rows reflects how the towers were positioned in the icebox [16, 17].

For example, T3Z4 refers to the 4th ZIP in tower 3, also known as zip16. In this analysis, we utilize the total charge energy estimator from CDMS-II to study the decay rate of  $^{32}\text{Si}$ . The total phonon energy estimator was not chosen for this analysis because the phonon channels of some Si detectors saturate between energies of 500-1500 keV.

### Ionization signal detection

In this section, we focus solely on the ionization signal measurement in CDMS-II detectors. When a particle enters a ZIP detector, it releases energy, generating  $e^-/h^+$  pairs. These



pairs are then accelerated by an applied bias towards the electrodes, depending on their polarity. The band gap of Ge/Si, which is around 0.74 / 1.17 eV at approximately 0 K [18], requires much more energy, about 3.0 / 3.8 eV [19], to create a single  $e^-/h^+$  pair in cryogenic Ge/Si. Consequently, only 25-30% of the deposited energy is used to surpass the band gap. Additionally, if the initially created primary electrons possess enough momentum, they can generate secondary  $e^-/h^+$  pairs in a cascade process, forming a “space charge cloud” near the deposition site. At low temperatures, carriers may be attracted to impurities in the crystal instead of the electrodes, trapping charges and reducing the field between the electrodes. To mitigate this effect, LEDs are periodically flashed (with a “bias flash time” of around 3000 s).

There exists a small gap between the electrodes and the detector’s surfaces. Consequently, the electrodes primarily measure image charges rather than the liberated charges themselves. In CDMS, a thin layer of amorphous silicon is placed in this region to minimize charge back-diffusion. The image charge  $Q$  created in the electrodes due to the drifting of charge  $q$  in the detector is determined by the Shockley-Ramo Theorem [20] as follows:

$$Q = qV(x) \quad (4.2)$$

where  $V(x)$  represents the “weighting” (or Ramo) potential. The ionization signal is processed through a Junction gate Field-Effect Transistor (JFET) charge amplifier [16], where the induced charge quickly accumulates into a feedback capacitor, resulting in a voltage spike at the output. This voltage then discharges through a feedback resistor with a time constant. A large biasing resistor is used to prevent current shorting, and a coupling capacitor shields the feedback loop from the biasing source. During the rapid rising edge, certain resistors can be ignored, leading to a voltage proportional to the induced charge. The shape of this edge depends on how charges propagate in the detector, occurring

within nanoseconds. This rising edge is recorded almost instantaneously compared to the digitization rate. The amplitude of the peak, directly linked to the induced charge, is the main variable. For oZIPs, the signal is digitized at a rate of 1.25 MHz, with 2048 samples

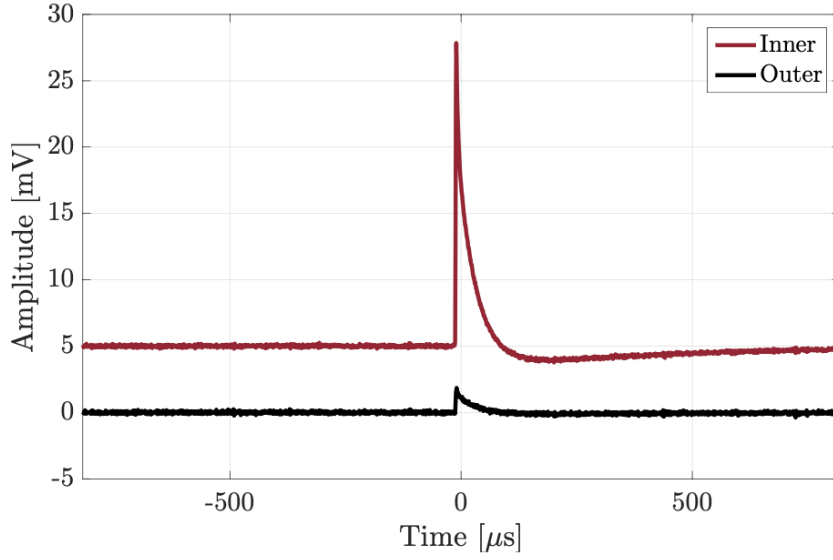


FIGURE 4.6: Example of ionization pulses from both inner and outer sides for a sample event with a recoil energy of around 511 keV. The pulses from the inner channel is moved up by 5 mV for better visibility [16].

stored per event [16]. An example of ionization pulses from a single side is depicted in Fig. 4.6, with a recoil energy of around 511 keV, primarily occurring in the inner channel. If  $N_{e^-/h^+}$  represents the number of  $e^-/h^+$  pairs, then ionization energy is the energy required to create these carriers, assuming 100% charge collection efficiency of charge channels.

$$E_Q = N_{e/h} \epsilon_\gamma \quad (4.3)$$

Assuming full collection efficiency for an electron recoil (ER) event, the initial recoil energy is:

$$E_r = E_Q \quad (4.4)$$

However, for nuclear recoils (NRs), we use a quantity called the “Ionization yield” ( $Y(E_r)$ ), which is defined as:

$$Y(E_r) = \frac{E_Q}{E_r} = \frac{\text{Ionization Energy}}{\text{True Recoil Energy}} \quad (4.5)$$

When ERs have complete charge collection efficiency,  $Y(E_r) = 1$ , but for NRs or ERs with incomplete charge collection efficiency,  $Y(E_r) < 1$ . This measured yield helps distinguish between NRs and ERs. This distinction is crucial in iZIP mode but is lost in high voltage due to Luke amplification.

### 4.2.2 Analysis flowchart

Flowchart of  $^{32}\text{Si}$  background analysis is shown in the Fig. 4.7 using data from combined runs 125-128 of CDMS-II. Our analysis consists of three main parts: data selection, modeling the beta decay spectrum of  $^{32}\text{Si}$  and  $^{32}\text{P}$ , and modeling other backgrounds. These inputs are used to estimate the decay rate of  $^{32}\text{Si}$  using the profile likelihood method. Various data selection cuts are applied to the WIMP search data to eliminate unwanted events, with cut efficiencies calculated as a function of charge energy. Other backgrounds for the analysis are identified and simulated, and the simulated spectrum is fitted with the data to get the contamination level. The Betashape software generates the  $^{32}\text{Si}$  and  $^{32}\text{P}$  beta decay spectrum using experimental data from nuclear data base. Finally, a log-likelihood function will be used to calculate the  $^{32}\text{Si}$  decay rate in terms of decays/kg-days.

### 4.2.3 Data selection criteria

In CDMS II, there were a total of 11 Si detectors: T1Z4, T1Z6, T2Z1, T2Z2, T2Z4, T2Z6, T3Z1, T3Z3, T4Z1, T4Z3, and T5Z3. The total charge energy (qsum) is calculated as the sum of inner charge (qi) and outer charge (qo) for each event, considering all detectors in each run and combining data from all four runs. Initially, the dataset contains 7213055

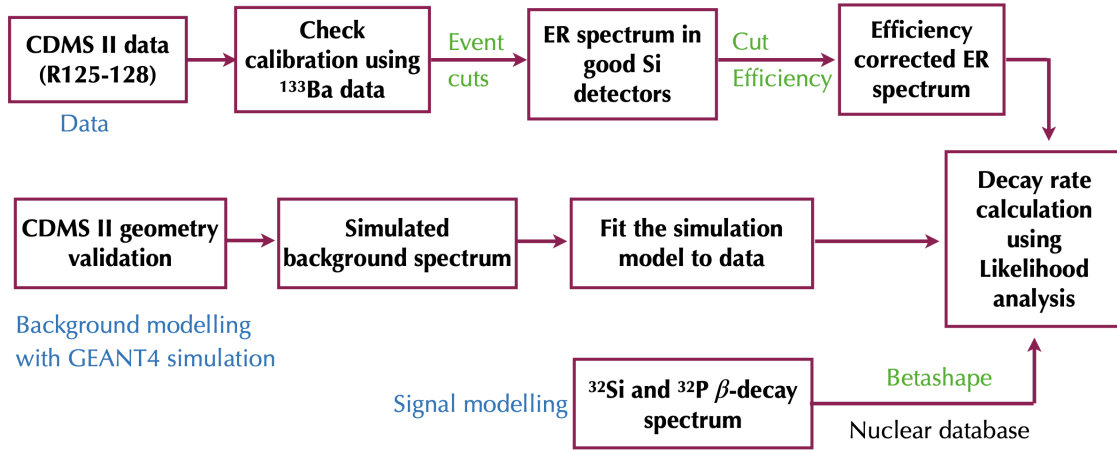


FIGURE 4.7: Analysis flowchart describing the steps for estimation of  $^{32}\text{Si}$  decay rate in Si detectors for CDMS-II experiment.

events before any cuts are applied. The data may contain unwanted events like glitches, pulses with baseline fluctuations, events not producing full Luke gain, or periods with improper hardware settings or data acquisition (DAQ) issues. In the following section, we briefly discuss the physics cuts used to exclude these events. After applying these exclusions, only data collected by the good Si detectors is considered for this analysis.

### Cut lists

The list of cuts used for this analysis is shown in Fig. 4.8. They are divided into two categories: Basic cuts and Quality cuts. Basic cuts ensure stable detector operating conditions and filter out events with hardware or data acquisition (DAQ) issues. Quality cuts are tailored specifically for this analysis to optimize the selection of data.

### Basic cuts

In this section, we discuss basic cuts used in this analysis. These cuts were applied to all 11 Si detectors for each of the four total runs: r125, r126, r127, and r128.

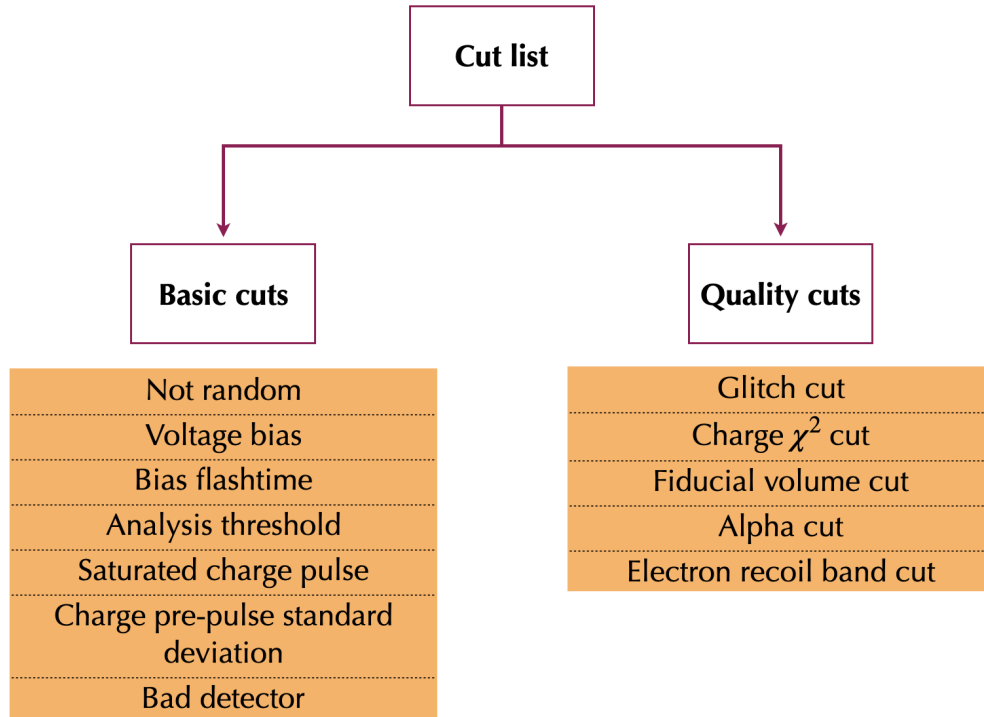


FIGURE 4.8: Tree diagram showing the different cuts applied in the analysis of  $^{32}\text{Si}$  background estimation. The cuts are grouped into two categories: (1) Basic cuts and (2) Quality cuts.

1. **Not Random:** There are three types of trigger condition in the CDMS-II experiment.

- **Global trigger:** If any of the detectors encounters a pulse above trigger threshold all the detectors will be readout. Condition is:  $\text{EventCategory} = 0$ .
- **Selective trigger:** A specific detector of interest encounters a pulse above trigger threshold and will take readout. Condition is:  $\text{EventCategory} = 6$ .
- **Random trigger:** Triggers randomly readout regardless of the type of pulse. This is useful for noise analysis. Condition is:  $\text{EventCategory} = 1$ .

In this analysis, we use all the events which are not triggered randomly. The cut is set as:

$$\boxed{\text{EventCategory} \neq 1} \quad (4.6)$$

2. **Voltage bias:** In CDMS-II experiment, the bias voltage applied to the Si detectors is 4V. This cut removes events when the detectors are not biased at 4V. Such a cut is important for this analysis because the bias voltage is a parameter in the conversion from nuclear recoil energy to phonon energy. So inaccuracies in the assumed bias voltage will lead to an incorrect yield determination. Cut is set on the two variables, charge inner bias (QIbias) and charge outer bias(QObias).

$$3.9 < \text{QIbias} < 4.1 \ \& \ 3.9 < \text{QObias} < 4.1 \quad (4.7)$$

3. **Bias Flashtime:** Each data-taking run nominally begins by flashing infrared LED light through the detector, which neutralizes the detector crystal i.e. liberates charges that were trapped in crystal impurities. If the detector is not neutralized,  $e^-/h^+$  pairs produced by a recoil event may not be fully collected, which results in a reduced ionization yield estimate. The time of the LED flash is recorded by the DAQ and stored in a BiasFlashTime variable. We set a cut on the BiasFlashTime to remove any events that were recorded after the nominal run length following the most recent detector flash, which could happen if the detector was for some reason not flashed before the next run.

$$\text{Bias Flashtime} < 20 \text{ hours} \quad (4.8)$$

4. **Analysis threshold:** The average energy of the  $^{32}\text{Si}$  beta decay spectrum is 69 keV. We set our lower analysis threshold cut at 50 keV, which is well below the average energy of  $^{32}\text{Si}$  beta decay. For our higher analysis threshold cut, we set it at 3000 keV, well above the  $^{32}\text{P}$  endpoint energy of 1710 keV. This higher threshold allows us to observe the  $^{208}\text{Tl}$  compton edge at 2614 keV, which can be used to calibrate the charge energy scale at higher energies. This cut is defined as:

$$50 < \text{qsum} < 3000 \quad (4.9)$$

5. **Saturated charge pulse:** Saturated charge pulse cut or Qsat cut select events that have saturated charge pulses. There are two variables for inner and outer charge channels, QIsat and QOsat that store events with 1 or more saturated digitizer samples in the charge pulses. So, for saturated charge pulses:  $\text{QIsat} > 0$  and  $\text{QOsat} > 0$ . To reject saturated pulses we set the cut as:

$$\boxed{\text{QIsat} == 0 \text{ QOsat} == 0} \quad (4.10)$$

6. **Charge Pre-pulse standard deviation:** The motivation of this cut is to remove pile-up events and events with high baseline noise primarily due to microphonic pickup of the vibrations induced by the cryocooler. Pre-trigger charge baseline standard deviation is stored for each charge channel in Q\*std where \* can be [I, O] for the charge inner and outer channels. We set the cut on Qstd distribution for a run which is then fit to a Gaussian with red curve shown in the Fig. 4.9, and any events with pre-pulse standard deviations more than  $4\sigma$  from the distribution mean ( $\mu$ ) are rejected.

$$\boxed{0 < \text{QIstd} < \mu + 4\sigma \ \& \ 0 < \text{QOstd} < \mu + 4\sigma} \quad (4.11)$$

7. **Bad detector:** In CDMS II c58 WIMP analysis some of the Si detectors from certain runs were tagged as bad detectors. We reinvestigated the previously tagged bad detectors for our analysis. We discarded only those detectors from our analysis which we found as bad after our investigation. The following detectors are tagged as bad due to poor neutralization:

- zip6 detector for r126, 127 and 128.
- zip4 detector for r126 and 128.
- zip12 detector for r126 and 127.

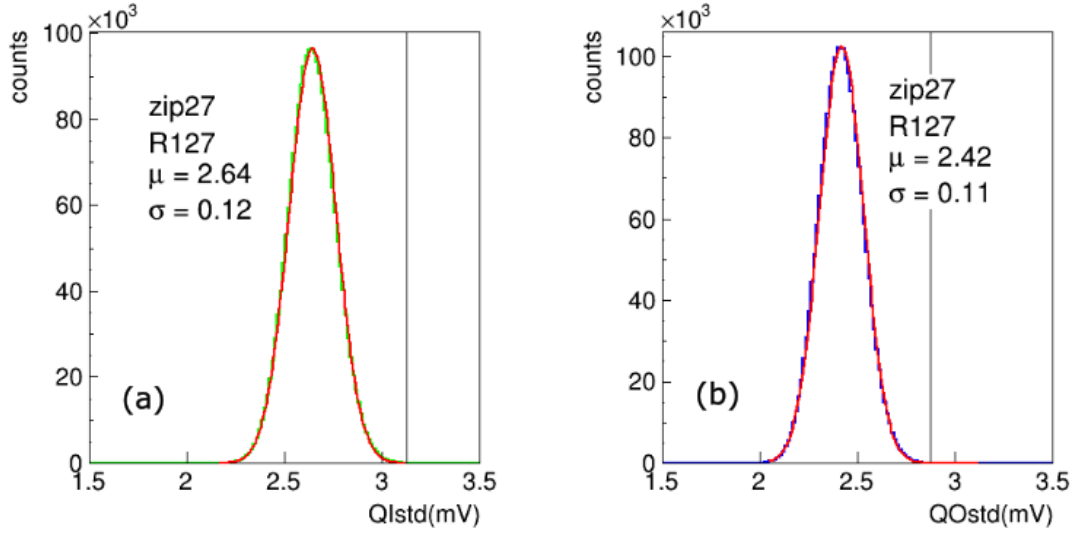


FIGURE 4.9: (a) and (b) show the distributions of QIstd (green curve) and QOstd (blue curve) for the zip27 detector in r125, respectively. The red curve shows the fitted Gaussian function. The mean ( $\mu$ ) and standard deviation ( $\sigma$ ) of the fitted Gaussian are indicated on the plot. The black solid line marks the position of the charge pre-pulse standard deviation cut on the QIstd and QOstd distributions.

### Quality cuts

In this section, we discuss quality cuts that have been specifically tailored for this analysis. After applying all the basic cuts, each of the quality cuts is then applied one after the other. Events that meet the criteria of individual detector cuts are chosen and combined to create a spectrum for each run.

1. **Glitch cut:** Electronic glitches can cause a nominally normal-looking global trigger to be issued. These glitches are believed to be the result of coherent noise on the QET bias lines, which can briefly heat the QETs and cause the phonon triggers to fire. The glitches are identifiable by comparing the number of phonon triggers (ntrigp) and the number of charge triggers (ntrigq) that were issued. The glitch events are defined as:

$$\boxed{(\text{ntrigp} - \text{ntrigq}) > 4 \parallel (\text{ntrigp} = 3 \ \& \ \text{ntrigq} = 0)} \quad (4.12)$$



Figure 4.10(a) shows the graphic representation of the number of charge and phonon triggers in r126 for zip8 detector while Fig. 4.10(b) demonstrates the removal of events above the cut, indicated by the black solid line.

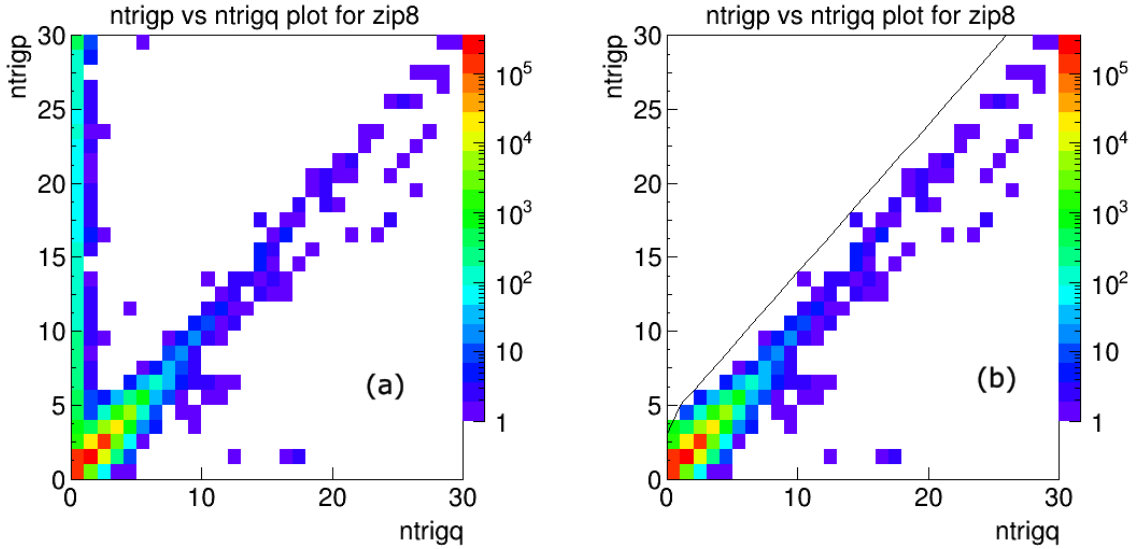


FIGURE 4.10: (a) A graphic representation of the number of charge and phonon triggers in r128 data. (b) The glitch cut removes events above the black line.

2. **Charge  $\chi^2$  cut:** The Chi-square ( $\chi^2$ ) value (QSOFchisq) measures how well the optimal filter template matches the ionization pulse, providing insight into the quality of event reconstruction for each event. This cut is particularly sensitive to "pileup" events and also remove low energy noises, where more than one recoil occurs within the recorded trace window after a trigger. To compute this cut, the data is first grouped into several energy bins. Within each bin, the  $\chi^2$  distribution is fitted with a Gaussian curve. Next, a quadratic function is fitted to the 3.5 standard deviation ( $\sigma$ ) points in the four energy bins to define the cut. The definition of the cut is:

$$\chi^2 < C_1 \cdot \text{qsum}^2 + C_2 \quad (4.13)$$

Figure 4.11(a) shows the Chi-square (QSOFchisq) values plotted against qsum in r125 for the zip19 detector. All events above the black solid line are removed from the dataset.

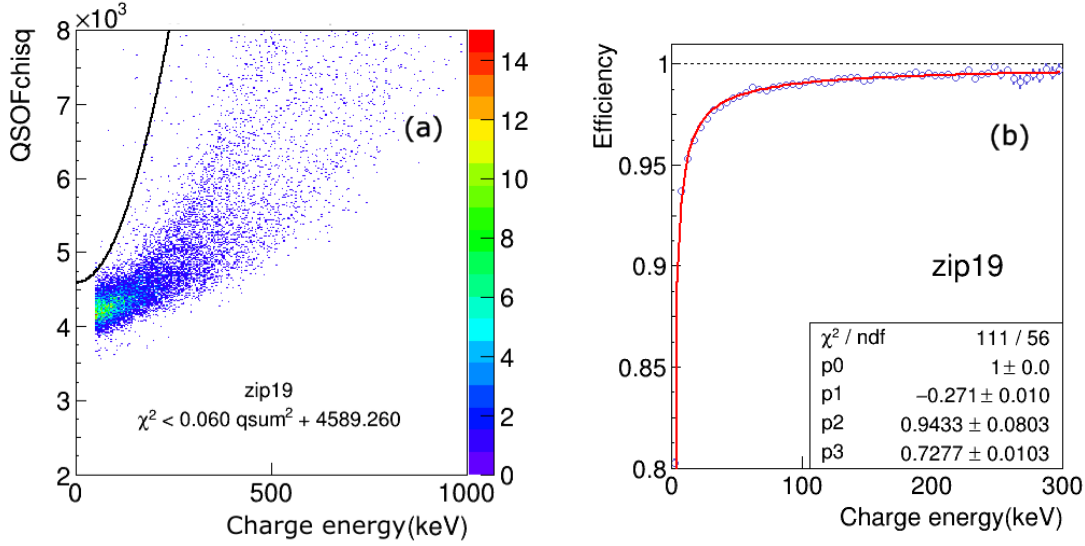


FIGURE 4.11: (a) Correlation between charge  $\chi^2$  and charge energy is shown for zip19 in r125. Black solid line shows the cut position. (b) Fit to the  $\chi^2$  cut efficiencies as a function of energy for zip19.

- **Efficiency:** We use  $^{133}\text{Ba}$  calibration data to determine the cut efficiency. This dataset is chosen because it mainly consists of good pulses, providing reliable signal events. We apply all the basic cuts and the Glitch cut to this dataset, and then calculate the efficiency using the formula:

$$\text{Efficiency} = \frac{\text{Number of events with } \chi^2 \text{ cut}}{\text{Number of event without } \chi^2 \text{ cut}} \quad (4.14)$$

Figure 4.11(b) displays the efficiency of the  $\chi^2$  cut as a function of charge energy. The charge energy of  $^{133}\text{Ba}$  data ends around 400 keV. We fit the data points in the charge energy range up to 300 keV and extrapolate the fitted function up to 3000 keV, which is our upper analysis threshold. The fit function

is expressed as:  $y(x) = a + b/(x - c)^d$ . During the fitting process, we set the parameter  $a$  to 1 to ensure that the efficiency never exceeds 1.

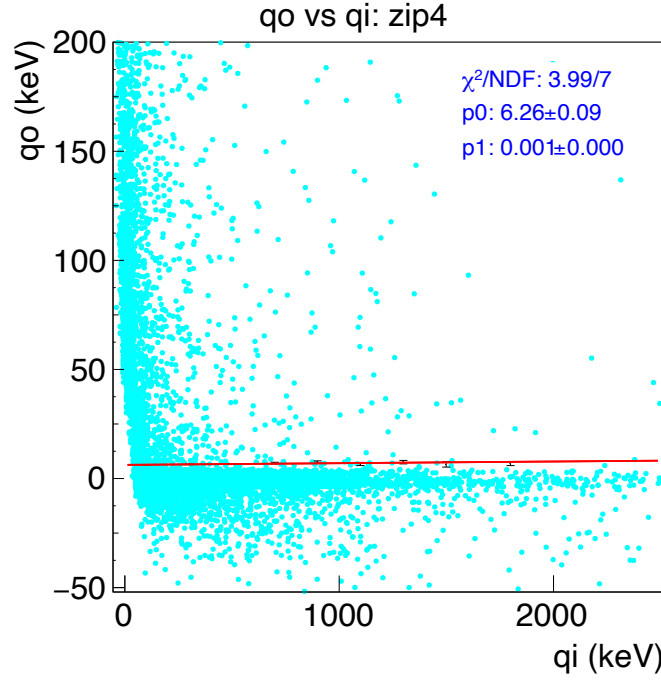


FIGURE 4.12: FV cut on  $q_i$  vs  $q_o$  parameter space is shown. Red solid line shows the cut position.

3. **Fiducial volume cut:** Events occurring at the outer edge of the detector are usually excluded from analysis because they are close to the side-walls, where the electric field might not be uniform, affecting charge collection. This cut removes these outermost events detected by the outer charge channels. After applying basic cuts, glitch cuts, and the  $\chi^2$  cut, we plot a distribution of outer charge ( $q_o$ ) versus inner charge ( $q_i$ ) in Fig. 4.12. Gaussian fits are used to determine the mean+ $3\sigma$  point for  $q_o$  distributions in different  $q_i$  intervals (indicated by black markers, errors are from the fit). Fig. 4.13 displays the  $q_o$  distribution in various  $q_i$  intervals fitted with a Gaussian. A straight line (red line) is fitted to these points in Fig. 4.12, and all events

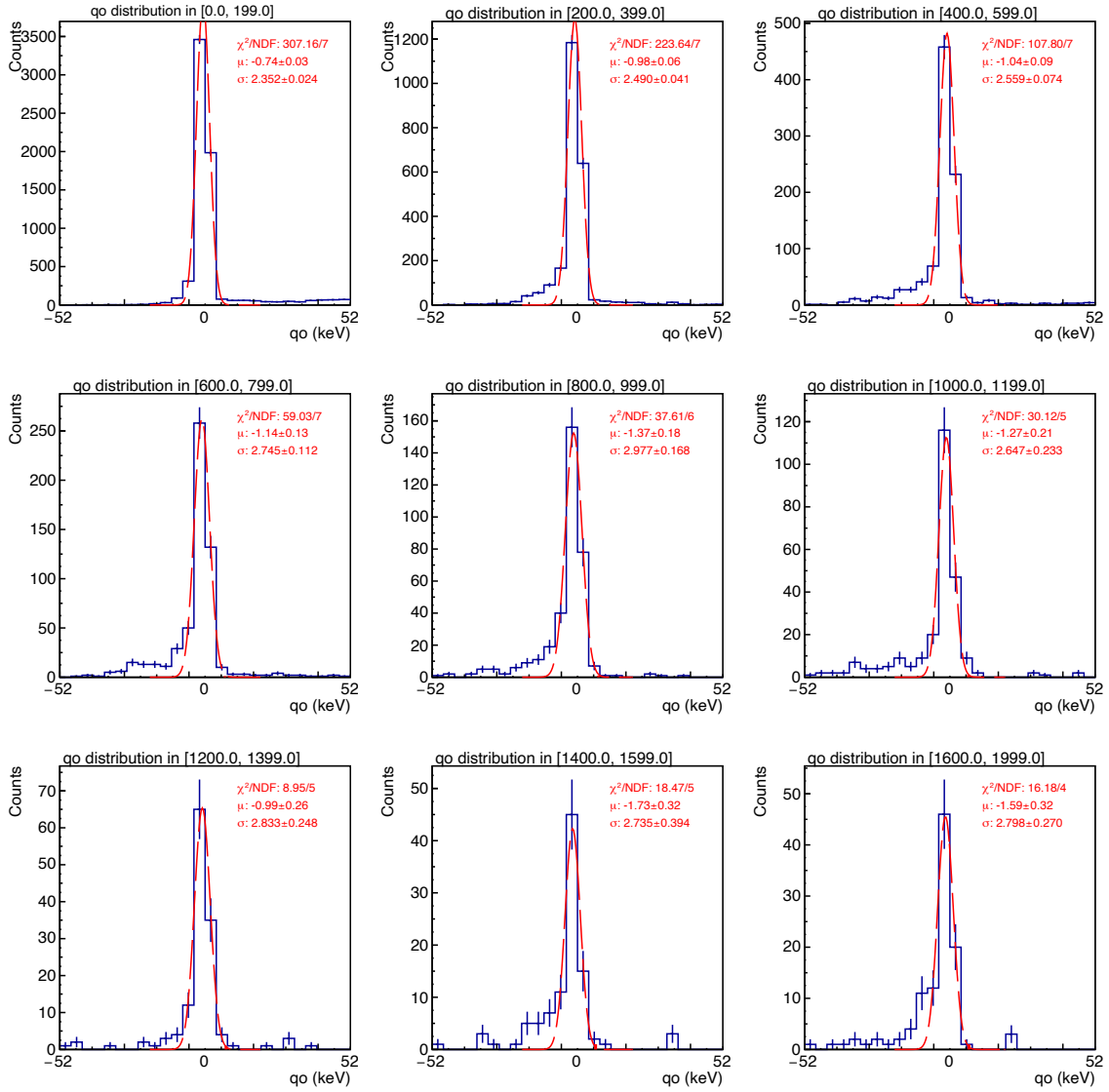


FIGURE 4.13: qo distribution for different energy ranges of energies are shown for zip4 for r125.

above the red line are removed. The cut is defined as:

$$q_o \leq p_0 + p_1 \cdot q_i \quad (4.15)$$

- **Efficiency:** To calculate the FV cut efficiency, we need to consider the phonon signal together with the charge signal because the phonon signal provides a more accurate measure of deposited energy. The phonon collection is relatively

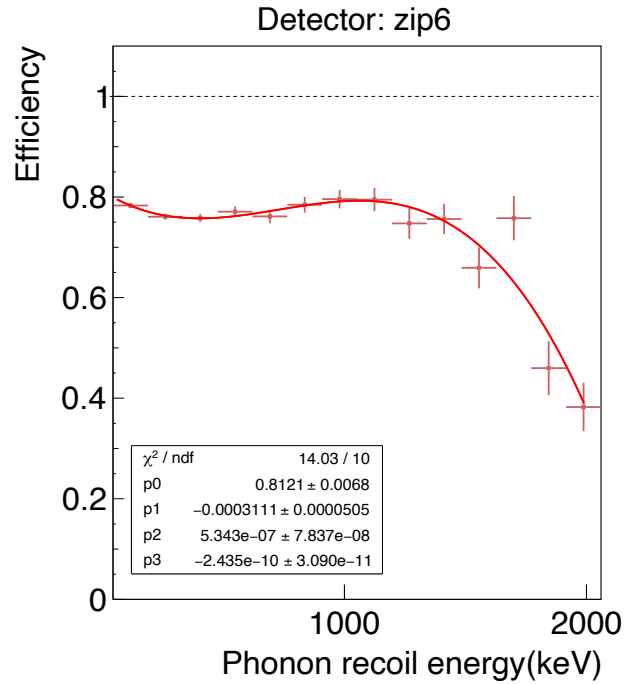


FIGURE 4.14: FV cut efficiencies as a function of phonon recoil energy for zip6 is shown. A polynomial3 function is fitted with the data points.

consistent throughout the detector, unlike the charge signal. By subtracting the NTL contribution from the total phonon signal we obtain a more accurate representation of deposited energy. After applying basic cuts and removing pile-up events, we calculate the efficiency as a function of phonon recoil energy using Eq. 4.14. Figure 4.14 shows the FV cut efficiency as a function of phonon recoil energy which is  $\sim 81\%$  for zip6 detector in r125. A decrease in efficiency is seen at higher energies due to the multiple scatter particles within a single detector. These events can deposit some of their energy in the outer guard ring, causing them to not pass the FV cut.

4. **Alpha cut:** Alpha particles could be a background in our analysis. Alphas of energy around  $\sim 5$  MeV are coming from the decay chain of  $^{222}\text{Rn}$  present in detector housing.

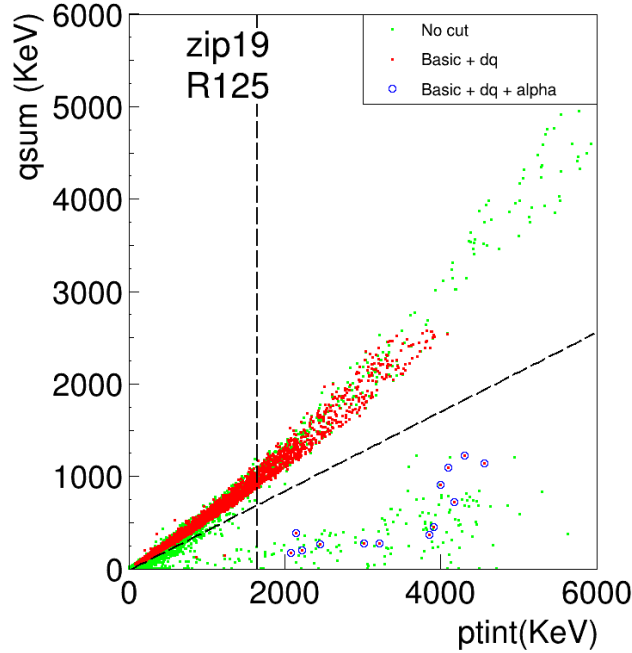


FIGURE 4.15: Alpha cut applied to the parameter space of charge energy (qsum) versus total integrated phonon energy (ptint). The green dots represent events without any cuts, the red dots show events with basic and quality cuts, and the blue open-circle markers denote events with basic, quality, and alpha cuts. The black dotted lines indicate the positions of the cuts where alpha-tagged events are depicted as blue open-circle markers.

It interacts with the nucleus and create a Nuclear Recoil. CDMS II data suggest that alpha events are populated at high energy range (MeV) in our integrated total phonon energy distribution. Figure 4.15 shows charge energy (qsum) vs integrated total phonon energy (ptint) distribution where we can see two different band for ER and NR events. Alphas are expected to lie in the NR band but some alpha events can transit from NR and to ER band as it induces more charge energy than a neutron or any other particles. Also, due to the early saturation of the detectors,  $\sim 5$  MeV alpha events can be populated at lower ptint energy. As our analysis range is upto  $\sim 3$  MeV, we need to identify alphas in our data and remove it. To identify alpha events, the following cut has been set in charge energy (qsum) and total integrated phonon

energy (ptint) parameter space.

$$q_{\text{sum}} < A_1 \cdot \text{ptint}^2 + B_1 \cdot \text{ptint} + C_1 \quad (4.16)$$

$$\text{ptint} > C_2 \quad (4.17)$$

Where  $A_1$ ,  $B_1$ , and  $C_1$  values are determined separately for each detector and for all four runs to efficiently select alphas while minimizing ER events. We select NR events by taking the  $3\sigma$  lower bound from the mean of the ER band and fitting it with a polynomial (black dotted curve seen in Fig. 4.15). The parameter values of this fitted polynomial provide the values of  $A_1$ ,  $B_1$ , and  $C_1$ . After applying all the basic, quality, and cut condition defined in Eq. 4.16, we set another cut (defined in Eq. 4.17) on ptint (black dotted vertical line as seen in Fig. 4.15) to tag alpha events in the NR band. To determine the  $C_2$  values, we take the  $3\sigma$  lower bound from the mean of tagged NR events (blue circle) distribution.

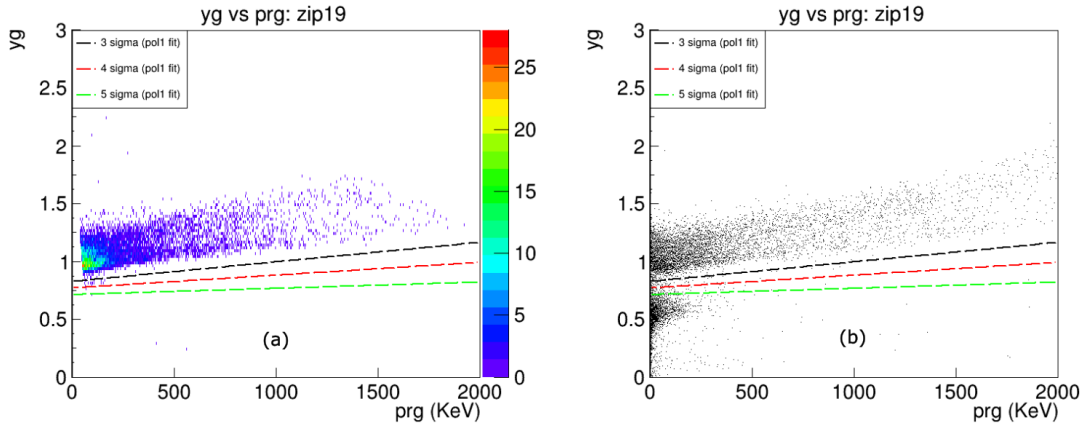


FIGURE 4.16: (a) Events in yield (yg) vs phonon recoil energy (prg) parameter space is shown. Black, red and green dashed lines represent  $3\sigma$ ,  $4\sigma$  and  $5\sigma$  ER cut. (b) Those above mentioned ER cuts position is shown in  $^{252}\text{Cf}$  data.

**5. Electron recoil band cut:** Since our analysis focuses on beta decay events, which are ER events, we need a cut to select only ER events and reject NR events. This

cut is established in the yield (yg) versus phonon recoil energy (prg) plane. After applying all basic cuts, charge  $\chi^2$  cut, glitch cut, and FV cut, we plot yg against prg and can be seen in Fig. 4.16(a). The yg distributions in various prg intervals are fitted with Gaussian to determine the corresponding  $3\sigma$  (black line),  $4\sigma$  (red line), and  $5\sigma$  (green line) lower bounds from their means. The cut definition used is:

$$\boxed{yg \geq s_0 + s_1 \cdot prg} \quad (4.18)$$

To select the ER band cut among the  $3\sigma$ ,  $4\sigma$ , or  $5\sigma$  lower bounds, we cross-check all cut positions using <sup>252</sup>Cf data (see Fig. 4.16(b)). We find that for most detectors, the  $4\sigma$  and  $5\sigma$  lower bounds overlap with the NR band. Therefore, for our analysis, we choose the  $3\sigma$  lower bound value as the ER band cut. The efficiency of this cut is 100%.

#### 4.2.4 Data spectrum

After applying these basic and data quality cuts, the total charge distribution for all good Si detectors is displayed in Fig. 4.17. The figure illustrates the co-added charge distributions with no cut, with basic cuts, and with both basic cuts and data quality cuts. Even after applying all the cuts, the number of events remaining is 188797 out of 7213055, which represents only about 3% of the total events. The black and red dotted lines indicate the end-point energies of <sup>32</sup>Si and <sup>32</sup>P, respectively. Additionally, the linearity of the energy scale is verified up to 2300 keV using calibration points from <sup>133</sup>Ba at 356 keV, <sup>40</sup>K compton edge at 1240 keV, and <sup>208</sup>Tl compton edge at 2381 keV.



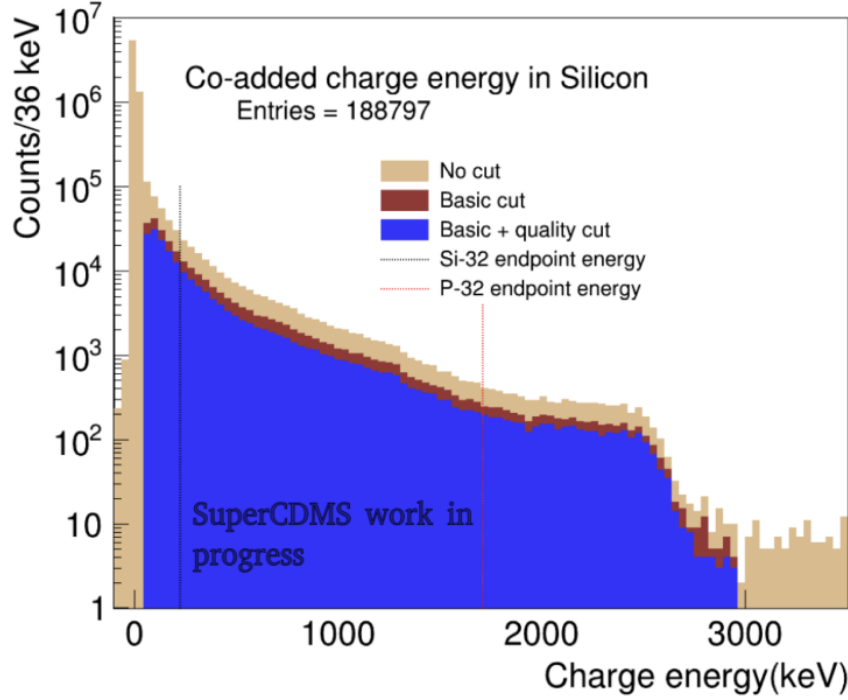


FIGURE 4.17: Combined charge distribution from all good Si detectors after applying all basic and data quality cuts, comprising a total of 188797 events.

#### 4.2.5 Detector resolution

In CDMS-II, charge energy scales and resolution in Si detector have been studied using  $^{133}\text{Ba}$  calibration data upto 350 keV.  $^{133}\text{Ba}$  gamma source has spectral lines at 27 (7%), 303 (18%), 356 (62%), and 384 (9%) keV. In Ge detectors these peaks are clearly visible. While in Si, due to their low stopping power, these peaks are either not visible or resolved. Therefore, charge energy scale for Si detector is calibrated using shared 356 keV events with the adjacent Ge detectors and hence the resolution is estimated.

The total charge energy resolution in a detector can be described by [16],

$$\sigma_T = \sqrt{\sigma_{BR}^2 + \sigma_F^2 + \sigma_{PD}^2} \quad (4.19)$$

where,

1.  $\sigma_{BR}$  is the baseline resolution of the detector due to the electronics noise and can be determined from the width of the noise distribution of randomly triggered events taken before and after of a run. It is independent of the energy. A detailed discussion can be found in section 4.2.5.

$$\sigma_{BR} = A_1 \quad (4.20)$$

2.  $\sigma_F$  term comes due to the Fano statistics which corresponds to Fano broadening [21]. If there are  $N$  number of  $e^-/h^+$  pairs produced in an interaction, the variance of  $N$  is  $\sigma_N^2 = FN$ , where  $F$  is the Fano factor and  $N = E/\epsilon_\gamma$  since  $\epsilon_\gamma$  is the average energy to create one  $e^-/h^+$  pair.

$$\sigma_F^2(E) = \sigma_N^2 \epsilon_\gamma^2 = FN \epsilon_\gamma^2 = F \epsilon_\gamma E \quad (4.21)$$

$$\sigma_F(E) = A_2 \sqrt{E} \quad (4.22)$$

$$A_2 = F \epsilon_\gamma \quad (4.23)$$

3.  $\sigma_{PD}$  corresponds to all other broadening effects including position dependence which is assumed to be linear with energy.

$$\sigma_{PD} = A_3 E \quad (4.24)$$

Plugging the Eq. 4.20, Eq. 4.21 and Eq. 4.24 into Eq. 4.19 gives a general resolution model as a function of energy described below:

$$\sigma_T = \sqrt{A_1^2 + A_2^2 E + A_3^2 E^2} \quad (4.25)$$

So, the overall resolution model involves three parameters:  $A_1$ ,  $A_2$ , and  $A_3$ . The parameters  $A_1$  and  $A_2$  are maintained at a constant value. We determine  $A_1$  in section 4.2.5, and  $A_2$  can be derived using Eq. 4.21. In our analysis, we aim to identify events shared with adjacent

Ge detectors at 356 keV from  $^{133}\text{Ba}$  calibration data. Therefore, to assess the resolution of Si detectors, we must characterize the combined resolution of both Ge and Si using the provided function  $\sigma_{T(E)}$  as described below.

$$\sigma_T = \sqrt{A_1^2 + A_{2,\text{Si}}^2 E + A_{2,\text{Ge}}^2 (356 - E) + A_{3,\text{Si}}^2 E^2 + A_{3,\text{Ge}}^2 (356 - E)^2} \quad (4.26)$$

### Baseline resolution

The Baseline resolution of total charge energy (qsum) is defined as  $1\sigma$  width of the combined noise distribution of the charge channels, outer (qo) and inner(qi) provided there is no noise correlation between these two channels. The noise distribution can be measured from the energy of random triggered events with zero-delay OF fit in order not to bias the charge energy fit. After selecting random triggered events with the cut condition EventCategory == 1, the combined distribution of qi and qo are used to calculate the baseline resolution. The combined channel (qi+qo) noise distribution (blue) with a gaussian fit (red) are shown in Fig. 4.18(a) for zip 10 detector for r125. Similarly. Figure 4.18(b) shows the noise correlation between the channels qi and qo. No significant correlation has been identified among the charge channels. Figure.4.19 compares the baseline resolutions by all the good Si detectors with adjacent Ge detector for each run. In Si detectors charge resolutions show less variation with the later detectors, except for zip21 which has poor resolution in r125.

### Resolution of 356 keV events in Si

The Si detector doesn't show the 356 keV line from the  $^{133}\text{Ba}$  source, and there are no activation lines available for Si. To assess the resolution of the Si detector, we examine the summed charge energy from the nearest neighbor Ge detector, observing how the 356 keV line splits between the two detectors. In Fig. 4.20, the X-axis represents the energy

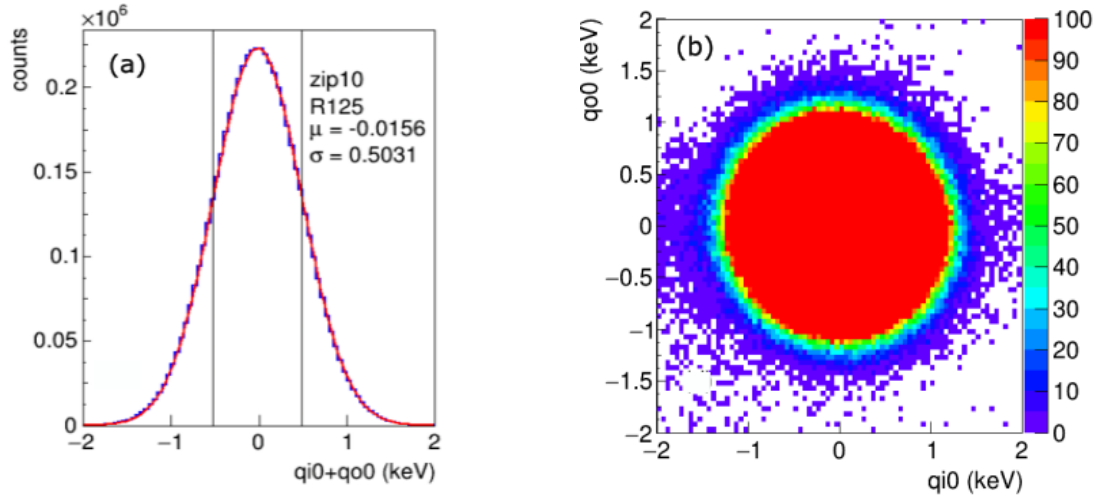


FIGURE 4.18: (a) The noise distribution of the combined channel  $q_i + q_o$  is shown for detector zip10 in r125. The baseline resolution, measured by the  $1\sigma$  width, is indicated by the black lines. (b) There is no observed correlation between the  $q_i$  and  $q_o$  channels.

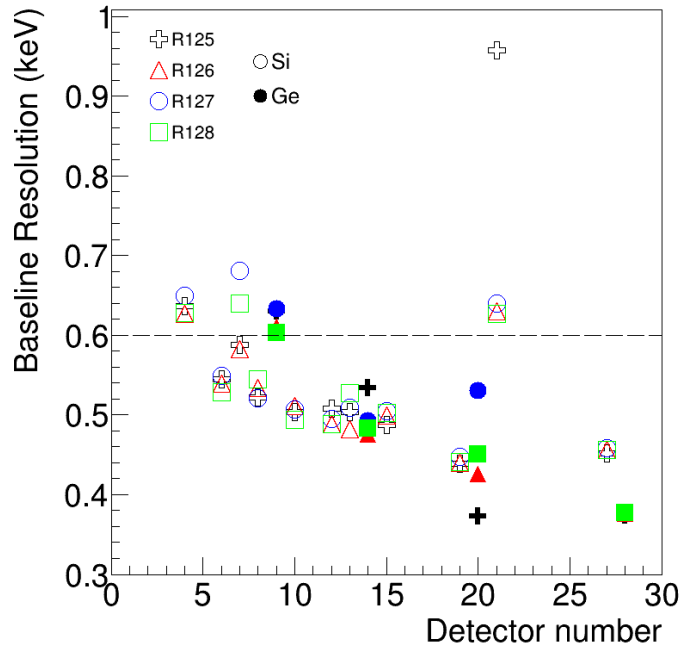


FIGURE 4.19: Baseline resolutions of all the Si and their neighboring Ge detector from r125-128 are shown. In the figure open markers represent Si detector baseline resolution and solid marker represent Ge detector baseline resolution.

deposited in zip15 (Si detector), while the Y-axis represents the energy deposited in the nearest neighbor zip14 (Ge detector). The red and green lines on the plot indicate summed energies of 356 keV and 384 keV, respectively.

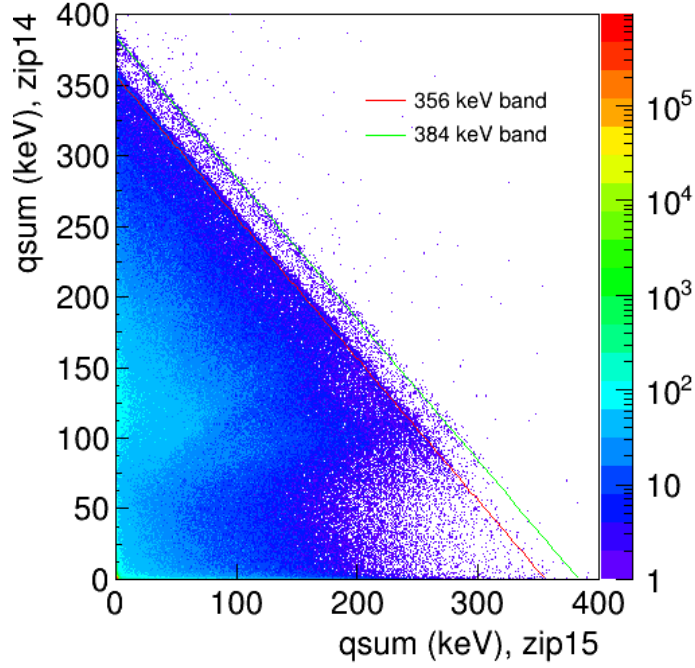


FIGURE 4.20: The graph shows the distribution of shared charge energy (qsum) between the closest Ge detector (zip14) and Si detector (zip15) from  $^{133}\text{Ba}$  events in the combined r125-128. The bands represented by red and green lines are the summed energies of 356 keV and 384 keV, respectively.

To compute the energy resolution across different energy ranges, we group the summed energy of 356 keV events for neighboring detectors into bins of varying energy for the Si detector. For instance, in Fig. 4.21(a), we have selected the energy bin from 15 keV to 30 keV for the Si zip15 detector. Then, Fig. 4.21(b) shows a histogram of the summed energy, focusing on the range from 325 keV to 370 keV, where the peak of 356 keV events appears. These histograms are fitted using a specific functional form.

$$f(x) = A \left( (1 - \alpha) \left[ \frac{1}{\sqrt{2\pi}\sigma^2} e^{-(x-\mu)^2/2\sigma^2} \right] + \frac{\alpha}{2\mu} \left[ \text{erf} \left( \frac{x}{\sqrt{2\sigma^2}} \right) - \text{erf} \left( \frac{x-\mu}{\sqrt{2\sigma^2}} \right) \right] \right) + B \quad (4.27)$$

which describes a Gaussian distribution where some fraction of the events,  $\alpha$ , have only a partial collection of energy in the two detectors under consideration. For these partially collected events, the distribution is taken to be a Gaussian convolved with a uniform distribution on 0 to  $\mu$ . A constant background, B is also included. The sum of both terms is shown in red.

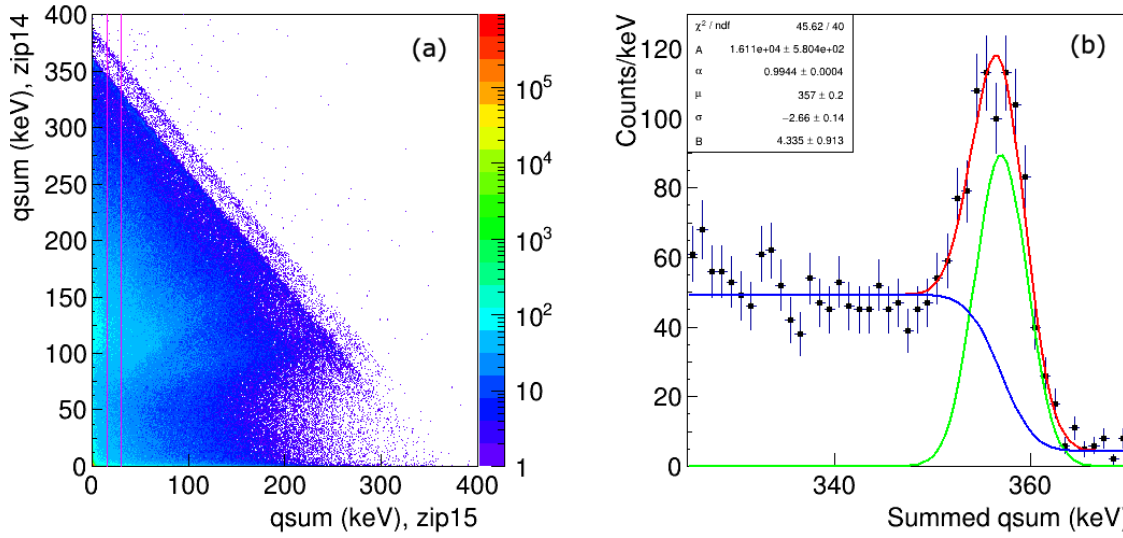


FIGURE 4.21: (a) Vertical lines show the energy bin 15-30 keV in Si detector, zip15. (b) Shows the histograms of the summed energy (Ge+Si) in the energy bin 15-30 keV.

### Energy dependent resolution

The combined resolution of Si and Ge detectors is determined using a function  $\sigma_T(E)$ , as defined in Eq. 4.26. Here,  $A_1^2$  accounts for the baseline resolution from both Si ( $A_{1, \text{Si}}^2$ ) and Ge ( $A_{1, \text{Ge}}^2$ ), such that:

$$A_1^2 = A_{1, \text{Si}}^2 + A_{1, \text{Ge}}^2 \quad (4.28)$$

The values for these parameters are established by the qsum baseline resolution outlined in section 4.2.5. For Si,  $A_{2, \text{Si}}^2$  and for Ge,  $A_{2, \text{Ge}}^2$  are set as 0.441 eV and 0.317 eV, respectively. These values are based on the assumption that the Fano factor for Ge is  $0.1057 \pm 0.0002$ ,

with  $\epsilon_\gamma$  at 3.0 eV, and for Si is  $0.1161 \pm 0.0001$ , with  $\epsilon_\gamma$  at 3.8 eV [22]. The coefficients of broadening for position and other dependencies for Ge,  $A_{3,Ge}$ , and for Si,  $A_{3,Si}$ , are left as free parameters. In Fig.4.22(a), the charge energy resolution of the 356 keV peak for Si and Ge detectors is displayed alongside the resolution model fit (red curve). The uncertainty on the model is computed by considering the uncertainty in all parameters using Eq.4.29, and shown in as a pink band.

$$\delta\sigma_T = \sqrt{\delta^2\sigma_{BR} + \delta^2\sigma_F + \delta^2\sigma_{PD}} \quad (4.29)$$

Since our analysis extends up to 3000 keV, we extrapolate the fit function to estimate the resolution at higher energies. Fig.4.22(b) depicts the resolution for all detectors extrapolated up to 2000 keV. The parameters derived from the fittings are listed in Table 4.2. The

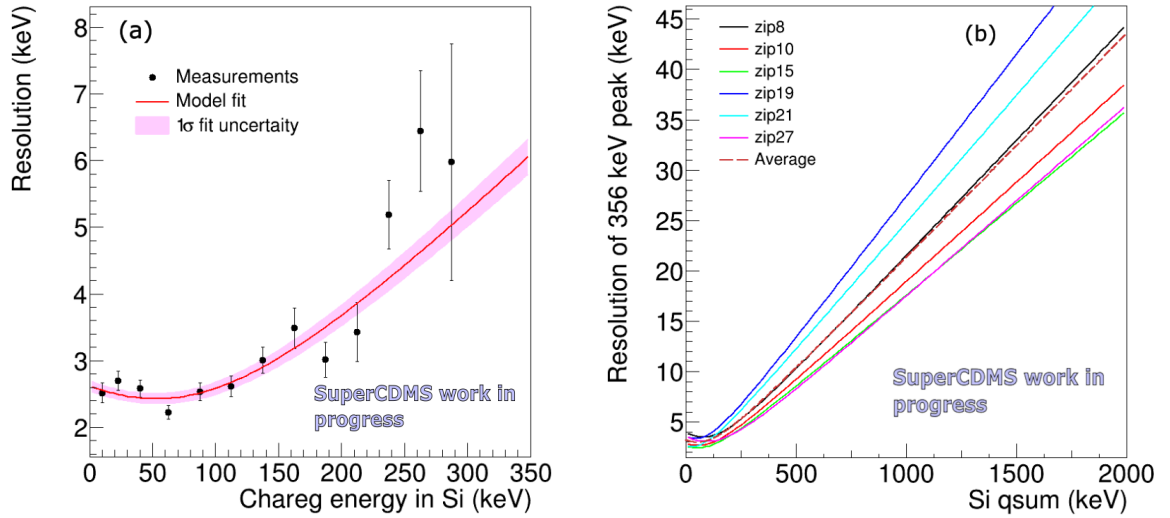


FIGURE 4.22: (a)  $^{133}\text{Ba}$  shared event energy resolution as a function of energy. The distribution is fitted with the resolution model where  $A_1$  and  $A_2$  are fixed for each detector pair with uncertainty on the model keeping  $A_3$  parameter free. (b) Charge energy resolution in Si detectors are shown upto 2000 keV. Solid curves are the resolution for each detectors where dotted line is an average over the resolution of all detectors.

parameters obtained for the Ge detectors closely align with those from a previous study.

Additionally, we computed an average resolution using data from all six Si detectors, shown as the brown dashed line in Fig. 4.22(b). This average resolution, derived from the six Si detectors, can be applied to detectors like zip4, zip6, zip7, zip12, and zip13, which lack neighboring Ge detectors.

TABLE 4.2: Charge energy resolution fit parameters

Si detector	Ge detector	$A_1$ (keV)	Si $A_3$	Ge $A_3$
zip8	zip9	0.6645	$0.0230 \pm 0.0014$	$0.0108 \pm 0.0002$
zip10	zip9	0.6367	$0.0183 \pm 0.0008$	$0.0078 \pm 0.0006$
zip15	zip14	0.4952	$0.0173 \pm 0.0008$	$0.0072 \pm 0.0002$
zip19	zip20	0.397	$0.0214 \pm 0.0007$	$0.0099 \pm 0.0003$
zip21	zip20	0.7302	$0.0260 \pm 0.0007$	$0.0069 \pm 0.0003$
zip27	zip28	0.3491	$0.0204 \pm 0.0005$	$0.0098 \pm 0.0005$

#### 4.2.6 Modeling other backgrounds with simulation

The primary aim of this study is to detect  $^{32}\text{Si}$  background in CDMS II data. Therefore, presence of any other backgrounds will be considered as background for this analysis. To identify potential backgrounds, we refer to a previous study that analyzed various backgrounds in the charge energy distribution. This study utilized Geant4 simulations known as GlobalGamma Monte Carlo (GGMC). Based on this analysis, a list of potential ‘other’ backgrounds is compiled, which could affect our analysis. Si has the largest stable isotope with 32 nucleons (with a half-life of 153 years), cosmic rays cannot produce nuclei with more than 32 nucleons through spallation. This condition eliminates many isotopes from consideration as backgrounds for the analysis of  $^{32}\text{Si}$ . Only isotopes with a mass number ( $A$ ) less than or equal to 32 are further investigated. Table 4.3 presents a list of all potential backgrounds for this analysis, categorized as cosmogenic and radiogenic. An isotope is considered relevant if it is either not present in the previous background study



or has a decay rate below a certain threshold. Looking at Table 4.3, we can see that the

TABLE 4.3: List of other backgrounds

Backgrounds	Isotope	Relevance
Cosmogenic	$^3\text{H}$	Beyond our analysis threshold
	$^7\text{Be}$	Not relevant as per GGMC
	$^{10}\text{Be}$	Negligible contribution
	$^{14}\text{C}$	Negligible contribution
	$^{22}\text{Na}$	Not relevant as per GGMC
	$^{26}\text{Al}$	Not relevant as per GGMC
Radiogenic	$^{40}\text{K}$	Relevant
	$^{60}\text{C}$	Relevant
	$^{238}\text{U}$	Relevant
	$^{232}\text{Th}$	Relevant

majority of backgrounds are radiogenic, originating from materials used in shielding. To model these backgrounds, we will employ a simulation platform called ‘SuperSim’ based on GEANT4. This tool replicates the geometry of the CDMS II setup, allowing us to simulate relevant backgrounds within various components of the experiment, including the cryostat, shielding, and detector towers.

### Gamma simulation for CDMS-II

To assess the presence of other background sources, we compare the data spectrum with the simulated spectra of common radioactive contaminants expected from various parts of the apparatus. Firstly, we modeled the CDMS-II geometry within the GEANT4 simulation. The actual CDMS-II layout is illustrated in Fig. 4.4(a). The corresponding simulated geometry is depicted in Fig. 4.23. The shielding consists of layers such as outer poly (green), outer lead (grey), inner lead (grey), inner poly (green), mu metal (yellow), and cryostat cans (blue). In the center lies the detector volume housing Si and Ge oZIPs

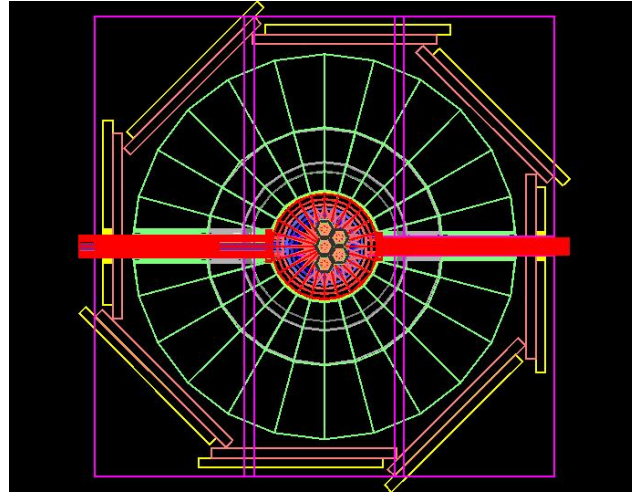


FIGURE 4.23: The CDMS-II setup is depicted in a GEANT4 simulation, showing its geometry. The shielding includes outer layers of poly (green) and lead (grey), followed by inner layers of lead (grey), poly (green), mu metal (yellow), and cryostat cans (blue). At the center of the setup are the detector volumes containing Si and Ge oZIPs arranged in five towers.

arranged in 5 towers. We simulate decays from the entire decay chain of isotopes like  $^{238}\text{U}$  and  $^{232}\text{Th}$ , as well as from isotopes such as  $^{40}\text{K}$  and  $^{60}\text{Co}$ . However, for our analysis, we focus solely on the inner components of the geometric sources. This decision is based on prior studies providing information on the main sources of contamination, which are primarily the inner lead layers, inner polyethylene, and the six copper cryostat cans. Each source is simulated uniformly throughout its volume. Additionally, surface sources, like the top surface of the bottom outermost cryostat can, are also included. The number of decays simulated for each source is detailed in Table 4.4, derived from previous study.

### Resolution applied

After simulating the decays, the next step involves adjusting for the difference in energy resolution between the simulated and measured data. While the simulation has perfect resolution, real detectors do not, and each may have a different resolution. In a previous section (Section 4.2.5), we estimated the charge energy resolution of Si and Ge detectors

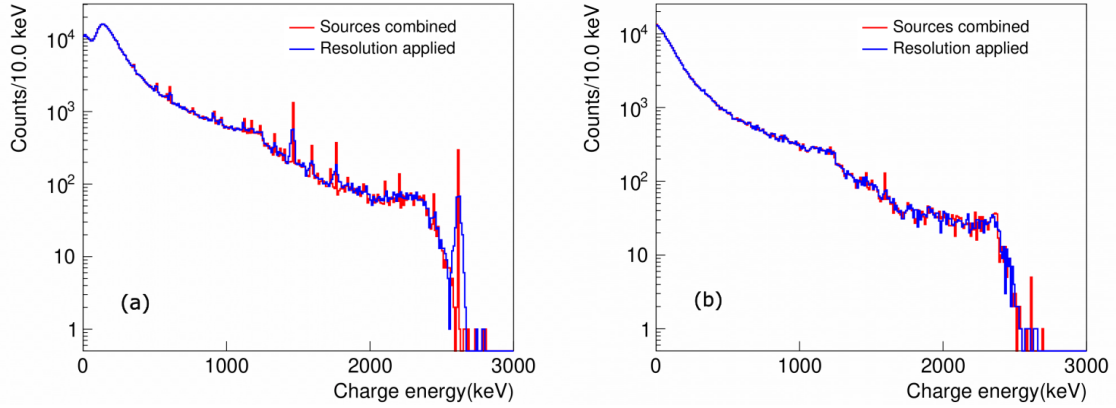


FIGURE 4.24: (a) and (b) Simulated energy spectrum with and without resolution applied for Germanium and Silicon detectors respectively. The effect of resolution can be seen by the boardening of gamma peaks for both the detectors.

TABLE 4.4: Number of simulated decays from each decay-geometry source.

Decay chain	Inner Lead ( $\times 10^5$ )	Inner Poly ( $\times 10^5$ )	OVC can ( $\times 10^5$ )	Liquid He- lium can ( $\times 10^5$ )	IVC can ( $\times 10^5$ )	Still can ( $\times 10^5$ )	Cold can ( $\times 10^5$ )	Base can ( $\times 10^5$ )	Top sur- face of Bottom OVC layer ( $\times 10^5$ )
$^{232}\text{Th}$	10000	1000	100	20	20	20	20	10	20
$^{238}\text{U}$	20000	2000	200	40	40	40	40	20	40
$^{60}\text{C}$	-	-	100	20	20	100	100	10	-
$^{40}\text{K}$	-	-	500	250	250	20	20	50	-

as a function of energy, resulting in the model shown in Equation 4.26. The resolution parameters for both Si and Ge,  $A_1$ ,  $A_2$ , and  $A_3$ , are listed in Table 4.2. Incorporating this resolution model into the simulation allows us to observe the effect of resolution in Fig. 4.24(a) and (b) for the Ge (zip14) and Si (zip15) detectors, respectively. We observe that full gamma peaks broaden in width due to resolution effects. For instance, the gamma peak of  $^{208}\text{Tl}$  at 2614 keV widens for Ge. However, in Si, the 2614 keV peak is hardly visible due to its low stopping power, and it disappears because of poor resolution.

### Fitting Results

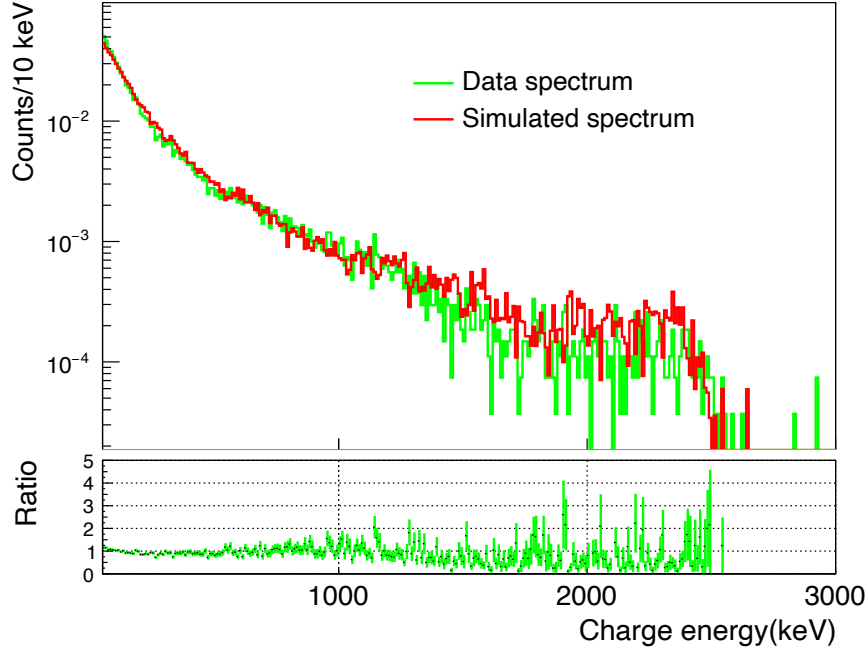


FIGURE 4.25: Charge energy spectrum (green) compared to the weighted sum of simulation spectra (red) shown for detector zip15 in r125. The fit matches well with the data.

We perform a  $\chi^2$ -minimization fit by comparing a combined weighted sum of the 9 sources with the measured data. This weighting process involves binning the spectra into 5 keV bins and summing up the simulation outputs within each bin as:

$$S_j^{total} = \sum_i^9 S_{ij}^{MC} w_{ij} \quad (4.30)$$

where,  $S_{ij}^{MC}$  represents the count number in the  $j^{th}$  bin from the  $i^{th}$  source, and  $w_i$  denotes the weight of that source. The weight is calculated as follows:

$$w_i = \frac{\rho_i L V_i}{N_i^{MC}} \quad (4.31)$$

Here,  $\rho_i$  is the radio-activity per volume,  $L$  is the experimental lifetime,  $V_i$  is the volume of the source and  $N_i^{MC}$  is the number of decays simulated for a contamination  $i$ .

The  $\chi^2$  quantity is then calculated between  $S_j^{total}$  and the data  $d_j$  in each bin  $j$  as:

$$\chi^2 = \sum_j \frac{(d_j - S_j^{total})^2}{S_j^{total}} \quad (4.32)$$

The  $\chi^2$  value is then minimized by adjusting the  $w_i$  values to find the best-fit combination of simulated sources for the data. During the fitting process, we incorporated contamination levels determined from a previous study, particularly for the inner poly and inner lead, based on screening results. The results of the best-fit are illustrated in Fig. 4.25, where the best-fit

TABLE 4.5: Contamination levels

Bulk contamination		
Source	Radio-activity (mBq/kg)	Screening results (mBq/kg)
$^{40}\text{K}$ cryogenic cans	0.38	-
$^{232}\text{Th}$ cryogenic cans	0.19	-
$^{238}\text{U}$ cryogenic cans	0.27	-
$^{232}\text{Th}$ inner poly	-	0.5
$^{238}\text{U}$ inner poly	-	0.59
$^{232}\text{Th}$ inner lead	-	0.7
$^{238}\text{U}$ inner lead	-	0.6
Surface contamination		
Source	Radio-activity (mBq/cm <sup>2</sup> )	Screening results (mBq/cm <sup>2</sup> )
$^{232}\text{Th}$ top of bottom lid OVC	1.8 (mBq/cm <sup>2</sup> )	-
$^{238}\text{U}$ top of bottom lid OVC	1.1 (mBq/cm <sup>2</sup> )	-

combined simulated spectra (shown in red) are compared to the measured data (shown in green) for detector zip15. Lastly, the contamination values corresponding to the best-fit weights for each source are listed in the Table 4.5.

### 4.2.7 Signal modeling

The last step in this analysis involves modeling the signal, which is the beta decay spectrum of  $^{32}\text{Si}$  and  $^{32}\text{P}$ . To achieve this, we begin by studying Fermi's theory of beta decay. We then

compare several software models with Fermi's theory and select the model that shows the smallest deviation from the theoretical predictions.

### Fermi theory of beta decay

The endpoint energies for beta decay are 227.2 keV for  $^{32}\text{Si}$  and 1710.6 keV for  $^{32}\text{P}$ . The half-lives of these isotopes are 153 years and 14.27 days, respectively. Fermi's theory [23] of beta decay gives the distribution of beta particles ( $N(T_e)$ ),

$$N(T_e) = C \sqrt{T_e^2 + 2T_e m_e} (Q - T_e)^2 (T_e + m_e) F(Z, T_e) \quad (4.33)$$

where  $T_e$  represents the kinetic energy of the emitted beta particle, and  $Q$  is the endpoint energy (227.2 keV for  $^{32}\text{Si}$  and 1710.66 keV for  $^{32}\text{P}$ ). In this theory,  $Z$  stands for the atomic number of the daughter nucleus,  $m_e$  is the mass of the beta particle,  $C$  is a normalization constant, and  $F(Z, T_e)$  represents the Fermi function, which considers the Coulomb interaction between the charged daughter nucleus and the emitted beta particle after decay. For this study, we select relativistic Fermi function as the end-point energy of beta particle from  $^{32}\text{P}$  is greater than the rest-mass energy of electron (511 keV).

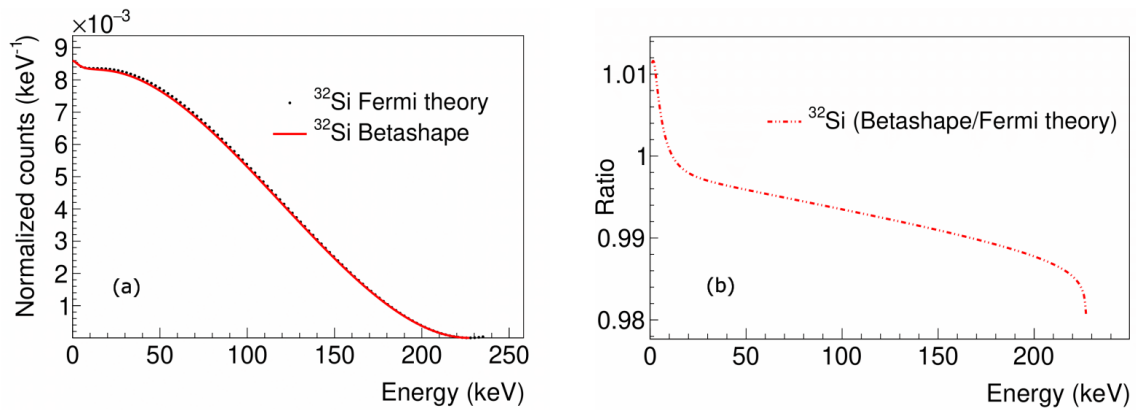


FIGURE 4.26: (a) Beta decay spectrum using Betashape is compared with the distribution from Fermi theory for  $^{32}\text{Si}$ . (b) Ratio plot between Betashape and Fermi theory showing a deviation of 2%.

**Relativistic Fermi function: Bethe-Bacher function**

A relativistic Fermi-function modeled by Bethe-Bacher is used which has an accuracy 1% upto  $Z = 84$  [24]. The function is defined as:

$$F(Z, T_e) = F_{NR}(Z, T_e) \{T_e^2(1 + 4\gamma^2) - 1\}^S \quad (4.34)$$

where,  $\gamma = \alpha Z$ ,  $S = (1 - \gamma^2)^{1/2} - 1$  and  $F_{NR}(Z, T_e)$  is the non-relativistic Fermi function [25] and can be defined as:

$$F_{NR}(Z, T_e) = \frac{2\pi\eta}{1 - e^{-2\pi\eta}} \quad (4.35)$$

$$\eta = \frac{\alpha ZE}{pc} \quad (4.36)$$

Here,  $\alpha$  represents the fine structure constant, approximately equal to  $1/137$ .  $E$ ,  $p$ , and  $c$  denote the total energy, momentum of the emitted beta particles, and the speed of light respectively. The Fermi theory for the decay spectrum of  $^{32}\text{Si}$  and  $^{32}\text{P}$  is shown in Fig. 4.26(a) with black markers and Fig. 4.27(a) with cyan markers respectively.

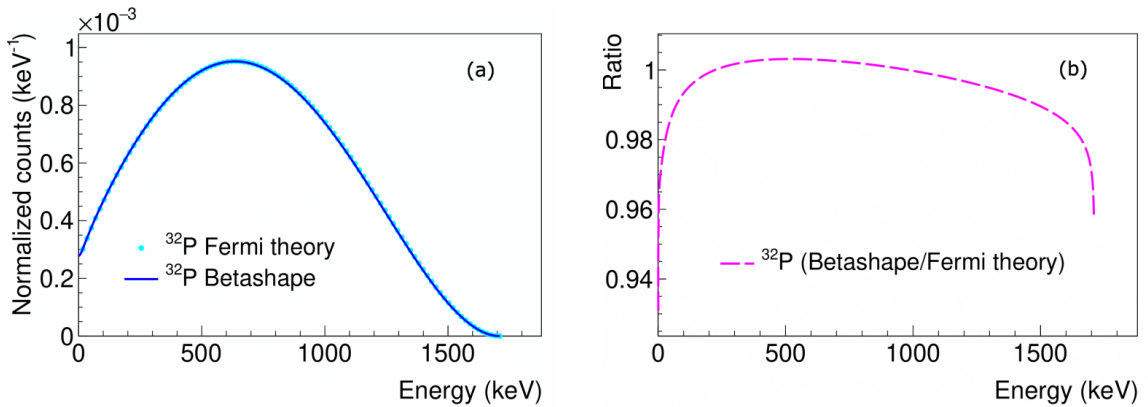


FIGURE 4.27: (a) Beta decay spectrum using Betashape is compared with the distribution from Fermi theory for  $^{32}\text{P}$ . (b) Ratio plot between Betashape and Fermi theory showing a deviation of 5%.

### Betashape

There are several softwares available such as DECDATA [26], Rad ToolBox [27], and Betashape [28] that produces beta decay spectrum using experimental data. In this study, we compare the output of the Betashape with the Fermi theory spectrum which shows least deviation. We selected Betashape, developed by Laboratoire National Henri Becquerel (LNHB), which utilizes experimental data from the Decay Data Evaluation Project (DDEP) [29]. In Fig. 4.26(a), the red curve represents the beta decay spectrum for  $^{32}\text{Si}$  using Betashape, showing the comparison with Fermi theory. Similarly, in Fig. 4.27(a), the blue curve depicts the beta decay spectrum for  $^{32}\text{P}$  using Betashape. These spectra from Betashape exhibit a deviation of about 2% for  $^{32}\text{Si}$  (Fig. 4.26(b)) and 5% for  $^{32}\text{P}$  (Fig. 4.27(b)) from the theoretical predictions.

## 4.3 Summary and outlook

In this chapter, we discuss an ongoing study to precisely measure the decay rates of  $^{32}\text{Si}$  and  $^{32}\text{P}$  using CDMS-II data collected between 2003 and 2012 at the Soudan Underground Laboratory. CDMS-II employed 19 Ge and 11 Si cryogenic detectors in a five-tower configuration to detect recoil energy from particle interactions, measuring both phonon and charge energy.

$^{32}\text{Si}$ , a naturally occurring isotope in Si detector material, decays to  $^{32}\text{P}$ , which further decays to stable  $^{32}\text{S}$ , emitting  $\beta$  particles contributing to background for DM signals. The DAMIC collaboration reported their first measured specific radioactivity of  $^{32}\text{Si}$  in their Si detectors at  $80^{+110}_{-65}$  decays/kg-day, and the second measurement gave a rate of  $11.5 \pm 2.4$  decays/kg-day. The reported activity variation is due to the use of different batches of Si detectors. Additionally,  $^{32}\text{Si}$  decays will significantly contribute to the background in



SuperCDMS Si High Voltage (HV) detectors. The precise measurement of  $^{32}\text{Si}$  decay rate with CDMS II data would help to estimate the background rates for dark matter searches.

This analysis unfolds in three phases. We combine data from CDMS II runs 125, 126, 127, and 128. We use charge energy as our main observable due to energy saturation in phonon channels at lower energies. Several basic and quality cuts that reject events with hardware/DAQ related issues, glitches, events with improper amplification, and events not related to this analysis are applied. We verify the linearity of the charge energy scale up to 2381 keV. We model the resolution of Si detectors as a function of charge energy, and energy-dependent cut efficiency is calculated.

The second part of the analysis is to model other backgrounds relevant for the analysis. The major source of backgrounds for  $^{32}\text{Si}$  decay signals is due to the interactions of gamma rays originating from natural impurities like  $^{40}\text{K}$ ,  $^{60}\text{Co}$ ,  $^{238}\text{U}$ , and  $^{232}\text{Th}$  (entire decay chain) present in both the detector and shielding materials. To simulate these backgrounds, we employ 'SuperSim', a GEANT4-based simulation platform mirroring the CDMS II setup. We focus on bulk contaminants within the cryogenic vessels, inner Polyethylene, and Lead shielding. The simulated spectrum is then normalized bin by bin according to simulation decays and source mass. This collective spectrum is subsequently corrected using an energy-dependent resolution model. We perform a  $\chi^2$ -minimization fit by comparing a combined weighted simulated spectrum with the measured data to estimate the contamination levels of other backgrounds present in the data.

In the third and final part of the analysis, we model the beta spectrum of  $^{32}\text{Si}$  and  $^{32}\text{P}$ . To study the beta decay spectrum of  $^{32}\text{Si}$  and  $^{32}\text{P}$ , we compare various software models to the theoretical Fermi curve. Among the software options (DECDATA, Rad ToolBox, and Betashape), Betashape closely matches the Fermi theory spectrum. We utilize Betashape, developed by Laboratoire National Henri Becquerel (LNHB), which

incorporates experimental data from the Decay Data Evaluation Project (DDEP). The spectra from Betashape for  $^{32}\text{Si}$  and  $^{32}\text{P}$  exhibit a deviation of approximately 2% and 5% from the theory, respectively.

The analysis is in progress, and in future we will calculate the systematic uncertainties and finally we will perform a profile likelihood analysis with inputs from the CDMS II Si data, beta decay spectrum of  $^{32}\text{Si}$  and  $^{32}\text{P}$  from Betashape, and the simulated background model discussed above. The precise measurement of  $^{32}\text{Si}$  is crucial not only for the SuperCDMS SNOLAB but also important for all the rare event search experiments that use Si detectors.

## Bibliography

- [1] Z. Ahmed et al. “Dark Matter Search Results from the CDMS II Experiment”. *Science* 327 (2010), p. 1619–1621. arXiv: [0912.3592 \[astro-ph.CO\]](#).
- [2] R. Agnese et al. “Silicon Detector Dark Matter Results from the Final Exposure of CDMS II”. *Phys. Rev. Lett.* 111 (2013), p. 251301. arXiv: [1304.4279 \[hep-ex\]](#).
- [3] R. Agnese et al. “Improved WIMP-search reach of the CDMS II germanium data”. *Phys. Rev. D* 92 (2015), p. 072003. arXiv: [1504.05871 \[hep-ex\]](#).
- [4] J. D. Lewin and P. F. Smith. “Review of mathematics, numerical factors, and corrections for dark matter experiments based on elastic nuclear recoil”. *Astropart. Phys.* 6 (1996), p. 87–112.
- [5] John L. Orrell et al. “Naturally occurring  $^{32}\text{Si}$  and low-background silicon dark matter detectors”. *Astropart. Phys.* 99 (2018), p. 9–20. arXiv: [1708.00110 \[physics.ins-det\]](#).
- [6] A. Aguilar-Arevalo et al. “Measurement of radioactive contamination in the high-resistivity silicon CCDs of the DAMIC experiment”. *Journal of Instrumentation* 10 (2015), p. 08014.
- [7] Rich G. “Status and plans for the DAMIC Experiment at SNOLAB and Modane”. *IDM Brown University* (2018).

- [8] R. Agnese et al. “Projected Sensitivity of the SuperCDMS SNOLAB experiment”. *Phys. Rev. D* 95 (2017), p. 082002. arXiv: [1610.00006 \[physics.ins-det\]](#).
- [9] R. Agnese et al. “Search for Low-Mass Weakly Interacting Massive Particles with SuperCDMS”. *Phys. Rev. Lett.* 112.24 (2014), p. 241302. arXiv: [1402.7137 \[hep-ex\]](#).
- [10] R. Agnese et al. “Low-mass dark matter search with CDMSlite”. *Phys. Rev. D* 97.2 (2018), p. 022002. arXiv: [1707.01632 \[astro-ph.CO\]](#).
- [11] D. S. Akerib et al. “Exclusion limits on the WIMP-nucleon cross section from the first run of the Cryogenic Dark Matter Search in the Soudan Underground Laboratory”. *Phys. Rev. D* 72 (2005), p. 052009. arXiv: [astro-ph/0507190](#).
- [12] D. S. Akerib et al. “First results from the cryogenic dark matter search in the Soudan Underground Lab”. *Phys. Rev. Lett.* 93 (2004), p. 211301. arXiv: [astro-ph/0405033](#).
- [13] D. S. Akerib et al. “Limits on spin-independent wimp-nucleon interactions from the two-tower run of the cryogenic dark matter search”. *Phys. Rev. Lett.* 96 (2006), p. 011302. arXiv: [astro-ph/0509259](#).
- [14] D. S. Akerib et al. “Limits on spin-dependent wimp-nucleon interactions from the cryogenic dark matter search”. *Phys. Rev. D* 73 (2006), p. 011102. arXiv: [astro-ph/0509269](#).
- [15] Z. Ahmed et al. “Search for Weakly Interacting Massive Particles with the First Five-Tower Data from the Cryogenic Dark Matter Search at the Soudan Underground Laboratory”. *Phys. Rev. Lett.* 102 (2009), p. 011301. arXiv: [0802.3530 \[astro-ph\]](#).
- [16] Mark David Pepin. “Low-Mass Dark Matter Search Results and Radiogenic Backgrounds for the Cryogenic Dark Matter Search”. PhD thesis. Minnesota U., 2016.
- [17] Zeeshan Ahmed. “A Dark Matter Search Using The Final CDMS II Dataset And a Novel Detector of Surface Radiocontamination”. PhD thesis. California Institute of Technology, Pasadena, California, 2012.
- [18] C. Kittel. *Introduction to Solid State Physics. 8th edition.* 2005.

- [19] F. E. Emery and T. A. Rabson. “Average Energy Expended Per Ionized Electron-Hole Pair in Silicon and Germanium as a Function of Temperature”. *Phys. Rev.* 140 (1965), A2089–A2093.
- [20] Zhong He. “Review of the Shockley–Ramo theorem and its application in semiconductor gamma-ray detectors”. *Nucl. Instrum. Meth. A* 463 (2001), p. 250–267.
- [21] U. Fano. “Ionization Yield of Radiations. 2. The Fluctuations of the Number of Ions”. *Phys. Rev.* 72 (1947), p. 26–29.
- [22] B.G. Lowe. “Measurements of Fano factors in silicon and germanium in the low-energy X-ray region”. *Nuclear Instruments and Methods in Physics Research Section A: Accelerators, Spectrometers, Detectors and Associated Equipment* 399 (1997), p. 354–364.
- [23] E. Fermi. “An attempt of a theory of beta radiation. 1.” *Z. Phys.* 88 (1934), p. 161–177.
- [24] H. A. Bethe and R. F. Bacher. “Nuclear Physics A. Stationary States of Nuclei”. *Rev. Mod. Phys.* 8 (1936), p. 82–229.
- [25] Bogdan Povh et al. “The Structure of Nuclei”. In: *Particles and Nuclei: An Introduction to the Physical Concepts*. Berlin, Heidelberg: Springer Berlin Heidelberg, 2008, p. 245–284.
- [26] A. Endo K. F. Eckerman. “User Guide To The ICRP CD and The DECDATA Software”. 2008. URL: <https://journals.sagepub.com/doi/pdf/10.1016/j.icrp.2008.10.001>.
- [27] K. F. Eckerman and A. L. Sjoreen. “Radiological Toolbox User’s Guide”. 2013. URL: <https://www.ornl.gov/crpk/software>.
- [28] “Software and tools developed by the LNHB”. 2005. URL: <http://www.lnhb.fr/home/rd-activities/spectrum-processing-software/>.
- [29] X. Mougeot. “Reliability of usual assumptions in the calculation of  $\beta$  and  $\nu$  spectra”. *Phys. Rev. C* 91.5 (2015), p. 055504.



---

## Conclusion

In this thesis, we address the critical challenges faced by rare event search experiments such as direct dark matter search, Coherent Elastic Neutrino-Nucleus Scattering (CE $\nu$ NS) and Neutrinoless Double Beta Decay (NDBD).

1. **Requirement of low-threshold detectors:** The lack of a positive laboratory signal for GeV scale dark matter is a compelling reason for researchers to shift their focus towards investigating low-mass dark matter. To explore the lower mass range of the parameter space, which is currently limited by existing detection technology, it becomes crucial to develop detectors that can detect nuclear recoils with a low energy threshold. Due to the extremely weak interaction cross-sections ( $\sim 10^{-43}$  cm<sup>2</sup>) of dark matter particles, these detectors should allow for the construction of large detectors systems for detection in a reasonable amount of time. Another process that requires low threshold detectors is CE $\nu$ NS, a phenomenon initially proposed in 1974 and subsequently observed by the COHERENT collaboration in 2017. In this interaction, a neutrino scatters off the entire nucleus of an atom coherently, meaning that it interacts with the entire nucleus as a whole rather than with individual protons or

neutrons within the nucleus. Given that the expected nuclear recoil energy deposition is on the order of  $\sim$  keV, CEvNS encounters similar challenges as low-mass dark matter detection necessitating the use of low threshold detectors.

2. **Understanding backgrounds:** Apart from having low recoil energy threshold detectors there is another challenge for these experiments. They need to tackle a very high background rate from the surroundings. There are mainly two types of background sources present in these experiments: radiogenic and cosmogenic. To reduce the effect of cosmogenic backgrounds most of these experiments are conducted in underground laboratories. Radiogenic backgrounds originate from radioisotopes present in the material surrounding the detectors. These must be shielded to an excellent level in order to achieve competitive science goals. The primary background reduction method in these experiments is either passive or active shielding. Apart from operating deep underground, a passive, multi-layer hermetic shield can be used to substantially reduce the rate of background gammas and neutrons. Unfortunately such measures are ineffective with respect to in-situ backgrounds present in the detector material itself. While passive shielding does reduce background event rates greatly, further reduction must be made to improve the sensitivity of the experiment. One way to aggressively reduce the impact of backgrounds is by applying active shielding. The active shielding includes veto system that can detect and identify background particles from potential dark matter particles.

In this thesis, we discuss the fabrication and performance of a newly developed annular cryogenic phonon-mediated active veto detector which allows substantial reduction of radiogenic backgrounds. For example, in the Super Cryogenic Dark Matter Search (SuperCDMS) Soudan experiment, WIMP search sensitivity was limited by the decays of  $^{210}\text{Pb}$

on the detector surface. This long-lived  $^{210}\text{Pb}$  (half-life 22.3 years) is a decay daughter of  $^{222}\text{Rn}$  which is usually present in the surrounding environment and housing material such as Cu. Three concerning radioisotopes are  $^{210}\text{Pb}$ ,  $^{210}\text{Bi}$  and  $^{210}\text{Po}$  which yield low energy beta particles, X-rays and gamma rays ( $\sim 46.5$  keV). Decay of  $^{210}\text{Po}$  also creates  $^{206}\text{Pb}$  which results in a nuclear recoil that can be observed in the signal region. In the upcoming SuperCDMS SNOLAB experiment, three of the primary backgrounds that may limit the sensitivity are (i) Compton scatters from the gamma rays, (ii) surface betas from surrounding materials, and (iii) recoils from the decay radiation of  $^{210}\text{Pb}$  and its progeny existing on the detector surfaces from radon exposure. The design of the active veto detector is such that it would tag and reject the events that will deposit energy both in the active veto and inner target detector. It would thus be possible to reject essentially all of the recoils from  $^{210}\text{Pb}$  and surface beta events, while also reducing the Compton backgrounds expected in SuperCDMS SNOLAB by an order of magnitude.

The annular active veto detector is produced with a thickness of 25 mm and the outer and inner diameters are 76 mm and 28 mm respectively. The inner detector which was mounted inside the veto has a diameter of 25 mm and a thickness of 4 mm. The veto and inner detector have a mass of  $\sim 500$  g and  $\sim 10$  g respectively. Both the detectors were produced and commissioned using the same methods as done for standard SuperCDMS detectors. In this thesis, we discuss several challenges that were addressed for instrumenting the detector setup.

A GEANT4 based simulation was performed with the annular veto and the inner target detector to tag Compton scatter events. An isotropic  $^{137}\text{Cs}$  point source was simulated at a distance of 50 cm from the detector. The tagging efficiency is calculated which is defined as the ratio of the events that deposit energy in both the inner and veto detector to the total number of events deposits energy in the inner detector and it is found that the efficiency by



the veto is expected to be between 50 - 80%. Also, an experiment was performed at the test facility in the Texas A&M University to confirm the ability to tag and veto Compton scatter events by using a  $^{137}\text{Cs}$  source. Further improvement was done with  $4\pi$  veto coverage where the annular active veto detector is sandwiched between two germanium detectors with similar dimensions. A GEANT4 simulation with the assembly showed a tagging efficiency of approximately 90% in the low energy ( $< 100$  keV) region of interest. We also simulate SuperCDMS SNOLAB backgrounds with the detector assembly which showed an order of magnitude reduction in backgrounds. With that we perform an experiment at the Mitchell Institute Neutrino Experiment at Reactor (MINER) experimental site which aims to look for  $\text{CE}\nu\text{NS}$ . We see same amount of background reduction in the experimental data as well.

By addressing all the fabrication difficulties and experimental challenges at the experimental site we can say that the detector is capable of rejecting the three major backgrounds (surface betas,  $^{210}\text{Pb}$ , Compton scatters) that are expected to limit sensitivity for the SuperCDMS SNOLAB experiment. With the background rejection efficiency as high as 90%, the active veto detector would be an excellent candidate for dark matter search and  $\text{CE}\nu\text{NS}$  experiments.

We discuss the performance of another low energy threshold cryogenic scintillator detector that has been fabricated in Texas A&M University. A 100 g single-crystal sapphire detector having a diameter of 76 mm and thickness of 4 mm was instrumented with transition edge sensors (TES). Chemical composition of sapphire is aluminum oxide ( $\text{Al}_2\text{O}_3$ ) and could be used in  $\text{CE}\nu\text{NS}$  search at MINER. MINER experiment at the Nuclear Science Center (NSC) at Texas A&M University, USA, aims to measure precisely the  $\text{CE}\nu\text{NS}$  cross-section utilizing the large neutrino flux from the  $1 \text{ MW}_{th}$  reactor with  $^{235}\text{U}$  core.  $\text{CE}\nu\text{NS}$  interaction requires neutrino energies of the order of a few MeV which results in a

nuclear recoil energy of 1 eV to few keV depending on the mass of the target nucleus. This demands low energy threshold detectors ( $\sim 100$  eV). If we consider a neutrino of mass  $M_\nu$  colliding with a target nucleus of mass  $M_T$  with an incoming velocity  $u_\nu$  and  $\theta$  describing the recoiling angle of the nucleus with respect to the direction of the incident neutrino particle, then the recoil energy is defined as,

$$E_R = \frac{2M_\nu^2 M_T u_\nu \cos \theta}{(M_\nu + M_T)^2} \quad (5.1)$$

As the neutrinos have very negligible mass ( $M_\nu \ll M_T$ ), this implies  $E_R \propto \frac{1}{M_T}$ . To detect low energy neutrinos, we need detectors made up with low atomic mass nuclei and have low energy threshold and resolution. The lower atomic mass of Al and O in sapphire makes it sensitive to lower nuclear recoil energies. Also, to increase the interaction rate with the target nuclei, the detector should have large mass. The 100 g sapphire ( $\text{Al}_2\text{O}_3$ ) detector was tested at TAMU and it showed a baseline resolution of  $39.6 \pm 0.6$  eV for all the four channels combined, while single channel baseline resolution was  $28.4 \pm 0.4$  eV. One advantage of having a sapphire detector is the enhanced phonon transmission between the Al substrate and the Al phonon absorber within the TES sensors. This improvement is due to the absence of an amorphous silicon layer, commonly found in CDMS-style detectors, which serves to protect the substrate surface from Al and W (tungsten) etchants. Instead, Al is directly deposited onto sapphire, resulting improved phonon transmission compared to other silicon or germanium detectors. Another advantage is that it can provide low energy threshold as well as particle identification capability at lower recoil energies. Particle identification between electron recoils and nuclear recoils can be done by the simultaneous measurement of phonon and scintillation light produced in the detector. The Sapphire detector produces very small amount of light. For example, the light yield of the sapphire detector for 60 keV photons from  $^{241}\text{Am}$  is about  $10\% \pm 3\%$ . The most challenging part is

to measure this small amount of light.

In this thesis, we discuss a procedure to collect this very small amount of light produced in sapphire. We utilize a phonon-mediated Si detector of 100 g to amplify the scintillation light from Sapphire. The Si detector can be operated at high voltage mode (HV) with bias voltage applied upto 240 V. The threshold of the Si detector can be improved exploiting Neganov-Trofimov-Luke (NTL) gain by applying high voltage bias across the detector. We show the results of the collected light from the sapphire detector paired with the Si detector which is operated at three different voltages. An expected linearity of amplified light with the applied voltages in the Si detector is observed. We also calculate the amount of light that we expected from sapphire and compare it with the light measured in Si detector which is in good agreement.

We have also discussed in this thesis, the results of three newly developed phonon-mediated detectors and compared their performance at the test facility and the NSC. A tower of three detectors, including a sapphire and two germanium detectors, has been characterized at NSC for the MINER experiment. We used a  $^{57}\text{Co}$  calibration source and identified the Compton edge at 39.43 keV and the gamma peak at 122 keV in the measured phonon energy distribution. We were also able to see the Al fluorescence peak after selecting single scatter and bulk events. The baseline resolution is quite high compared to the test facility due to the reactor environment. Currently, the MINER experiment is being upgraded from testing to continuous mode with a better DAQ system and improved data handling resources. Primary shielding is also optimized to minimize noise and background levels at the experimental site. All these low-threshold, Hybrid, and veto detectors will be deployed in tandem at MINER in the search for  $\text{CE}\nu\text{NS}$ .

In India, there is an ongoing initiative focused on conducting a  $\text{CE}\nu\text{NS}$  experiment utilizing the Apsara reactor located at the Bhabha Atomic Research Centre (BARC). The

experiment is known as the “India-based Coherent Neutrino Scattering Experiment at Apsara-U, Mumbai”, aims to investigate neutrino interactions through coherent scattering with atomic nuclei from the reactor. These new detectors, designed to detect low-energy signals while rejecting background noise, could be utilized in this experiment. They are essential for analyzing the signals generated by neutrino interactions, offering valuable insights into fundamental particle physics phenomena.

This thesis also discusses an ongoing study to precisely measure the decay rate of  $^{32}\text{Si}$  and  $^{32}\text{P}$ , which are considered as one of the major backgrounds in Si detectors for upcoming SuperCDMS SNOLAB.  $^{32}\text{Si}$  is a radioactive isotope of Si which is produced by the spallation of  $^{40}\text{Ar}$  due to cosmic rays. This cosmogenically created  $^{32}\text{Si}$  is an inherent impurity in Si detectors from the time of fabrication. It decays to  $^{32}\text{P}$  which further decays to stable  $^{32}\text{S}$  with half-lives of 153 years and 14.27 days respectively. These  $\beta$  particles act as a source of background. The endpoint energies of the  $\beta$  spectrum are 227 keV for  $^{32}\text{Si} \rightarrow ^{32}\text{P}$  and 1710 keV for  $^{32}\text{P} \rightarrow ^{32}\text{S}$ . The DAMIC collaboration reported their first measurement of the specific radioactivity of  $^{32}\text{Si}$  in their Si detectors at  $80^{+110}_{-65}$  decays/kg-day and second measurement gave a rate of  $11.5 \pm 2.4$  decays/kg-day. The reported activity variation is due to usage of different batches of Si detectors. Previously, only the CDMS II experiment, the precursor to SuperCDMS, employed silicon detectors, operational from 2003 to 2012 at the Soudan Underground Laboratory (780 m underground) in Minnesota, USA. These detectors, 30 in total, were Z-sensitive Ionization and Phonon (ZIP) detectors consisting of 19 Ge and 11 Si detectors, all operated at temperatures  $\sim 40$  mK, measuring both ionization and phonon energies. In this thesis, we focus on precisely measuring the  $^{32}\text{Si}$  decay rate using CDMS II data to estimate background rates for dark matter searches. Our analysis unfolds in three phases. We combine data from CDMS II runs 125, 126, 127, and 128. We use charge energy as our main observable due to energy saturation in

phonon channels at lower energies. We apply various data selection criteria, including identifying and excluding problematic Si detectors. Specific cuts are developed for our analysis, and we verify the linearity of the charge energy scale up to 2381 keV. We model resolution of Si detectors as a function of charge energy and energy-dependent cut efficiency is calculated. The second part of the analysis is to model other backgrounds relevant for the analysis. The major source of backgrounds for  $^{32}\text{Si}$  decay signals is due to the interactions of gamma rays originating from natural impurities like  $^{40}\text{K}$ ,  $^{60}\text{Co}$ ,  $^{238}\text{U}$ , and  $^{232}\text{Th}$  (entire decay chain) present in both the detector and shielding materials. To simulate these backgrounds, we employ ‘SuperSim’, a GEANT4-based simulation platform mirroring the CDMS II setup. We focus on bulk contaminants within the cryogenic vessels, inner Polyethylene, and Lead shielding. The simulated spectrum is then normalized bin by bin according to simulation decays and source mass. This collective spectrum is subsequently corrected using an energy-dependent resolution model. We perform a  $\chi^2$ -minimization fit by comparing a combined weighted simulated spectrum with the measured data to estimate the contamination levels of other backgrounds present in the data. In the third and final part of the analysis, we model the beta spectrum of  $^{32}\text{Si}$  and  $^{32}\text{P}$ . To study the beta decay spectrum of  $^{32}\text{Si}$  and  $^{32}\text{P}$ , we compare various software models to the theoretical Fermi curve. Among the software options (DECDATA, Rad ToolBox, and Betashape), Betashape closely matches the Fermi theory spectrum. We utilize Betashape, developed by Laboratoire National Henri Becquerel (LNHB), which incorporates experimental data from the Decay Data Evaluation Project (DDEP). The spectra from Betashape for  $^{32}\text{Si}$  and  $^{32}\text{P}$  exhibit deviations of approximately 2% and 5% from the theory, respectively. The analysis is in progress, and the systematic uncertainties will be calculated. Finally, we will use a likelihood analysis with inputs from the CDMS II Si data, beta decay spectrum of  $^{32}\text{Si}$  and  $^{32}\text{P}$  from Betashape, and the simulated background model discussed above. The

precise measurement of  $^{32}\text{Si}$  is crucial not only for the SuperCDMS SNOLAB but also important for all the rare event search experiments that use Si detectors.



## Noise and Optimal Filter algorithm

### A.1 Preliminaries: Fourier transforms and convolution theorem

To begin with the noise power spectral density, Fourier transforms are defined. The forward and reverse Fourier transforms of  $p(t)$  defined as  $\tilde{p}(f)$ :

$$\begin{aligned}\tilde{p}(f) &= \int_{-\infty}^{\infty} dt p(t) e^{-j\omega t} \\ p(t) &= \int_{-\infty}^{\infty} df \tilde{p}(f) e^{j\omega t}\end{aligned}\tag{A.1}$$

For convinience,  $\omega \equiv 2\pi f$  is used so that the correspondence  $\frac{d}{dt} \leftrightarrow j\omega$  and  $df = \frac{d\omega}{2\pi}$  which is made to express  $\tilde{p}(f)$  in units of volts/Hz if  $p(t)$  carries a unit of volts.

#### A.1.1 Convolution theorem

The convolution theorem is defined as:

$$\tilde{p}(f)\tilde{q}(f) \xleftrightarrow{\mathcal{FT}} [p * q](t) \equiv \int_{-\infty}^{\infty} dt_1 p(t_1) q(t - t_1)\tag{A.2}$$



where  $[p * q](t)$  describes the convolution of  $p$  and  $q$ . If  $p$  and  $q$  have units of volts then the unit of the convolution will be  $\text{volts}^2/\text{Hz}$ . The convolution has the property:

$$[p * q](t) = [q * p](t) \quad (\text{A.3})$$

The convolution theorem is a helpful concept for understanding linear systems, including filters. It states that the behavior of a linear system can be easily analyzed in the frequency domain through multiplication by a transfer function. This theorem establishes a relationship between the filter's characteristics in frequency space and its behavior over time.

Now, using the convolution theorem one can define cross-correlation of  $p$  and  $q$  (with same the units),  $[p \otimes q](t)$ :

$$\begin{aligned} \tilde{p}^*(f)\tilde{q}(f) &\xleftrightarrow{\mathcal{FT}} [p \otimes q](t) \equiv \int_{-\infty}^{\infty} dt_1 p(t_1) q(t + t_1) \\ &= \int_{-\infty}^{\infty} dt_1 p(t_1 - t) q(t_1) \end{aligned} \quad (\text{A.4})$$

The cross-correlation and convolution is related by a time reversal:

$$[h \otimes g](t) = [g \otimes h](-t) \quad (\text{A.5})$$

## A.2 Noise Power spectral density

In many cases, the variations in a voltage signal are assumed to follow a Gaussian distribution,  $a(t)$ , meaning they behave like random numbers. This distribution is characterized by its variance  $\langle [a(t)]^2 \rangle$  (for simplicity we assume  $\langle a(t) \rangle = 0$ ), which tells us how much the signal fluctuates on average. However, this variance alone does not tell us everything about the noise characteristics in the system. It does not include information about how the signal at one time relates to the signal at another time. This is important because in real

systems, there can be correlations between fluctuations at different times. For example, if there is a temperature change at one moment, it takes some time for the system to adjust and for that change to affect the temperature later on. This relationship between fluctuations at different times is described by something called the autocorrelation function,  $C(\tau)$ .

$$\begin{aligned}
 C(\tau) &= \langle a(t)a(t+\tau) \rangle \\
 &= \lim_{T \rightarrow \infty} \frac{1}{2T} [a \otimes a](\tau) \\
 &= \lim_{T \rightarrow \infty} \frac{1}{2T} \int_{-T}^T dt a(t) a(\tau + t)
 \end{aligned} \tag{A.6}$$

The definition of autocorrelation differs from cross-correlation by a factor of  $2T$ . This adjustment is made to ensure that the autocorrelation function has meaningful units. Since the signal  $a(t)$  extends infinitely into the past and future, the integral for autocorrelation would be infinite. Adding the factor of  $2T$  makes it finite.

These correlations between signal fluctuations are also reflected in the frequency spectrum of the noise. The Fourier transform of the autocorrelation function gives us the noise power spectral density (PSD), denoted as  $N(f)$ .

$$N(f) = \lim_{T \rightarrow \infty} \int_{-T}^T dt C(t) e^{-j\omega t} \tag{A.7}$$

$N(f)$  has a unit of  $V^2/\text{Hz}$ . All noises must decrease at higher frequencies, or else the noise PSD ( $N(f)$ ) would not approach zero as the frequency ( $f$ ) increases without bound, causing the autocorrelation function ( $C(t)$ ) to become infinite. Perfect “white noise” where  $N(f)$  is constant, does not actually exist. However, any noise that follows a particular pattern can be considered white for frequencies much smaller than the reciprocal of the characteristic time constant. This indicates that, for times much larger than the characteristic time constant, the autocorrelation function tends to zero, meaning the noise appears uncorrelated over

time. So the PSD can be defined as:

$$C(t) = \int_{-\infty}^{\infty} df N(f) e^{j\omega t} \quad (\text{A.8})$$

and

$$\langle [a(t)]^2 \rangle = C(0) = \int_{-\infty}^{\infty} df N(f) \quad (\text{A.9})$$

This expression justifies  $N(f)$  represents the frequency behaviour of the noise. The integral of the noise PSD provides the noise variance over time. The units of  $N(f)$ ,  $\text{V}^2/\text{Hz}$ , make sense in this context. The quantity commonly discussed in noise spectra is  $\sqrt{N(f)}$ , which has units of  $\text{V}/\sqrt{\text{Hz}}$ . Usually, the context or units clarify whether  $J(f)$  or its  $\sqrt{J(f)}$ , is intended when mentioning “power spectral density”. This relationship can serve as a validation tool to ensure that calculation routines have been implemented correctly.

### A.3 Optimal filter algorithm

In an optimal filter (OF) fit, the goal is to estimate the amplitude of a signal with a known shape by maximizing the signal-to-noise ratio. This is achieved by minimizing a  $\chi^2$  parameter in frequency space, which involves transforming the signal traces into the frequency domain using Fourier transformations. The OF fit is preferred over a simple time-domain  $\chi^2$  minimization because non-white noise can create correlations in the time domain fit, whereas in the frequency domain fit, the noise tends to be uncorrelated between different frequency bins. A real pulse can be defined as:

$$p(t) = Av(t) + n(t) \quad (\text{A.10})$$

where,  $v(t)$  is the pulse template (true pulse shape normalised to have peak height of 1),  $A$  is the amplitude to be calculated and  $n(t)$  is the Gaussian noise. Let the noise PSD be

given as  $N(f)$ . We want to find the ‘best’ estimator for  $A$ . This is determined by the  $\chi^2$  value, which measures how well the event fits the expected pulse shape.

$$\chi^2 = \int_{-\infty}^{\infty} df \frac{|\tilde{p}(f) - A\tilde{v}(f)|^2}{N(f)} \quad (\text{A.11})$$

We can easily find the best estimator  $\hat{A}$  by minimizing the  $\chi^2$  value with respect to  $A$ ,  $\partial\chi^2/\partial A|_{A=\hat{A}} = 0$ :

$$\hat{A} = \frac{\int_{-\infty}^{\infty} df \frac{\tilde{v}^*(f)\tilde{p}(f)}{N(f)}}{\int_{-\infty}^{\infty} df \frac{|\tilde{p}(f)|^2}{N(f)}} \quad (\text{A.12})$$

With variance

$$\sigma_A^2 = \left[ \int_{-\infty}^{\infty} df \frac{|\tilde{v}(f)|^2}{N(f)} \right]^{-1} \quad (\text{A.13})$$

This formula is very valuable. It shows the highest resolution we can achieve based on the assumed pulse shape and noise power spectral density. It helps us assess whether the fitting process is performing as expected. In theoretical comparisons of various particle detection methods, this formula can be used to estimate the best possible performance of each method.

Sometimes, the start time of the pulse in the signal trace may differ from the start time of the template. In such cases, an additional delay term  $t_0$  is included in the signal definition, which becomes

$$p(t) = Av(t - t_0) + n(t) \quad (\text{A.14})$$

The delay  $t_0$  is then determined using the same  $\chi^2$  minimization method described earlier. A detail discussion can be found in [1, 2].

## Bibliography

- [1] Sunil Ramanlal Golwala. “Exclusion limits on the WIMP nucleon elastic scattering cross-section from the Cryogenic Dark Matter Search”. PhD thesis. University of California, Berkeley, 2000.

- [2] Mark David Pepin. “Low-Mass Dark Matter Search Results and Radiogenic Backgrounds for the Cryogenic Dark Matter Search”. PhD thesis. Minnesota U., 2016.